Departamento de Física Teórica

Universidad Autónoma de Madrid

Beam Test of the Drift Tube Track Finder Muon Trigger at CMS

Memoria del Trabajo de Iniciación a la Investigación realizado por
Ignacio Jiménez Alfaro
presentada ante el Departamento de Física Teórica
de la Universidad Autónoma de Madrid
para la obtención del Diploma de Estudios Avanzados.

Trabajo de Iniciación a la Investigación tutelado por
Dr. Jorge Fernández de Trocóniz

Madrid, Marzo 2006

Contents

Chapter 1

Introduction

The High Energy Physics Community is involved in the construction of the next generation particle accelerator, the Large Hadron Collider (LHC). Experimental results from the latest 50 years have lead to the verification of the Standard Model as the correct framework describing the fundamental blocks of nature and their interactions. The most recent results have come from the Large Electron Positron (CERN, Switzerland), the Tevatron (FermiLab, USA) and HERA (DESY, Germany).

However, a prominent piece is still missing in the Standard Model puzzle. Within the Standard Model, particles obtain their masses through the interaction with the Higgs field. Such mechanism demands the existence of the Higgs boson, a fundamental particle so far undetected at experiments. LEP experiments established a lower limit (114.4 GeV at a 95% confidence level) to the Higgs boson mass [1], while experiments at the Tevatron have established an upper limit on its production cross section at hadron colliders [2] [3].

The LHC machine will make collide protons at a center-of-mass energy of 14 TeV and at a design luminosity of $\mathcal{L} = 10^{34}$ cm^{-2}s^{-1}. The main goal of the LHC experiments will be the discovery of the Higgs boson. The LHC parameters were designed to ensure that the full allowed Higgs mass range is covered. The second goal is discovery of new physics. Many theoretical models extend the Standard Model, as Supersymmetry, while adding to its consistency and/or predictive power. LHC collisions will allow to search for experimental evidence of these models. Third, the LHC will allow measurements of many Standard Model parameters with unprecedented accuracy. Finally, the LHC programme includes the study of the quark-gluon plasma in heavy ion collisions.

Four experiments are currently being installed at different points of the LHC tunnel: two general purpose experiments, ATLAS and CMS; one experiment for the study of CP-violation in the B-meson sector, LHC-b; and another for the study of heavy ion collisions, ALICE. The work presented in this report has been developed within the CMS Collaboration.

At the LHC, proton beams will cross each other at a rate of 40 MHz. At the design luminosity ($\mathcal{L} = 10^{34}$ cm^{-2}s^{-1}) and considering the total inelastic p-p cross section at 14 TeV, about 55 mb, an average of 17 head-on proton-proton inelastic collisions will take place at every bunch crossing (25 ns). Approximately 10^9 p-p collisions per second will deliver signals in the detector. Cross sections of processes involving new physics are $\mathcal{O}(1$

pb) or less. The corresponding rate is about 1 event every 100 s. Therefore, from every 10^{10} events produced, only 1 will be interesting from the point of view of discovering new physics.

High beam-crossing rates at the LHC, namely 40 MHz, are needed to achieve enough statistics for discovery in a reasonable period of time. The main drawback of such a high beam-crossing rate is related to the limited capacity of current mass storage devices. A typical event size is 1 MByte, leading to a data storage rate of 40 TBytes/s which is not reachable nowadays. Therefore, the event rate has to be reduced. The CMS Trigger system is responsible for this rate reduction. It has to decide whether to store an event on tape or reject it forever. At CMS, the Trigger system will reduce the event rate to a maximum of 100 MB/s, approximately 5 orders of magnitude.

The purity considerations outlined above, combined with the high rate reduction that must be achieved, make triggering an outstanding issue for the CMS experiment. The CMS Trigger system must be able to select interesting physics signals with high efficiency and reject unwanted backgrounds every 25 ns, without dead time.

The CMS Trigger system is structured in two levels: a Level 1 (L1) Trigger , based on customized electronics; and a High Level Trigger (HLT), running in a farm of commercial processors. The task of the L1 Trigger is to reduce the event rate from 40 MHz to 100 kHz which is the maximum input rate admitted by the HLT. The HLT will reduce the rate from 100 kHz to 100 Hz. The L1 Muon Trigger is particularly important due to the central role played by muons in the physics studied at CMS. Triggering on muons is performed by processing the information from the different muon detectors, Drift Tube (DT) chambers, Cathode Strip Chambers (CSC) and Resistive Plate Chambers (RPC).

The work presented in this report is related to the Drift Tube Track Finder (DTTF) Muon Trigger system. The DTTF implements the Regional Trigger of the CMS Drift Tube detector. In particular, the analysis of the DTTF performance at the 2004 CERN Beam Test is presented. It was the first time that the complete Drift Tube Trigger chain was faced with real muons.

The report is structured as follows: the LHC and the CMS experiment general features, as well as a brief summary of the main physics goals pursued, are described in Chapter 2. The CMS Trigger system, especially the Level 1 Muon Trigger system, is explained in Chapter 3. The DTTF Trigger motivation, hardware implementation and expected performance are discussed in detail in Chapter 4. A complete description of the work developed before, during, and after the 2004 Beam Test is given in Chapter 5 and Chapter 6. First, the experimental setup and the tools used at the Beam Test are described in Chapter 5. Then, the complete Beam Test data analysis is presented in Chapter 6, including results on muon efficiency, background rejection power and transverse momentum resolution. Finally, Chapter 7 summarizes the most important results.

Chapter 2

The LHC and the CMS experiment

2.1 The Large Hadron Collider

The Large Hadron Collider (LHC) [4] project was approved by the CERN Council in December 1994. This machine will store and collide protons at a center-of-mass energy of 14 TeV, one order of magnitude higher than the highest energies reached at current colliders (Tevatron).

Bunches of $1.05 \cdot 10^{11}$ protons will collide every 25 ns. The bunches will be 7.5 cm long and will have a transverse section of 15.9 μm. The LHC will reach a maximal luminosity of $\mathcal{L} = 10^{34}$ cm^{-2}s^{-1}, two orders of magnitude higher than current colliders. However, during the startup phase, the LHC will run at a lower luminosity ($\mathcal{L}_{low} = 2 \cdot 10^{33}$ cm^{-2}s^{-1}).

In addition to p-p collisions, the LHC will collide heavy ion beams with a center-of-mass energy of more than 1000 TeV and a luminosity in excess of 10^{27} cm^{-2}s^{-1}. The LHC is being constructed at CERN and it is expected to start operating in 2007.

The LHC is currently being installed in the LEP 27 km long tunnel. In order to reach a center-of-mass energy of 14 TeV, protons will be accelerated through five different stages. Accelerator devices which already existed at CERN will be used. Fig. 2.1 shows the schematics of the LHC accelerator complex. The LINAC2 will accelerate protons to 50 MeV, then the BOOSTER will increase the energy to 1 GeV, the PS to 26 GeV, the SPS to 450 GeV and, finally, the LHC to 7 TeV. High magnetic fields are need to keep the 7 TeV proton beams within the circular trajectory of the 27 km LHC tunnel. Superconducting dipoles have been designed to provide a maximum magnetic field of 8.36 T. Such dipoles are cooled to 1.9 K by a cryogenic system that uses superfluid Helium. The system is formed by a total number of 1296 dipoles.

Proton bunches will collide in four different points of the beam pipe. A different experiment will detect the collisions' products at each of these points. Two general purpose experiments will be located at opposite points of the ring, 'A Toroidal LHC ApparatuS' (ATLAS) and the Compact Muon Solenoid (CMS). A detector designed to study heavy ion collisions (ALICE) and another one dedicated to the study of the b-quark physics (LHC-b) complete the experiments that will study the LHC physics. Fig. 2.2 shows the schematics of the LHC tunnel and the location of the four experiments.

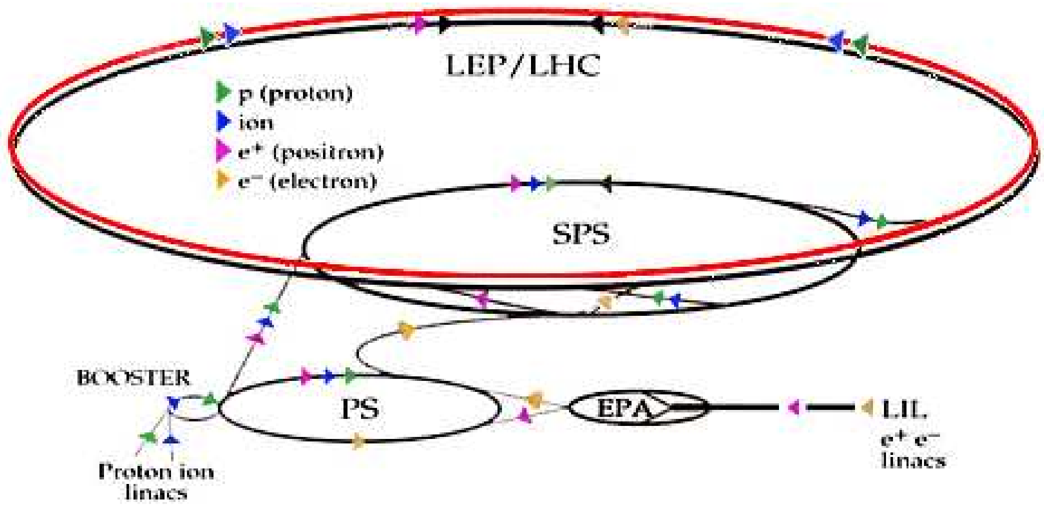

Figure 2.1: *Schematic view of the CERN accelerator complex.*

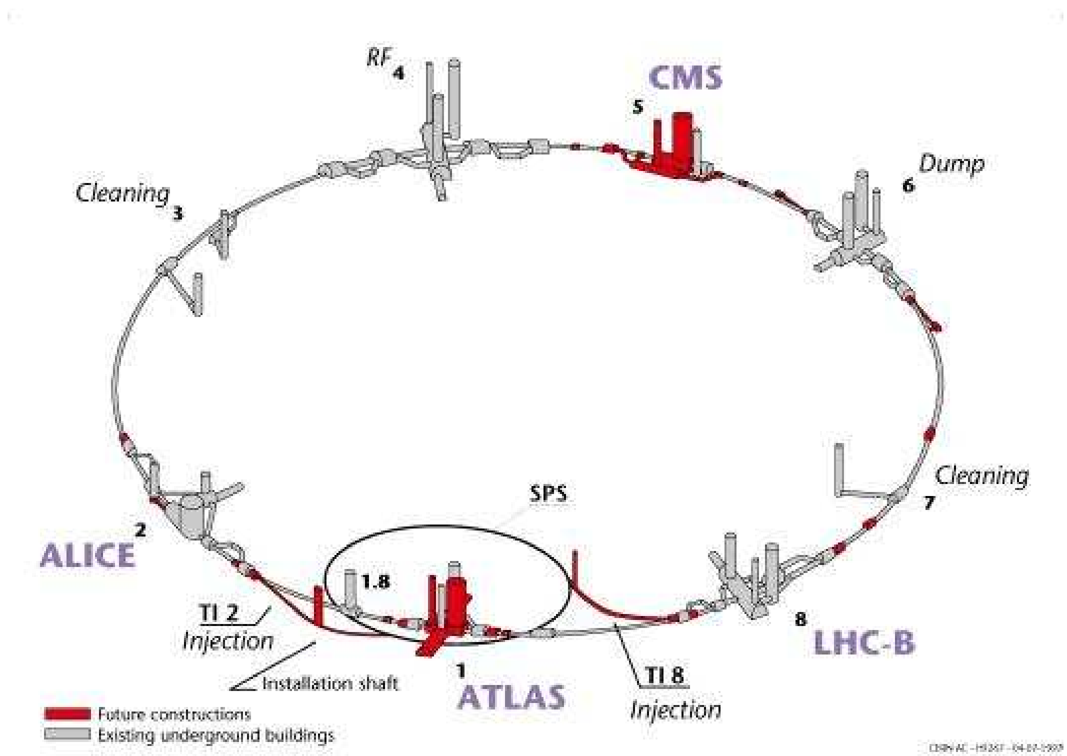

Figure 2.2: *Layout of the the LHC tunnel with the four experiments: ALICE, ATLAS, CMS and LHC-b.*

2.2 Physics Goals at the LHC

It is expected that processes which could not be observed in previous accelerators will be reachable at the LHC center-of-mass energy and nominal luminosity. Cross sections and production rates (at the LHC nominal luminosity) of some interesting processes are shown in Fig. 2.3. The expected total inelastic cross section at the LHC is very high (about 55 mb), thus high event rates will be reached. Processes that could not be produced at previous accelerators (namely LEP and Tevatron) will be observable at the LHC. The drawback is that cross sections and production rates at the LHC vary by many orders of magnitude. The $b\bar{b}$ production cross section will be about 500 μb. Production cross section of processes involving new physics (Higgs boson production) will be $\mathcal{O}(1 \text{ pb})$, or less. Due to the big difference between the event rate production of already known processes and of those involving new physics, triggering is a main task for new physics discovery at the LHC experiments.

The physics programme of the LHC experiments is discussed in the following.

2.2.1 Standard Model Higgs

All experimentally known particle physics phenomena are described by the Standard Model (SM). However, many theoretical questions still remain unanswered. Among them, the most important is the origin of particle masses and its hierarchy. Within the Standard Model, particles obtain mass by their interaction with the Higgs field. This implies the existence of a new particle, the Higgs boson, which mass is not predicted by the Standard Model.

The search of the Standard Model Higgs particle is the most important task of the two general purpose experiments at LHC, ATLAS and CMS. Its mass and its coupling to massive particles, as well as its quantum numbers, have to be measured.

For several years, LEP and the Tevatron have been operating in an energy range which allows its search. A lower limit of 114.4 GeV (95% C. L.) was set by LEP experiments [1]. More restrictive limits, excluding a mass below 130 GeV, coming from the Tevatron will have to wait until the end of 2007. An upper limit of approximately 1 TeV is imposed by theory consistency arguments. At the LHC, the full allowed Higgs mass range, i.e. 100 GeV $\lesssim m_H \lesssim$ 1 TeV, will be explored.

The Higgs boson can be produced in proton-proton collisions through several mechanisms. The most important are listed in the following. Their corresponding Feynman diagrams are shown in the top of Fig. 2.4. In the bottom of the figure the corresponding production cross sections as a function of the Higgs boson mass are shown. The two main processes are:

- fusion of two gluons through a b- or t-quark loop: $gg \to H$. This process dominates the Higgs production, at least for $m_H \lesssim 150$ GeV.
- fusion of two bosons: $qq \to W^+W^-$, $ZZ \to Hqq$.

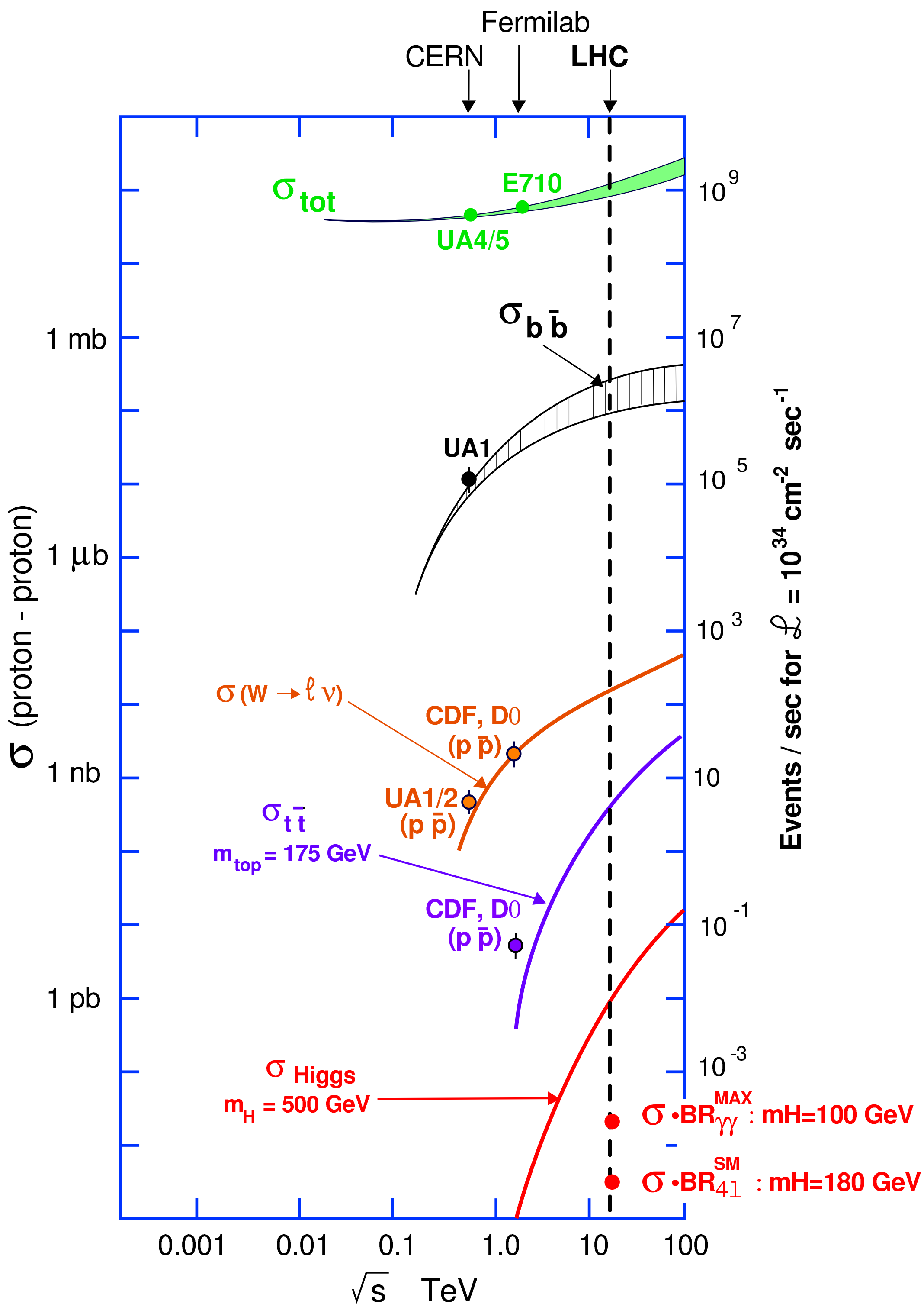

Figure 2.3: *Inclusive p-p cross sections for some physics processes as a function of the center-of-mass energy. In the right vertical axis the event production rates for the LHC design luminosity are plotted.*

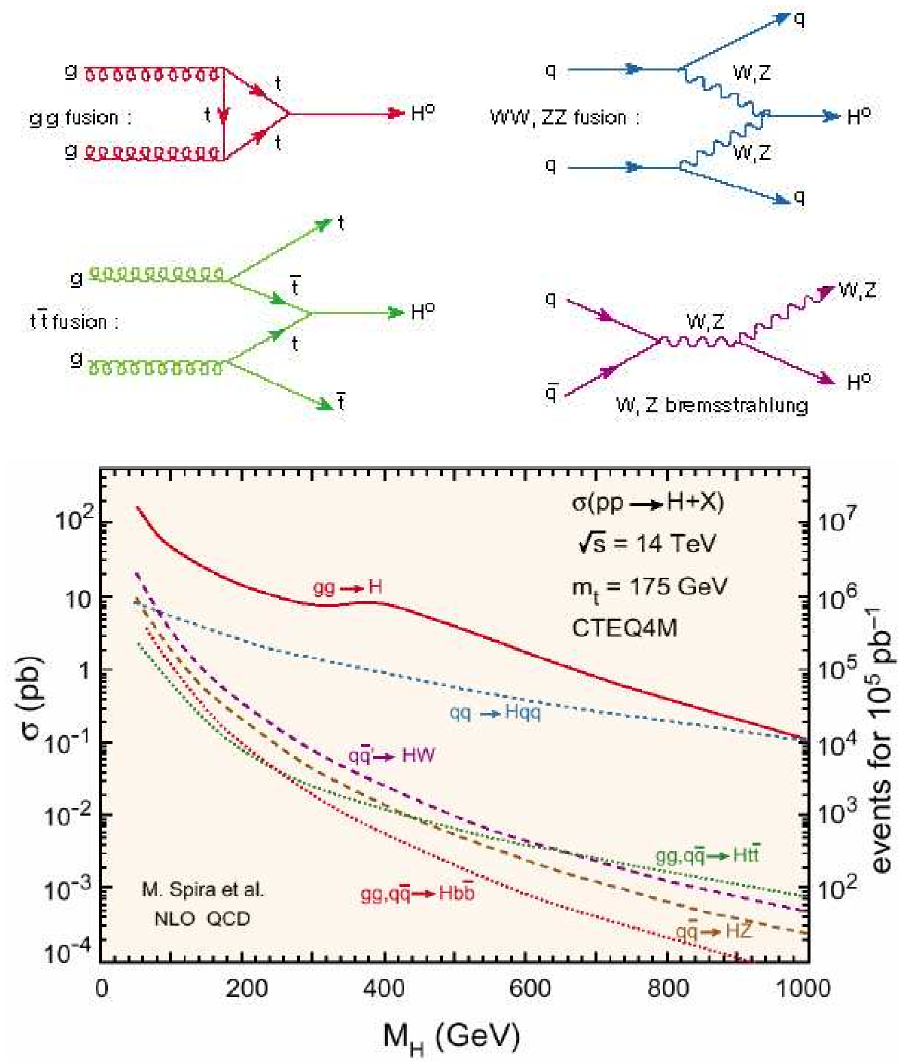

Figure 2.4: *Production of the SM Higgs boson at p-p collisions. Top: Feynman diagrams of the most important processes. Bottom: corresponding cross sections as a function of the Higgs mass.*

Decay channels

The Feynman diagrams of the different Higgs decay channels are shown in Fig. 2.5. The branching ratio of these channels are shown at the bottom of the figure. Even if the Higgs mass is still unknown, for a given mass the branching ratios for the several decay channels are fixed by theory. There is not a single decay channel that dominates the whole mass range from 100 GeV to 1 TeV. Therefore, different channels have to be investigated depending on the Higgs mass.

Although QCD Higgs production and decay dominates the overall event rate, those processes can not be easily resolved due to the overwhelming background. Therefore, decay channels with leptons or photons in their final states are preferred for Higgs discovery. The small branching ratios of these channels lead to low event production rates. However, cleaner experimental signatures are available. Table 2.1 summarizes the main Higgs discovery strategies at CMS depending on the Higgs mass. They will be briefly discussed in the following. The expected signal significance of these processes for an integrated luminosity of 10^2 fb^{-1} (one year of data taking at $\mathcal{L} = 10^{34}$ cm^{-2}s^{-1}) is shown in Fig. 2.6.

Higgs Mass Range (GeV)		Decay Channel
Lower Limit	Upper Limit	
100	150	$H \rightarrow \gamma\gamma$
130	200	$H \rightarrow ZZ^* \rightarrow 4l$
140	180	$H \rightarrow WW \rightarrow l\nu l\nu$
200	750	$H \rightarrow ZZ \rightarrow 4l$
500	1000	$H \rightarrow ZZ \rightarrow 2l2\nu$
~ 1000	~ 1000	$H \rightarrow WW \rightarrow l\nu + 2\ jets$
~ 1000	~ 1000	$H \rightarrow ZZ \rightarrow ll + 2\ jets$

Table 2.1: *Higgs Decay Channels exploited for discovery depending on its mass.*

At a Higgs mass below 150 GeV, the $H \rightarrow \gamma\gamma$ is the preferred channel for discovery. At this decay channel, the performance of the electromagnetic calorimeter is crucial. A very good mass resolution ($\frac{\Delta m_H}{m_H} < 1\%$) must be achieved. Besides, the main source of reducible background comes from events producing a γ and a $\pi^o \rightarrow \gamma\gamma$. In order to reduce this background, the electromagnetic calorimeter must achieve a very good impact parameter resolution so the two photons produced by the π^o can be resolved. This reducible background accounts for less than a 15% of the irreducible background, which comes from $qq \rightarrow \gamma\gamma$, $gg \rightarrow \gamma\gamma$ and isolated bremsstrahlung.

For a heavier Higgs boson scenario, decay channels including leptons are preferred. They can be used over a large mass range, namely 130 GeV $\lesssim m_H \lesssim$ 750 GeV. It has the cleanest experimental signature, specially in the four-muon channel, where the signal selection is based on the identification of two isolated oppositely charged muon pairs coming from a common vertex. In the following, we discuss the main experimental signatures expected in this mass range:

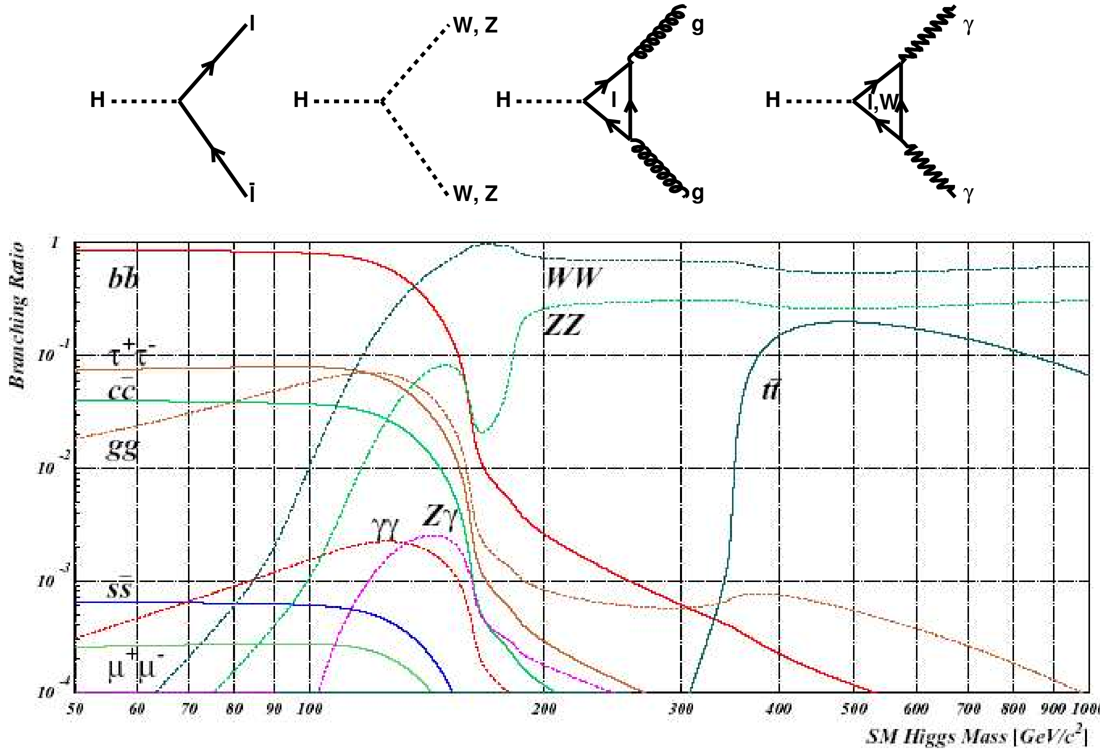

Figure 2.5: *Decay branching ratios of the Standard Model Higgs boson as a function of its mass.*

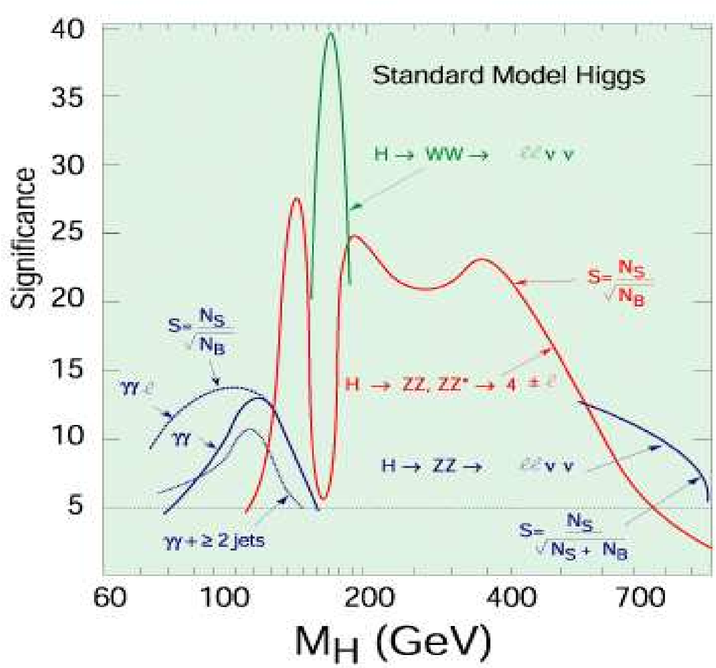

Figure 2.6: *Signal significance for the Higgs discovery channels as function of the Higgs boson mass for an integrated luminosity of* 10^2 fb^{-1} *(one year of data taking at* $\mathcal{L} = 10^{34}$ $cm^{-2}s^{-1}$*).*

- $m_H \leq 2m_Z$: In this mass range the most important decay channel is $H \rightarrow ZZ^* \rightarrow 4l$. As one of the Z's is off-shell, the event rate is low, thus high luminosity is required to observe these signal. When $m_H{\approx}2m_W$ this channel is suppressed and the $H \rightarrow WW \rightarrow l\nu l\nu$ has larger branching ratio and can be exploited. No mass peak can be reconstructed in this latter channel as there are two escaping neutrinos, therefore the background has to be known very well.

- $m_H > 2m_Z$: The $H \rightarrow ZZ \rightarrow 4l$ decay channel is preferred in this mass range. Two $Z \rightarrow \mu^+\mu^-$ mass peaks are well defined and both Z's can be reconstructed. This decay channel gives a very clear signal.

- $m_H >$ 500 GeV: the decay width increases and production rates decrease. Thus, channels with larger branching ratios, i.e. $H \rightarrow ZZ \rightarrow 2l2\nu$, $H \rightarrow WW \rightarrow l\nu{+}2\ jets$ and $H \rightarrow ZZ \rightarrow ll + 2\ jets$, must be used.

All these channels will be triggered by single-, di-muon triggers (or the corresponding electron triggers when $l = e$) and by combined triggers. Therefore, a good muon system, a high resolution tracker and an excellent calorimeter are needed.

2.2.2 Precise measurements of Standard Model parameters

In addition to the search of the remaining brick of the Standard Model, i.e. the Higgs boson, CMS will measure several Standard Model parameters with much more precision than preceding experiments did.

Electroweak interactions

Precise measurements of the the top quark and the W boson masses and of the couplings of the electroweak gauge bosons will be performed. These measurements will help to measure the parameters of the combined theory.

B-meson physics

Given the high production rate of b-quarks, CMS will be able to measure the decay of B-hadrons. It will help to measure the Cabibbo-Kobayashi-Maskawa (CKM) mixing matrix parameters, including precise measurements of CP-violation in B-mesons decays.

Strong interactions

Precision measurements of the strong coupling constant (α_S), as well as of the parton distribution functions will be performed.

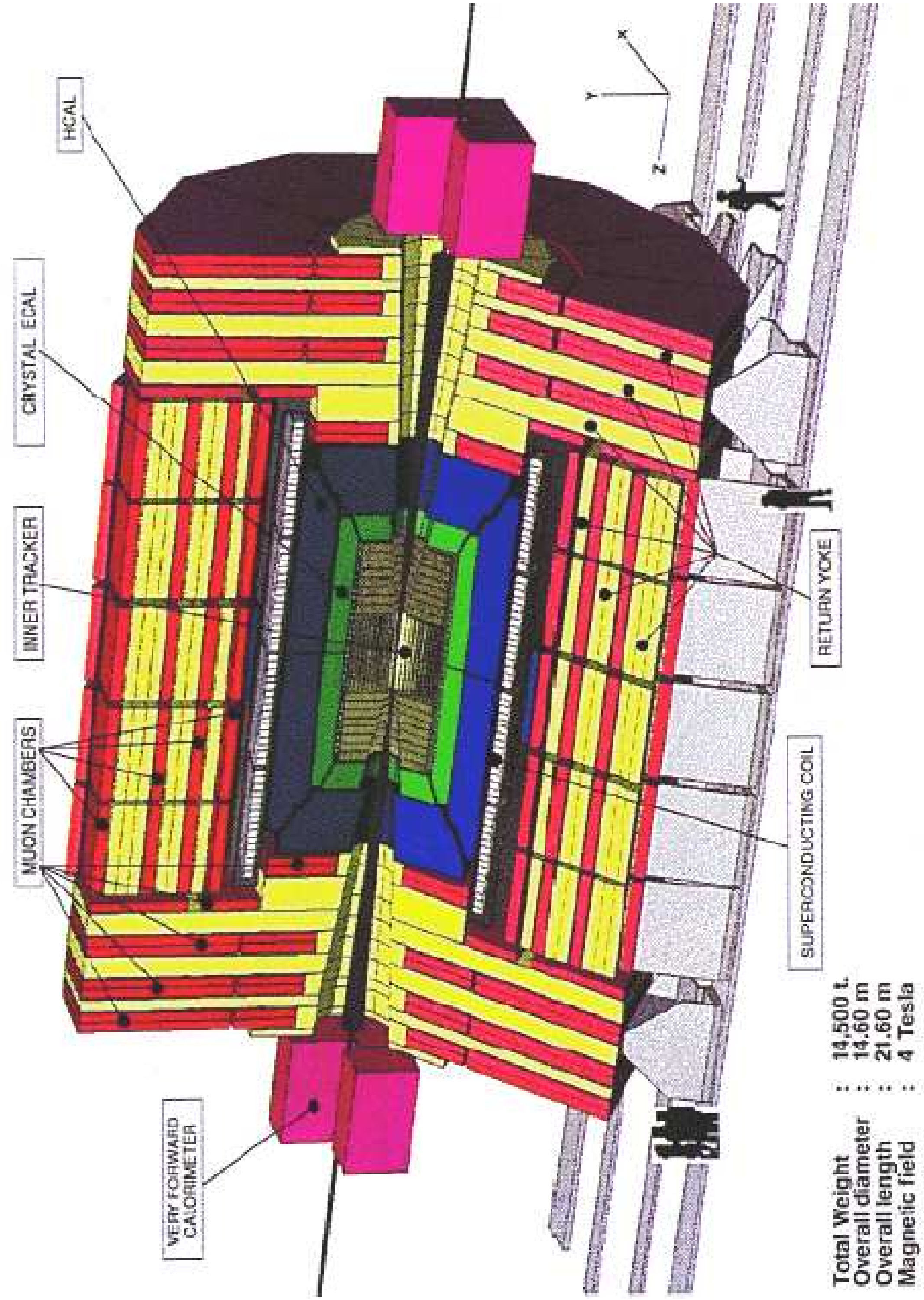

Figure 2.7: *Tridimensional CMS Elevation view.*

2.2.3 Physics beyond the Standard Model

Experiments at the LHC will search for experimental evidences of Supersymmetry (SUSY) and extra dimensions. Both theories predict new particles at the TeV scale. If they exist, they should be observed at the LHC.

In particular, connecting with the discussion in Section 2.2.1, the discovery of more than one Higgs boson would be a clear signature of new physics. For example, the Minimal Supersymmetric Model (MSSM) has five supersymmetric Higgs particles, two neutral scalars (h and H), one neutral pseudoscalar (A) and two charged ones ($H^{\pm}$).

2.2.4 Heavy Ion Physics

Finally, the LHC Heavy Ion collisions programme will allow to study the properties of a deconfined state of hadronic matter, the 'quark-gluon' plasma. Although both general purpose experiments, ATLAS and CMS, foresee the analysis of heavy ion collisions, a specially dedicated detector, namely ALICE, has been optimized for the detection of the phenomena associated to heavy ion collisions.

2.3 The CMS experiment

The Compact Muon Solenoid (CMS) [5] is one of the two multi-purpose experiments that will run at the Large Hadron Collider. It is designed to reconstruct the physics processes involved in the proton-proton and heavy ion collisions provided by the LHC machine.

After every LHC collision, different types of particles are produced at the interaction point (located at the center of the detector). Only particles with a mean lifetime over a threshold interact with the detector material. The production of the remaining particles is measured through their decay products. CMS is designed to measure with the adequate precision the properties of the particles that cross the detector. From this information, all interesting processes produced after the LHC collisions can be reconstructed.

2.3.1 Requirements

The physics goals described in section 2.2 defined the CMS detector design goals, which were outlined in [5]. They can be summarized in four main features:

- A very good and redundant muon system.
- The best possible electromagnetic calorimeter consistent with the muon system.
- A high quality central tracking compatible with the muon system and the electromagnetic calorimeter.
- A hermetic hadron calorimeter.

Based on this requirements, an overall compact design was chosen. It is a cylindrical structure of approximately 15 m of diameter and an overall length of 22 m. Fig. 2.7 shows a three dimensional elevation view of the detector. The main feature of CMS is the strong solenoidal magnetic field (4 Tesla) generated by a long (13 m) superconducting coil of large radius (3 m). Such a magnetic field configuration was chosen to ensure high transverse momentum resolution for charged particles.

2.3.2 Detector Overview

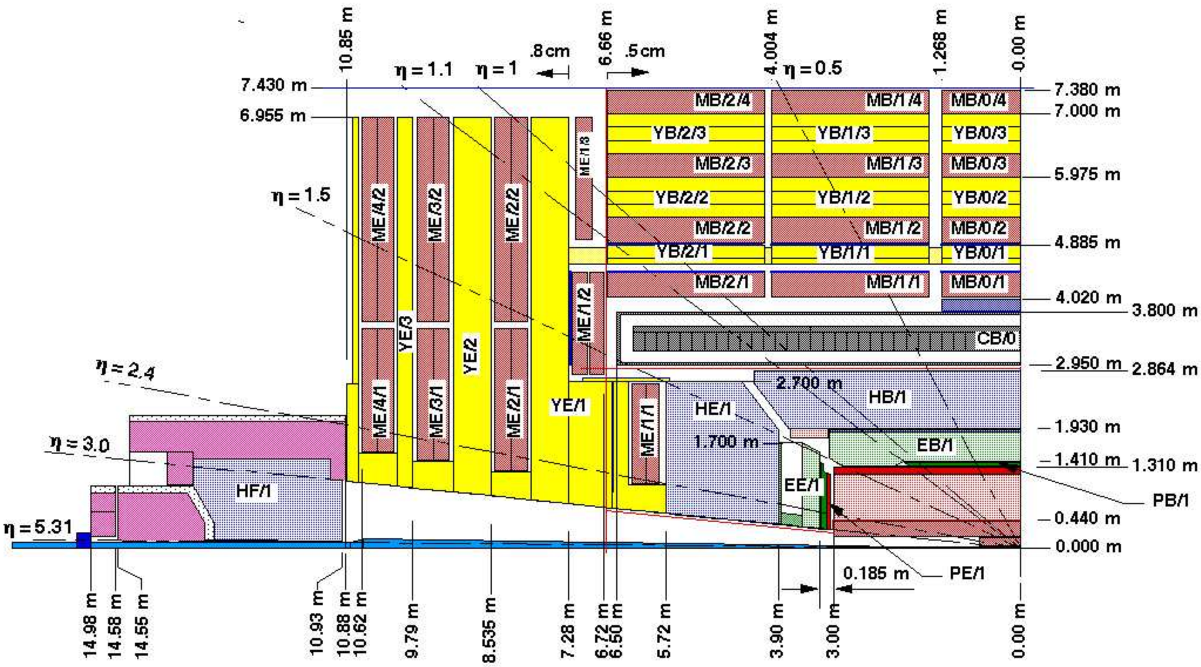

Figure 2.8: *Longitudinal view of the CMS detector.*

CMS is a general purpose experiment, thus the physics program of the collaboration requires the efficient detection of several type of particles. Particles expected to cross the detector are photons, electrons, muons, hadrons and neutrinos. All these particles must be identified and their energies, momenta and position within the detector measured. Due to the very different properties of the particles involved, it is not possible to achieve this goal with a single device by itself. Therefore, CMS is designed as a complex machine composed of several subsystems (subdetectors) organized in a cylindrical onion-like structure. Figs. 2.8 and 2.9 show a longitudinal and a transversal view of the detector, respectively.

Each subdetector is optimized for the measurement of a different set of physical properties of the particles to be detected. Combining the measurement of all the subdetectors it is possible to identify the particles produced in a collision and to determine

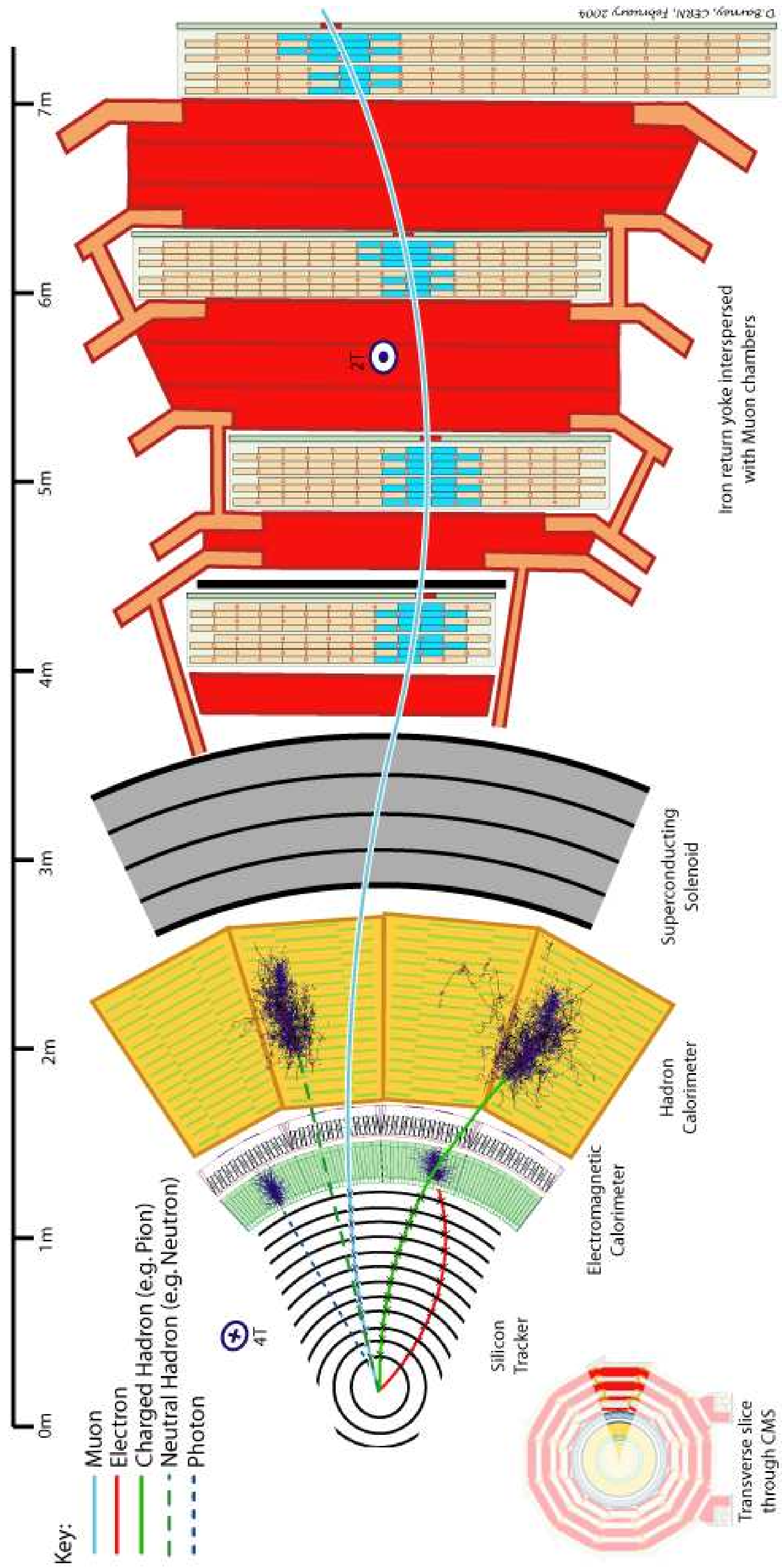

Figure 2.9: *Transverse slice of the CMS detector. The passage of different particles and their interaction with the detector elements are shown.*

their properties. From this information, the physics processes involved in a collision can be reconstructed. The task of each subdetector is illustrated in Fig. 2.9.

Starting from the beam pipe in the radial direction, the different subdetectors of which CMS is composed are organized as follows:

Embedded in the magnet, first there is a silicon inner tracker, composed of a pixel detector close to the vertex and a strip detector surrounding it. Charged particles, namely leptons (e, μ, τ) and charged hadrons, leave their signature when they pass through the tracker detector.

A crystal electromagnetic calorimeter and a copper scintillator hadron calorimeter are placed beyond the tracker inside the magnet coil. Photons, which do not leave any signal in the tracker, and electrons are stopped at the electromagnetic calorimeter. Neutral and charged hadrons are stopped at the hadronic calorimeter. High precision energy measurements, including missing and total transverse energy, are performed at the calorimeters.

The muon system is located outside the coil. It consists of four stations embedded in the magnetized flux return iron yoke, both in the barrel and in the endcaps of the detector. Muons, due to its high penetration power into matter, cross the calorimeters without being stopped. They are expected to provide clean signatures for the wide range of physics processes expected at CMS. Therefore, triggering on muons and achieving high precision measurements of their properties were decisive issues for the CMS detector design.

The only remaining particles to be detected are neutrinos. It is expected that neutrinos will not interact with the detector material, thus they can not be directly detected by the different subdetectors. Still, their passage through the detector can be indirectly detected as a lack in the energy measured. As protons are not elementary particles, the total energy can not be used. However, the total transverse energy is used. From it, the total missing transverse energy is calculated and used to measure the production of neutrinos in a LHC p-p bunch crossing. In order to do so, the detector must be as hermetic as possible. Very forward hadron calorimeters in the detector endcaps improve the detector geometrical coverage, fulfilling the requirement of a hermetic calorimeter.

In the following we will briefly describe each of the mentioned subdetectors, as well as the magnet system.

2.3.3 The Magnet

The CMS magnetic field (Fig. 2.10) is one of the most important aspects of the experiment. The measurement of the transverse momentum of charged particles crossing the detector is based on the bending of their trajectories caused by the magnetic field. The requirement for a good momentum resolution leads to the choice of a high magnetic field. Both toroidal and solenoidal fields could be considered. The CMS collaboration based its election of a solenoidal system on two main reasons. First, a strong bending in the transverse plane facilitates the task of triggers based on tracks pointing back to the vertex. Second, the momentum measurement in a solenoid starts at $r = 0$, thus, for a similar bending power, the overall size of a solenoidal system is smaller than that for a

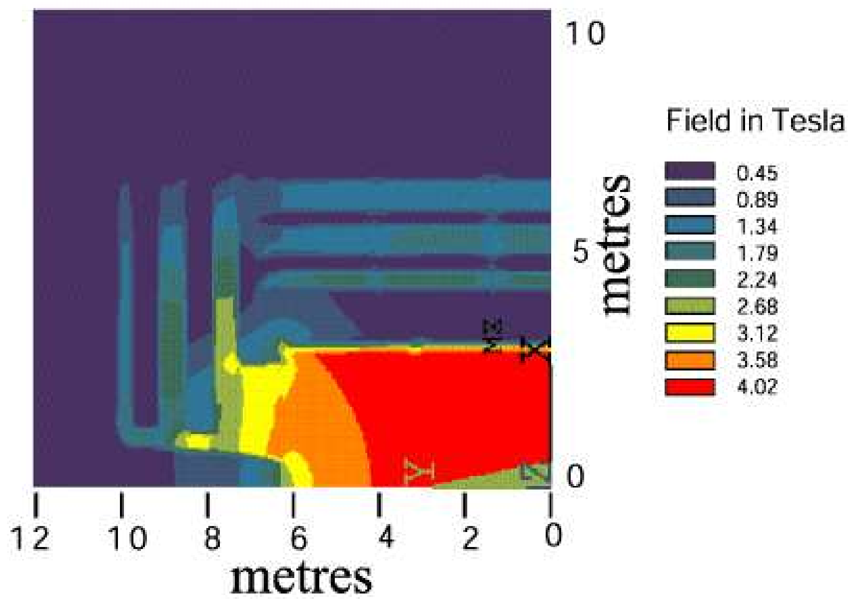

Figure 2.10: *The CMS solenoidal magnetic field. A maximum magnetic field of 4.0 Tesla is reached inside the solenoid.*

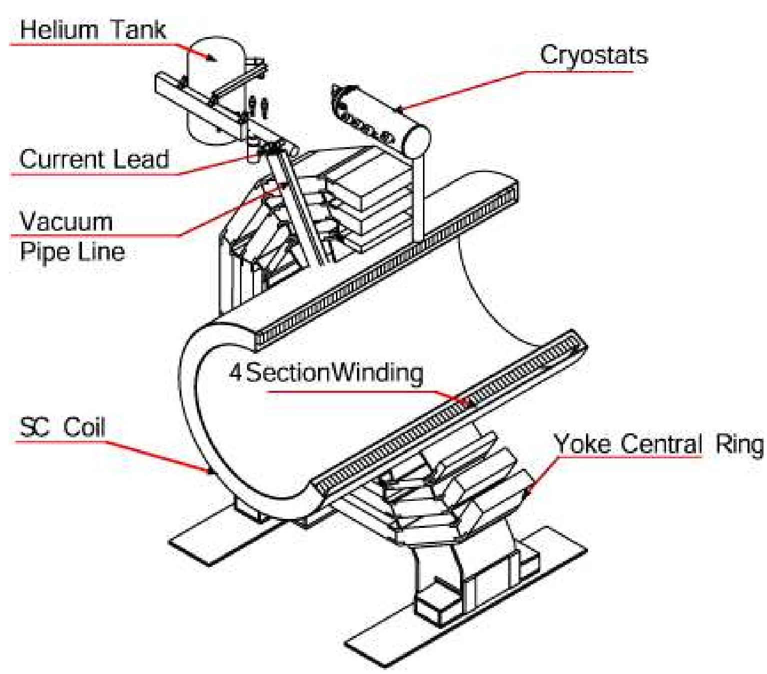

Figure 2.11: *A open view of the CMS magnet system. The superconducting coil is placed inside a vacuum tank.*

toroid.

The election of a 4.0 Tesla field was based on calculations that consider its benefits not only for the muon tracking and inner tracking but also for electromagnetic calorimetry. A high magnetic field allows to perform efficient muon triggers already at the first level trigger. The high momentum resolution (10% for 1 TeV muons) achieved with a 4 T field is a crucial feature for inner tracking tasks. Finally, the magnetic field reduces the flux of charged particles reaching the electromagnetic calorimeter and allows an accurate calibration of it.

The magnetic field is implemented by the Magnet system [6]. The CMS magnet system (Fig. 2.11) consists of a superconducting coil and the magnet yoke (barrel and endcap). The 4 Tesla field is generated by a long (L=13 m) superconducting solenoid with a diameter of 6.0 meters and without iron core inside it. The solenoid is composed of five different modules, built independently. The modules were assembled together at CERN keeping the coil in its vertical position (Fig. 2.12). During September 2005 the solenoid was swiveled to its horizontal position and inserted into the cryostat barrel (Fig. 2.13). In order to maintain the coil's superconducting properties, it will be cooled down by liquid helium to 2 K. The vacuum tank is made of stainless steel. It houses and supports the superconducting coil.

The magnetic flux generated by the coil is returned through an iron yoke. A 2.7 Tesla magnetic field is generated within the yoke, allowing muon tracking in this region. The iron yoke is composed of a barrel yoke (YB) and an endcap yoke (YE). The barrel yoke is a 12-sided cylindrical structure, divided into five rings. Each ring is formed of three iron layers. The endcap yoke consists of two endcaps. Each of them is built from three independent disks. When CMS starts up its operation the endcaps will be pulled towards the barrel by the 85 MN force generated by the magnetic field.

2.3.4 The Tracker

The CMS collaboration decided to use an all-silicon solution for the inner tracker system. The total area covered by it will be $\sim$220 m^2. This is the largest ever designed silicon detector surface.

The inner tracking detectors [7], [8] are designed to reconstruct isolated high-p_T tracks with an efficiency better than 95%, and tracks within jets with an efficiency of better than 90% over the region $|\eta| < 2.5$. It is also designed to allow the identification of tracks coming from detached vertexes. To fulfill these requirements the inner tracker detector has been split in two sub-detectors (Fig. 2.14).

The Silicon Pixel Tracker

Close to the beam pipe, where the density of tracks is larger, a highly granular design with layers of silicon pixels was chosen. Its main purpose is to measure the impact parameter of charged tracks allowing efficient tagging of jets originating from the decay of heavy hadrons containing b and c quarks.

Figure 2.12: *The CMS superconducting solenoid completely assembled in its vertical position.*

Figure 2.13: *Insertion of the CMS solenoid magnet into the cryostat barrel during September 2005. As the solenoid was assembled in its vertical position, before the insertion it had to be swiveled to its horizontal position.*

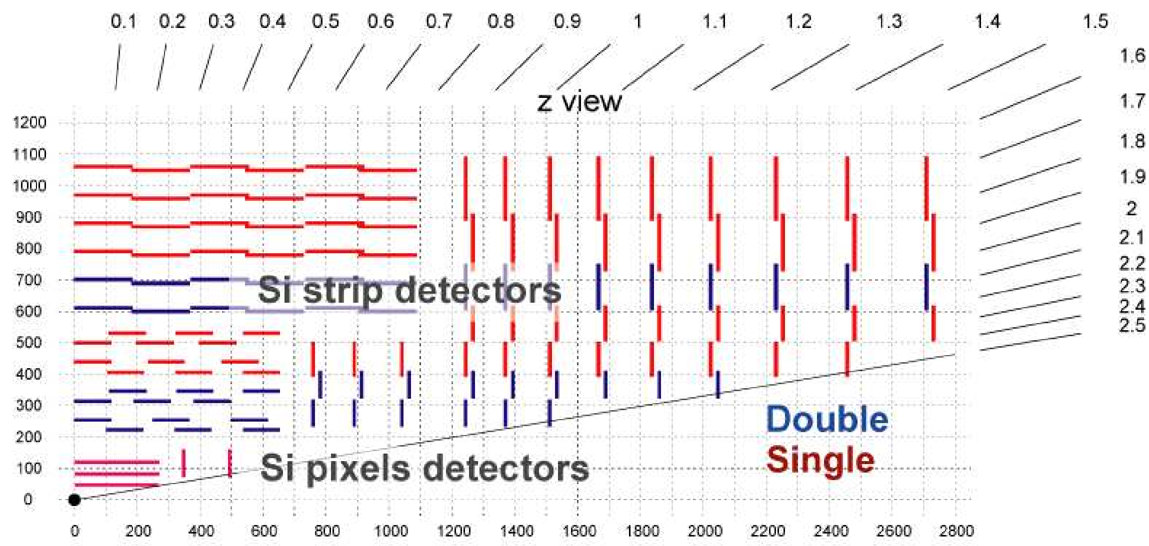

Figure 2.14: *CMS Inner Tracker Layout.*

There are two layers of pixel detectors in the barrel and two disks in each endcap. Each layer is composed of modular detector units. Each module consists of a thin, segmented (pixeled) sensor plate with highly integrated readout chips connected to them. Each pixel in a module has dimensions of 150×150 μm^2 and is able to achieve a resolution of 10-15 μm. A schematic representation of the pixel detector is shown in Fig. 2.15.

The Silicon Micro-strip Tracker

Further away from the beam pipe, where the density of tracks is lower, a silicon strip detector is used. Layers of one-sided silicon strip detectors, as well as layers equipped with two detectors mounted back-to-back (double sided) are used.

The Silicon Micro-strip Tracker can be split in an inner and an outer part. The inner part consists of four layer in the barrel (TIB) assembled in shells, the 2 first layers are double-sided, and two endcaps (TID) each composed of three small disks. Layers are 320 μm thick and their pitch size ranges between 60 and 270 μm. The length of the detectors varies between 7 and 12.5 cm.

The outer part is formed by six concentric layers (layer 1 and 2 are double sided) in the barrel (TOB) and two endcaps (TEC) each composed of 9 disks. The TEC ensures a pseudorapidity coverage of $|\eta| = 2.5$. Layers in this part are thicker (500 μm) while they have a pitch of 140 μm. A photo of one of the Silicon Strip Layers being constructed at Pisa (Italy) is shown in Fig. 2.16.

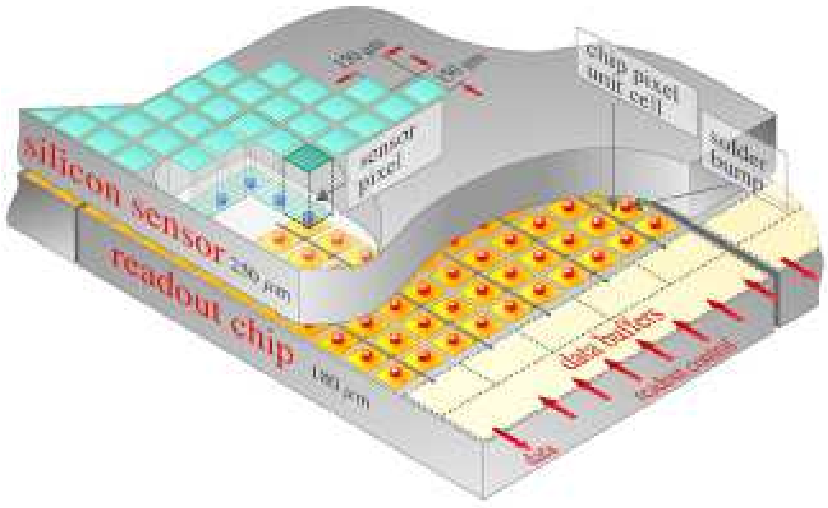

Figure 2.15: *Schematic view of the silicon pixel detector. Each of the silicon pixels is connected to its own electronic circuit by a tiny sphere measuring 15 to 20 microns in diameter.*

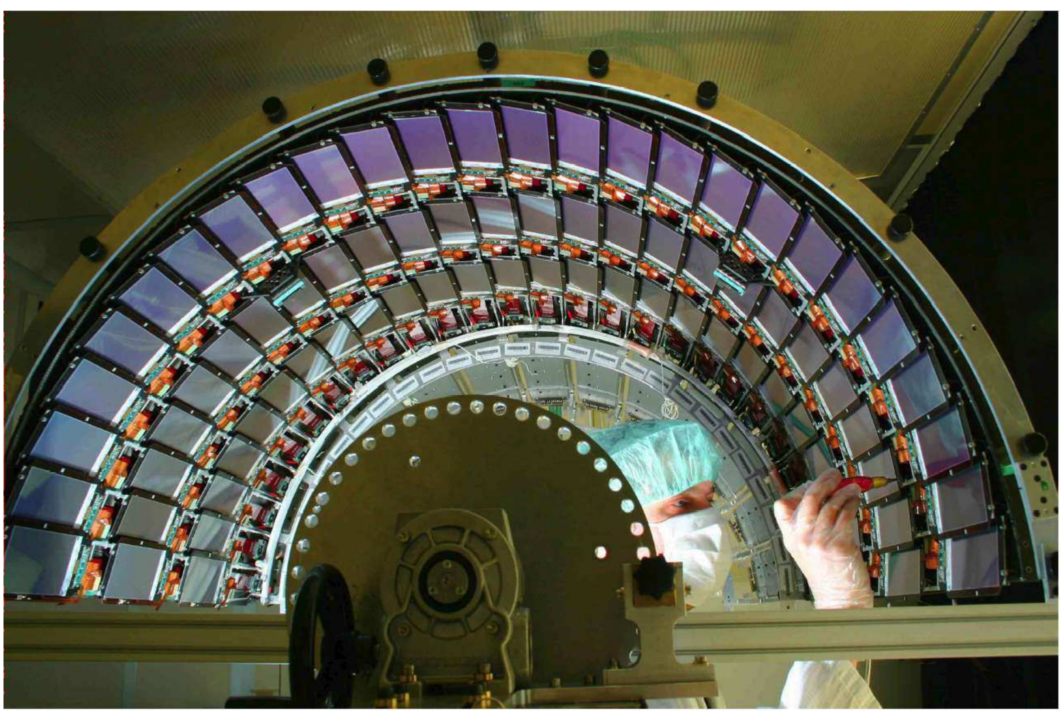

Figure 2.16: *Photo of a CMS Silicon Micro-Strip Tracker Layer being assembled at Pisa (Italy).*

2.3.5 The Calorimeters

The Electromagnetic Calorimeter

The electromagnetic calorimeter (ECAL) [9] is designed to reconstruct energy and direction of electrons and photons with high precision. For a Higgs boon with a a mass in the range 110-140 GeV, the decay $H \to \gamma\gamma$ will be the most clear discovery signature. This channel imposes the strictest performance requirement on the ECAL, namely a mass resolution of $\Delta m_H/m_H < 1\%$ must be achieved.

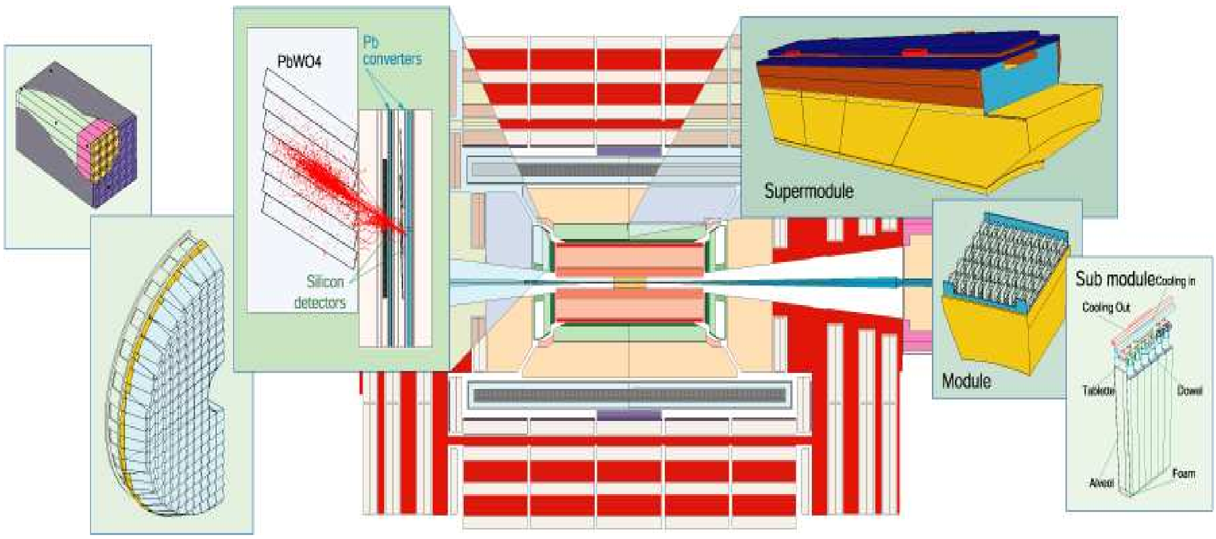

Figure 2.17: *Schematic representation of the CMS Electromagnetic Calorimeter.*

A homogeneous design has been chosen, consisting of over 80000 lead tungstate (PbWO4) crystals. PbWO4 is a fast scintillator which has high density, a small Molière radius and a short radiation length, allowing for a very compact system. The spatial arrangement and the dimensions of the crystals depend on their location within the detector. Two different regions (Fig. 2.17) can be distinguished: the barrel (EB) and the endcap (EE). In the barrel the crystals have a front face of about 22×22 mm^2 and a total thickness of 26 radiation lengths, corresponding to a crystal length of only 23 cm. In the endcaps the crystals are slightly wider, with rear faces measuring 30×30 mm^2, but are slightly shorter (22 cm). The light produced in the crystals is detected by silicon avalanche photo-diodes and vacuum photo-triodes in the barrel and endcaps, respectively. The coverage of the ECAL extends up to $|\eta| < 3$, but the high radiation dose of pile-up energy will limit precision energy measurements to the range of $|\eta| < 2.6$.

To provide $\gamma\gamma$ separation in π^o decays, the endcap region is equipped with a 'preshower' detector (PE), covering the region of $1.65 < |\eta| < 2.61$. It consists of two thin lead converters followed by silicon strip detector planes. The impact position of the electromagnetic shower is determined with very good accuracy (~300 μm at 50 GeV). Given the fine granularity of the detector, it is possible to separate single showers from overlaps of two close showers due to the photons from π^o decays.

The resolution of the energy measurement of the electromagnetic calorimeter is driven by three major parameters: the shower containment and photostatictics, the electronic noise and pileup energy and the intrinsic term. The full energy resolution is the sum in quadrature of these terms (Fig. 2.18) and is expected to be:

$$\frac{\sigma(E)}{E} = \frac{3\%}{\sqrt{E}} \oplus \frac{150\ MeV}{E} \oplus 0.40\% \tag{2.1}$$

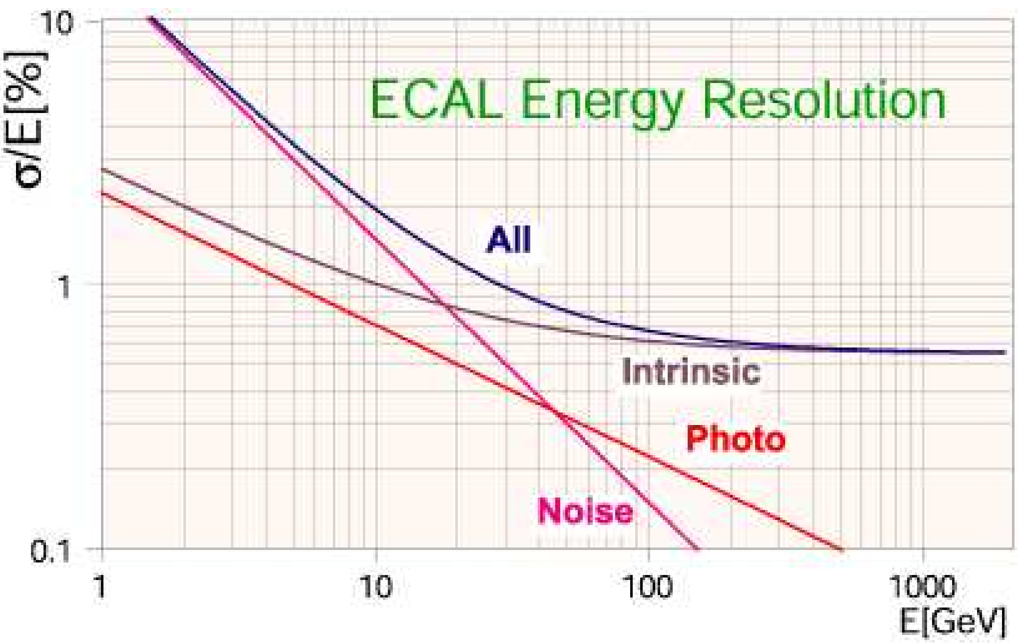

Figure 2.18: *Full energy resolution of the CMS Electromagnetic Calorimeter as a function of the energy.*

In October 2004 the first fully dressed ECAL supermodule was tested with high energy electrons. Results on the energy resolution were consistent with expectations (Expr. 2.1).

The Hadronic Calorimeter

The Hadronic Calorimeter (HCAL) [10], plays an essential role in the identification and measurement of quarks, gluons, and neutrinos by measuring the energy and direction of jets and of missing transverse energy. For good missing energy resolution, a hermetic calorimetry coverage to $|\eta| = 5$ is required. The HCAL will also collaborate in the identification of electrons, photons and muons in conjunction with the tracker, electromagnetic calorimeter, and muon systems.

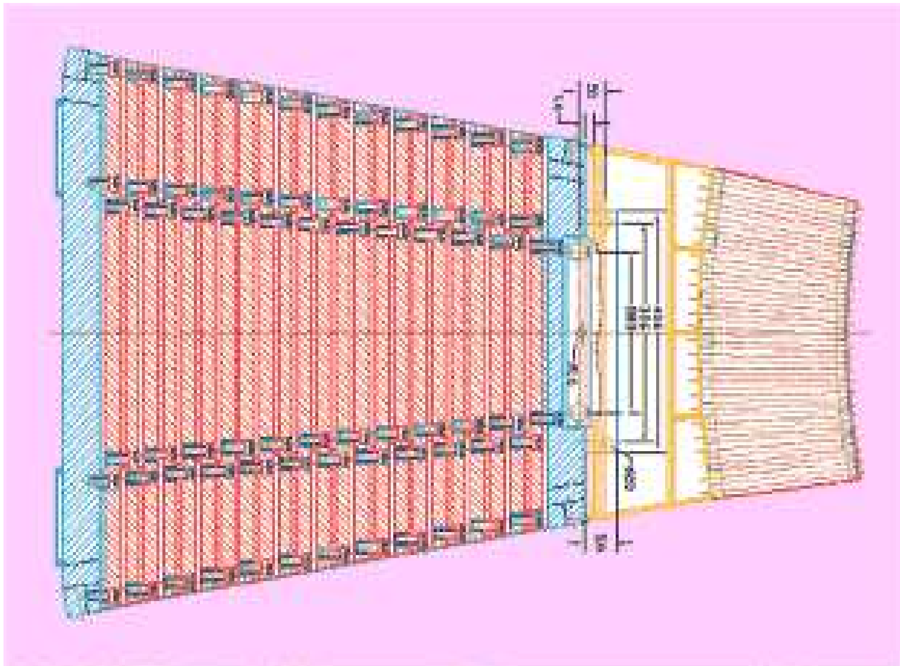

Figure 2.19: *Schematic representation of a transversal wedge of the Hadron Barrel (HB) Calorimeter detector.*

The HCAL consists of two separate systems: the central calorimeter, inside the magnet with a coverage up to $|\eta| < 3.0$, that is separated in a barrel (HB) and an endcap (HE) part, and the the very forward calorimeter (HF) which is placed around the beam pipe outside the muon system and extends the coverage up to $|\eta| < 5.3$.

The HB and HE calorimeters are sampling calorimeters with 50 mm thick copper absorber plates interleaved with 4 mm thick plastic scintillator tiles that are read out with wavelength shifting fibers. The light is detected by hybrid photo-diodes. The HB consists of two half-barrels each 4.3 meter long (Figs. 2.19 and 2.20). The HE (Fig. 2.21) consists of two large structures, situated at each end of the barrel detector and within the region of high magnetic field. Because the barrel HCAL inside the coil is not sufficiently thick to contain all the energy of high energy showers, additional scintillation layers (HO) are placed just outside the magnet coil. The full depth of the combined HB and HO detectors is approximately 11 absorption lengths.

The HF detectors cover the $3.0 < |\eta| < 5.3$ region outside the muon system around the beam pipe. Thus, they are situated in a harsh radiation field and cannot be constructed of conventional scintillator and wave-length materials. Hadronic showers are sampled at various depths by radiation-resistant quartz fibers, which are inserted into steel absorber plates. The energy of jets is measured from the Cerenkov light signals produced as charged particles pass through the quartz fibers.

The energy resolution of the HCAL is given by: $\frac{\sigma(E)}{E} = \frac{65\%}{\sqrt{E}} \oplus 5\%$ in the barrel, $\frac{\sigma(E)}{E} = \frac{85\%}{\sqrt{E}} \oplus 5\%$ in the endcaps and $\frac{\sigma(E)}{E} = \frac{100\%}{\sqrt{E}} \oplus 5\%$ in the forward part (HF). For all

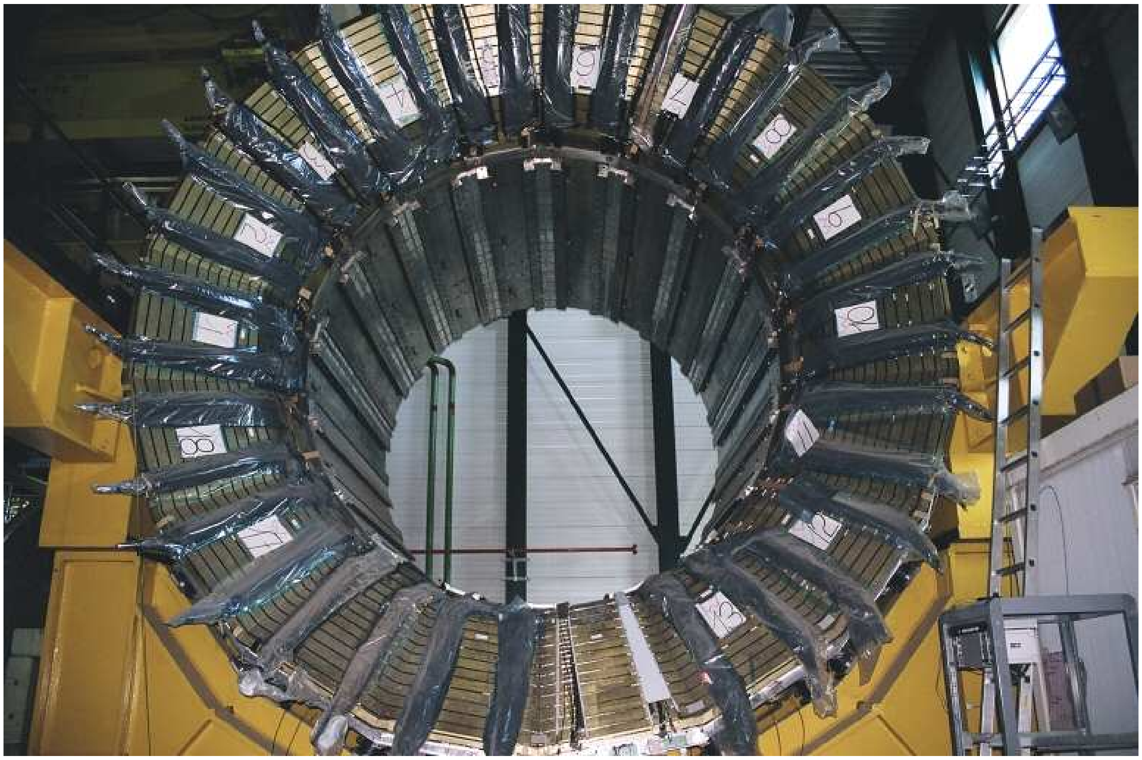

Figure 2.20: *Photo of the Hadron Calorimeter Barrel (HB) in the test-bench, ready for its calibration with cosmics and a radioactive source.*

Figure 2.21: *Photo of the Hadron Calorimeter Endcap (HE).*

the expressions, energy is measured in GeV.

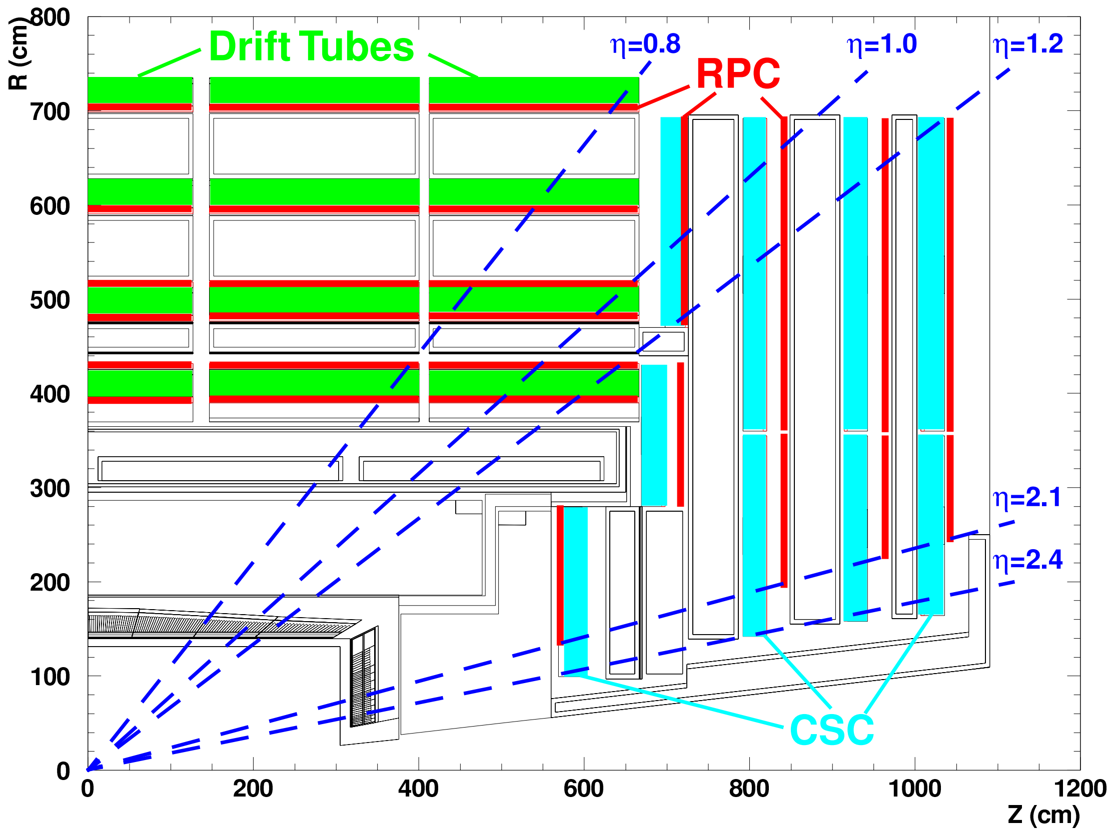

Figure 2.22: *Longitudinal view of the CMS muon system.*

2.3.6 The Muon System

The ability to trigger on and reconstruct muons is central to the concept of CMS, as the name reveals. The task of the Muon System [11] is to identify muons and provide, in association with the tracker, a precise measurement of their momentum. In addition, the system provides fast information for triggering purposes. The muon system consists of four stations integrated in the return yoke of the magnet. The yoke is organized in five wheels along the detector axis and four iron disks in each endcap.

CMS will combine three different technologies for precise muon detection and efficient triggering: drift tube (DT) chambers in the barrel region ($|\eta| < 1.2$), cathode strip chambers (CSC) in the forward region ($0.8 < |\eta| < 2.4$), and resistive plate chambers (RPC) in both regions ($|\eta| < 2.1$). Fig. 2.22 shows a longitudinal view of the CMS muon detectors.

Both, DT and CSC detectors, are tracking detectors equipped with bunch crossing identification capabilities. Thus, apart from reconstructing the passage of muons, they are able to generate a muon trigger. Mounted on both the DT and CSC chambers, the RPC detectors are dedicated trigger chambers which provide additional and complementary trigger information.

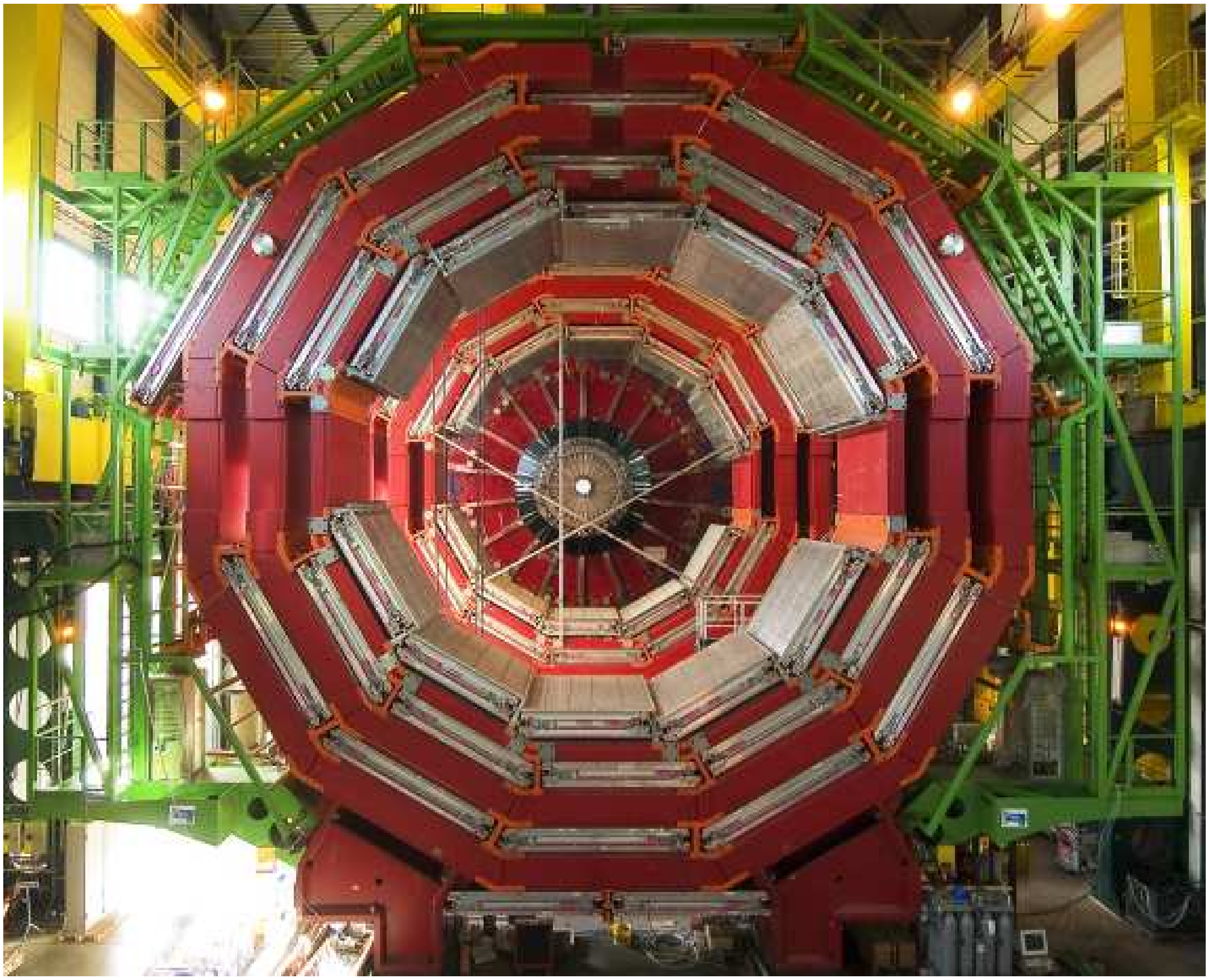

Figure 2.23: *Frontal view of two CMS wheels and one endcap. Muon chambers are being installed in the iron yoke.*

Drift Tube Chambers

The barrel muon system is organized in five wheels in the beam direction and four concentric stations in the radial direction: MB1, MB2, MB3, MB4. Each wheel is divided in twelve 30° wedges in azimuth.

The DT muon chambers are located in the gaps of the barrel iron yoke. The basic sensitive element of the chambers is a 40 mm$\times$11mm drift cell (Fig. 2.24) of approximately

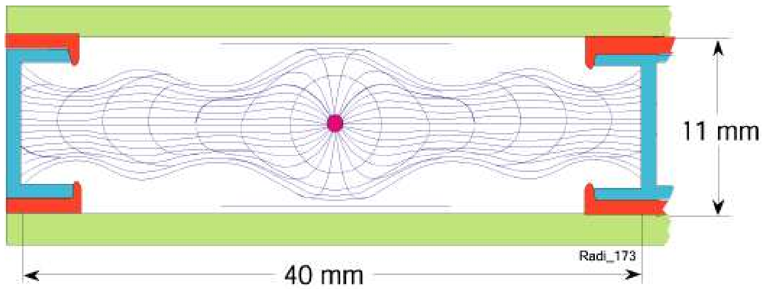

Figure 2.24: *Cross section of a Drift Tube. An electric field is generated inside the tube due to the different potential between the wire and the aluminum I-beams. Electrons from the gas, liberated by the crossing ionizing particle, move along the field lines to the wire.*

380 ns maximum drift time. When an ionizing particle passes through the tube, it liberates electrons which move along the field lines to the wire, which is at positive potential. The coordinate on the plane perpendicular to the wire is obtained with high precision from the time taken by the ionization electrons to migrate to the wire. This time (measured with a precision of 1 ns), multiplied by the electron drift velocity in the gas, translates to the distance from the wire.

In every station in a wedge, one DT muon chamber (Fig. 2.25) contains twelve layers of drift cells organized in two $r-\phi$ superlayers and one $r-z$ superlayer (except the MB4 chambers that do not contain $r-z$ superlayer). Within a superlayer the four layers are staggered by half a cell. By correlating the drift times in different planes it is possible to calculate the position and angle of the crossing muon and to identify its parent bunch crossing without any external time reference.

The muon chambers are currently being installed in the detector. Fig. 2.23 shows one of the wheels with some muon chambers already installed.

Cathode Strip Chambers

Each endcap of CMS has four muon stations of CSCs: ME1, ME2, ME3, ME4. These chambers have trapezoidal shape and are arranged in a series of concentric rings centered on the beam line. They are separated by iron disks.

CSCs are used in the Endcap regions where the magnetic field is very intense and very inhomogeneous. They are multiwire proportional chambers in which one cathode plane is segmented intro strips running across wires. An avalanche developed on a wire induces a charge on several strips of the cathode plane. In a CSC plane two coordinates per plane are made available by the simultaneous and independent detection of the signal induced by the same track on the wires and on the strips. The wires give the radial coordinate whereas the strips measure the ϕ coordinate. Each CSC chamber has six layers of wires interleaved between cathode panels. Therefore, each chamber provides six measurements of the radial coordinate (wires) and six measurements of the ϕ coordinate (strips). A schematic illustration of a CSC chamber is shown in Fig. 2.26. The signal detection

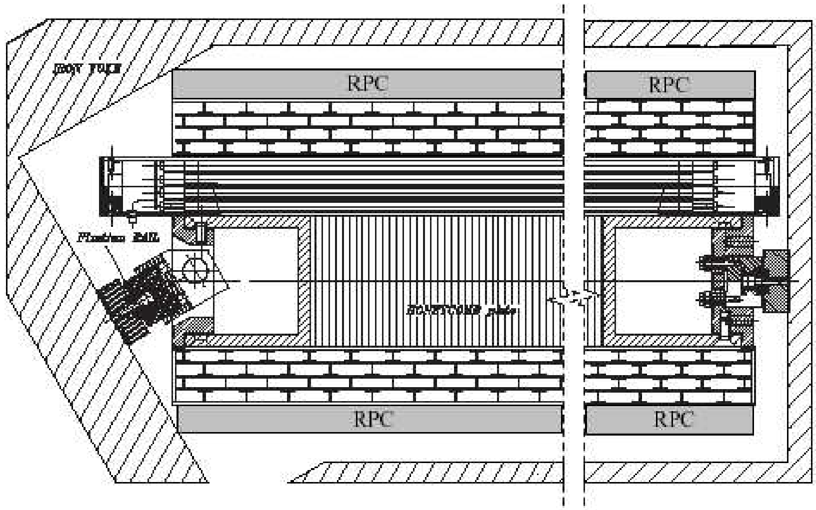

Figure 2.25: *Cross section of a Muon Barrel Chamber. The two outers superlayers measure the ϕ coordinate, while the inner superlayer measures the theta coordinate.*

mechanism of the chamber is sketched in the figure.

In addition to providing precise space and time information, the closely spaced wires make the CSC a fast detector suitable for triggering. CSC stations provide both a robust pattern recognition for rejection of non-muon backgrounds and also efficient matching of external muon tracks to internal track segments.

The CSC chambers are currently being installed in the detector endcaps. Fig. 2.28 shows one of the CMS endcaps with some of the CSC chambers already installed on it.

Resistive Plate Chambers

Planes of RPCs are added in both the barrel and endcaps to provide an additional and complementary muon trigger. They provide a faster timing signal and have a different sensitivity to backgrounds. They are mounted on the DT and CSC chambers, thus they will roughly cover the same area. Six layers of RPCs will be installed in the barrel, two layers in each MB1 and MB2, and one layer in each MB3 and MB4. In the endcap region each of the CSC stations will have a layer mounted on it.

Resistive Plate Chambers are fast gaseous detectors. They combine a good spatial resolution with a time resolution of 1 ns, comparable to that of scintillators. A RPC is a parallel plate counter with the two electrodes made of very high resistivity plastic material separated by a few millimeters gas gap. An illustration of the detection mechanism is shown in Fig. 2.27.

The high resistivity electrodes are transparent to the electric signals generated by the current of the avalanche: the signals are picked up by external metallic strips. The strips are oriented parallel to the ϕ tubes in the barrel and to the radial strips in the endcap CSCs. The segmentation in 'z' and 'r' matches approximately the η segmentation of the

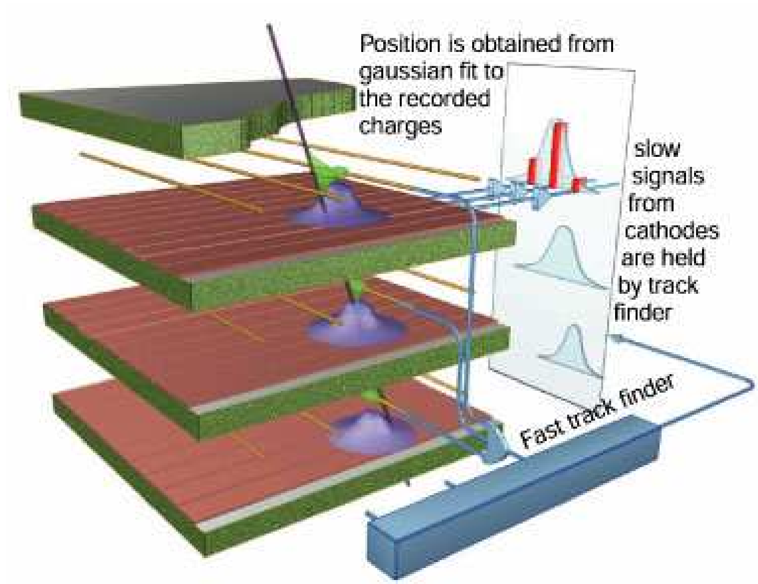

Figure 2.26: *Schematic illustration of the CSC chambers signal detection mechanism. Electrons are collected by the wire. In addition, a cloud of positive ions moving away from the wire and towards the cathode induces a current on the cathode strips perpendicular to the wire direction.*

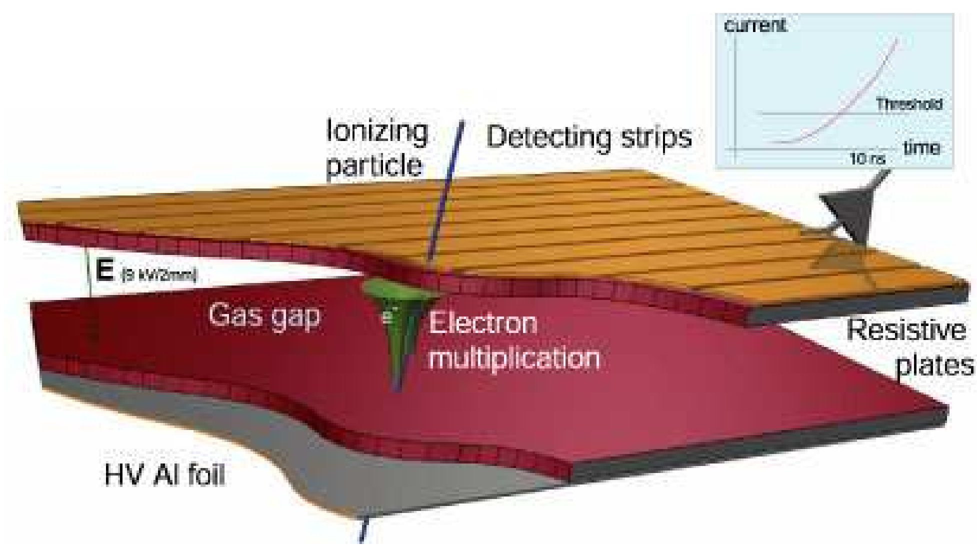

Figure 2.27: *Schematic illustration of the RPC chambers signal detection mechanism.*

calorimeter towers.

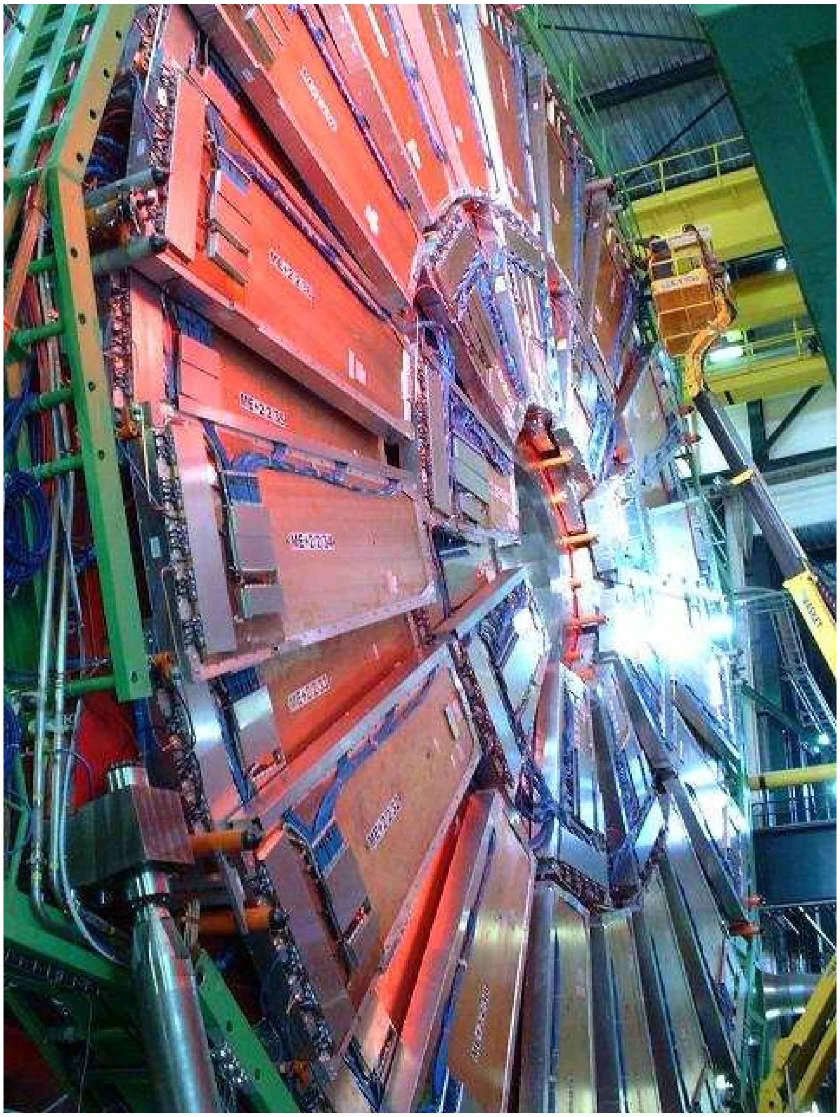

Figure 2.28: *View of one of the iron disks of a CMS endcap. The CSC chambers are currently being installed in the iron yoke.*

Chapter 3

The CMS Trigger System

As we already mentioned in Chapter 1, triggering is an important issue at the CMS experiment. In this chapter we will discuss in detail the CMS Trigger system implementation, highlighting its role in the experiment performance. More information about the CMS Trigger system can be found in [12] and [13].

3.1 Introduction

The task of the CMS Trigger system was already defined in Chapter 1. In short, the task of the CMS Trigger system is to reduce the input event rate of 40 MHz to 100 Hz by selecting interesting events from the physics point of view. These events are produced within an overwhelming background. Therefore, the Trigger system event selection must be performed with very high efficiency. Furthermore, unwanted backgrounds must be rejected in order to achieve the necessary trigger rate reduction, about 5 orders of magnitude.

The CMS Trigger system is structured in two different stages, as illustrated in Fig. 3.1. The first step of the rate reduction, i.e. from 40 MHz to 100 kHz, is performed by the Level-1 (L1) Trigger. It is a fully pipelined system based on custom electronics and processes data from every bunch crossing. When an event is accepted by the L1 Trigger, the Data Acquisition (DAQ) system transmits data from the readout buffers to the Event Builder (EVB). The EVB is implemented by a switching network. Its task is to reconstruct full events from the different data sources (different subdetectors). Reconstructed events are passed to the next step of the CMS Trigger system, the High-Level Trigger (HLT). Its task is to reduce the event rate from 100 kHz to 100 Hz. The HLT is implemented through several algorithms running on a a farm of $\mathcal{O}(10^3)$ commercial PCs. Finally, events passing the HLT filters are stored to tape for offline reconstruction and analysis.

3.2 Level 1 Trigger Overview

The CMS Level 1 (L1) Trigger [12] must select interesting collisions at a rate smaller than 100 kHz. At every bunch crossing, coarsely segmented data from the calorimeters and the muon system are analyzed. Full high precision data of all sub-detectors are stored in buffers while the L1 Trigger processes its decision. Data are only read out and sent to the Event Builder if the event is accepted, otherwise it is not considered any more and thrown away.

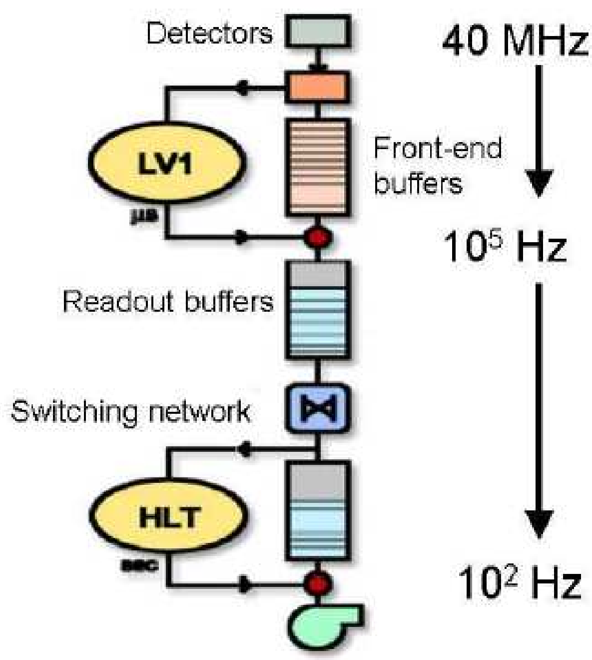

Figure 3.1: *CMS Trigger schematic layout. Two different stages are implemented. The Level 1 Trigger reduces the rate from 40 MHz to 100 kHz while the High Level Trigger performs the final reduction to 100 Hz.*

The L1 Trigger is implemented on a fully pipelined electronics system that takes a decision with a latency of 3.2 μs, i.e. 128 bunch crossings, including signal propagation delays. It is based on custom built processors using two main technologies: Application Specific Integrated Circuits (ASIC) and Field Programmable Gate Arrays (FPGA). The latter technology provides the capability of modifying the trigger algorithm during the experiment life, depending on the actual experimental conditions.

The overall structure of the CMS Level 1 Trigger is shown in Fig. 3.2. The system is organized into three main subsystems: the L1 Calorimeter Trigger, the L1 Muon Trigger and the L1 Global Trigger. Data from the electromagnetic (ECAL), hadronic (HCAL) and hadronic-forward (HF) calorimeters are processed by the Calorimeter Trigger. The Muon Trigger uses data from the three muon detectors, namely Drift Tubes (DT), Cathode Strip

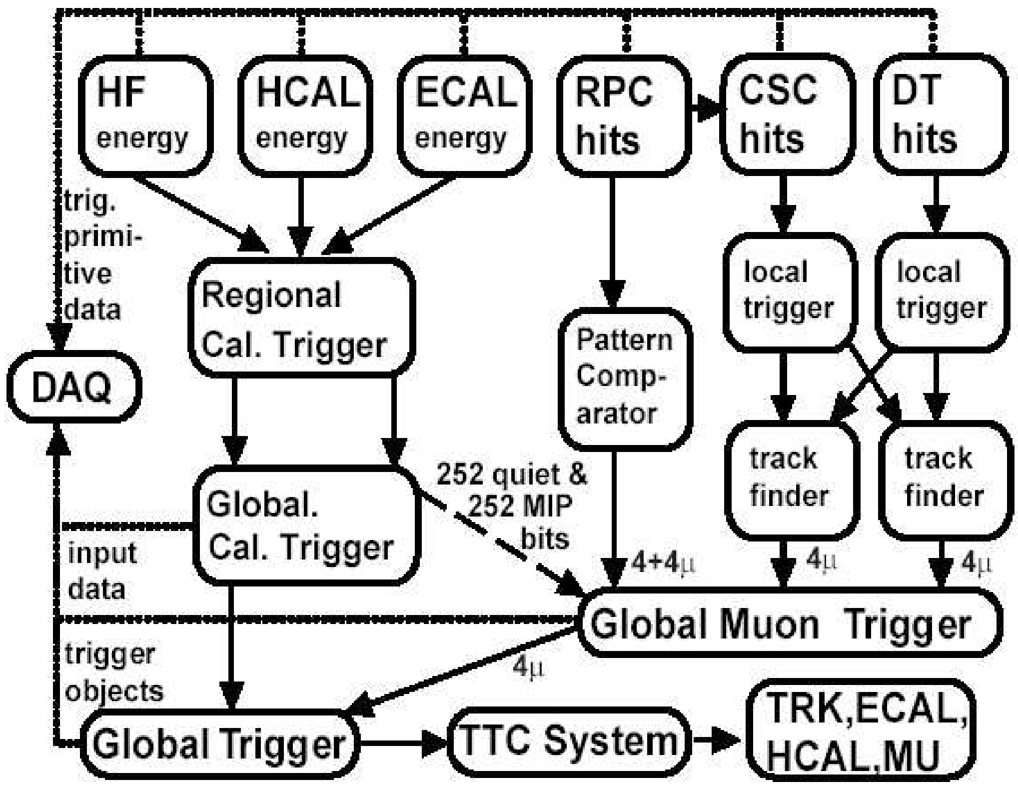

Figure 3.2: *CMS L1 Trigger block diagram. The L1 Global Trigger combines the Global Calorimeter Trigger and the Global Muon Trigger decisions and produces the final L1 Accept (L1A) signal.*

Chambers (CSC) and Resistive Plate Chambers (RPC), and combines this information at the L1 Global Muon Trigger (GMT).

The Global Trigger (GT) processes the information from the the Calorimeter Trigger and the Muon Trigger and decides whether the corresponding bunch crossing data is processed further or not. The trigger decision is transmitted to the sub-detectors through the Trigger Timing and Control (TTC) system. If a bunch crossing is accepted, all data involved in the trigger decision, as well as the readout data stored in the subdetectors buffers, is transmitted by the Data Acquisition (DAQ) system. The Event Builder performs its operation on these data and finally the HLT implements the last triggering step.

First-Level triggers of most other collider experiments, [14] to [18], count trigger objects passing certain programmable transverse energy or momentum thresholds. In CMS, trigger objects are sorted according to their rank, determined from transverse energy or momentum and quality information. The highest rank objects are sent to the Global Trigger. In addition to particle energies or momenta, the Global Trigger also receives location, i.e. ϕ and η, quality and charge information from the trigger subsystems. Trigger conditions are not only based on exceeding energy or momentum thresholds but also on event topology. This concept distinguish the CMS Level 1 Trigger from previous similar L1 Trigger systems.

3.3 The L1 Calorimeter Trigger

The L1 Calorimeter Trigger job is to detect electrons/photons and jets and to measure the total and missing transverse energy. Coarsely segmented data from the calorimeters are used for this purpose. Since tracker data are not available at Level 1, electrons and photons are not distinguished. In addition, the L1 Calorimeter Trigger provides also two bits of information to the GMT for each calorimeter region: a 'MIP' bit denoting an energy deposit compatible with the passage of a minimum ionizing particle (MIP) like a muon and a 'Quiet' (or 'ISO') bit identifying isolated muons. A certain maximum energy deposit determines the Quiet bit value [19].

Energy deposits in Trigger Towers are the first step in the Calorimeter Trigger algorithm. Trigger Towers consists of groups of subdetector modules whose structure depends on the corresponding subdetector and the location in CMS. In total, the CMS Calorimeter Trigger has 4176 towers. Fig. 3.3 shows the layout of the Calorimeter Trigger Towers in the r-z projection. The so called Trigger Primitive Generators (TPG) calculate transverse energy sums in the Trigger Towers from the individual calorimeter cell transverse energies.

Trigger Towers are organized in Calorimeter Regions, each one formed by 4×4 Trigger Towers. From the TPG information, the Regional Calorimeter Trigger (RCT) finds candidate electrons, photons, τ's, and jets. Both isolated and non isolated electron/photon candidates are found by the RCT. Candidates and sums of transverse energy are then transmitted to the Global Calorimeter Trigger (GCT).

The GCT sorts the candidate electrons, photons, τ's, and jets and forwards the 4 of each type with the highest rank to the L1 Global Trigger. The total transverse energy and

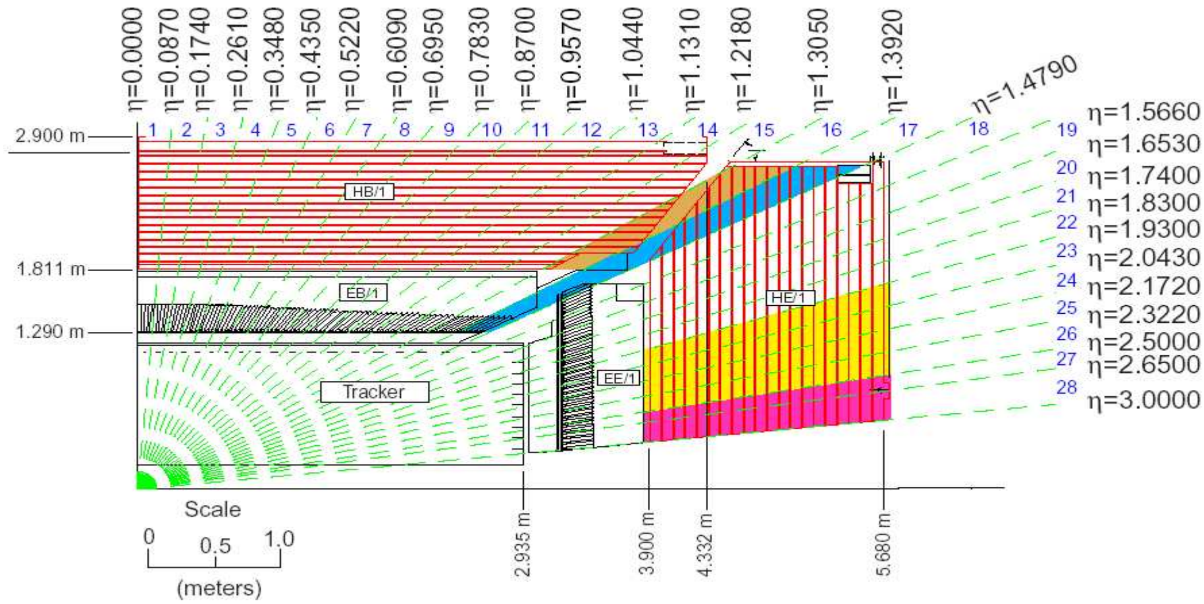

Figure 3.3: *The CMS L1 Calorimeter Trigger system segmentation in the r-z projection. Trigger Towers limits are represented by the green dashed lines.*

total missing transverse energy vector are also calculated at the GCT level and transmitted to the L1 Global Trigger.

3.4 The L1 Muon Trigger

The CMS Level 1 Muon Trigger at CMS has to perform three basic tasks: efficiently identify and reconstruct muons, measure their transverse momentum (p_T) and unambiguously identify their parent bunch crossing. High resolution in the momentum measurement is a main issue. It allows to efficiently cut low-p_T muons, which are mostly decays-in-flight and fakes, and keep events with high-p_T. Moreover, to achieve the design output rate of the L1 Trigger (100 kHz), the output rate of the muon trigger should be kept below 15 kHz.

The L1 Muon Trigger must perform its job in the presence of large background rates from: low-energy photon interactions, where the photons originate from neutron-induced nuclear reactions; decay-in-flight muons, especially at the lowest momenta and in the first muon station; punch-through pions, particularly in the first muon station; primary muons having low energy, and bremsstrahlung showers from the high-momentum muons themselves.

A detailed block diagram of the L1 Muon Trigger, including the logical structure of its different subsystems, is shown in Fig. 3.4. This is a more detailed version of Fig. 3.2 focused on the Muon Trigger.

In order to satisfy the requirements outlined above, the Level 1 Muon Trigger system

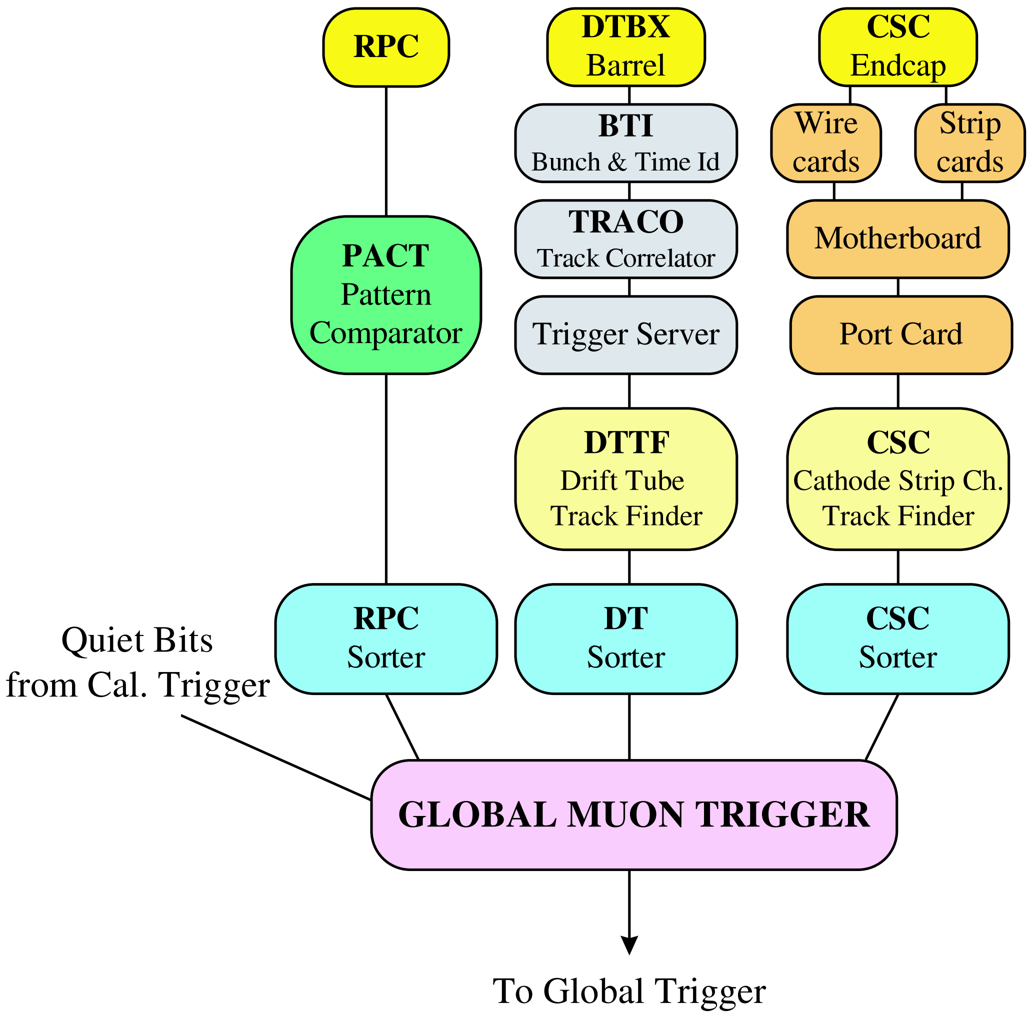

Figure 3.4: *CMS L1 Muon Trigger block diagram. Signals from the three CMS muon detectors (RPC, CSC and DT) are processed and finally combined at the Global Muon Trigger Level.*

uses the three kinds of muon detectors at CMS: DT, CSC and RPC. The layout of the CMS Muon system was already shown in Fig. 2.22. The excellent spatial precision of the DT and the CSC detectors ensures sharp momentum threshold. Their multilayer structure provides the possibility of effective background rejection. On the other hand, RPC provide superior time resolution allowing a more precise bunch crossing identification at the prize of a higher background.

Each of the three systems finds muons separately and send their outputs to the Global Muon Trigger. Identification of muons in the DT/CSC Trigger systems is performed through a different algorithm than in the RPC Trigger system. The DT and the CSC systems locally reconstruct track segments in the muon chambers (Local Triggers) and after combine them to deliver full muon tracks in their Regional Trigger systems (Track Finders). On the other hand, the RPC uses a Pattern Comparator method. Therefore, different information of muon tracks is delivered by the muon subsystems to the GMT. The GMT makes use of the complementary features of muon chambers (DT/CSC) and dedicated trigger detectors (RPC) to trigger on muons. It combines information from the three systems achieving high triggering efficiency and powerful background rejection.

3.4.1 RPC Trigger

The RPC covers the barrel and endcap regions up to $|\eta| < 2.1$. The logical segmentation of the RPC trigger is projective in ϕ and η. It is defined by the strips in the reference plane, i.e. station 2 both in the barrel and in the endcap. In ϕ the trigger is divided into 12 sectors, 30^o each. The segmentation in η consists of 33 towers numbered from -16 to 16. Typical tower size is about 0.1 η units. More details on the RPC Trigger can be found in Chapter 13 of [12].

The principle of the RPC Trigger is illustrated in Fig. 3.5. The solenoidal field bends tracks in the $r-\phi$ plane. A pattern of hits recorded by RPCs carries the information about the bending and can be used to determine the transverse momentum (p_T) of the track. This is done by comparison to a predefined set of patterns corresponding to various p_T^{cut}. Therefore, this device is called PAttern Comparator Trigger (PACT). The current baseline algorithm requires coincidences in a minimum number of hit planes. This minimum number depends on the trigger tower number and p_T^{cut}.

Up to four highest p_T muons in the barrel and four in the endcaps are selected and sent to the Global Muon Trigger (GMT). The information about number of hit planes ('trigger quality') is sent to the GMT together with measured p_T and can be used for further selection.

Recently, the conceptual design of an improved CMS RPC muon trigger using the Hadron Outer (HO) scintillators located around the CMS coil was proposed, [20]. This proposal is now part of the CMS Level 1 Trigger baseline. A RPC trigger algorithm that considers information from HO scintillators reduces the rates up to a factor 100 achieving a $\sim 90\%$ efficiency.

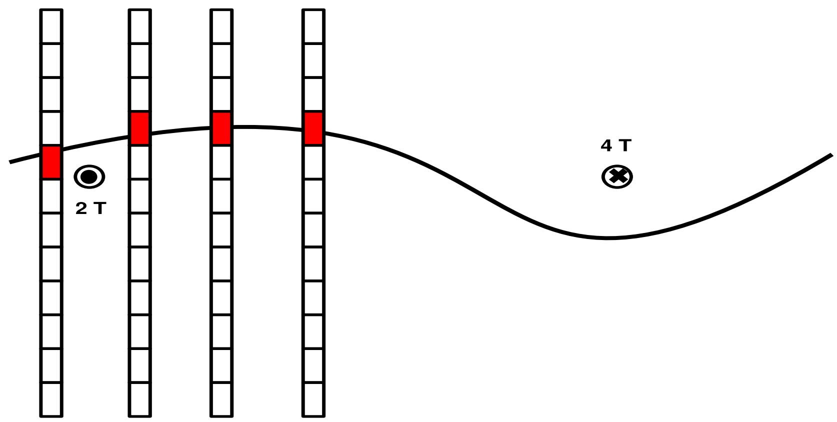

Figure 3.5: *The RPC Pattern Comparator Trigger (PACT) principle.*

3.4.2 CSC Trigger

The task of the Cathode Strip Chamber (CSC) Trigger system is to reconstruct muon tracks in the CSC Endcap Muon system and to measure the transverse momentum (p_T), pseudo-rapidity (η), and azimuthal angle (ϕ) of each muon found. A p_T resolution of about 25% is necessary to have sufficient rate reduction at L1 with a reasonable threshold.

Although the magnetic bending in the endcap is much reduced compared to the barrel, the CSC Trigger system achieves a precision similar to that of the DT Trigger.

The CSC Muon Trigger is divided into a Local Trigger and a Regional Trigger. The CSC Local Trigger finds muon segments, also referred to as Local Charged Tracks (LCT), in each of the 6-layer endcap muon CSC stations. The Regional Trigger is implemented by the so called CSC Track Finder. It links the muon segments reconstructed by the CSC Local Trigger into full muon tracks and assigns them transverse momentum, location and quality.

CSC Local Trigger

The Local Charged Track (LCT) forms the most primitive trigger object of the endcap muon system. Both cathode and anode front-end LCT trigger cards search separately for valid patterns from the six wire and strip planes of a CSC station.

The CSC anode trigger determines the exact muon bunch crossing with high efficiency and provides η information. On the other hand the CSC cathode trigger measures precisely the ϕ coordinate in order to allow precise p_T measurement. The working principle of both anode and cathode triggers are shown in Fig. 3.6. A Trigger Motherboard collects the LCT information from one station, associates the wire data to the cathode data, tags the bunch crossing time, and selects the two best candidates.

The combined LCTs are funneled through Port Cards to reduce the bandwidth sent to the CSC Track-Finder. Each Port Card collects track segments from up to nine stations (18 associated LCTs) and selects the three best candidates. The selected track segments contain precision measurement of the bend coordinate position and angle, approximate measurement of the non-bend angle coordinate, and identification of the correct muon bunch crossing with high efficiency.

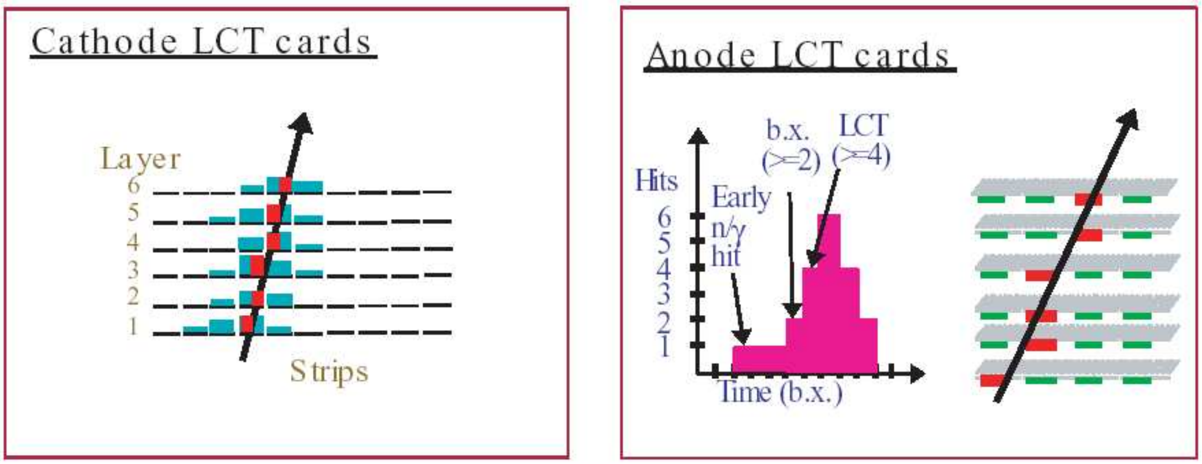

Figure 3.6: *The CSC Local Trigger principle.*

CSC Track Finder

Muon segments are sent from the Port Cards to the CSC Track Finder electronics which links them into full muon tracks. The CSC Track Finder algorithms are implemented in 12 (6+6) Sector Processors cards. FPGA technology is used for the hardware implementation of the sophisticated track finding algorithms.

The track segments from the CSC Local Trigger Port Cards are received by the CSC Track-Finder in Sector Receiver cards. The Sector Receiver cards receive the LCTs from all four stations in one 60° sector, reformat the track segments into global coordinates suitable for the track-finding algorithms, and apply alignment corrections to the data to account for placement errors of the CSC stations.

From the information received at its Sector Receiver, each Track Finder Sector Processors finds muon tracks in a 60° sector. Because of the limited bending in the endcap region, information is not shared across sector boundaries. Each CSC Track Finder Sector Processor finds up to three muon candidates and assigns them physical parameters: transverse momentum, a quality word, sign and position (ϕ and η coordinates). A CSC muon sorter module selects the four best CSC muon candidates and sends them to the Global Muon Trigger. More details about the CSC Track Finder Muon Trigger can be found in Chapter 12 of [12].

3.4.3 DT Trigger

The information delivered by the DT muon chambers is processed by the DT L1 Muon Trigger, which is divided into a DT Local Trigger and a DT Regional Trigger. Hits in the DT muon chambers are first organized in segments and assigned a beam crossing by the DT Local Trigger (DTBX), and delivered to the DT Regional Trigger. The Drift Tube Track Finder (DTTF) system implements the DT Regional Trigger, by linking segments into tracks consistent with the trajectory of a muon, and assigning them physical parameters. Finally, the DT Sorter selects the best four muons in the barrel detector and outputs them to the Global Muon Trigger system for further processing.

3.4.4 The DT Local Trigger

The input to the DTTF are the muon segments reconstructed by the Drift Tube Local Trigger (DTBX) of each MB chamber. Each DTBX delivers segments both from the '$r-\eta$' plane (η projection) and the '$r-\phi$' plane (ϕ projection). The ϕ segments are obtained by using the measurements of the two ϕ superlayers on a MB chamber. The η segments are obtained by using the measurements in the orthogonal θ superlayer, interleaved between the ϕ superlayers, of MB1, MB2 and MB3 chambers. MB4 stations have only ϕ superlayers. The MB chambers description has been already covered at Section 2.3.6. In this section we will summarize the DT Local Trigger algorithm.

The main task of the DTBX is to identify muons crossing the MB chamber and assign them to a LHC bunch crossing (BX). In addition to identifying the muon's parent bunch crossing, the DTBX measures the impact position and the bending angle of the muon trajectory. The DTBX is structured in three logical units: the Bunch and Track Identifier (BTI), the Track Correlator (TRACO) and the Trigger Server (TS). All the DTBX electronics is located in a Mini-Crate hosted at each MB chamber.

The Bunch and Track Identifier (BTI)

A BTI finds tracks in a portion, formed by 9 DT cells, of one of the superlayers (SL) of a MB chamber. Fig. 3.7 shows a schematic representation of the BTI work. A BTI performs the parent bunch crossing identification and calculates the track impact parameters, i.e. the position and the angle. The number of BTIs at each SL depends on the size of the MB chamber.

The BTI algorithm is based on the generalized mean-timer method [21]. It was explicitly developed to extend the technique to work on groups of four layers of staggered drift tubes, aiming to the identification of the tracks giving signals in at least three out of four measurement planes.

The method relies in the fact that the muon trajectory within a superlayer is a straight line and the measurement points, i.e. the wires of each DT cell, are equidistant. Considering the drift time (T_{Li}) of any three adjacent planes of staggered tubes (Fig. 3.7) and the maximum drift time (T_{max}) to the wire of a cell (380 ns), relation 3.1 holds independently of the track impact point and the angle of incidence.

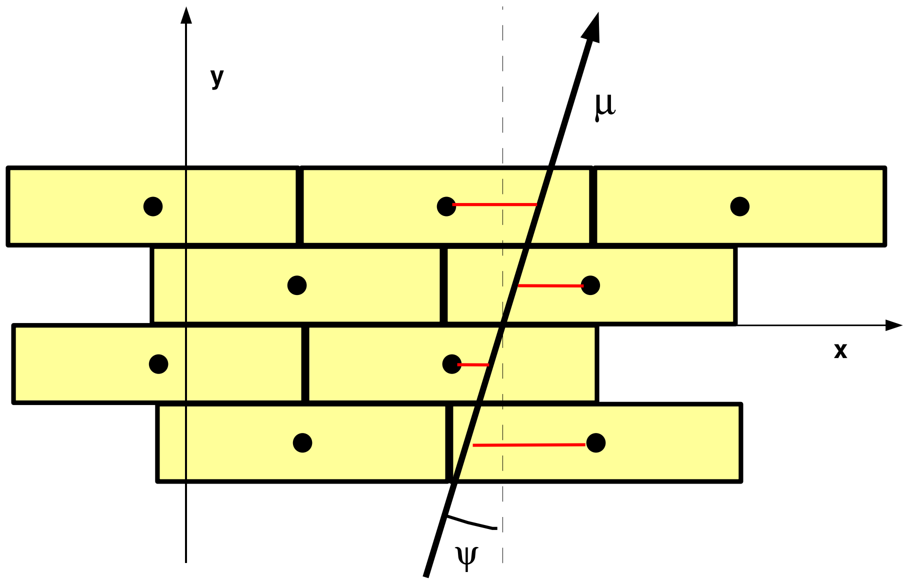

Figure 3.7: *Geometric Layout of a BTI unit. A BTI is formed by 9 DT cells in the 4 layers of one of the SL of a MB chamber. From the alignment of the drift times at 4 or 3 cells the impact parameters and the parent bunch crossing of the muon are calculated.*

$$T_{max} = \frac{T_{L1} + 2T_{L2} + T_{L3}}{2} \tag{3.1}$$

This constant time difference, between the particle crossing and the validity of relation 3.1, allows the identification of the parent bunch crossing. At the time T_{max} after muon crossing the drift times are aligned. The hits form an image of the muon track, thus it is possible to extract full information of the track (impact position and direction).

Extending the method to four layers, implies that the bunch crossing identification is possible even if the drift time of a tube is missing, due to inefficiency, or wrong, due to the emission of a δ-ray masking the good hit, since there are still three useful cells giving the minimum requested information. The method is also insensitive to all uncorrelated single hits and it is therefore well-suited to a high radiation environment.

The BTI output is formed of three parameters:

- A quality tag is assigned to the segment. It defines how many layers were used for the reconstruction. If an alignment of four hits occurred, the segment is tagged as a 'High Quality Trigger' (HTRG). If only three hits were aligned, it is tagged as a 'Low Quality Trigger' (LTRG).

- An angular 'k-parameter', k=$h \cdot \tan \Psi$ with 'Ψ' being the angle of the track with respect to the normal to the chamber plane in the transverse projection (Fig. 3.7) and h=13 mm being the distance between the wire planes. An angular coverage of $\Psi_{MAX} = \pm 45^o$ is achieved.

- The impact position of the muon respect to the SL center is computed at the end of the process.

The request of the alignment of any three hits is a substantial source of background, since it introduces effects creating false triggers, called 'ghosts'. There is a probability that the alignment of four hits at some clock step produces the alignment of only three of them at the step just before or after the HTRG signal, thus generating ghost LTRG candidate tracks. There is also some probability that a random LTRG could happen at any clock step due to the left-right ambiguity, that is duplicating the possible choices for every hit. Finally the δ-rays produced inside the cell will provide wrong time measurement enhancing the probability of an out of time trigger generated using the wrong measurement.

The BTI algorithm and its hardware implementation are used at the two types of DT superlayers in a MB chamber, the ϕ superlayers and the θ superlayers.

The Track Correlator (TRACO)

The TRACO is the next step in the DTBX trigger chain. It interconnects the two ϕ-SLs of a MB chamber by correlating the track segments received from the BTIs within the SLs. Each TRACO uses information from 4 BTIs in the inner layer of a chamber and 12 in the outer.

The algorithm starts by converting received track segments from local BTI coordinate system to the TRACO reference one. Then, the best BTI segment at each SL is selected according to the following criteria: first, the quality (HTRG or LTRG) of the segment is considered; for equal quality, the segment with the highest transverse momentum, which is computed considering the proximity to the radial direction to the vertex, is selected. After this selection, the correlation of the segments position is performed. If no correlation is possible, the highest quality segment is used.

The parameters computed are converted, using programmable Look-Up-Tables, to the chamber reference system. The position, in terms of the radial angle ϕ, and the bending angle, ϕ_b, are calculated and forwarded to the next step of the chain, the Trigger Server (TS). Fig. 3.8 shows a schematic definition of the TRACO output parameters. A quality word is also added to the information delivered to the TS, codifying which layers were used to reconstruct the track. Quality codes are summarized in Table 3.1.

The Trigger Server (TS)

The task of the Trigger Server is to select the two best track segments among all the candidates delivered by the different TRACOs at a MB chamber. The selected segments are delivered to the Sector Collector (SC) which acts as the interface between the Local Trigger and the the Regional Trigger, the Drift Tube Track Finder (DTTF).

The TS consists in two subsystems, one for the ϕ projection (TSϕ) and the other for the η projection (TSθ).

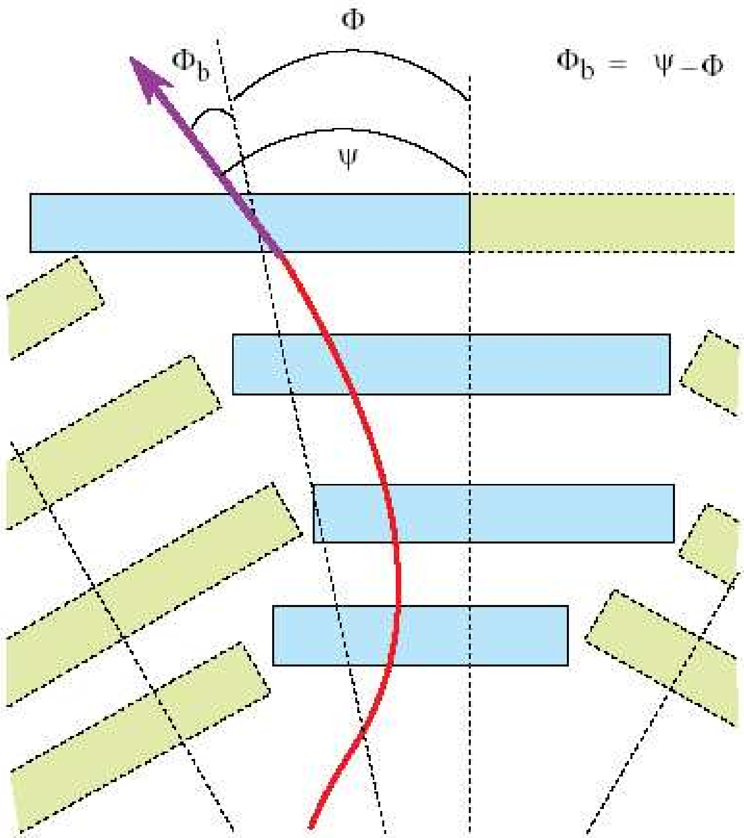

Figure 3.8: *Schematic drawing of the TRACO output parameters. Impact position* (ϕ) *and local bending angle* (ϕ_b) *are defined in terms of the absolute bending angle* (Ψ) *at the MB chamber.*

Inner ϕ SL quality	Outer ϕ SL quality	Symbol	Code
HTRG	HTRG	HH	6
HTRG	LTRG	HL	5
LTRG	HTRG	LH	5
LTRG	LTRG	LL	4
HTRG	-	H_o	3
-	HTRG	H_i	2
LTRG	-	L_o	1
-	LTRG	L_i	0
-	-		7

Table 3.1: *Tracks' Quality codes at the TRACO.*

The TSθ detects triggers produced by the BTIs at the θ-SL. First, all the BTIs of the SL are grouped into 7 groups. Each group of BTIs is represented by a bit that is calculated by ORing the results of the BTIs within the group. The result is a pattern of 7 bits that represents the positions where a muon hit the θ-SL. A quality pattern is also calculated depending on the quality (HTRG or LTRG) of the ORed BTI. Both bit patterns, hits and qualities, are sent to the DTTF.

The TSϕ selects the two best segments from all the TRACOs in the chamber (up to 24). First, the segments quality is considered. For equal quality, the segment with the higher p_T (estimated from the bending angle) is selected. The TSϕ algorithm is split in two processing levels. The first level consists on several 'Track Sorter Slave' (TSS) units. Each of them selects two segments from a group of 4 TRACOs. After, the 'Track Sorter Master' (TSM) selects the two best segments from up to 6 TSSs (12 segments). The two selected track segments are forwarded to the corresponding Sector Collector, which in turn will send them to the DTTF system.

3.4.5 The DT Regional Trigger

The DT Regional Trigger is implemented in the DT Track Finder (DTTF) system. The DTTF system is discussed in detail in Chapter 4.

3.4.6 The Global Muon Trigger

The task of the Global Muon Trigger (GMT) is to combine the results of the three muon trigger subsystems by finding the best four muons in every bunch crossing and to transmit them to the Global Trigger (GT). It receives 16 muon candidates: 4 from the DT Muon Trigger in the barrel, 4 from the CSC Muon Trigger and 4+4 from the RPC Muon Trigger. The GMT achieves excellent efficiency values and control of trigger rates by choosing muon parameters from the most suitable system, DT/CSC Trigger or RPC Trigger.

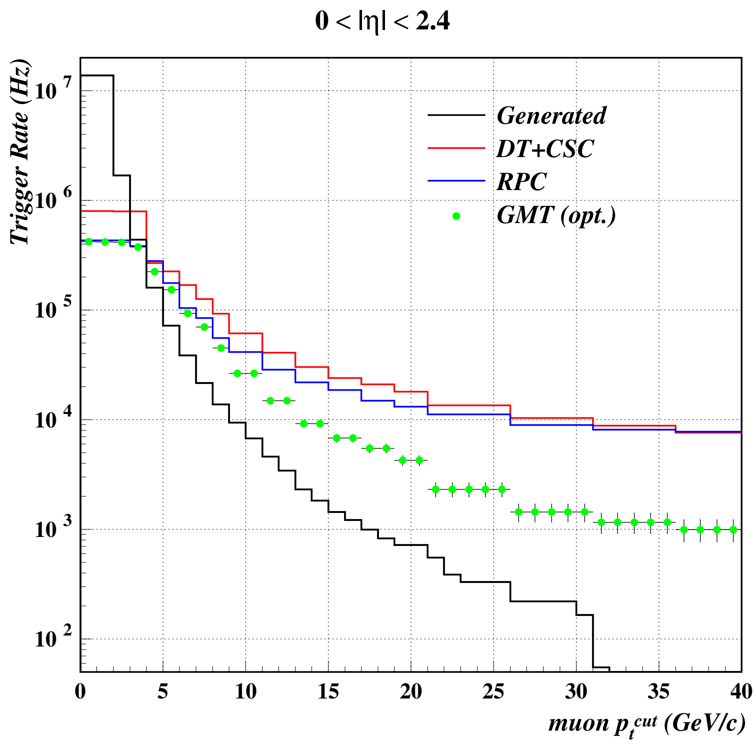

Figure 3.9: *Integrated L1 single muon rate at $\mathcal{L} = 10^{34}\ cm^{-2}s^{-1}$ as a function of the trigger transverse momentum threshold.*

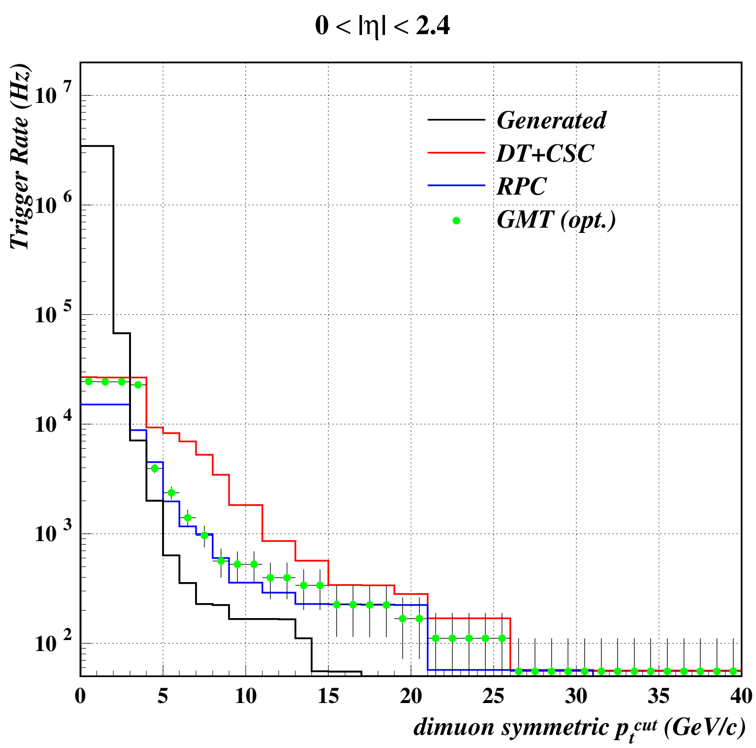

Figure 3.10: *Integrated L1 dimuon rate at $\mathcal{L} = 10^{34}\ cm^{-2}s^{-1}$ as a function of the symmetric trigger transverse momentum threshold.*

Due to the complementarity features of the muon detectors (RPC and DT/CSC), correlating the three subdetectors information ensures the robustness of the trigger decision. The two extreme cases of combining the muon candidates would be the logical OR, which is optimized for efficiency, and the logical AND, which is optimized for background rejection. Making use of the quality information associated with the muon tracks, the GMT can apply a more sophisticated algorithm. A candidate will be forwarded if it was seen by both RPC and DT/CSC system regardless of quality. If the candidate was seen by only one system, quality criteria are applied to decide whether to forward it. Specific quality criteria can be applied depending on detector types, detector regions and transverse momenta. Using this algorithm the GMT achieves high overall efficiency, a smoothing effect in problematic regions such as cracks and a powerful background rejection. It also reduces the number of fake muons found in any single regional trigger.

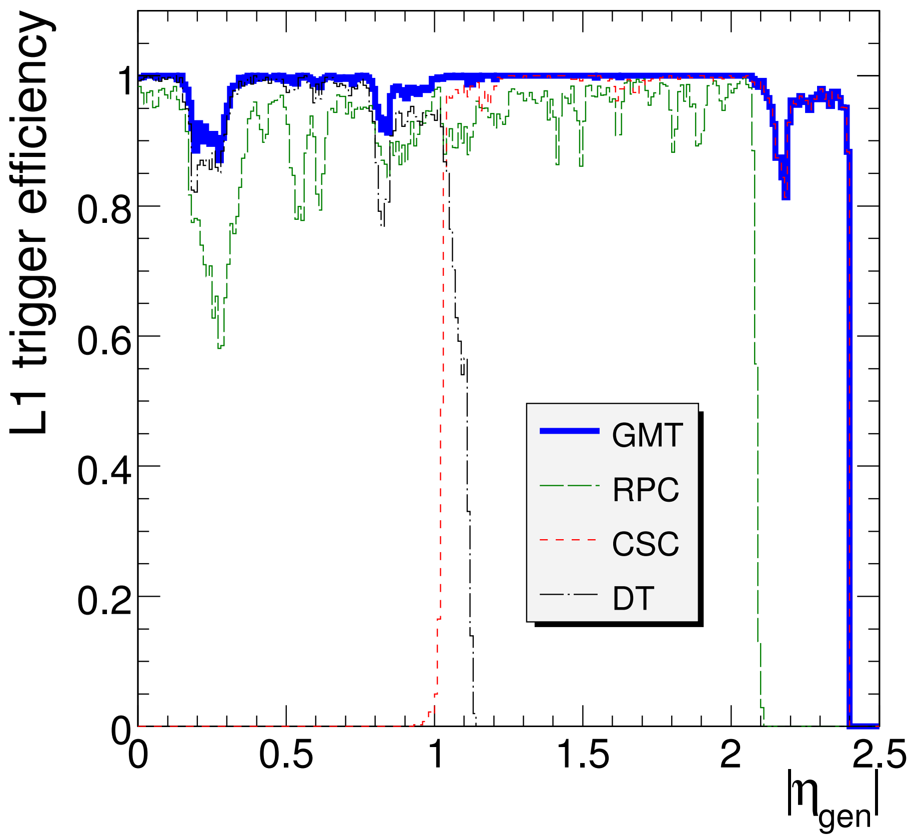

Figure 3.11: *Efficiencies for single muons as a function of the pseudorapidity (η) for the three muon trigger subsystems (DT, CSC and RPC) and for the GMT.*

Latest results [22] on the integrated L1 Muon Trigger rates for single muon and dimuon from simulated samples at $\mathcal{L} = 10^{34}$ cm^{-2}s^{-1} are shown in Figs. 3.9 and 3.10 respectively. The GMT trigger rates are compared with the DT+CSC trigger rate and with the RPC trigger rate.

The integrated single muon trigger rate as a function of the transverse momentum cut (p_T^{cut}) is shown in Fig. 3.9. For $p_T^{cut} > 20$ GeV/c muons, the GMT reduces by a factor 5 the standalone rates of the DT+CSC and the RPC subsystems. The rates are reduced by excluding low-quality muons that are triggered by one subsystem and not confirmed by the complementary subsystem and by optimally combining the p_T measurements. It must be noted that a $p_T^{cut} = 11$ GeV/c ensures the L1 Muon Trigger design output rate (15 kHz).

The integrated dimuon trigger rate as a function of a symmetric transverse momentum cut (p_T^{cut}) (the same cut is applied to both muons) is shown in Fig. 3.10. For low-p_T ($p_T < 3$ GeV/c) the trigger rate is dominated by two single muons from different p-p interactions in the same bunch crossing (pile-up). On the other hand, for high-p_T ($p_T > 5$ GeV/c) the rate is dominated by real dimuons (two muons coming from the same p-p interaction). The contribution to the trigger rate from two muons from different events in the same bunch crossing (pile-up) scales approximately with the square of the luminosity, while the contributions of real dimuons scales linearly with luminosity. Therefore, the LHC low luminosity phase could be exploited for the study of physics associated to dimuon production.

It must be noted that for both figures (3.9 and 3.10) the generated muon rates are lower than the trigger rates for $p_T^{cut} > 4$ GeV/c. Details on the trigger subsystems p_T assignment explain this effect. First, the limited resolution on the position, which is used by the subsystems to assign transverse momentum to the muon, in combination with the shape of the generated distribution lead to an overestimation of the muon p_T. Second and more important, the transverse momentum assignment is performed in order to achieve 90% trigger efficiency turn-on curves. Meaning that, for a given p_T^{cut}, a 90% of the muon tracks are assigned a $p_T > p_T^{cut}$. A trigger rate higher than the generated rate ensures the efficiency of the thresholds applied at the Level 1 Trigger.

The efficiency of the GMT and of the three muon trigger subsystems as a function of the position in the η coordinate is shown in Fig. 3.11. The GMT improves the subsystems efficiencies by optimally combining their trigger decisions.

In addition to finding the best four muons, the GMT appends two bits set by the Calorimeter Regional Trigger, a MIP bit and a Quiet bit (Isolation bit) to every muon track sent to the GT. The MIP bit is set if the calorimeter energy is consistent with the passage of a minimum ionizing particle, the ISO bit identifies isolated muons [19]. Both bits are used in the GT to suppress background and to improve selectivity.

3.5 The L1 Global Trigger

The last step of the CMS Level 1 Trigger is the Global Trigger (GT). Its task is to decide whether to accept or to reject an event and to generate the corresponding L1 Accept signal (L1A). The Timing Trigger and Control (TTC) systems sends the L1A signal to the readout units of all subdetectors to move data of the current bunch crossing from their pipeline buffers into derandomizing memories. Later, all or part of this data will be fetched by the data acquisition, first to run the High Level Trigger (HLT) algorithms and

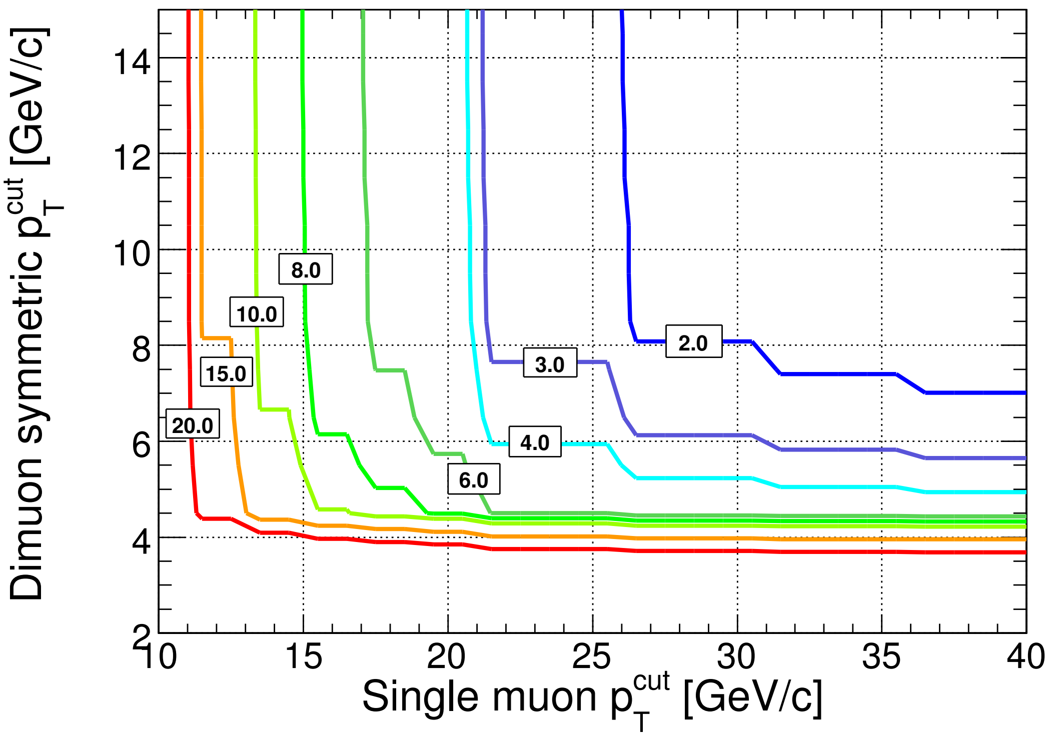

Figure 3.12: *Trigger rate contour levels for single muon and dimuon transverse momentum thresholds at* $\mathcal{L} = 10^{34}\ cm^{-2}s^{-1}$.

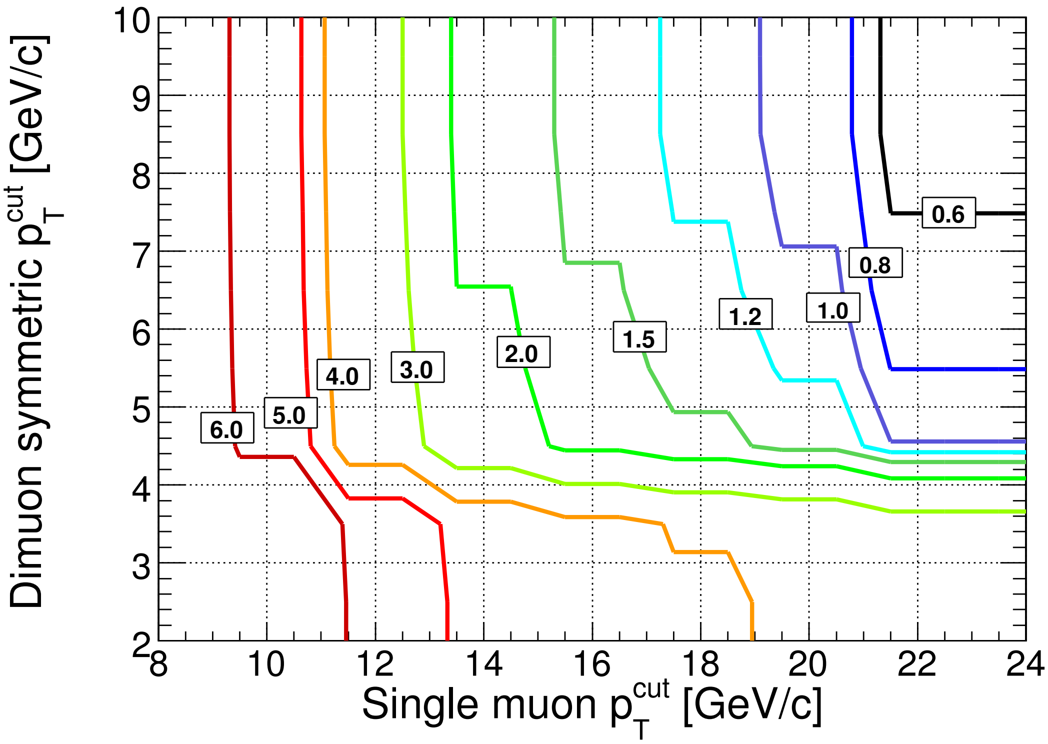

Figure 3.13: *Trigger rate contour levels for single muon and dimuon transverse momentum thresholds at* $\mathcal{L} = 2 \cdot 10^{33}\ cm^{-2}s^{-1}$.

finally to store accepted events.

The GT receives the best four of each of the following objects from the L1 Trigger subsystems: muons, isolated electrons or photons, non-isolated electrons or photons, central jets, forward jets and isolated hadrons or τ-jets. These trigger objects, are ordered by rank, which is a function of transverse energy or momentum and quality. In addition, the GT receives the magnitude and the direction of the missing transverse energy as well as the total transverse energy and eight numbers of jets passing different E_T thresholds.

A basic principle of the CMS L1 Trigger, which distinguishes it from classic L1 Triggers, is that details of the highest rank trigger objects are always sent to the Global Trigger, rather than histograms or summarized information. Moreover, the L1 GT not only receives particle energies or momenta but also location information, namely η and ϕ. For muon candidates charge information is also delivered.

The task of the GT is to apply thresholds and other selection criteria based on this detailed information. These criteria may be adapted as needed. There is no dependence on local or regional level thresholds. Cuts and threshold are applied only at the GT level. Not only classic L1 trigger conditions (inclusive triggers) can be applied but also trigger conditions based on event topology can be applied already at L1. Furthermore, the space coordinates can be used in the Higher Level Triggers to select regions of interest.

The heart of the Global Trigger Processor is the logic performing the trigger algorithm calculations. An algorithm is a combination of trigger objects satisfying defined thresholds and spatial conditions. The GT logic can be programmed to calculate up to 128 different trigger algorithms in parallel for every bunch crossing. A final OR-function combines all active algorithms and generates the L1A signal.

Rates can be kept under control by adjusting energy or momentum thresholds of physics objects or by prescaling algorithms selecting processes with large cross-sections. Concerning the muon trigger rates, latest results [22] are summarized in Figs. 3.12 (high luminosity) and 3.13 (low luminosity). They plot the trigger rates contour levels for transverse momentum threshold (p_T^{cut}) applied for single muons and dimuons (a symmetric p_T^{cut} is defined). Depending on the physics to be studied and the maximum muon trigger rate, thresholds for single muons and dimuons are chosen.

More details on the Global Trigger concept and on its hardware implementation can be found in [12] and [23].

3.6 The DAQ System and the High Level Trigger

The L1 Trigger decision is handled by the Data Acquisition (DAQ) system that acquires the detector data, inspects it, provides the final selection stage and stores the selected events. The CMS High Level Trigger (HLT) system is responsible of the final CMS Trigger rate reduction, from the 100 kHz L1 Trigger output rate to the 100 Hz final storage rate. The functionality of the CMS DAQ/HLT system is three fold:

- perform the readout of the front-end electronics after a L1 Trigger Accept (L1A) signal. This is the task of the Event Builder (EVB).

- execute physics selection algorithms on the events readout, in order to accept the ones with the most interesting physics content. This is the task of the HLT.
- forward these accepted events, as well as a small sample of the rejected events, to the online services which monitor the performance of the CMS detector and also provide the means of archiving the events in mass storage.

The architecture of the CMS DAQ system is shown schematically in Fig. 3.14. In the following we overview the systems related to the CMS Trigger: the Event Builder and the High-Level Trigger. More information of the CMS DAQ system can be found in [13].

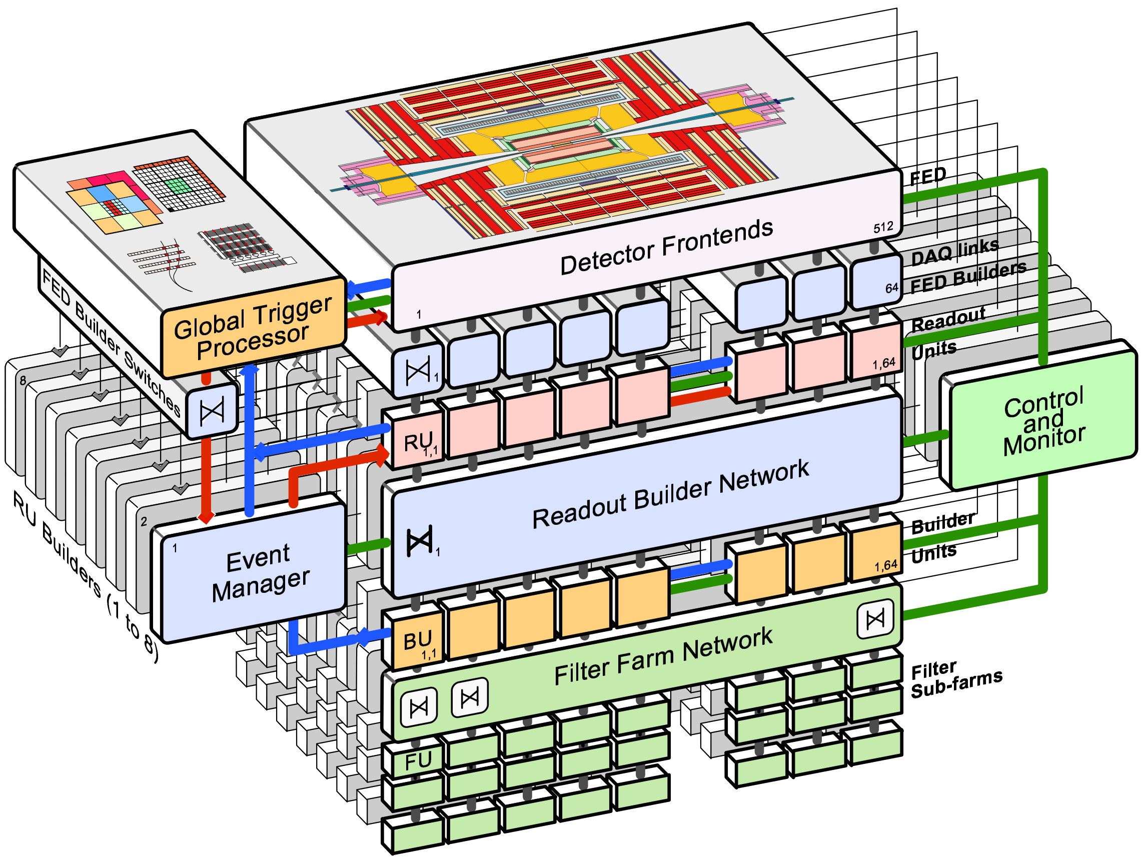

Figure 3.14: *Schematic representation of the CMS DAQ system architecture.*

3.6.1 The Event Builder

The Event Builder (EVB) consists of all the entities involved in collecting the data from the various readout buffers into a single 'event buffer', which is then sent to a PC for analysis. It is the central component of the DAQ system.

The EVB is implemented by a switching network (Fig. 3.15). It assembles event fragments into full events. This task is performed in two stages. In the first, the data for each event in the Front-End Drivers (FEDs) are merged into Readout Units (RUs). The RUs read the data from 8 FEDs, and perform a first concatenation of the event data fragments into larger data blocks, referred to as super-fragments. This stage is implemented by 64 FED Builders, each of them comprises 8 FEDs, a 8×8 switch and 8 RUs. At the end of this first stage, the data from a single event are contained in 64 RUs. In the second stage, the RUs are in turn read out by Builder Units (BUs) which combine the 64 super-fragments into a single event. The collection of 64 RUs, the 64×64 switch that connects them to the BUs and the actual 64 Builder Units is referred to as a RU Builder. There are eight RU Builders in the full system.

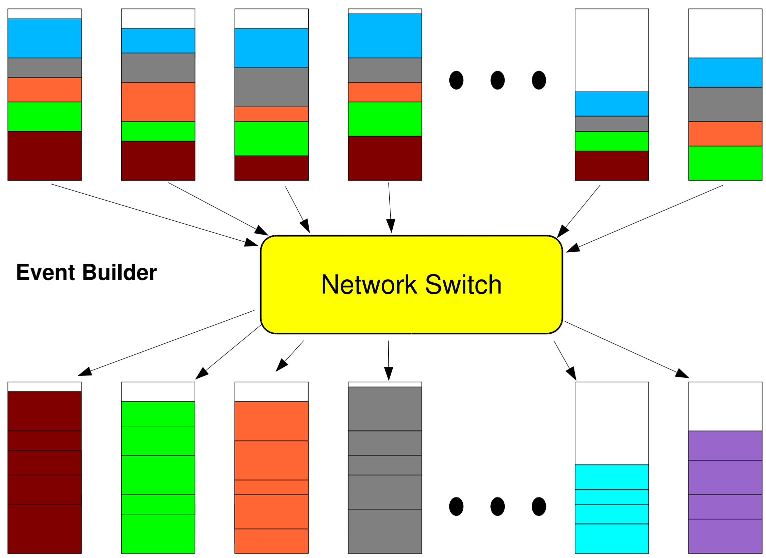

Figure 3.15: *The Event Builder task is to build complete events from the readout buffers of the different subdetectors. Different colors represent different events data.*

Once a full 'physics event' is reconstructed, it is forwarded to a filter farm, where the HLT algorithms run, for the final decision on whether the event should be discarded or directed to permanent storage.

3.6.2 The High Level Trigger

The event selection responsible of reducing the trigger rate from 100 KHz to 100 Hz is performed by the High-Level Trigger (HLT). The CMS HLT is completely software implemented, thus it is extremely flexible. The HLT algorithms run on a farm of $\mathcal{O}(10^3)$ commercial PCs, represented as 'Filter Farm' at the bottom of the schematic drawing shown in Fig. 3.14.

Each event is processed by a single PC, which has access to the full raw event data. The High-Level Trigger reconstruction code will be as close as possible to the full offline analysis code, the main differences resulting from limited processing time and the possible lack of precise calibration constants.

Although the HLT system is hardware implemented in the same PC, it can be virtually split in different stages according to the experimental conditions. Currently it is divided in two levels. In the first level, 'L2', the physics object reconstruction is performed without the inner tracker information. The goal of the L2 trigger is to reduce by about an order of magnitude the L1 output rate on single objects by applying the same thresholds used at L1. As full detector, instead of Local Trigger output, information is available at L2, better resolution on the physics objects parameters (transverse momentum) is achieved. Therefore, it is possible to reduce the trigger rate without imposing more restrictive thresholds. The next and last step, 'L3', is accomplished by using full detector data. In particular, the inner tracker data are used. At this level, similar cuts to those applied in offline analysis are applied in order to reduce the rate to the final value of 100 Hz. More details on the High-Level Trigger system physics object selection are found in Part 4 of [13].

Chapter 4

The DTTF Muon Trigger System

The Drift Tube Track Finder (DTTF) Trigger implements the Regional Trigger of the DT Muon system. Using the trigger primitive data delivered by the Drift Tube Chambers (DTBX), the DTTF reconstructs muon candidates joining together track segments. After a muon track is found, the DTTF assigns physical parameters to it, namely transverse momentum, a ϕ and a η coordinate, and a quality word. Finally, the DTTF performs a sorting process. The four highest rank muon tracks in the detector barrel are selected and forwarded to the Global Muon Trigger system. The logical position of the DTTF system within the CMS Level 1 Muon Trigger has been shown in Fig. 3.4.

In this chapter we will discuss the DTTF Trigger system. Both its concept and its hardware implementation. First, we will overview the system structure. After, the different units that form the DTTF system will be described. Results on the DTTF Trigger performance from simulated data will be discussed as well. Finally, both hardware and software tools used for the system tests will be described.

4.1 System Overview

The CMS DT detector was already described in Section 2.3.6. However, it is worth to remind the reader its geometrical structure. The DT system is organized in five wheels in the beam direction and four concentric stations in the radial direction: MB1, MB2, MB3, MB4. Each wheel is divided in twelve 30^{o} wedges in azimuth. Figs. 2.7, 2.22 and 2.23 illustrate this description.

The DTTF system logical segmentation replicates the CMS barrel detector geometrical structure, Fig. 4.1. The core components of the DTTF are the Phi Track Finder (PHTF), which finds tracks in the $r-\phi$ projection, and the Eta Track Finder (ETTF), which finds tracks in the $r-z$ projection. Due to the magnetic field configuration, parallel to the z axis direction, the DTTF system main and most critical unit is the Phi Track Finder (PHTF) Unit, also called Sector Processor. A PHTF performs its track finding job covering one Muon Detector Sector with all its four Muon Barrel (MB) stations. Every PHTF Unit processes muons which tracks start in their sector.

As muons can cross more that one Muon Detector Sector, to follow the muon tra-

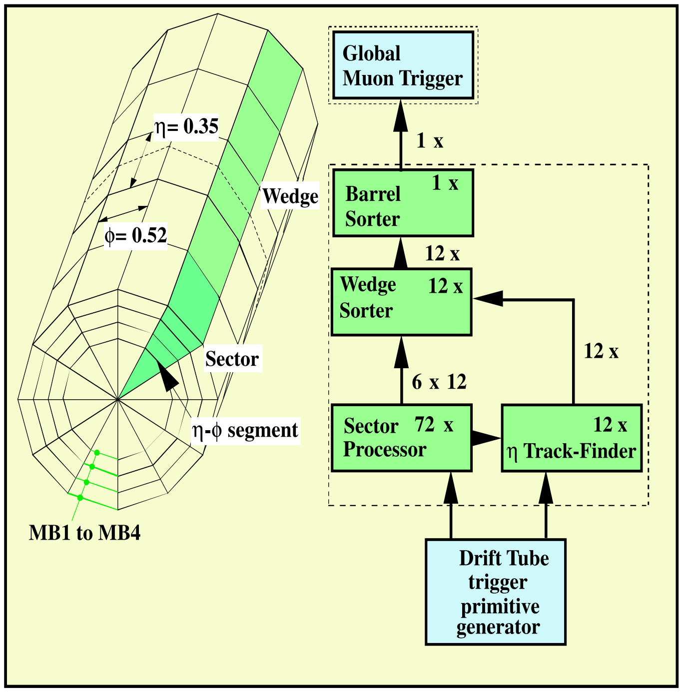

Figure 4.1: *Logical segmentation and block diagram of the DTTF Trigger.*

jectories to neighboring sectors the PHTF Units need connections to the other PHTF boards that perform track finding in the neighboring sectors. Through this connections the PHTF Units receive segments from stations MB2, MB3 and MB4 of the neighboring sectors. A large number of neighbor connections is therefore necessary. In order to minimize the number of these connections the PHTF Units are organized in a 'Wedge' structure. One DT detector wedge is made up of the five sectors that share the same ϕ coordinates. Each wedge covers a $\Delta\phi = 30^o$ portion of the barrel detector, as it is illustrated in Fig. 4.1.

Concerning the η direction, the PHTF Units get segments information from those PHTF units that serve higher η ranges. An opposite data transfer is not necessary as the muons do not fold back in η. Thus the PHTF units of Wheel 0 get information from Wheels ±1; the units of Wheel -1 get information from Wheel -2, the Wheel +1 units from Wheel +2. The outer PHTFs of Wheels ±2 do not get information from next wheel neighbors but from the CSC Muon Detectors of the endcap region.

Concerning the ϕ range, the PHTF Units exchange information in both sideways directions as muons can leave the sectors on both sides depending on their charge. A PHTF Unit needs segments from the neighboring PHTFs of the same Wheel and also from those neighbors in the next Wheel. They do not get information from the previous wheel as described above. Thus, every PHTF Unit forwards its input to five other PHTFs, one previous wheel neighbor in the same wedge, and two sideways neighbors of both sides of the same wheel and previous wheel. A schematic representation of a PHTF unit neighbor connections is shown in Fig. 4.2.

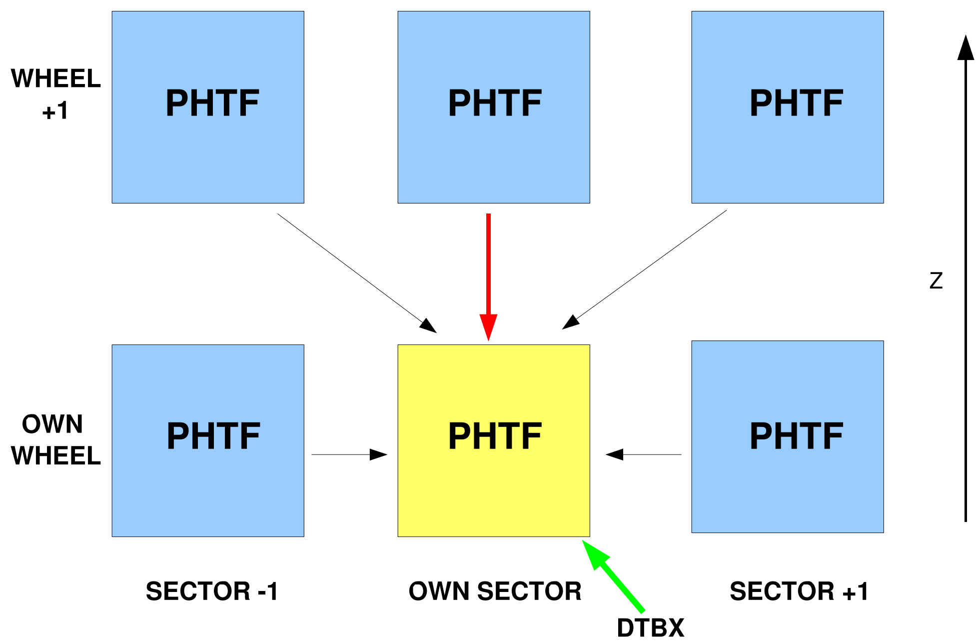

Figure 4.2: *Schematic representation of the neighboring connections of a PHTF board. A Sector Processor receives information from its own wheel neighbors and from neighbors in the next wheel at a higher η range. Input from th DT Local Triggers (DTBX) at its Muon Detector Sector come through optical Links.*

Due to the large number of required neighbor connections the tasks of Wheel 0 are shared by two PHTF Units per wedge. One of them processes muons that remain in Wheel 0 in all 4 MB stations and those leaving Wheel 0 in positive η direction. The other PHTF processes muons that leave Wheel 0 in negative η direction. Therefore, 6 PHTF units per wedge are need. One ETTF Unit covers one wedge. In total there will be 72 (6×12) PHTF and 12 ETTF Units in the system.

The outputs of the 6 PHTF Units and the ETTF Unit of one wedge are forwarded to the Wedge Sorter (WS) Unit. This block sorts out fakes that may be found in two neighboring PHTF Units and determines the two highest quality muons in the wedge, which are then forwarded to the Barrel Sorter (BS). There is a single BS for all the system. It receives the Wedge Sorters outputs and determines the four highest quality muons of the whole DT Muon Trigger System. It also cancels out fakes that were found in two different wedges. The four highest quality DT Muons are sent to the Global Muon Trigger Unit of the Global Trigger System.

The DTTF System also delivers data for the CMS DAQ System. The data blocks are composed of all input and all output signals of the Track Finders. Data from each L1 Accept, the previous and successive (L1-1, L1+1) bunch crossings are collected. The data stream is sent as a bit stream to the Data Link Boards of each Crate and then forwarded using a Channel Link connection to the Data Concentrator Board (DCC). The Data Concentrator compresses the data blocks in real time and sends them via S-Link64 to the CMS DAQ system.

4.1.1 Hardware Implementation

The DTTF Trigger is physically realized using a sophisticated electronic system which replicates the description given above. The system electronics is organized in twelve modules stored in six crates. Each module processes the information that originated in a 30^o wedge of the barrel detector.

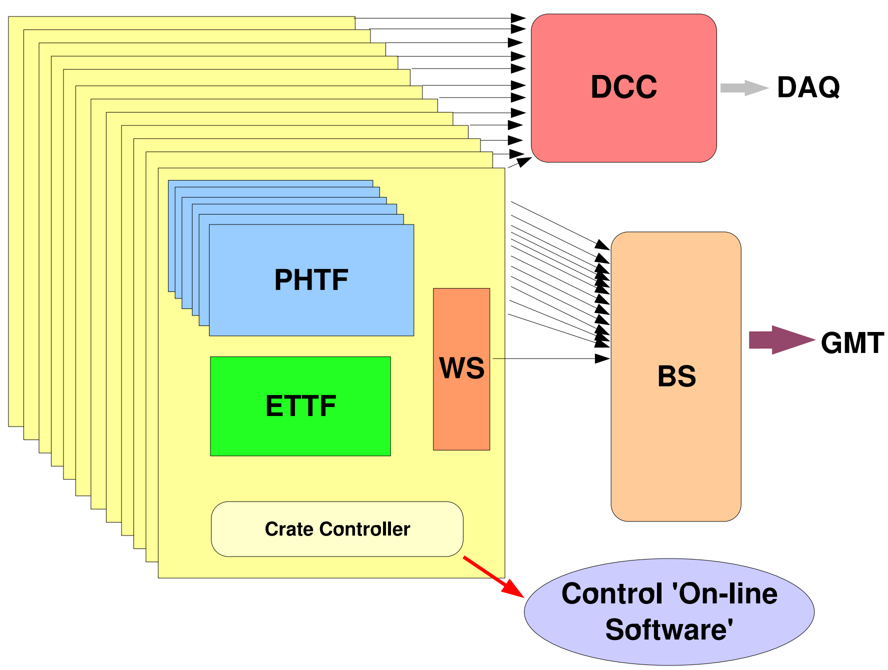

Figure 4.3: *DTTF System block segmentation. Each block is implemented in hardware by a 'module'.*

Therefore, one module is formed by eight boards: six Phi Track Finder sector processors (one PHTF for wheels ±1 and ±2, and two PHTF boards for wheel 0), one Eta Track Finder (ETTF), and one Wedge Sorter. Two modules share the same crate and the same VME Controller, Timing (TIM), and Data Link (DLI) boards. Fig. 4.4 represents a DTTF crate, formed by two modules and the shared boards.

The DTTF System occupies three racks in the CMS underground counting Room.

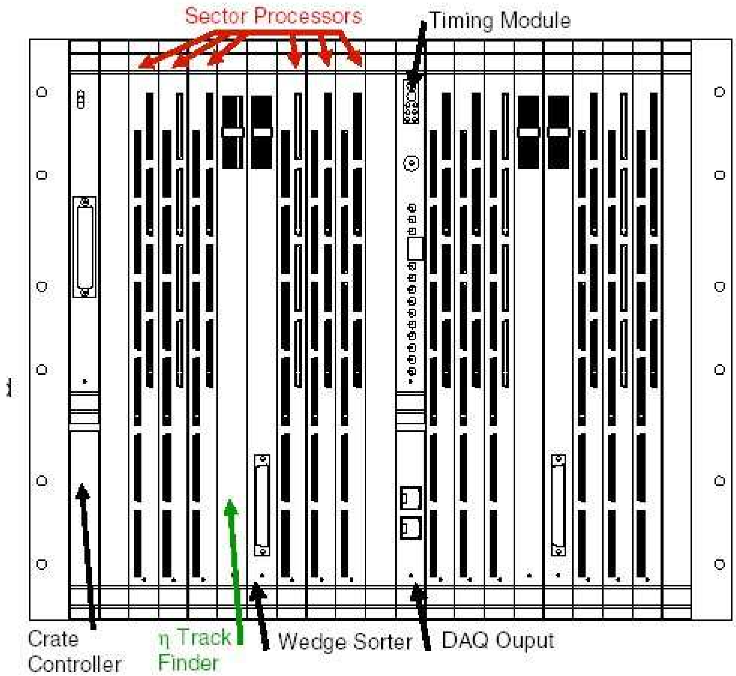

Figure 4.4: *A DTTF Crate is shared by two modules. Each module covers a* 30° *wedge of the Muon Barrel detector.*

Six DTTF crates as described above are located in two racks. The third rack contains a crate where the Barrel Sorter, the TTC system, the fast signaling, the DCC board and the control PC are located.

4.2 The Phi Track Finder

The Phi Track Finder (PHTF) Units are the central instances of the DTTF System. They receive the segments from the Trigger Server and join those that belong to the same muon track, they classify the found tracks and assign physical parameters to them. The output of each PHTF Unit contains the physical parameters of the best two found muons and also a quality value representing the number and position of the segments belonging to those muon tracks. Their parameters are sent from all PHTF Units of a wedge to the local Wedge Sorter. In order to filter out ghosts (identical muons found by two different PHTFs) the PHTF Units also send segment address information to the WS.

The Block Diagram of the PHTF is shown in Fig. 4.5. The diagram clearly shows the pipelined structure of the PHTF. This means that the PHTF does not perform all track finding tasks during one single bunch crossing (BX), but it operates in several stages. Every stage performs one calculation step and forwards its results to the next step. The PHTF needs a time equivalent to 17 BX to perform all steps of track finding.

The PHTF track finding algorithm is implemented in three logical steps (Fig. 4.6)

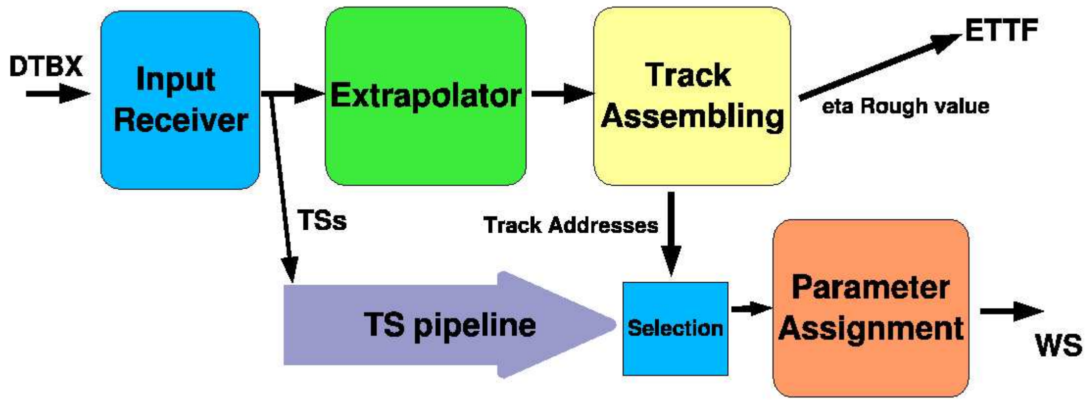

Figure 4.5: *PHTF electronics block diagram.*

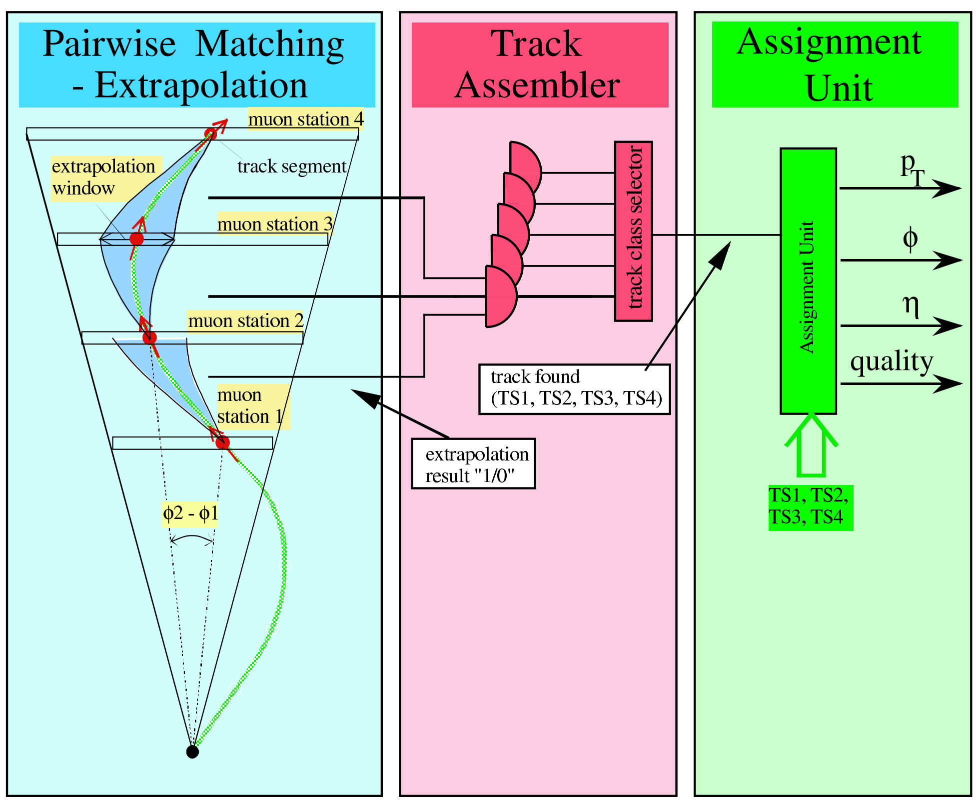

Figure 4.6: *Schematic representation of the PHTF three-step algorithm.*

which in turn are implemented in the different PHTF electronics blocks (Fig. 4.5). First, segments from the DTBX are received, synchronize and deserialize in the Input Receiver Unit. Those segments are the sent to the Extrapolator Unit which implements the first step of the track finding algorithm. It tries to match segments pairs of different MB stations using a pairwise matching method based on a extrapolation principle. The successfully matched pairs are used in the next PHTF block, the Linker Unit. It implements the next logical step of the algorithm by linking the track segment pairs into full muon tracks. Finally, the Assignment Unit assigns physical parameters to the found muon track. It considers the segments used in the track reconstruction that were kept and after selected in the Pipe and Selection Unit. The PHTF also assigns a η code to the track based on the position where the muon crossed wheel boundaries. This code is used by the ETTF for the η assignment.

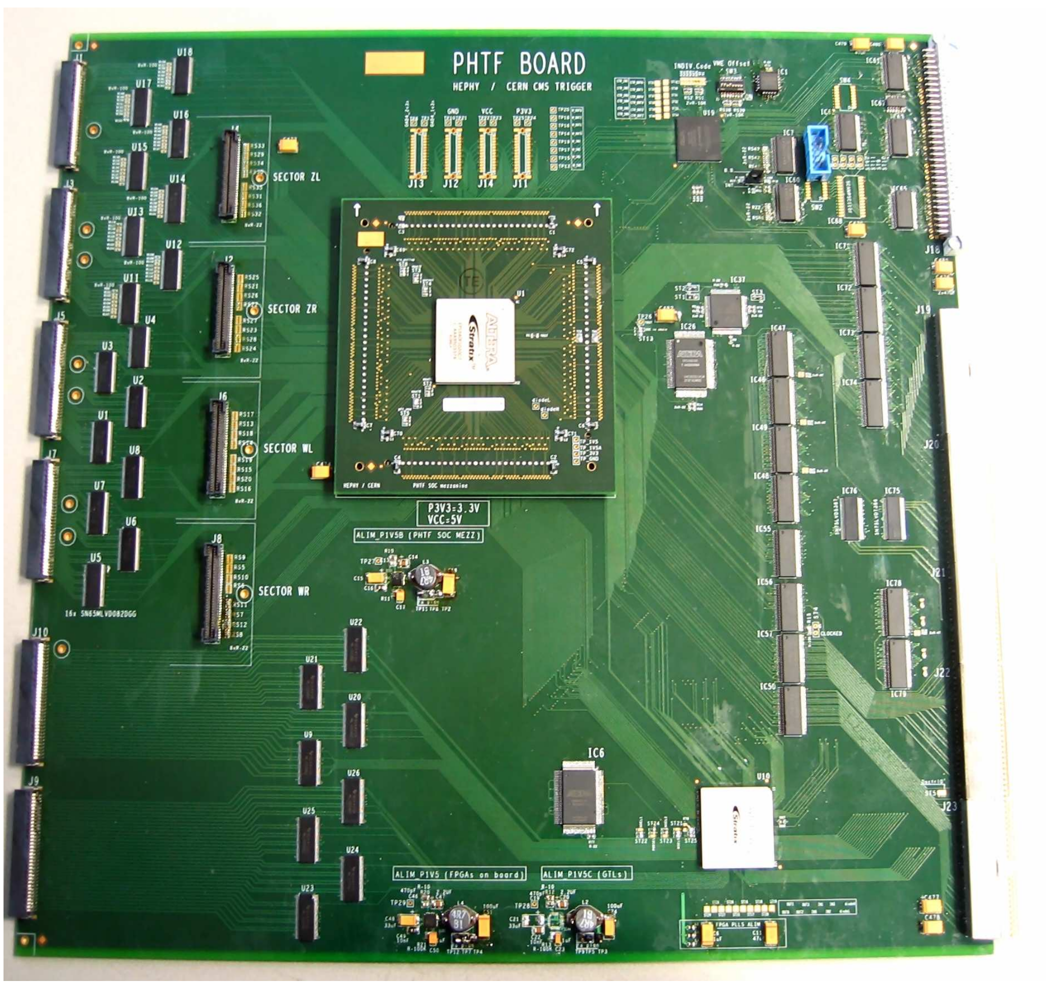

Figure 4.7: *The First PHTF Production board.*

A photo of the first PHTF production board is shown in Fig. 4.7. This board was the first PHTF production board assembled. It was used to validate the final design before the beginning of the full PHTF boards production (72+6 boards).

4.2.1 The Input Receiver

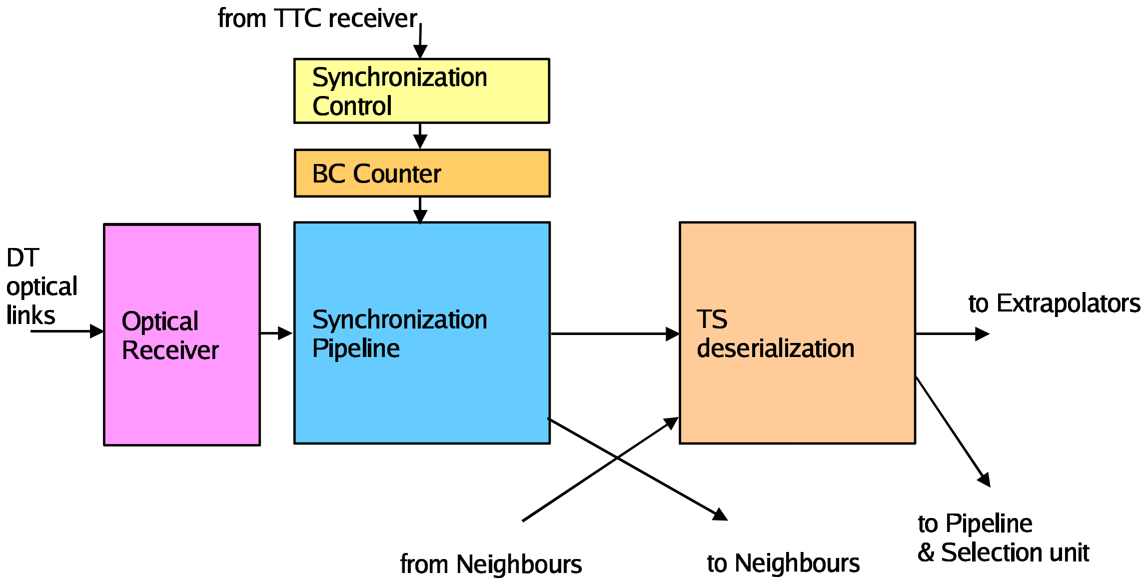

Figure 4.8: *Input Receiver block diagram.*

The Input Receiver (Fig. 4.8) is composed of two independent Units, the Optical Receiver and the Data Receiver. The Optical Receiver is a separate Card that receives and decodes the Optical Link data stream. It forwards 110 parallel bits to the PHTF Card. The Data Receiver performs synchronization on Input Data. The goal of this is to have all PHTF Units in the DTTF System to work in a totally synchronized way, i.e. all the pipeline stages of the Units should work on the data of the same BX. The synchronization is realized in a two stage circuit. The rough synchronization determines the correct BX, while the fine synchronization allows clock phase corrections. Both values can be considered as run parameters, but as they are not expected to be changed after an initial setup they can also be stored as default values.

The segment deserialization is necessary as the Trigger Server sends only one segment from each MB station in one BX. If there is a second segment in the same BX, it will be sent during the subsequent BX. This happens only, however, if no segment was generated during that next BX. One tag bit signals to the Input Receiver if the segment belongs to the present BX or it is the second segment of the previous BX. The segments Deserialization Block puts both segments belonging to the same BX in parallel. This is necessary as the further blocks of the PHTF work on both segments in parallel.

4.2.2 Extrapolation

The Extrapolation principle

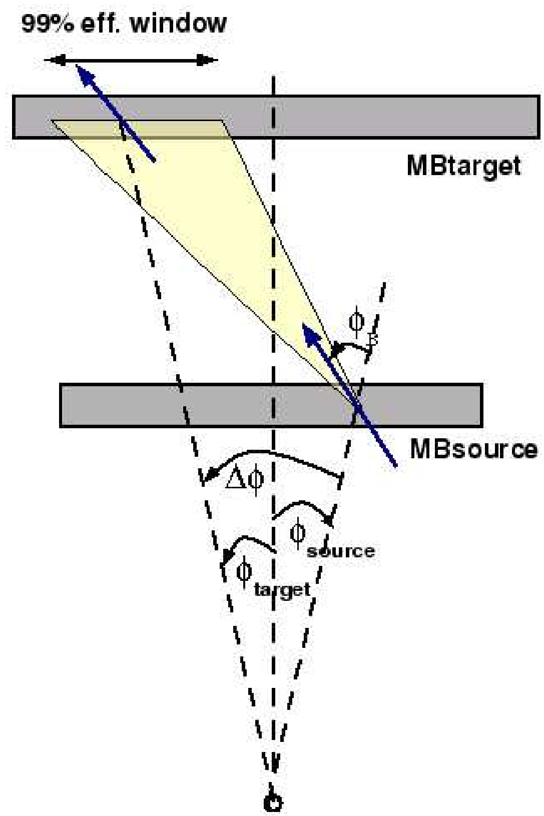

Figure 4.9: *Schematic illustration of the extrapolation principle.*

The segment pairs matching is based on a extrapolation principle, i.e. the correlation between the change in the azimuthal coordinate ($\Delta\phi$) and the bending angle (ϕ_b). Using the spatial position, ϕ_{source}, and the angular measurement, ϕ_b, of a segment in a Muon Barrel (MB) station (MB_{source}), the extrapolated coordinate, ϕ_{target}, in an outer MB station (MB_{target}), can be calculated according to Expr. 4.1.

$$\phi_{target} = \phi_{source} + \Delta\phi(\phi_b) \tag{4.1}$$

Fig. 4.9 schematically illustrates this principle. In the absence of magnetic field and dead material between the MB stations, the muon path from the source MB station to the target MB station is a straight line, thus $\Delta\phi(\phi_b)$ would be a linear correlation[1]. More

[1]The relation is linear when the variables ϕ and ϕ_b are the tangents of the angles represented in Fig. 4.9. The DT Local Trigger already provides the tangent values instead of the angle values.

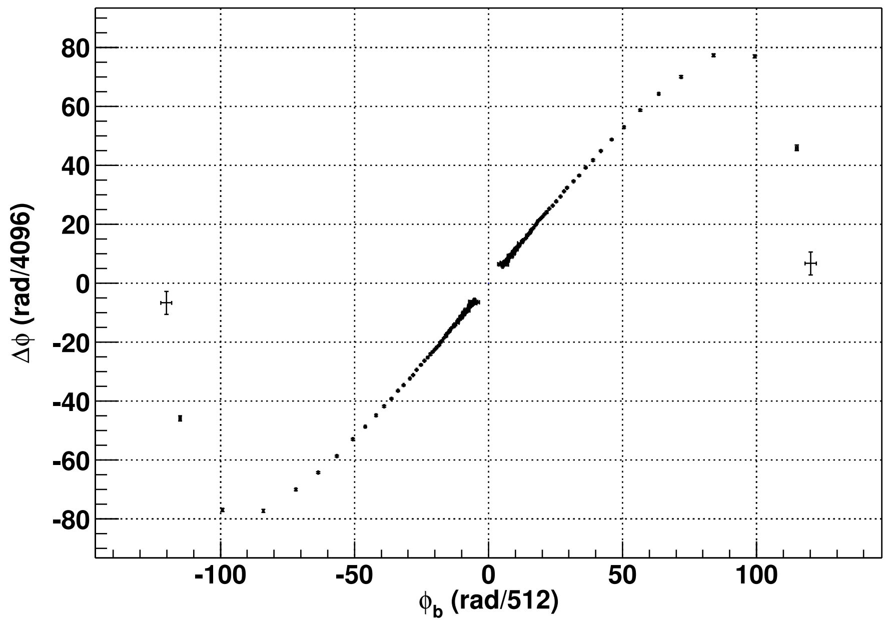

Figure 4.10: *$(\Delta\phi, \phi_b)$ correlation for the $2 \rightarrow 3$ stations pairing. Points correspond to muons with p_T in 1 GeV/c bins.*

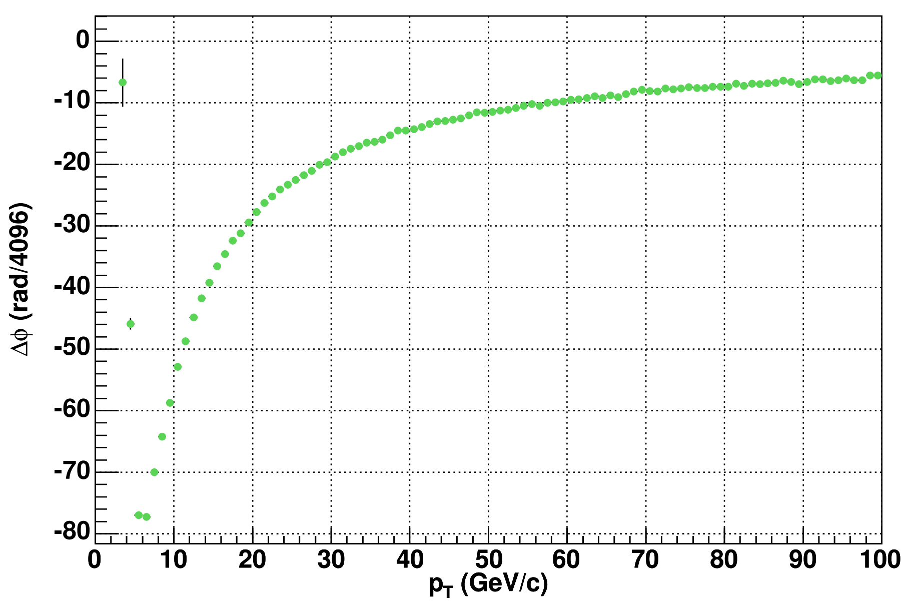

Figure 4.11: *Relation between the change in the azimuthal coordinate ($|\Delta\phi|$) and the transverse momentum (p_T) for MB2-MB3 stations pairing.*

important, it is a well defined correlation: for a given ϕ_b and ϕ_{source}, the value of ϕ_{target} is unambiguously defined.

However, at CMS, the high magnetic field in the iron yoke bends the muon trajectory. Therefore the $\Delta\phi(\phi_b)$ correlation is not linear anymore, but still exits: given a value of ϕ_b, the corresponding value of $\Delta\phi$ can be predicted for real muons. This is illustrated in Fig. 4.10 when the station pairing MB2-MB3 is considered. This correlation will allow extrapolating from one station to another one.

Furthermore, inside the magnetic field, there is a relation between the muon p_T and $\Delta\phi$ (or ϕ_b). This relation is shown implicitly in Fig. 4.10, where different points correspond to muons with p_T in 1 GeV bins. More explicitly, Fig. 4.11 shows the average $\Delta\phi - p_T$ correlation. This correlation will be used for p_T assignment, as discussed in Section 4.2.5.

To complete the description, the interaction of the muons with the iron yoke must be considered. Two main processes disturb the expected muon trajectory in its flight from the MB source of the extrapolation to the target MB station. First, multiple scattering processes can deflect the muon trajectory. Second, energy loss (dE/dx) processes can bend more than expected the muon trajectory. These processes are introduced as fluctuations from the expected mean correlation depicted in Fig. 4.10. As a consequence, the $\Delta\phi(\phi_b)$ correlation is not fixed anymore. The muon trajectory can only be parametrized trough efficiency windows: for a given ϕ_b, which is equivalent to p_T, a $\Delta\phi$ range is defined with a fixed efficiency.

For the calculation of the extrapolation windows, simulations of the system are used. The simulation tools are described in Section 4.7. Two main reasons justify their usage in the efficiency windows calculation. First, it is easier to calculate the mean $\Delta\phi(\phi_b)$ correlation than through analytical procedures. Second and more important, it is the only way to introduce the fluctuations produced by the interaction of muons with the iron yoke.

Attending to the $(\Delta\phi, \phi_b)$ parametrized correlations, an extrapolation is considered successful when the spatial position in the target MB is found to be inside a 99%-efficient extrapolation window. The 99%-efficient windows are downloaded to the hardware in the form of Look-Up-Tables (LUTs). A LUT is downloaded into the hardware for each station pairing to be evaluated. Fig. 4.12 shows the calculated 99%-efficient LUT for the MB1-MB2 stations pairing.

From the physics point of view, Look-Up-Tables are the most important issue of the DTTF system. They provide the electronics with the physics information necessary to implement its triggering tasks, i.e. decide whether a combination of electronics signals is associated to the passage of a muon through the detector. Details on the LUTs calculation exceed the scope of this report.

The Extrapolator Unit

After synchronization and deserialization the segments are sent to the Extrapolator Block for evaluation, but they are also kept in a pipeline for a later evaluation. The

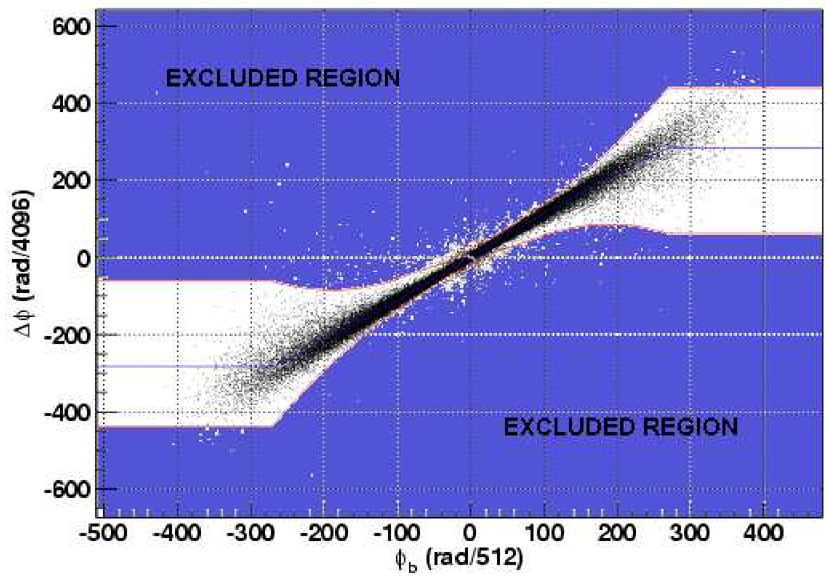

Figure 4.12: *The* 99%*-efficient* $1 \to 2$ *extrapolation LUT limits (white region) the valid* $(\Delta\phi, \phi_b)$ *correlation for a segment pair.*

Extrapolator Block (Fig. 4.13) evaluates every segment-pair if it can be part of the same muon track. The following segment pairs are evaluated:

- MB1 $\to$ MB2; MB1 $\to$ MB3; MB1 $\to$ MB4
- MB2 $\to$ MB3; MB2 $\to$ MB4
- MB4 $\to$ MB3

The pairs from MB3 are not evaluated as the ϕ_b value in MB3 does not show dependence on the track's path.

In the PHTF System the input segments are indexed. The indexing system is derived from their internal representation. Thus the segments that come from the same Wheel as the PHTF Unit elaborating them ('Own Wheel') have four bit indexes, while those segments coming from the next neighboring Wheel ('Next Wheel') have three bit indexes.

Wheel	Right side Neighbor	Own Sector	Left Side Neighbor
Own	10, 11 (1010, 1011)	8, 9 (1000, 1001)	12, 13 (1100, 1101)
Next	2, 3 (010, 011)	0, 1 (000, 001)	4, 5 (100, 101)

Table 4.1: *Segment Indexes used by the PHTF.*

For each segments pair there is a Look-Up Table (LUT) containing the acceptance window depending on the ϕ_b (bending angle) value. For each segments pair the Extrapolator checks if the ϕ position in the target station is inside the window predicted by the LUT. If this is the case the Extrapolator sets a '1' in the corresponding entry of the Extrapolation Result Table. There is a possibility to perform an Extrapolation from MB2 toward station MB1. The result of this Extrapolation can be used as a verification for the 1→2 Extrapolations in case MB1 is noisy. This feature can be et as a Run Parameter.

The output of the Extrapolator Sub-Unit are the Extrapolation Result Tables. There are 12 bit or 6 bit Tables for each Extrapolation Source Segment. The 12 bit Tables are the results of the segments pairs that have the source in the own Wheel of the PHTF Unit. The 6 bit Tables belong to the segments that have the source in the next Wheel. This is because a source segment in the own wheel can have 12 potential Targets, 6 ones in the own Wheel, 6 ones in the next Wheel. A source segment in the next Wheel can, however, only have 6 targets in the next Wheel, because a muon that left the own Wheel never returns. Thus the Extrapolation Result Tables #8,9,10,11,12 and 13 contain 12 bits while Tables #0,1,2,3,4,5 contain 6 bits. The total bit count of all Extrapolation Result Tables is 180 bit.

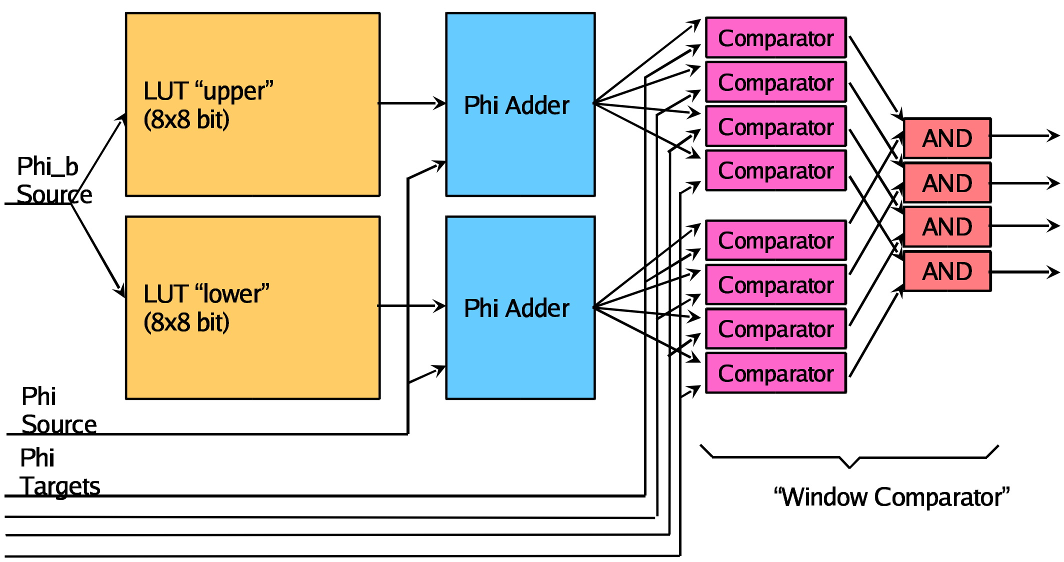

Figure 4.13: *The basic Extrapolator Unit.*

The 2→1 Extrapolations do not form an Extrapolation Result Table. When used their Table is set in a bit-wise AND with the Result Table of the 1→2 Extrapolations.

The Extrapolator Block has an additional task. The ORCA Simulations showed that there is a certain amount of segments that are assigned to more than one BX. The segments assigned to a wrong BX usually have, however, a lower quality value. This gives a possibility to filter them out. This also happens in the Extrapolator Block. To save latency, the cancellation conditions are set in parallel to the Extrapolation. When the cancellation feature is activated it resets the Extrapolation Result Table bits that were generated by a wrong segment.

4.2.3 The Linker

The Extrapolator determines which segment pairs might belong to the trajectory of one muon. The Linker joins these valid extrapolations to make a full track. The goal is to find the longest possible track. The Linker finds the longest track first, after which it cancels out all used parts from the data set. Then it finds the second longest track that can be combined together from the remaining Extrapolation data.

To find a track the Linker sets up 68 possible basic combinations of AND connections of extrapolation results. These combinations are set into a priority order, the combination resulting in the longest track. As no hardware realization can be generated for a 68 bit priority encoding the AND results are grouped first. A secondary level priority encoder finds out the highest priority group having a valid combination and a multiplexer chooses from the results of the highest group priorities.

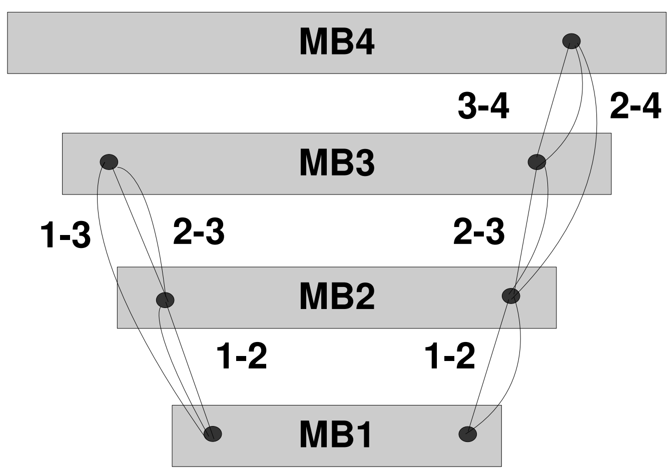

Figure 4.14: *Two examples of a track linking process. The track on the left is labeled as a 123 track, as all possible extrapolations could be performed. Although extrapolation 1-2 was successful, the track on the right is labeled only as a 234. A successful 1-2 extrapolation needs to be validated by the remaining possible extrapolation originating at MB1 (1-3, 1-4).*

After finding the first track, i.e. the longest one, all its subtracks are canceled by using a Cancellation Table. This table shows all sub-tracks for each possible track combination. It will be used as a mask to cancel them out. The result has only 56 basic combinations. This is due to the fact that a second track cannot be the longest one any more, as the longest one has been already found as the first track. The second track will be found in the same way as the first one was. Due to the pipelined structure the same hardware cannot be used for this task, as it is already searching for the first track of a next BX. Thus the hardware blocks are repeated to find the second track. The addresses of the first found track are kept in a pipeline during the search. After 7 BX both tracks are found.

Depending on which segments, i.e. which MB station delivered them to the DTTF, are used, different track classes can be reconstructed. Up to eleven track classes are possible: T1234, T123, T124, T134, T234, T12, T13, T14, T23, T24, T34 (the digits denotes the MB station where the segment came from). Fig. 4.14 clarifies the track linking algorithm.

The Linker generates its output in several different forms. The basic output data set contains the addresses (Indexes) of each segment participating in the found track as can be seen in Table 4.1. This data set will be sent to the Pipe and Selection Unit. A reduced data set will be sent to the Parameter Assignment Unit to find out the correct procedure for its assignment process. A special coded form (DAW) will be sent to the Wedge Sorter that needs this for finding ghosts. As the ghost finding is based on the track addresses in stations 2 and 3 the coded output contains information only about these two. Another coded data set (DAE) will be sent to the ETTF Block. This block only contains information about the track's features in the η-plane: where the muon track crossed wheel boundaries.

4.2.4 The Pipe and Selection Unit

The Pipe and Selection Unit keeps all the input segments until the two longest track's addresses are found. There are 12 pipelines for each station containing also the neighbors' segment data. When the addresses are available a multiplexer at the end of the Pipeline chooses the segment parameters of the found track and forwards them to the Parameter Assignment.

4.2.5 Parameter Assignment

The Parameter Assignment unit is responsible of assigning physical parameters to the muon tracks. Transverse momentum (p_T), direction (ϕ and η), and electric charge, as well as a quality code are assigned. These parameters form the output of the Sector Processor. The information of the segments used to assemble the muon track and stored in pipeline memories (Fig. 4.5) are used in the assignment algorithm.

For both output muon data set two separate Parameter Assignment Units are available. Their internal structures are identical.

The parameters are all assigned by stand alone assignment blocks. The assigned p_T value is based on the ϕ difference, $\Delta\phi$, in the lowest two stations participating in the track (Fig. 4.11). Look-Up-Tables containing the $p_T(\Delta\phi)$ relation are used for the assignment. As two different p_T values (one high and one low) correspond to the same $\Delta\phi$ value (Fig. 4.11), there are two different LUTs. The ϕ_b value in the lower station determines if the low-p_T or the high-p_T LUT will be considered. The Charge Assignment is also part of the same structure. The charge of the muon is given by the sign of the $\Delta\phi$ measured in the lowest two stations.

The ϕ assignment is necessary because the PHTF uses local ϕ values, with their zero values fixed at the centerline of the given Sector. The PHTF Output, however, should forward CMS wide ϕ values. Therefore a LUT reformats the local ϕ value into a global one. This LUT is different for every sector's PHTF.

A different situation arises if the found muon track had no segment in MB2. As the muon's ϕ parameter should be given at the level of MB2 by definition, Extrapolation LUTs are used to determine the ϕ position at MB2. The lowest possible station is always used as the Extrapolation Base.

The Output Quality is a 3 bit value that shows the quality of the found muon derived from the number of stations participating in the track. A value '0' shows that no muon has been found, a value '7' represents a muon that was reconstructed from segments in all four stations. Table 4.2 shows the relation between the quality code and the track class.

Quality Code	7	6	5	4	3	2	1	0
Track Class	T1234	T123 T124	T134	T234	T12 T13 T14	T23 T24	T34	Null Track

Table 4.2: *Output quality codes relation with the possible track classes. Track classes names represent the MB stations to where the track segments used in the reconstruction belongs to.*

As in the Extrapolation stage, LUTs are the physics core of the Parameter Assignment. They contain the information necessary to convert the electronics signals produced by a muon into its physics properties.

4.3 The Eta Track Finder

The ETTF finds tracks in the $r - z$ projection (polar plane). The ETTF uses a different Track Finding method than the PHTF. As the Trigger Server sends only hit and quality information rather than Segments from the Eta Drift Tube Layers there is no possibility to perform Extrapolations. A pattern matching procedure is used instead (Fig. 4.15). A block diagram of the ETTF track finding algorithm is shown in Fig. 4.16.

The geometry, the magnetic field configuration and the pattern matching method prevent the ETTF to determine all physical parameters of a muon track in a stand alone way. Thus the ETTF's task is first to find tracks in the η projection, and subsequently to try to match them with those found by the PHTF. If a matching is possible, the ETTF assigns the value of the η coordinate to the muon found by the PHTF. If no matching can be obtained, a rough value of η is assigned using the PHTF DAE code.

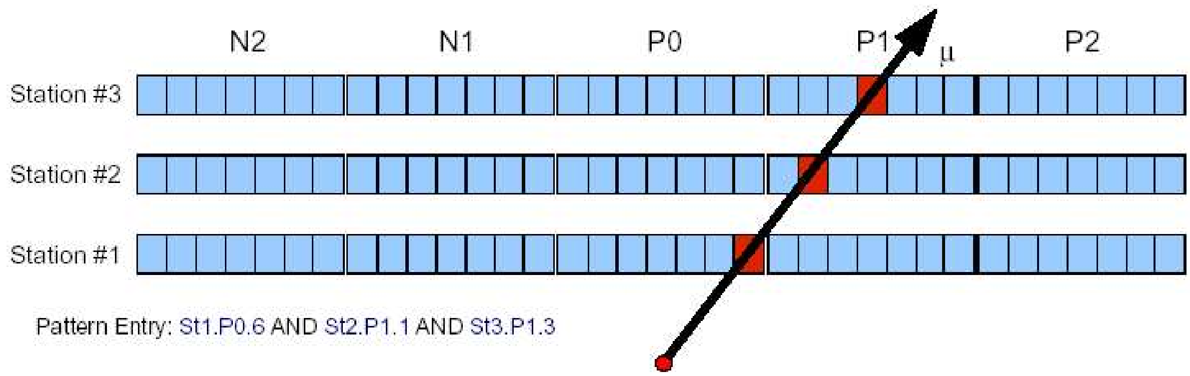

Figure 4.15: *Illustration of the ETTF track finding method. A pattern matching method is performed.*

The patterns of possible tracks are grouped according to the geometrical features determined by the output η values. These groups contain all possible patterns belonging to the same output η value ordered by quality. The patterns of muons crossing more stations have higher priority. For patterns with the same station hit structure, the higher η value patterns have higher priority. The quality bit attached to each hit bit also allows to set up a pattern with different priority. While the number of quality bits results in different patterns, their position is irrelevant. A muon with a high quality hit in the first station and a low quality hit in the other two stations delivers the same pattern value as a muon with low quality hits in the first and second stations but a high quality hit in the third one. To create the patterns the ETTF hardware sets up AND conditions for the corresponding hit and quality bits. The combinations with the same priority are OR-ed afterwards.

The highest priority pattern showing a muon in each group will be selected by a priority encoder. The outputs of this first level priority selection are also grouped by their positions in the η category delivered by the PHTF Unit. Inside each Category a new priority list will be generated using the same principles as in the previous priority setup. The result of this selection is used for matching.

Matching will be performed if one of the 6 PHTF Units of a wedge also found a muon in the corresponding category group. If a matching is possible, a 'fine' global η value will be assigned to the muon. If the ETTF does not find any muon in the group where the PHTF has found one, it assigns a 'rough' global η value and sets the 'Rough' tag in the output to indicate to the Global Muon Trigger how the muon's η value was generated.

If the PHTF delivers more than one muon inside one group or if the ETTF finds more than one muon inside one group, no matching is performed; the ETTF delivers a 'rough' η output value.

The ETTF delivers the η values at the same time as the PHTF delivers the physical parameters of the found tracks to the Wedge Sorter (WS). Therefore the WS can handle them as a single entity.

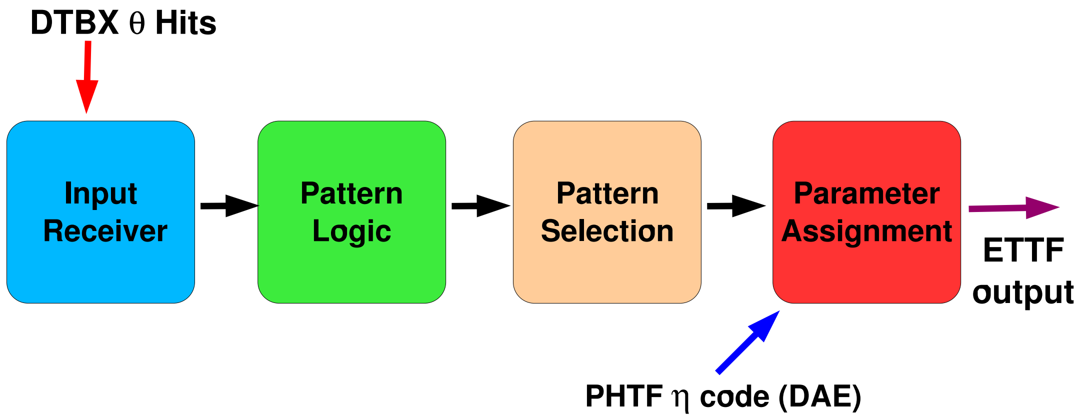

Figure 4.16: *Logical Block diagram of the ETTF track finding algorithm. Three logical steps implement the pattern matching method.*

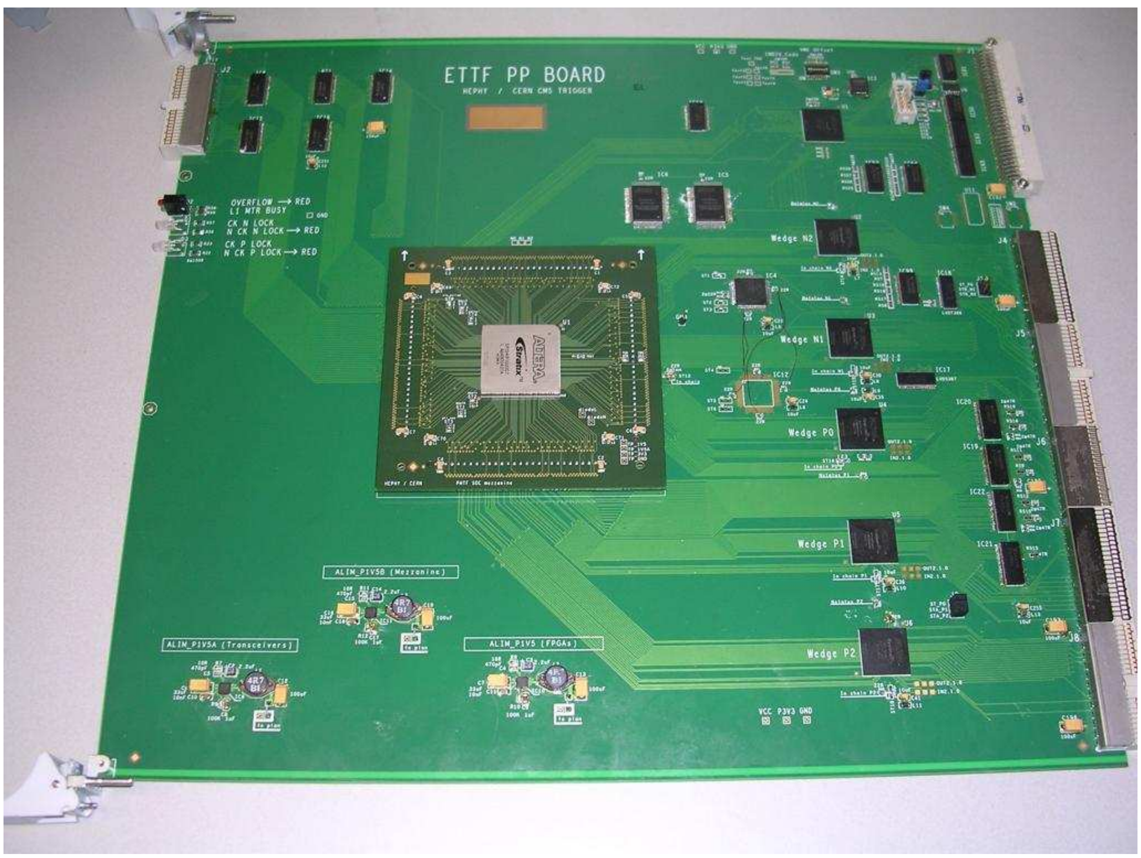

Figure 4.17: *The ETTF PreProduction Prototype (PPP) board.*

Every wedge electronics contains an ETTF Unit. It is plugged into the slot in the center of the wedge slots in order to minimize the number and lengths of the Backplane connections. Thus the ETTF Block receives η code information from three PHTFs on the left side and three PHTFs on the right side.

A photo of the ETTF PreProduction Prototype (PPP) is shown in Fig. 4.17. This prototype was used to evaluate the ETTF design before the final production begins. More details on the ETTF algorithm and hardware implementation can be found in [24].

4.4 The Drift Tube Muon Sorter

The DT Sorter selects the four highest rank DTTF muons in the barrel detector, after a clean-up procedure (removal of duplicate tracks), and forwards them to the Global Muon Trigger. The highest rank muons are those with highest quality and highest transverse momentum. The sorting process is implemented in two steps, Wedge Sorting and Barrel Sorting. Each of this logic blocks is implemented in the hardware through different modules.

Wedge Sorter

In every sector, one Wedge Sorter (WS) receives the addresses and muon physical parameter information from the six PHTFs and the ETTF of its wedge. Using this information, it selects the two best muon tracks out of (at most) twelve candidates. This task is performed in two steps. First it cancels out the ghosts, i.e. muons that were found by two different PHTFs. This action uses the segments addresses information. If two tracks have the same addresses in stations MB2, MB3 and MB4, the shorter one will be canceled out. As the address information from the PHTF is available 1 BX earlier than the full muon output, the WS can start this step during the PHTF's parameter assignment activity. Fig. 4.18 shows a schematic representation of the Wedge Sorter ghost cancellation scheme.

If the muon tracks found by the PHTF arrive with the full physics information, the WS skips the ghosts and only evaluates the real muon candidates. They will be sorted by their track quality and transverse momentum values. At the end of the sorting the best two muons, i.e. higher quality and higher p_T, are forwarded to the DT Barrel Muon Sorter (BS). Both the addresses and the physical parameters are forwarded.

Barrel Sorter

There is one DT Barrel Sorter for all the DTTF Trigger system. It selects the four highest rank muons among the, at most, 24 delivered by the 12 Wedge Sorters and forwards them to the Global Muon Trigger.

The Ghost Cancellation in the Barrel Sorter is necessary to filter out ghosts in the sideways neighboring wedges, as their function is independent up to this point. The ghost cancellation is made on the same way as in the WS, based on the track addresses in the stations MB2, MB3 and MB4. The sorting procedure is also made on a similar way. The output of the BS is sent to the Global Muon Trigger.

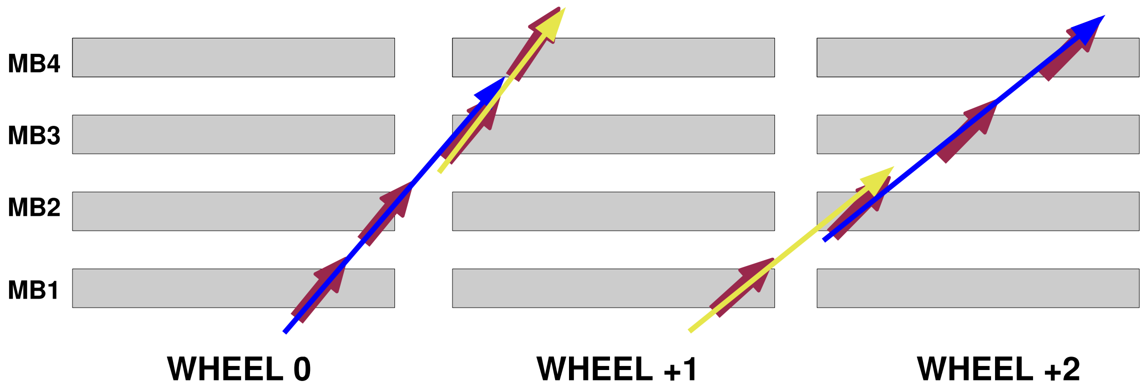

Figure 4.18: *Schematic drawing of the WS ghost cancellation scheme. Tracks represented by the yellow arrows are ghost (doubled) reconstructions of tracks represented by the blue arrows. Therefore, the WS cancels them out.*

4.5 The Data Concentrator Card (DCC)

The Data Concentrator Board receives the Data Acquisition (DAQ) information from all the DTTF System when a Level-1 Accept signal is issued by the Timing Trigger and Control (TTC) System. As the DT Trigger Front-End level has no connection to the CMS DAQ system all the DTTF Input Data should be forwarded to the CMS DAQ. In addition, the PHTF units' output to the WS will also be included in the data set for DAQ. The DAQ output contains all bits belonging to an L1 Accept and one BX before and one after the L1 Accept (L1-1 and L1+1), which will make it easier to trace possible synchronization errors.

The DAQ System allocates one 'DAQ-partition' to the DTTF System. This means that the DTTF system can send 2 kByte of data for each L1 event on average, resulting in a data bandwidth of 200 MByte/s. The DAQ S-Link64 Interface boards can forward 64 bits in parallel using a max. 100 MHz input clock, which can transmit up to 800 MByte/s during short transmission peaks. The DTTF DAQ interface is designed to use the standard LHC 40.08 MHz Clock to drive the output, achieving therefore a maximum rate of 320 MByte/s.

The total sampled DTTF system data rate of 5.32 Gbit/s corresponds to 665 MByte/s, 3.32 times more than the DAQ bandwidth allocated for the DTTF System. Therefore, data compression is required. However, and according to system simulations, a simple Zero Suppression procedure satisfies the compression requirements.

This, however, should happen on segments basis, as on the Sector basis noise induced data would not be effectively suppressed. In order to minimize the data handling overhead, the zero suppression is performed in the central Data Concentrator Unit. This also means that all data bits have to be forwarded from the PHTF and ETTF Cards to that Unit. A Data Link system performs this task.

The DTTF DAQ system is composed of three different type Blocks - the Local DAQ Block as part of the PHTF and ETTF Chips, the Data Link (DLI) Boards in every wedge and the central DAQ Data Concentrator (DDC) Unit. This unit also contains the S-Link64 Boards, which forward the DAQ Data to the CMS DAQ System. Fig. 4.19 illustrates the DTTF DAQ system organization.

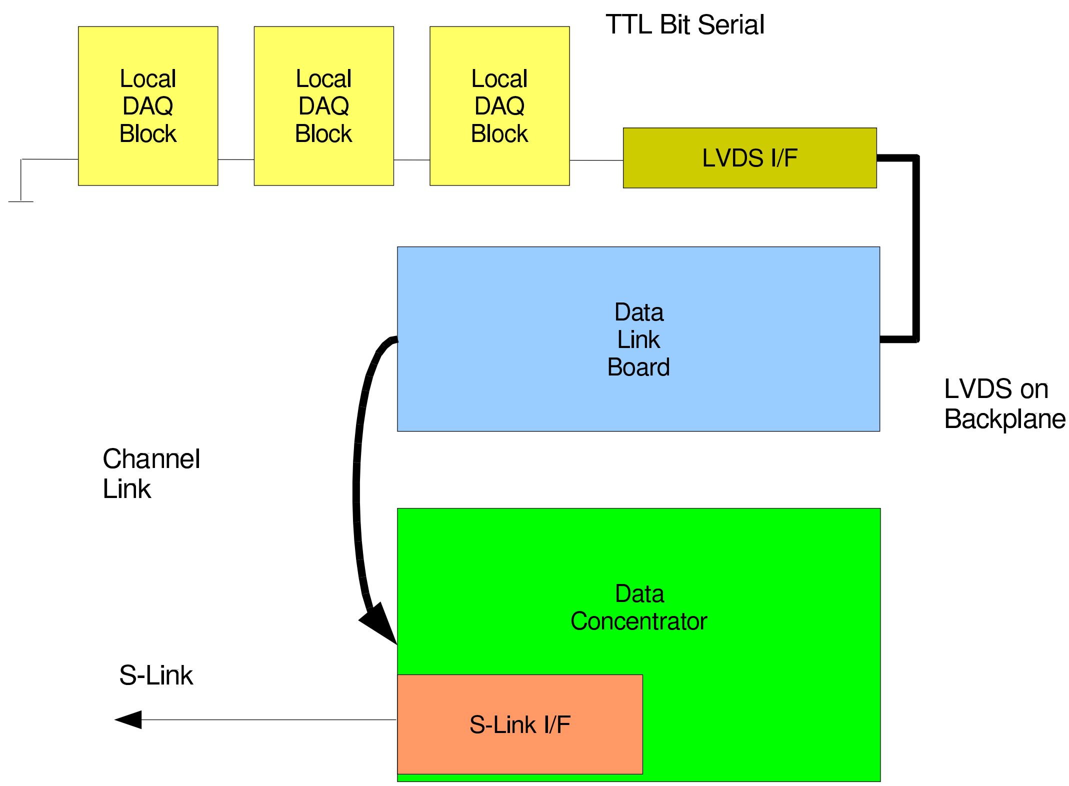

Figure 4.19: *Schematic drawing of the DTTF DAQ system. PHTF and ETTF units in a crate send data to the DLI board. The DLI boards at every crate forward the data to the DCC which performs its operations and sends it output to the CMS DAQ system through a S-Link.*

The Local DAQ Blocks are functional units of the FPGAs in the PHTF and ETTF that sample, deserialize and send data to the Data Concentrator through the Data Link Interface (DLI) Board in their wedge.

As every wedge contains 7 Data Sources, 6 PHTF and 1 ETTF Boards with 3 Lines each, the DLI receives 2 wedges x 7 Boards x 3 BX = 42 Lines. The DLI Board outputs DAQ data from two wedges of the Crate.

The Data Concentrator's task is to perform a Zero Suppression on the incoming DAQ data, organize them according the DAQ requirements and prepare the Data Blocks to be forwarded to the DAQ System. It also contains the S-Link64 Mezzanine Board, which sends DAQ data to the DAQ System.

The zero suppression task is performed immediately after the input. This saves logic and memory resources. The zero suppression is made on segment or on a data logical unit basis.

The DAQ data remaining after zero suppression will be loaded into the DAQ FIFO together with its source (Board, segment number) and the L1 number it belongs to. Every input channel has its own DAQ FIFO. The Readout Controller organizes the data readout procedure. It also prepares DAQ Data Blocks by adding Header and Trailer information and calculates the CRC (cyclic redundancy code) number.

4.6 The Spy System

All boards in the DTTF system are equipped with a Spy Module for checking and maintenance purposes. Each Spy Unit in a chip allows to follow up, sample and store information about input and internal signals of the chip in real time. It can be thought as a on-board logic analyzer, allowing real time access to all the logic blocks of the DTTF algorithm, e.g. optical input, extrapolation or assignment units. A spy operation is performed by making a snapshot of a sequence of consecutive data words processed by the chip. As the triggering of the spy process is centrally controlled, it is possible to obtain a snapshot of the whole board.

Such a tool plays a main role in the system testing and development process. The DTTF system electronics is designed as a fully pipelined logic. Each sub-unit of the system performs a fast evaluation data and forwards the result to the next sub-unit every 25 ns. Therefore, the system never contains fully consistent data, with the exception of input and output. A tool which allows full access to all the steps of the reconstruction algorithm is of main interest.

The Spy system is the hardware basis of the DTTF Local DAQ system used during the October 2004 Beam Test. In the following, we summarize its working principle. A full description of the Spy system can be found in [25].

The Spy system is logically divided in three main blocks: a Local Spy Unit, a Spy Master Trigger Unit and a Spy Control Unit.

The Local Spy Unit

The main component of the Spy Unit is the Spy memory. This is a 512 Word deep on-chip memory that is organized as a ring buffer. Its width depends on the size of the data bits to be observed. The number of sample cycles after which a Spy Trigger occurs are defined by the user through the so-called 'Spy Offset'. When the Spy Trigger condition is met, the Spy Offset will be loaded into the downward counting Spy Counter. When the Spy Counter reaches the value '0', the sampling process is stopped. At this moment the Spy Memory contains the content of the observed lines, whose number is determined by the Spy Offset, the number of words before the Spy Trigger is stored in the remaining memory location of the 512 Word memory. At the moment of a Spy Trigger the content of the ring buffer pointer will be loaded into the Input Address Register for later retrieval.

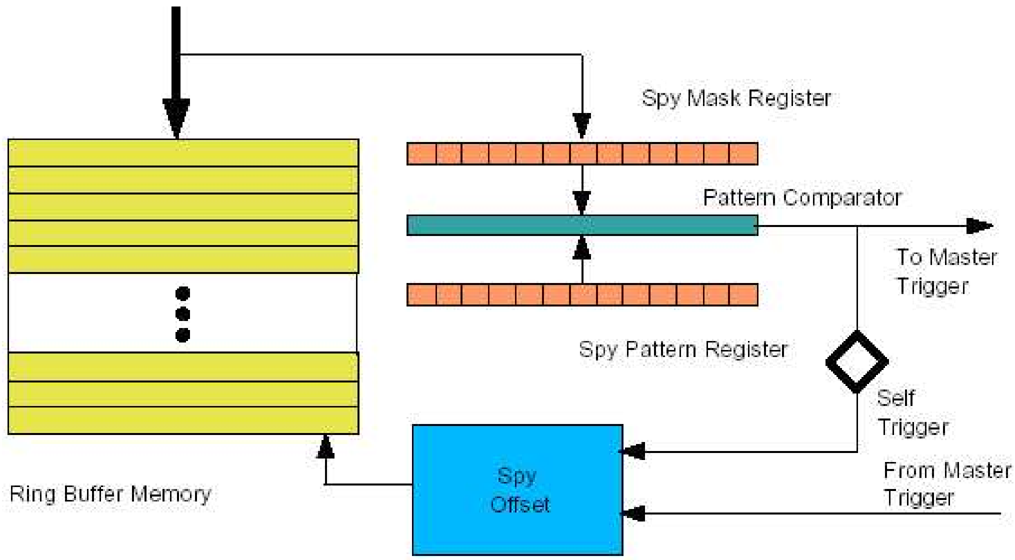

Figure 4.20: *The Local Spy Unit logical structure. When the Spy Condition is met, the Spy Memory is filled with the content of the spied block. The length of the spying processes is determined through the spy offset.*

The Spy Trigger Unit contains two registers, the Spy Mask register and the Spy Pattern Register. Both have the same length as the Spy Memory width. The Spy Mask Register contains the bitmap of the input bits to be observed, the Spy Pattern Register determines the value that fulfills the Spy Trigger Condition. If the bits under observation have the value of the Spy Pattern, the Spy Condition is met.

Fig. 4.20 shows the Local Spy Unit blocks.

The Spy Master Trigger

All Spy Blocks of a PHTF or ETTF Board and the Master Trigger Control Block in the Board Controller Chip constitute the Spy System. The Spy Trigger Unit of the local Spy Block can start the sampling only for itself (Self Trigger) but it can also send a Spy Trigger signal to the Master Trigger Unit in the Controller Chip. This Unit contains two registers, programmable from the VME bus. Their lengths correspond to the number of independent Spy Units on the Board. The Master Trigger Accept Register determines which Spy Unit is allowed to release a Master Spy Trigger signal. The other register, the Master Trigger Enable Mask Register, determines which Spy Units are triggered. The Spy Master Trigger acts on all Spy Units of the Board at the same time, thus all Spy Units will have a snapshot of the same BX data of the whole system.

The Spy Master Trigger feature requires 3 BX time in total to perform the centralized Master Trigger, thus the Spy Counter will start 3 BX after the Spy Condition was met. This also means that the Spy Memory of all chips in the system will contain 'Spy Offset-3' words after the Spy condition.

The Master Trigger Unit has been extended to handle BC0 and L1 signals and include Spy Conditions with BX Counter and L1 Counter. This way the CMS timing system will be part of the DTTF Spy System. In particular the L1 signal handling was necessary for the implementation of a Local DAQ based in the Spy system.

The Spy Control

The Spy system control uses different ways to access the Spy Master Trigger and the Local Spy Units. The Spy Master Trigger is part of the Board's Controller chip. As this chip contains the VME controller as well, the Master Trigger registers are directly accessible from the VME bus. They have their own VME addresses

The Local Spy Units are distributed among several Chips on the Boards. In order to minimize the layout resources needed by the Spy System these Blocks are accessible by a JTAG Chain. For this purpose a secondary JTAG Chain is constructed on the Board. This is controlled by the VME Controller in the same way as the primary JTAG chain that serves to program the FPGAs and perform Boundary Scan.

The secondary JTAG chain is a standard JTAG chain whose JTAG interfaces are constructed as programmed Blocks in the FPGA chips. They are programmed to include all standard JTAG registers and follow all standard JTAG commands like Reset, Read-ID or Bypass. The standard 'Sample-Instruction' and the 'Extest' commands allow to read out the Spy memory rather than to perform a pin-test. Additional commands were defined to load the Spy Offset, the Spy Mask and Spy Pattern Registers. It is also possible to define Readout Address and to load the Spy Control Register. A readable Spy Status register shows the state of the Spy Unit.

4.7 DTTF System Simulation

An important issue for both the system's development and for physics reconstruction during the experiment life is the use of software simulations of the system. During the development stage, simulations are the only way to understand the behavior of the system as a whole entity. In this section we discuss the DTTF system simulation tools and some results on the trigger performance from simulation results.

4.7.1 C++ Simulation

The DTTF Trigger is simulated by an Object Oriented system for which C++ has been chosen as programming language. An Object Oriented design allows to modularize the simulation replicating the DTTF hardware organization. In particular, all hardware modules of the DTTF Trigger system are represented by classes' instances. This approximation allows to describe the system in great detail in all its different components, easing the simulation development.

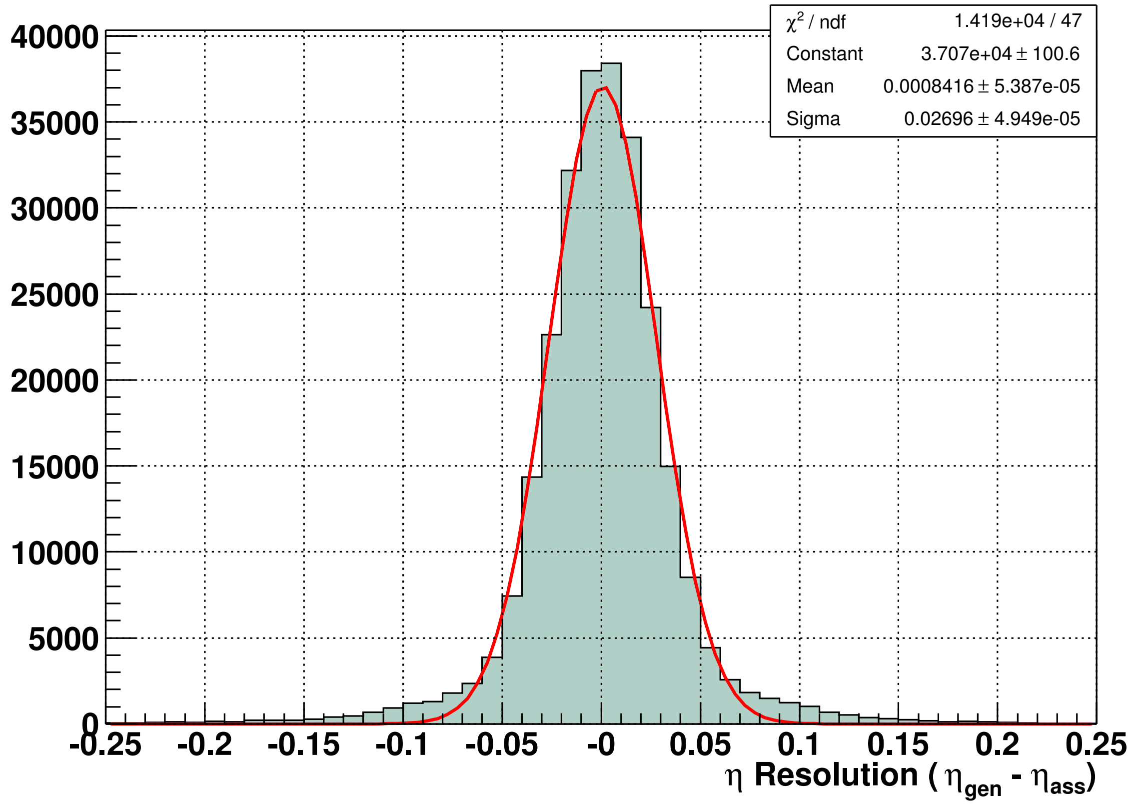

Figure 4.21: *Position resolution in the η direction.*

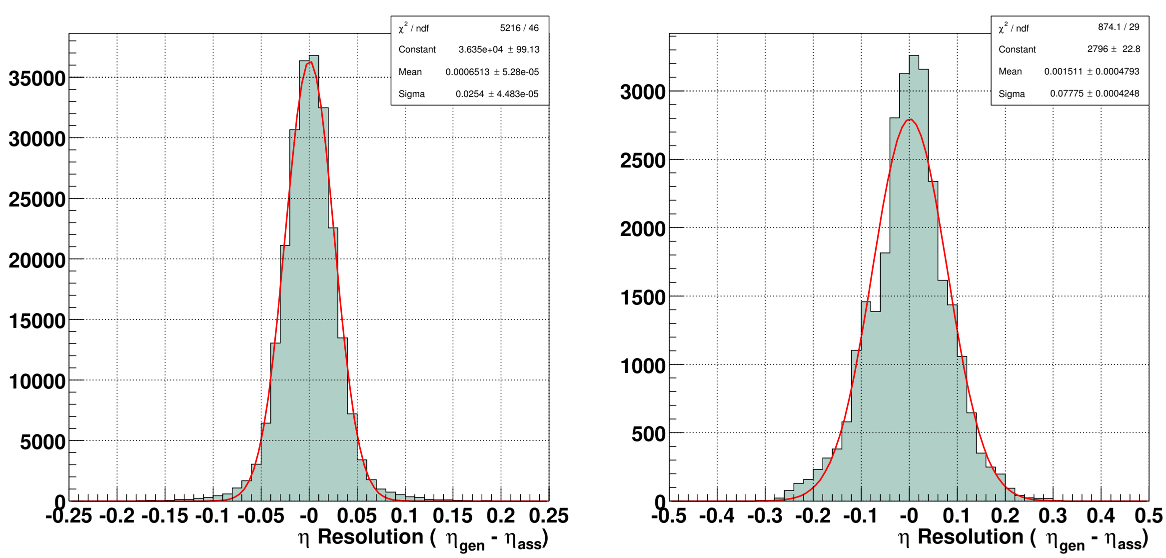

Figure 4.22: *η-position resolution for the 'fine' (left) and 'rough' (right) assignment.*

System simulations and hardware prototypes participate in a feedback process used to fine tune the performance of both realizations of the system. A 100% agreement between the simulation and the hardware implementation must be (and have been) reached. The simulation is not only used for the system development but also for physics reconstruction during the experiment life.

Although the DTTF simulation module is designed and used as an independent package, it can be integrated in the CMS simulation framework for reconstruction: the Object-oriented Reconstruction for CMS Analysis (ORCA) [26].

As it has already been mentioned, the C++ DTTF simulation has been used for the calculation of the physics core of the system, the Look-Up-Tables. Moreover, the expected DTTF Trigger performance can be estimated from simulation results.

4.7.2 Simulation Results

The DTTF Trigger behavior could not be studied with real data until October 2004 beam test. Nevertheless, the overall DTTF Trigger performance has been estimated using simulated data. The main results are discussed in this section.

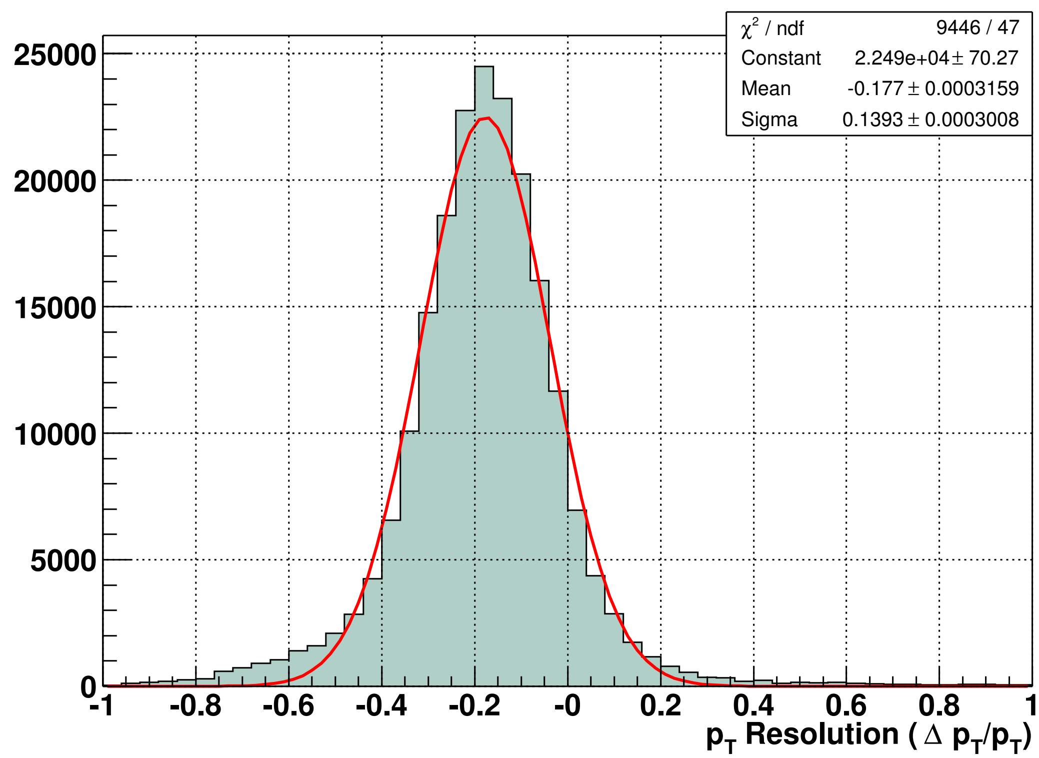

Figure 4.23: *Transverse momentum resolution* ($\Delta p_T/p_T$). *A negative offset is obtained due to the* 90% *efficiency* p_T*-assignment Look-Up-Tables.*

A sample of about 500,000 single muon events, positively and negatively charged, was used. The muon sample is flat distributed in the ϕ coordinate ($0 < \phi < 2\pi$ rad), flat distributed in η ($|\eta| < 1.4$) and the p_T spectrum ($3 < p_T < 100$ GeV/c) follows a $1/p_T$ distribution. The passage of particles through the material of the CMS detector and the detector response was simulated with the CMSIM package, based on GEANT3. For the reconstruction version 8_7_1 of ORCA was used.

Resolution

The position resolution in the azimuth (ϕ) coordinate is dominated by the DTTF output bin size (0.02 rad).

The position resolution in the pseudorapidity (η) coordinate has been studied. The resolution in η is shown in Fig. 4.21. A 0.027 resolution is achieved. As it has already been explained (Section 4.3), the η assignment can be done through two different methods, labeled as 'rough' and 'fine'. The position resolution for both assignment strategies has also been studied. Fig. 4.22 shows the results. A 0.025 resolution is achieved using the θ superlayers of the MB chambers (fine assignment). When only coarse assignment is performed, the resolution drops to 0.078.

The resolution of the transverse momentum assignment is given in terms of the $1/p_T$ residual distribution. The overall resolution, calculated considering the barrel region ($|\eta| < 0.8$), is 13.9%. Fig. 4.23, shows the p_T resolution, $\Delta p_T/p_T$, for the latter conditions. A negative mean value is found due to the definition of the p_T assignment Look-Up-Tables at a 90% efficiency.

Efficiency

The single muon efficiency plateau (0.9%) is only limited by the geometrical acceptance, both in the η and ϕ coordinates. Figs. 4.24 and 4.25 show the DTTF Trigger efficiency respect to the ϕ and η coordinates respectively. The efficiency drops only in regions where muons cross the detector without interacting with its sensitive parts (gaps). In the ϕ coordinate, gaps correspond to the detector's wedges boundaries, i.e. every 30°. In the η coordinate, the full coverage of the muon barrel system is achieved for $|\eta| < 0.8$. This explains the efficiency drop for $|\eta| > 0.8$, that is recovered by the Global Muon Trigger system, which uses the information from the RPC system and the CSC Track-Finder. The efficiency drop around $|\eta| \sim 0.2$ is due to muons crossing the gap between wheel 0 and wheels ± 1. The gaps between wheels ± 1 and wheels ± 2 do not affect significantly the overall efficiency.

With respect to the transverse momentum the full efficiency is reached at $p_T > 5$ GeV/c. Fig. 4.26 shows the efficiency respect to the transverse momentum of the muon.

The combined effects of the overall efficiency and the transverse momentum resolution are summarized by the 'turn-on' curves shown in Fig. 4.27. In the turn-on curves, the DTTF efficiency is represented as a function of the muon transverse momentum, for different transverse momentum thresholds.

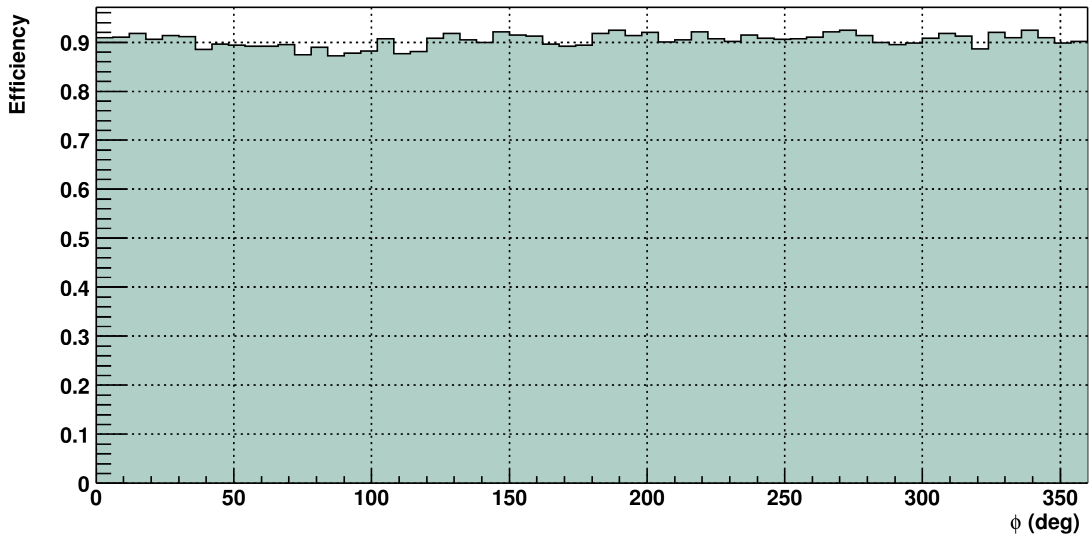

Figure 4.24: *DTTF Efficiency respect to the ϕ coordinate.*

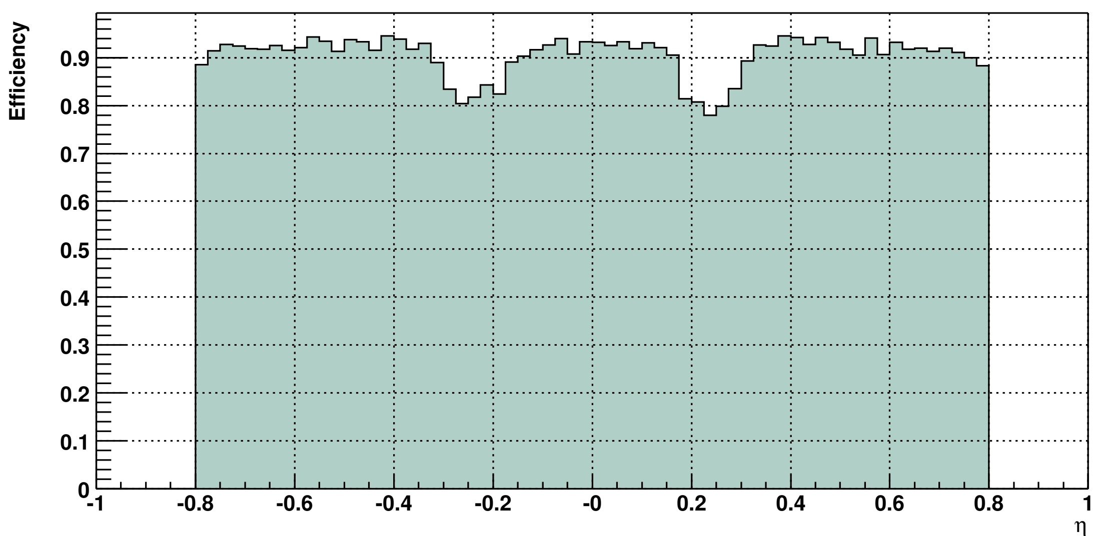

Figure 4.25: *DTTF Efficiency respect to the η coordinate.*

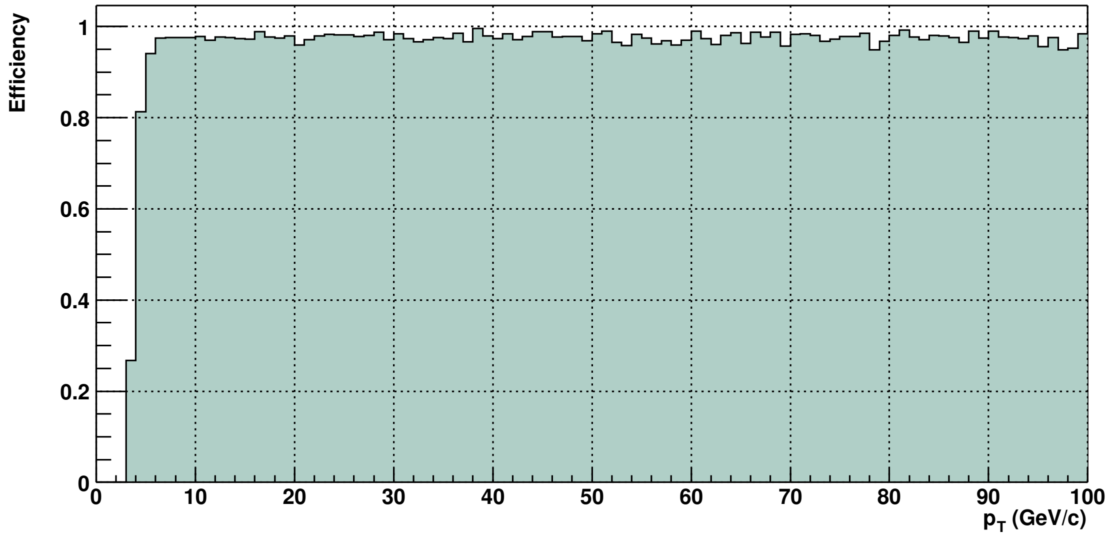

Figure 4.26: *DTTF efficiency with respect to the muon transverse momentum.*

Trigger Rates

Finally, the study of the accumulated inclusive muon DTTF trigger rates at $\mathcal{L} = 10^{34}$ cm^{-2}s^{-1} has been performed. A sample of minimum bias events was used. Fig. 4.28 shows the integrated single muon trigger rate as a function of the transverse momentum threshold. The higher trigger rate achieved by the DTTF system with respect to the generated rate for $p_T^{cut} > 4$ GeV/c is explained by the effect of the limited p_T resolution. At low-, intermediate- and high-p_T the rate is dominated by real muons (decays-in-flight, heavy quarks, and vector bosons, respectively). A trigger rate of 1.6 kHz can be achieved by setting a transverse momentum threshold of 21 GeV/c.

4.8 DTTF On-line Software

In addition to simulation programs, the DTTF system requires a complete on-line software infrastructure. That are the software tools needed for the configuration, control and monitoring of all devices involved in the system. At the CMS collaboration a homogeneous approach has been taken for the design and implementation of all the subsystems' on-line software. A detailed description of the CMS on-line software architecture can be found at Part 3 of [13].

The overall CMS on-line software architecture is shown in Fig. 4.29, the main goal of this architecture is to achieve the functionality required to operate the data acquisition system of the CMS experiment. In order to achieve this goal all subsystems must develop their software tools in the distributed processing environment provided by the DAQ group, XDAQ [28]. This is motivated by the expected ease of integration and configuration of

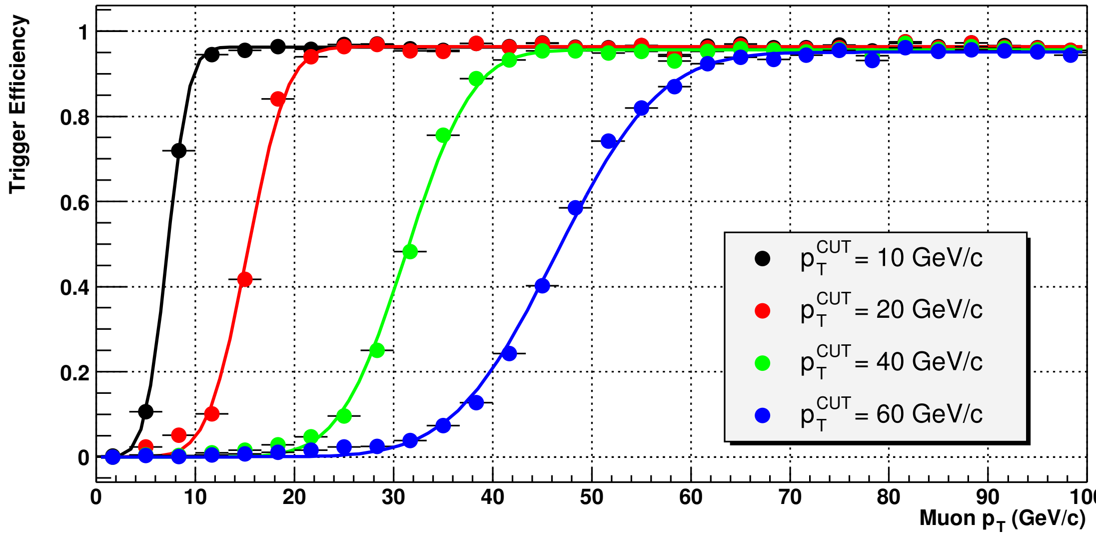

Figure 4.27: *Turn on curves for the DTTF. The efficiency is plotted as a function of the transverse momentum for different transverse momentum thresholds.*

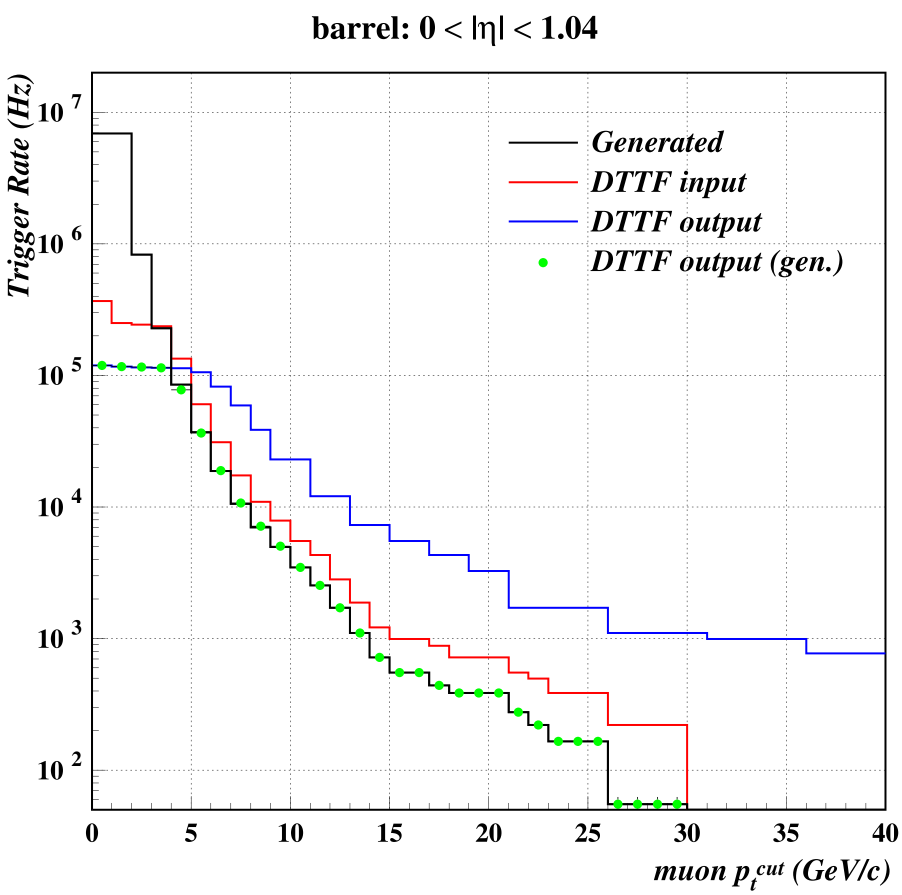

Figure 4.28: *Inclusive DTTF muon trigger rate as a function of the transverse momentum cut at* $\mathcal{L} = 10^{34}\ cm^{-2}s^{-1}$.

multiple and diverse subsystems. Using common and standardized software technologies reduces the effort associated with the maintenance and evolution of the system over the long lifetime of the experiment.

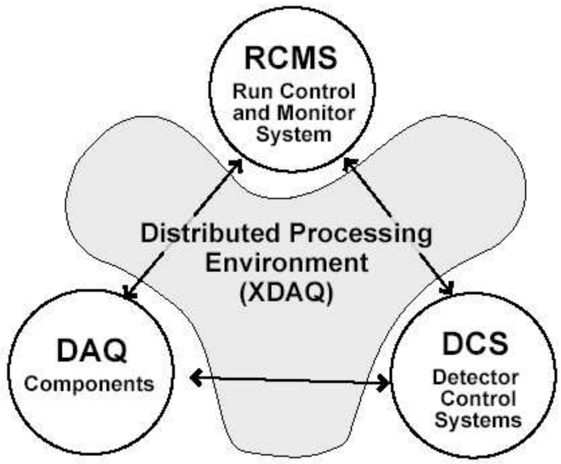

Figure 4.29: *Overall software architecture at CMS. XDAQ is the distribution processing environment under which all the subsystem's on-line software of CMS will be developed.*

The core of the on-line software tools are the so called XDAQ applications. They are simply C++ classes that may export any function to the framework, connecting their activation to incoming messages. They make use of the framework functions to communicate with other programs (or applications), to read from databases, to notify the cluster operator and to access custom hardware. For hardware access, a software package is included in XDAQ, the Hardware Access Library (HAL) which implements a C++ interface for VME read and write of electronic devices. Applications can be controlled, monitored and configured through a client, typically referred as a Graphical User Interface (GUI).

4.8.1 DTTF Control and Configuration Programs

The aim of the DTTF on-line software is to control, test and monitor all devices involved in the system. During the DTTF system development (prototyping) a complete set of programs has been implemented. The goal of these programs is to control and test the functionality of the DTTF boards.

All boards of the DTTF system have a VME interface providing direct access to a set of control and status registers [27]. Besides, all boards are equipped with two JTAG chains which are also controlled through the VME interface. The first chain provides Boundary Scan facilities while the second chain is used to operate the Spy System (Section 4.6).

For hardware control purposes, software packages were developed in order to allow full access to the boards features through the VME interface. All board's registers and the two JTAG chains functionalities are accessible through a customized Java based Graphical User Interface (GUI). Such GUI communicates with the control programs through a user friendly interface. The Boundary Scan tool and its on-line software interface allows to test the hardware functionality and is used for the debugging of a board design. However, due to the pipelined design of the DTTF algorithm, the Boundary Scan does not allow tests with dynamic input data patterns. For this purpose the Spy System (Section 4.6) was developed. Software tools to operate the Spy system have also been developed. The most important is the 'Spy-DAQ' tool.

4.8.2 DTTF Local-DAQ

From the point of view of the software, the Spy system is totally controlled through VME registers. The software programs to operate the Spy system has been developed under the name of 'Spy-DAQ'. Given a spy trigger condition, the Spy-DAQ system is able to readout the whole state of the module for the trigger bunch crossing and a maximum 511 bunch crossings around.

Spy conditions are determined through the 'Spy Pattern' and the 'Spy Mask' parameters. The user can determined which piece of data of the spied block is used to trigger a Spy process. Typically, data which determine that a muon track was found, e.g. the output quality word, could be used. However, the system can also be triggered by external signals, namely a Level 1 (L1) Accept signal. Due to the pipelined structure of the DTTF electronics, to obtain consistent data at all spied blocks, relative delays have to be measured and introduced as parameters into the control software. Hard developing work was carried out to reach a stable system able to perform long data acquisition processes without errors.

The utility of the Spy-DAQ system evolved through two main stages: test programs and data acquisition tasks.

The Spy-DAQ tool allows systematic and long run tests of the board's functionality and of the Spy system itself. Statistical analysis of the Spy behavior were performed. As a result, Spy-DAQ showed up to be an appropriate and stable tool to perform more detailed tests of the elements of the DTTF system. The Spy system makes 512 bunch crossings size snapshots of the whole state of a given module of the system. Thus, it allows to systematically test the algorithm hardware implementation. Not only the input and the output can be analyzed, but the different logical steps of the algorithm, as structured in Data Spy Blocks, can be checked. In particular, it is possible to analyze the response of the board to simulated data (ORCA) at the inputs. Furthermore, an 'event-by-event' comparison of the hardware response with respect to the ORCA simulated result is possible. Large samples ($\mathcal{O}(10^4)$) of single- and di-muon data patterns are injected both to the ORCA simulation and to the prototypes/boards. If differences in the output arise, all the steps preceding the trigger decision can be checked and compared with the simulation.

However, the Spy System is not only used for testing and maintenance purposes but also for Data Acquisition (DAQ) tasks. A Local DAQ system has to be developed for the DTTF. It must be able to perform DAQ tasks independently of the Central DAQ system of the experiment. The Spy has been the hardware tool chosen for that purpose. The Spy-DAQ was chosen as the software solution in which the DTTF Local DAQ system would be based on. A first version was used at October 2004 Beam Test at CERN. Details on its implementation and the performance at the Beam Test are given in Chapter 5.

4.8.3 DTTF Monitoring

A system to monitor the behavior of the DTTF has to be installed in the CMS Control Room. The goal is to monitor the behavior of the DTTF Trigger hardware during the lifetime of the CMS experiment.

A monitor system allows a preliminary visualization of the DTTF data, both the input and the output. This information characterizes the DTTF behavior and is used to warn about possible misbehaviors.

4.8.4 DTTF Emulator

A software tool to emulate the DTTF Trigger response must be developed. The goal is to validate the DTTF Trigger hardware decision during the experiment lifetime.

The emulator is based in the system simulation tools described in Section 4.7. It processes the input data delivered by the DT Local Trigger devices and simulates the DTTF response. The emulator output, which is the expected DTTF Trigger decision, is compared with the hardware decision.

Chapter 5

The 2004 Bunched Beam Test

Before October 2004, the DTTF Trigger performance had been estimated using simulated muon data. Results have been described in Section 4.7.2. They validated the DTTF algorithm and its overall design. However, the system had never been tested under real experimental conditions, i.e. reconstructing muon tracks from real muons.

In October 2004 two Muon Barrel (MB) chambers were exposed to a muon beam at the H2 area (North Area) at CERN. The beam had the same time structure of the LHC, i.e. bunches every 25 ns. The Beam Test was intended as a benchmark for the DT trigger electronics together with all the hardware and software tools for configuration, synchronization and operation. It was the first time the full Drift Tube (DT) Trigger chain (Fig. 4.1), from the DTBX to the Wedge Sorter, was tested.

In particular, the DT Track Finder faced, for the first time, real muon data. Previous Beam Tests involving the DT chambers were dedicated to prove the chambers [29] and the DT Local Muon Trigger [30] performance. The main and innovative goal of this Beam Test was to test the performance of the DTTF muon trigger on real muon data delivered by the DT Local Trigger devices.

In this chapter we present all the work developed before and during the Beam Test, from the system setup to the data taking program. The setup of the DTTF system began some months before the Beam Test. From the hardware side of the system, the electronics components involved in the Beam Test were thoroughly tested and some firmware modifications performed. New extrapolation Look-Up-Tables which take into account the Beam Test conditions were calculated and loaded into the system electronics. From the software side, several programs had to be prepared for the Beam Test. In addition to control, configure and monitoring tools, a Local data acquisition (Local DAQ) system was developed.

The chapter is structured as follows. First, the experimental layout will be described. Second, the setup of the DTTF system from the hardware point of view is explained. After, details on the Beam Test Extrapolation Look-Up-Tables calculation are given. Then, all the software tools prepared for the Beam Test are presented. Next, the Beam Test data taking program is summarized. Finally, the performance of the Local DAQ system, is discussed. The Beam Test data analysis is covered in Chapter 6.

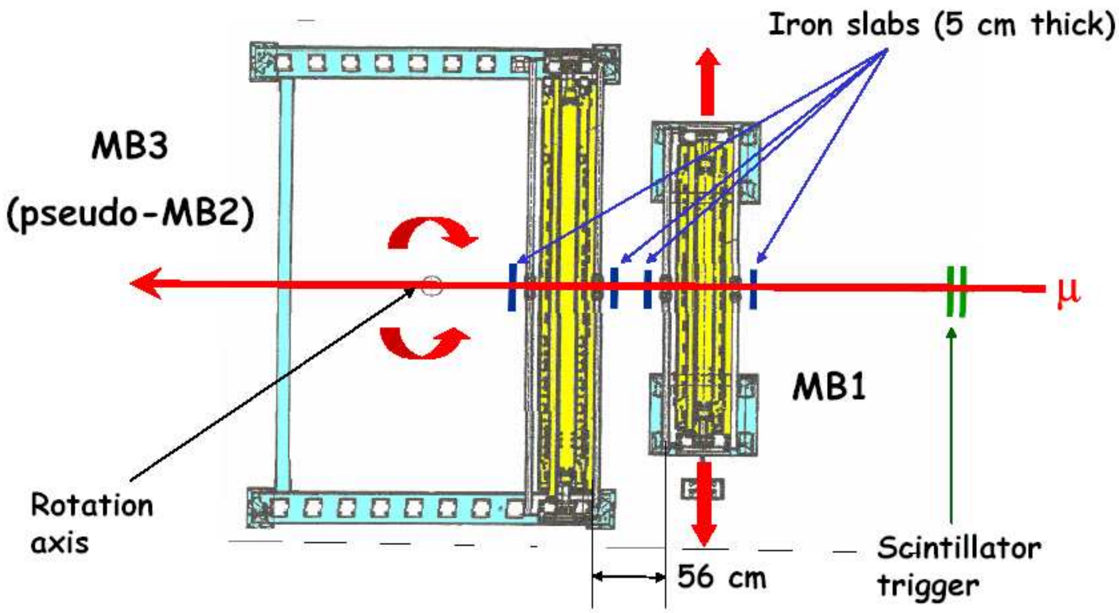

Figure 5.1: *Schematic layout of the Drift Tube Chambers experimental setup at the Beam Test.*

Figure 5.2: *Photo of the Drift Tube Chambers experimental setup. In the photo, MB2 is partially rotated around a central vertical axis.*

5.1 Experimental Layout

Two MB chambers equipped with front-end electronics for readout and trigger, and connected to prototypes of the ROS-master (the DT Local Trigger interface to the DAQ system) and of the DTTF, were exposed to a muon 40 MHz bunched beam.

A MB1 and a MB3 chamber were used. The ϕ wires of both chambers were in the vertical direction. Respect to the muon beam, the MB1 chamber was placed upstream while the MB3 was placed downstream (Fig 5.1). The distance between the two chambers' plates was 56 cm. The MB3 was placed on a support that allowed coarse rotations around a central vertical axis. The support where the MB1 was placed did not allow rotations but transversal translations could be performed with 1 mm precision. To simulate the effect of the CMS iron yoke on the muon trajectory, 10 cm thick iron slabs could be placed in front and between the chambers. Two plastic scintillators were placed upstream in the muon beam. They covered a $10 \times 10 cm^2$ area. A L1 Accept (L1A) trigger signal was generated from the scintillators trigger coincidence. This signal was used to trigger both the Central and the DTTF Local Data Acquisition (DAQ) systems.

An schematics of the MB chamber experimental layout is shown in Fig. 5.1 while Fig. 5.2 shows a photo.

In order to reproduce the most interesting conditions for a DT Trigger chain test, the MB3 Local Trigger devices were configured to simulate a MB2. In particular, TRACO Look-Up-Tables calculated for the geometry of a MB2 were used. Thus, from the DT Trigger point of view the MB3 chamber can be considered as a MB2. Therefore, in the following we will refer to the MB3 chamber as 'MB2'.

As a conclusion, the MB chambers configuration reproduced the trigger conditions of a MB1 and a MB2 at 'Wheel 0 - Sector 0' in CMS. In contrast to the CMS conditions, the chambers, thus muons, were not exposed to a magnetic field.

MB chambers calibration

The chambers were calibrated and aligned following the procedure established in [31].

5.2 DTTF Hardware Setup

Only one DTTF sector processor (a PHTF Unit) was used. Therefore, the DTTF electronics was located in a single crate (Fig. 5.3). The crate was loaded with one PHTF, one Wedge Sorter, a VME controller and a Timing Module (TIM). It was not foreseen that the θ superlayers of the MB chambers delivered trigger information, thus none ETTF unit was involved in the Beam Test.

The inputs to the DTTF system are the data delivered by the DT Local Trigger devices. The DT Local Trigger information is sent from each chamber Mini-Crate electronics in a DT Sector to a Sector Collector (SC). The SC sends the data to DTTF crate back side. At CMS, this data will be sent (received by the DTTF) through an Optical connection. At the Beam Test, the SC data were send through flat LVDS cables to an Interface Input Card, which is normally used at the DTTF test bench. The PHTF board

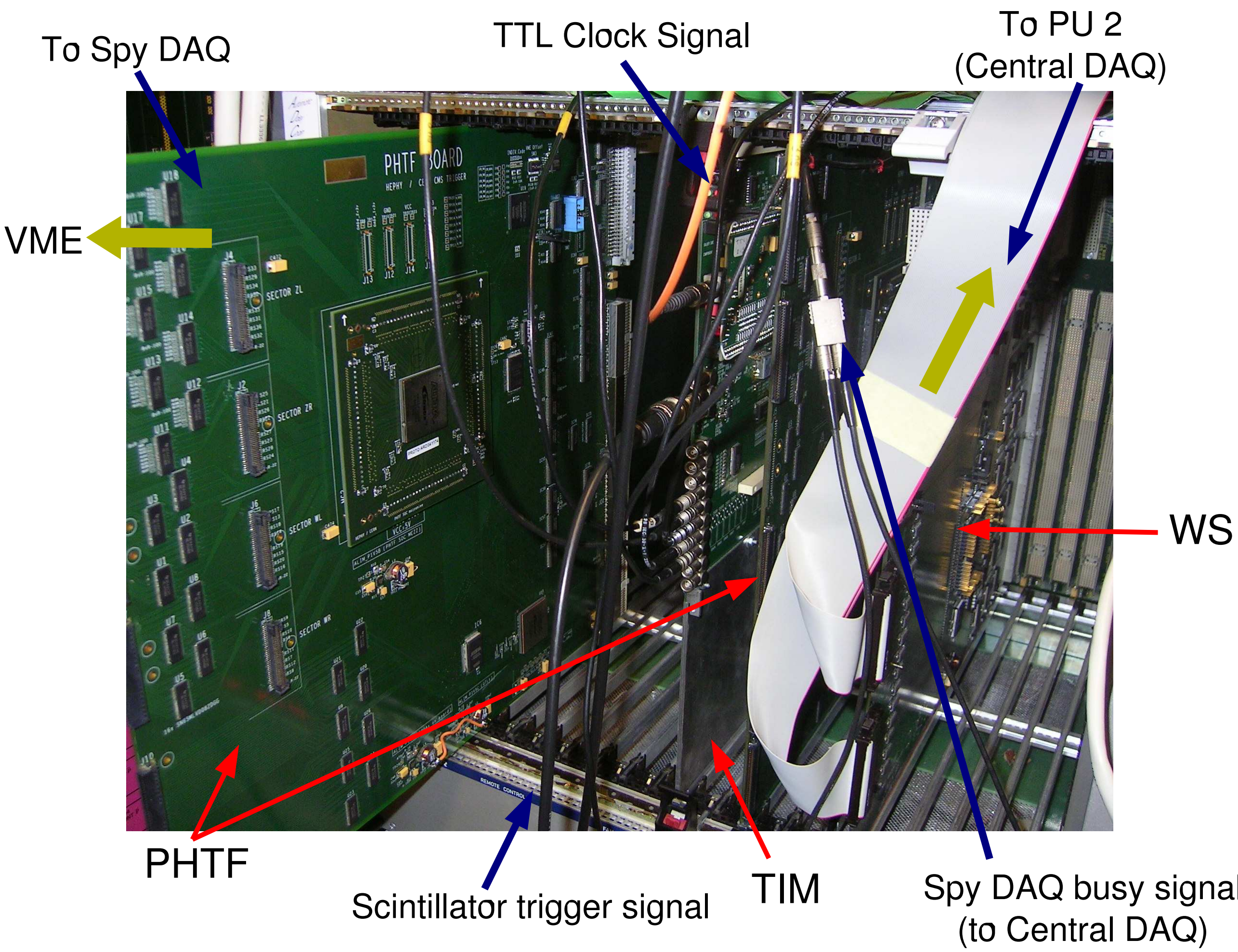

Figure 5.3: *Front side view of the DTTF Crate at the Beam Test.*

receives this information through the crate backplane, processes it and forwards its trigger decision to the Wedge Sorter board through the backplane of the crate.

The Wedge Sorter and the Sector Collector boards also sent their respective output to two different Pattern Units (PUs). A PU is a very deep FIFO that stores data at a 40 MHz frequency. Both PUs were started by the L1A trigger signal. They stored the information of 40 bunch crossings (BX) around the triggering one. Therefore, the Central DAQ recorded full information about the DTTF input and output.

The PHTF board used at the Beam Test was the first PHTF Pre-Production Prototype (PPP). It arrived at CERN at the end of August 2004. The PHTF algorithm had been tested and validated through the previous prototyping stages. However, the PHTF PPP implemented a new design of the board. Therefore, thorough tests of the PHTF PPP board were carried out before the Beam Test. All tests were performed using the control and functionality test programs described in Section 4.8. The tests, including a comparison with the ORCA simulated response of the PHTF, validated the board behavior. Integration tests with the Sector Collector and the Wedge Sorter boards (produced by the Bologna-CMS group) were also carried out before the Beam Test. The first task carried out at the Beam Test was the synchronization of the DTTF system wit the remaining components of the DT Trigger chain.

A first version of the Local DAQ system that will be present in the CMS Control Room was developed for the Beam Test. Such a system is triggered by a L1A trigger signal. In order to run synchronized with the Central DAQ system, a Busy signal has to be sent to it while the local data readout is performed. The PHTF board, both the hardware and the firmware, had to be adapted to deal with these signals: trigger the data local readout when the the L1A signal was received and send a Busy signal while local readout tasks were being performed. The L1A signal was received at the TIM board, which distributed it to the boards in the crate through the backplane. The Busy signal was directly sent to the central DAQ system from the PHTF board. In Fig. 5.3 the hardware implementation of the L1A and Busy signals handling is shown. Fig. 5.4 shows a screen-shot of the scope when a L1A signal arrives. As the L1A signal is distributed by the TIM, a delay is observed between the scintillators trigger and the arrival of the L1 trigger signal to the PHTF. The L1 triggers the local data readout, implemented by the Local DAQ software. When the local data readout begins the PHTF sends a Busy signal to the Central DAQ system. The output of the track is observed 17 bunch crossings after the L1 trigger signal.

Experimental conditions at the Beam Test different from CMS conditions. As far as the DTTF is concerned, two main issues were expected to have impact on the system setup. First of all, as two aligned MB chambers delivered trigger information to the system, only one PHTF was used. Therefore, the board did not receive trigger information from neighbor sector processors. Slight modifications to the PHTF firmware logic were performed to avoid electronic noise at the neighbors' connections on the board. More interesting is the fact that muons crossing the MB chambers were not exposed to the CMS magnetic field. Furthermore, muons did not interact with the CMS iron yoke in their path between the MB chambers. Therefore, the expected geometry of muon tracks

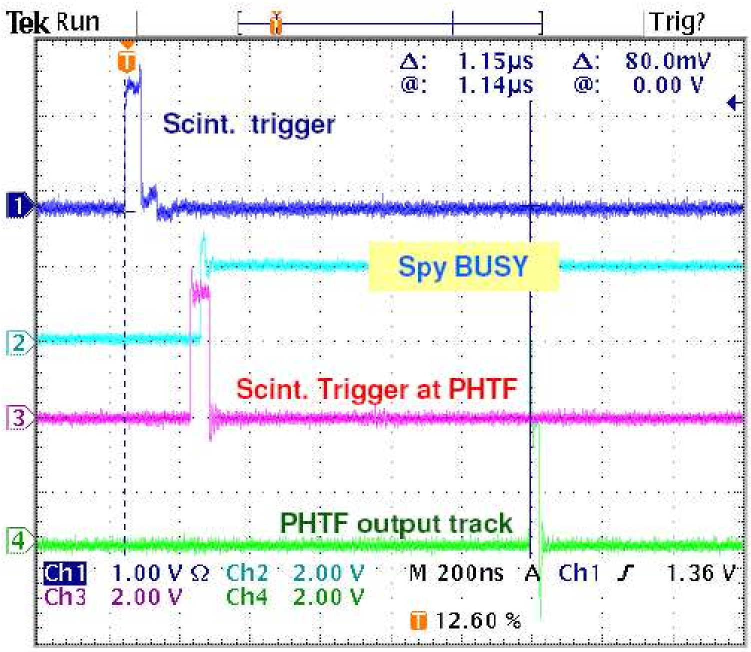

Figure 5.4: *Screen-Shot of the scope when a L1A Trigger signal arrives to the PHTF board. As the L1 trigger signal is distributed to the crate through the Timing Module, a short delay happens before the PHTF receives it. A Busy signal is sent to the Central DAQ when the Local Data Acquisition begins.*

at the Beam Test differed from the CMS situation. The consequences are explained in depth in next section

5.3 Beam Test Extrapolation Look-Up-Tables

As described in Section 4.2.2, the DT Track Finder extrapolation principle relies on Look-Up-Tables (LUTs) downloaded into the hardware. LUTs are the core of the physics principles on which the DTTF trigger decision is based. They parametrize the geometry of muons crossing two MB chambers in 99%-efficient windows. Only segments pairs satisfying the correlation codified in the LUTs are considered in further steps of the track finding algorithm. The 'standard' LUTs are calculated from simulated data, which are generated according to the 'standard' CMS configuration.

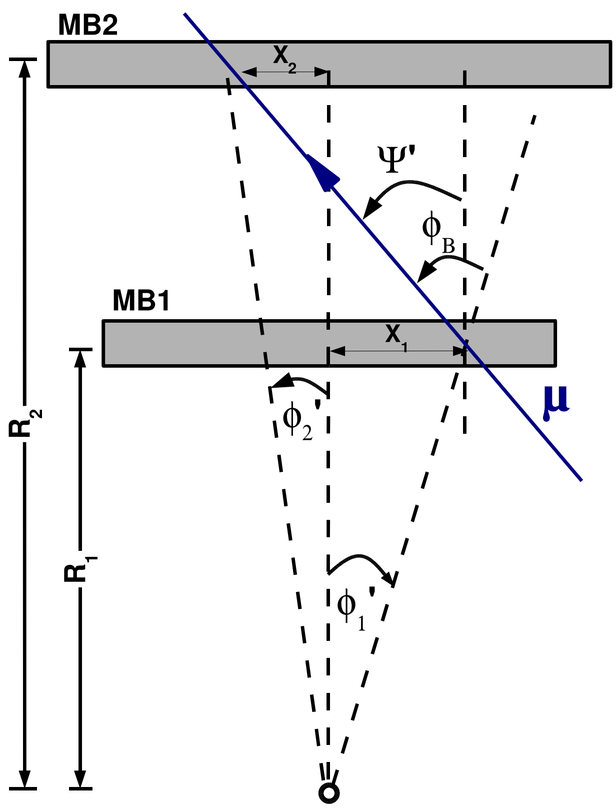

Figure 5.5: *Schematics of the TB geometry when considering an extrapolation from MB1 to MB2.*

Experimental conditions at the Beam Test differed from those expected at the CMS startup. Neither magnetic field nor dead material (the CMS iron yoke), were present at the Beam Test. Thus, the muon tracks' geometry differed from the expected at CMS. The muon trajectory from the source MB station to the target MB station was not deflected, neither by a magnetic field nor by the interaction with dead material. Therefore, muons followed a straight path from one chamber to the other. The main consequence on the DTTF system was that the extrapolation LUTs usually downloaded to the hardware (Section 4.2.2) were not useful at the Beam Test. A new set of LUTs that took into account the Beam Test geometry had to be calculated and downloaded into the hardware. It is the aim of this section to describe in detail this calculation.

At the Beam Test, only the '$1 \rightarrow 2$' extrapolation LUT was used. It relates the bending angle at MB1 (ϕ_b) with the change in the azimuthal coordinate ($\Delta\phi = \phi_{MB2} - \phi_{MB1}$). If muons follow a straight trajectory from one chamber toward the other, the ($\Delta\phi, \phi_b$) correlation is fixed and linear and can be easily calculated. A schematic representation of the track geometry expected at the Beam Test is shown in Fig. 5.5. The most general case is represented.

A remark concerning the DT Local Trigger's output variables definition (Section 3.4.4) must be done. The incident angle of the muon in the MB chamber (Ψ) is calculated in terms of its tangent ($\Psi = \tan\Psi'$). The angular position at the MB chamber (ϕ) is calculated from the TRACO Look-Up-Tables loaded in the DT Local Trigger devices. Such Look-Up-Tables output the tangent of the angular position rather than the angular position itself ($\phi = \tan\phi'$)[1]. Finally, the bending angle (ϕ_b) is defined as the difference of Ψ and ϕ:

$$\phi_b = \tan\Psi' - \tan\phi' = \Psi - \phi \tag{5.1}$$

It must be noted that the variables delivered by the DT Local Trigger devices to the DTTF are ϕ and ϕ_b (in contrast with ϕ' and ϕ'_b). This statement was confirmed by early Beam Test data. Therefore, $\Delta\phi$ is defined as the difference of the angular position's tangents (ϕ_1 and ϕ_2).

The change in the azimuthal coordinate ($\Delta\phi$) can be expressed in terms of the change in the linear position at the chambers (Expr. 5.2). Furthermore, the position in the target MB chamber can be expressed in terms of the position and the incident angle (Ψ) at the source MB chamber (Expr. 5.3).

$$\Delta\phi = \phi_2 - \phi_1 = \frac{x_2}{R_2} - \frac{x_1}{R_1} \tag{5.2}$$

$$x_2 = x_1 + \tan\Psi'(R_2 - R_1) \tag{5.3}$$

If Expr. 5.3 is introduced in Expr. 5.2 and the position at the source MB chamber (x_1) is given in angular coordinates, we reach to the general correlation between the change in the azimuthal coordinate and the segment coordinates at the source MB chamber (Expr. 5.4).

$$\Delta\phi = (\tan\Psi'_1 - \tan\phi'_1)\left(\frac{R_2 - R_1}{R_2}\right) \tag{5.4}$$

[1]Note that for small Ψ' and ϕ' angles, $\phi = \phi'$ and $\Psi = \Psi'$.

However, at the extrapolation LUTs, $\Delta\phi$ is expressed in terms of the bending angle at the source MB station (ϕ_b). For that purpose, Expr. 5.1 is introduced in Expr. 5.4, leading us to the $(\Delta\phi, \phi_b)$ correlation for muons that follow a straight path from the source MB chamber to the target one:

$$\Delta\phi = \phi_b \cdot \left(\frac{R_2 - R_1}{R_2}\right) \tag{5.5}$$

Therefore, the $(\Delta\phi, \phi_b)$ correlation depends only on the MB chambers configuration parameters loaded in the MB Local Trigger devices (TRACO). The values of these parameters at the Beam Test were:

$$R_1 = 4311.50 \text{ mm} \tag{5.6}$$

$$R_2 = 5124.75 \text{ mm} \tag{5.7}$$

Finally, the units used for $\Delta\phi$ and ϕ_B for the PHTF calculations have to be considered:

$$[\Delta\Phi] = \text{rad}/4096 \tag{5.8}$$

$$[\Phi_b] = \text{rad}/512 \tag{5.9}$$

All together lead us to Expr. 5.10 which defines the expected average $(\Delta\phi, \phi_b)$ relation at the Beam Test:

$$\Delta\phi = 1.27 \cdot \phi_b \tag{5.10}$$

Furthermore, the finite resolution of the Local Trigger measurements involved has to be considered. To determine whether a pair of segments reconstructed by the MB chambers Local Triggers correspond to a muon, a efficiency window has to be opened from the average $(\Delta\phi, \phi_b)$ correlation (Expr. 5.10). The efficiency of such a window is a parameter that has to be defined. In the simulation of the DTTF system it is set to a 99%. However, this efficiency can be tuned according to the needs of the experiment. For the Beam Test it was decided to use the same efficiency value as in the simulation, i.e. 99%.

It is not possible to analytically determine the 99%-efficient window limits with the required precision. Instead, the DTTF simulation has to be used. The deviation of a muon sample from the average $(\Delta\phi, \phi_b)$ relation was parametrized using a $4 \cdot 10^5$ simulated muon data sample. Fig. 5.6 shows the $(\Delta\phi - \Delta\phi_{avg}, \phi_b)$ used to open the 99%-efficiency window. Look-Up-Tables are finally calculated by adding to this windows the average $(\Delta\phi, \phi_b)$ relation defined in 5.10. Fig. 5.7 plots the Look-Up-Tables and the average $(\Delta\phi, \phi_b)$ relation.

As explained in Section 4.2.2, extrapolation Look-Up-Tables in the backward direction are also used by the DTTF system. The PHTF makes use of the $2 \to 1$ extrapolation

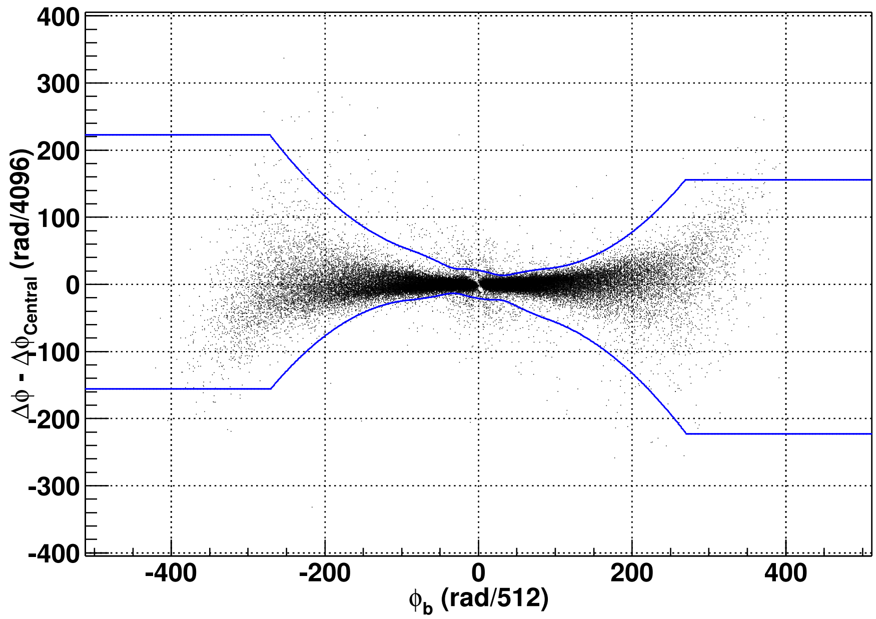

Figure 5.6: *Deviation from the average $(\Delta\phi, \phi_b)$ relation for a simulation of the DTTF system. A $4 \cdot 10^5$ single muon sample was used.*

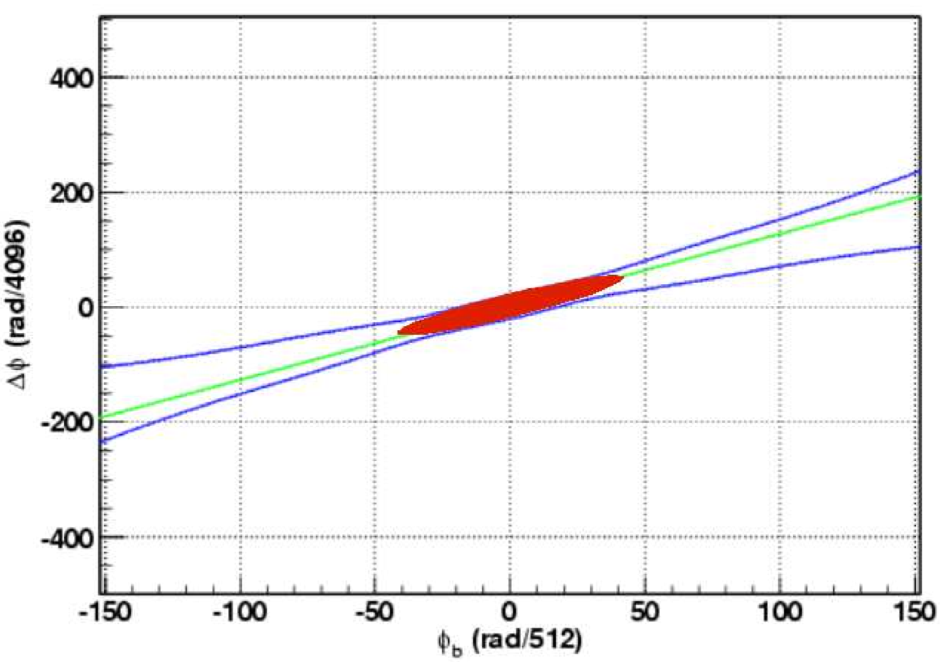

Figure 5.7: *Look-Up-Tables used at the Beam Test and the average $(\Delta\phi, \phi_b)$ relation used to compute them. The expected beam spread, used to emulate different p_T values, is depicted in the figure by the red spot.*

LUT to switch on one of the foreseen solutions to suppress noise and ghost muon tracks[2]. It was planned to test this feature during the beam test. Therefore, the extrapolation LUT 2 → 1 had to be calculated. The general calculation of a backward extrapolation, similar to the one described above, lead us to the following expression:

$$\Delta\phi = -\phi_b \cdot (\frac{R_1 - R_2}{R_1}) \tag{5.11}$$

We remind to the reader that in this case $\Delta\phi = \phi_{MB2} - \phi_{MB1}$ and ϕ_b is defined as the bending angle at MB2. Considering the R_1 (Expr. 5.6) and R_2 (Expr. 5.7) values and taking into account the proper unit conversion (Exprs. 5.8 and 5.9), we obtain the average $(\Delta\phi, \phi_b)$ correlation expected at the Beam Test:

$$\Delta\phi = -1.51 \cdot \phi_b \tag{5.12}$$

Again, the 99%-efficient '2 → 1' LUT is calculated using the deviation from the average $(\Delta\phi, \phi_b)$ correlation shown in Fig. 5.6.

Finally, an outstanding consequence of the Beam Test geometry must be highlighted. The muon beam trajectory was perpendicular to both MB chambers (Fig. 5.8). Therefore, the incident angle of muons in the MB chambers is negligible:

$$\Psi_i \simeq 0 \;\Rightarrow\; \phi_i \simeq -\phi_{bi} \tag{5.13}$$

The most interesting consequence of Expr. 5.13 is that the muon beam spread (different ϕ values) was observed as different ϕ_b values (Fig. 5.7). If the extrapolation LUT follows the beam spread distribution, as is the case for the LUTs calculated above, different ϕ_b values are seen by the PHTF as different $\Delta\phi$ values. Therefore, considering the transverse momentum assignment algorithm (Section 4.2.5), the beam spread simulates different p_T values. This fact could be exploited to study the DTTF transverse momentum assignment performance.

The Look-Up-Tables as defined above were downloaded to the PHTF board before the Beam Test. However, as the Beam Test conditions could change due to unexpected problems, a back-up solution was foreseen. Look-Up-Tables accepting all possible $(\Delta\phi, \phi_b)$ relation, thus achieving a 100% efficiency (open LUTs), were also prepared. With this solution, the acquisition of PHTF output information is guaranteed, whatever the MB chambers configuration could be.

The possibility of switching different PHTF configurations, i.e. using different extrapolation LUTs, during the Beam Test could be performed, and was actually performed, by manually downloading the firmware, both the logic and the Look-Up-Tables, into the PHTF electronics.

[2] The description of this feature is explained in Section 4.2.2. The analysis of its application during the Beam Test will also be covered.

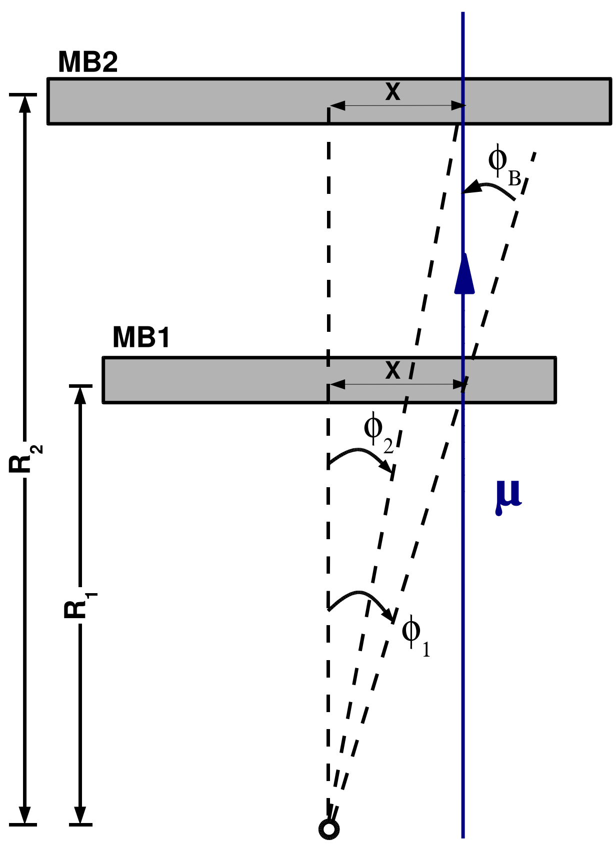

Figure 5.8: *Schematics of the TB geometry when considering an extrapolation from MB1 to MB2.*

5.4 Software Tools

From the software point of view, the main goal for the Beam Test was to prepare working versions of all tools expected to be present at the CMS Control Room. This tools can be classified in four groups: control and functionality test programs, a Local DAQ system triggered by an external L1 signal, a monitor for online data visualization and an emulator program.

5.4.1 Control and functionality test programs

During the DTTF system development a complete set of programs (online software) has been implemented. The main goal of these programs is to control and test the functionality of the DTTF boards. An overview of the DTTF online software was given in Section 4.8.

Before the Beam Test, thorough tests to check the PHTF functionality were carried out. First, the different features of the PHTF board, including chips interconnectivity and functionality of the Boundary Scan and the Spy System tools, were tested. Then, more complex tests evaluated the PHTF response to different data patterns. Finally, the PHTF response to large samples of simulated (ORCA) single- and di-muon events was tested and compared with the simulated response produced by the DTTF ORCA module.

At the Beam Test, all the test and control programs were available. The PHTF customized Java based GUI allows full access to the board's features. The default configuration setup of the boards is automatic at power up. However, the possibility to switch on alternative noise and ghost suppression schemes during the Beam Test could be done using these control programs. Early data were used to calibrate the software tools and to evaluate the hardware behavior.

5.4.2 Local DAQ system

As we have already mentioned, two DAQ systems reproducing the situation at the CMS Control Room, a Central DAQ and a Local DAQ, had to be working at the Beam Test.

A Local DAQ tool (TB DAQ) was developed in order to access the PHTF information directly from the board. It allows to check the quality of the input data received from the DT Local Triggers and the quality of the output data produced. However, not only input and output are accessible but intermediate steps of the algorithm as well, allowing full control of possible misbehaviors. This tool was based in the Spy-DAQ tool (Section 4.8.2). Spy-DAQ was modified to cope with the Beam Test conditions: it had to be triggered by an external L1 Accept signal and a Busy signal should be sent to the central DAQ system in order to run synchronized with it. Therefore, full Data Acquisition flexibility was available. The system could run in three different data acquisition modes. First, the Central DAQ could run in standalone mode, providing full DTTF data information. Besides, the Central DAQ and the Local DAQ could run synchronized, allowing an event-

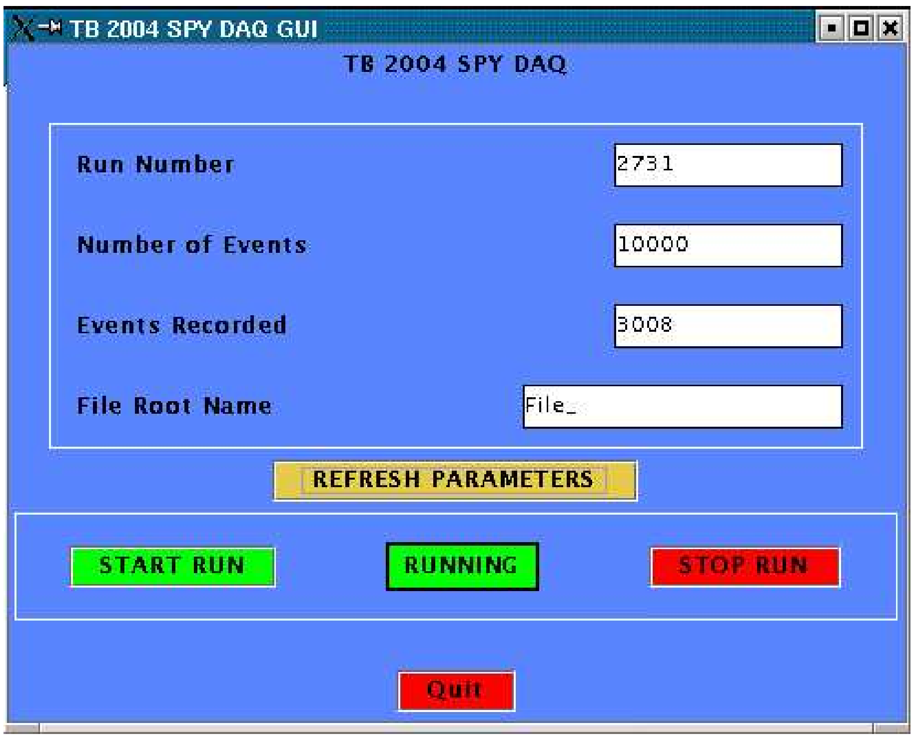

Figure 5.9: *Screen-Shot of the TB DAQ tool during data acquisition at the Beam Test. It is implemented in the common CMS framework, XDAQ.*

to-event comparison of the data provided by both systems. Finally both DAQ systems could run in parallel.

The TB DAQ system was thoroughly tested before the Beam Test in order to ensure its performance and stability during data taking. The TB DAQ working parameters, e.g. the delay of the 'Spy' trigger with respect to the scintillator trigger, were measured using early data. At the Beam Test, the TB DAQ system acquired data at the bunch crossing of the L1 trigger and 10 bunch crossings around achieving a DAQ rate of 150 Hz.

The performance of the Local DAQ system during the Beam Test is discussed in detail in Section 5.6.

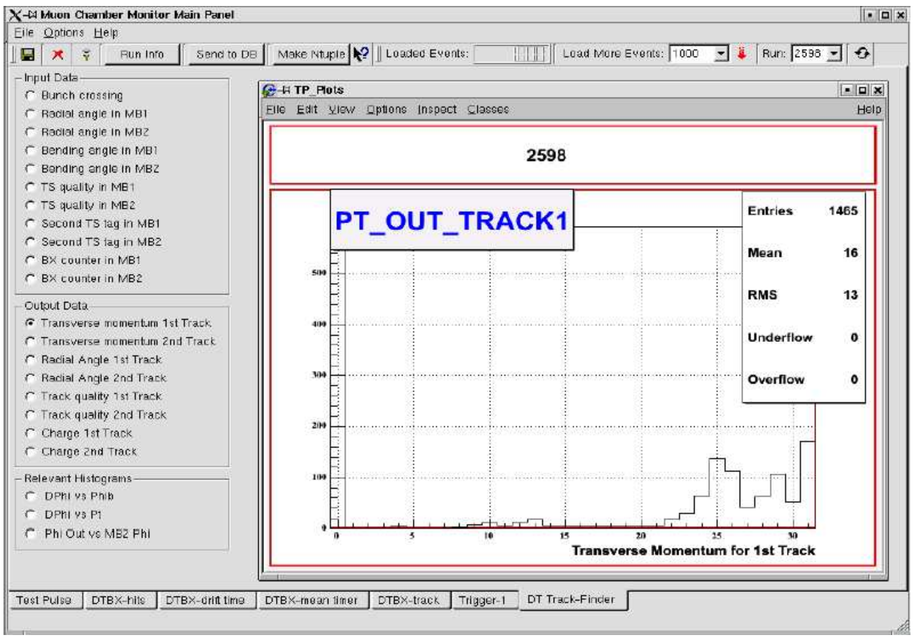

Figure 5.10: *Screen-Shot of the online Monitor showing the transverse momentum of the muon track as reconstructed by the PHTF.*

5.4.3 Online Monitor

A monitoring tool was also developed in collaboration with the Pavia-CMS group. The main goal of such a tool is to have a preliminary visualization of data. For instance, alignment of the chambers could be performed by using this tool. Moreover, problems with the data acquisition or the experimental setup could be detected and corrected during data taking. A monitoring tool will also be need at the CMS Control Room when the experiment starts its operation.

The Monitor tool was developed under the ORCA framework. The analysis tool used to plot the relevant DTTF variables was ROOT, a data analysis framework developed at CERN. The graphical interface to allow a user friendly access to the plots was developed under the common QT package, modified to interface with ROOT. All these tools are implemented in an object oriented software language, C++. The monitor (Fig. 5.10) allows to visualize all input and output data of the PHTF board as well as outstanding correlations of the output variables.

5.4.4 PHTF Emulator

In addition to the online software tools, a program to emulate the PHTF response was also developed. A comparison of the hardware response with the simulated response is need to evaluate the behavior of both sides of the system.

The emulator was developed using the CMS experiment simulation framework, ORCA (Section 4.7.1). The DTTF Trigger module of ORCA was adapted to the Beam Test conditions.

Inputs to the PHTF are used to feed the emulator. An event-to-event comparison of the PHTF and the emulator response is possible. In case of disagreement, the emulator is used to understand the hardware response.

5.5 Data Taking Program

All runs taken during the Beam Test included by default DTTF information. However, 50 runs (around 2 million triggers) were specially devoted to DTTF studies. They can be classified in four different groups:

- Local DAQ tests and PHTF algorithm validation: two $4 \cdot 10^4$ triggers runs were taken with both DAQ systems fully synchronized. The aim was to test the Local DAQ performance and cross check the quality of both DAQ systems' data. These runs were also used to validate all the PHTF algorithm's stages.

- Energy scan (50, 100, 150, 300 GeV): As our test was parasitic of Hadron Calorimeter tests, the energy of the beam could not be chosen. Nevertheless, runs at different beam energies, with and without the iron slabs, were taken. The systematic analysis of the DTTF occupancy, efficiency and rejection power was carried from this set of data.

- Transverse momentum assignment performance: a set of runs with different configurations of the MB chambers at the same beam energy was taken. The transverse momentum assignment resolution and the DTTF Trigger turn-on curves were studied from this data set.

- Alternative noise and ghost suppression schemes: Four runs of $4 \cdot 10^5$ triggers each were dedicated to study the performance of the optional noise and ghost suppression schemes foreseen for the PHTF. Two runs ware taken with the two possible schemes switched on. Another two (used as reference) runs at the same beam condition were taken with the schemes switched off.

5.6 Local DAQ Performance

The DTTF Local DAQ system at the Beam Test, TB-DAQ, was normally used during the Beam Test. It run in standalone mode providing data for DTTF calibration and testing tasks. It also run synchronized to the Central DAQ and in parallel to it. Two runs of $4 \cdot 10^4$ triggers each were dedicated to test the TB-DAQ performance. For these runs, TB-DAQ run fully synchronized with the Central DAQ system. The first goal was to validate the handling of the L1 and Busy signals, thus the synchronization with the Central DAQ system. The performance was excellent. An image of the scope when the scintillators triggered on a muon has been already shown in Fig. 5.4. The system did never hang-up and both DAQ systems run fully synchronized. In Fig. 5.11, a comparison of the occupancy plots for the two DAQ systems is shown. TB-DAQ concentrated the data taking in 10 bunch crossings around the scintillator trigger while the Central DAQ read 40 bunch crossings.

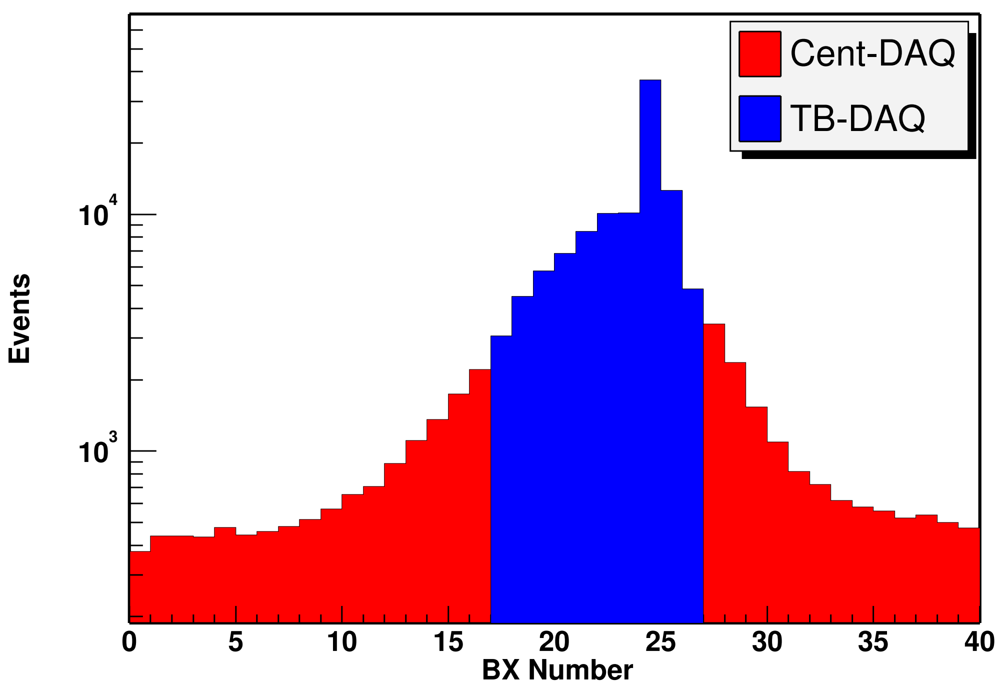

Figure 5.11: *Occupancy plot with data from both systems. TB-DAQ concentrates in 10 BX around the trigger while the Central DAQ reads data from 40.*

As the behavior of TB-DAQ was perfect, i.e. no events are missing, it is possible to perform an event-to-event comparison with the Central DAQ data. All the DTTF variables can be compared. Such a comparison lets us cross-check the performance of both systems revealing possible misbehaviors of any of them. In fact, disagreement between the two DAQ systems was found for three variables' data.

A stuck bit was discovered in the Sector Collector pattern unit (PU1), related to the PHTF input. It affected the MB1 ϕ_b value. Fig. 5.12 illustrates the differences in the DAQ's data. For some events a ±128 (rad/512) difference in the MB1 ϕ_b value is observed. The anomalous distribution of the ϕ_b data provided by the Central DAQ relates the DAQ systems disagreement to this system.

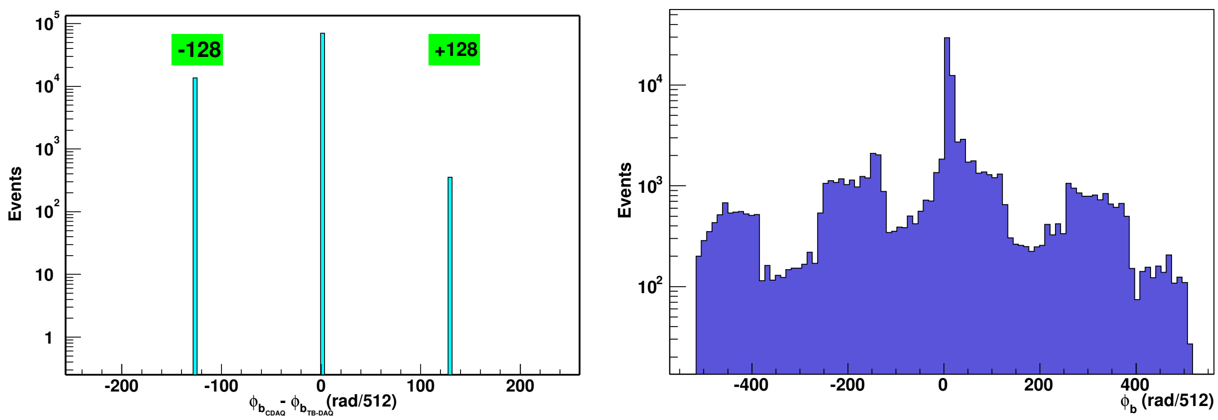

Figure 5.12: *Comparison of the two DAQ systems readout of ϕ_b at MB1. The ±128 difference between the two DAQ systems data is shown in the left figure. The figure on the right shows the distribution of the angle ϕ_b at MB1 as read by the Central DAQ System. Cloned peaks appear at $\phi_b \sim 0 \pm n \cdot 128$ as a result of a stuck bit in the Central DAQ's PU1.*

Two more errors were found in the data provided by the Central DAQ's PU2 (DTTF output). First, a disagreement on the value of the azimuthal position of the first muon track reconstructed by the PHTF was found. The analysis of the data provided by both DAQs showed the erroneous behavior of the Central DAQ. Fig. 5.13 plots the value read by the Central DAQ as a function of the value read by TB-DAQ. Second, a disagreement was also found for the quality word associated to the second muon track. Again, the Central DAQ was the misbehaving system, as the values it delivered do not have sense in the Beam Test context, where only two MB chambers were used. Fig. 5.14 illustrates the disagreement in this variable.

Summarizing, TB-DAQ achieved all the functionalities expected from the DTTF Local DAQ system. Its behavior was completely stable during the Beam Test. It provided high quality data without causing any hang up. Furthermore, it was very useful, in combination with the Monitor tool, in the detection of problems on the Central DAQ system. As a conclusion, the software tool that lies beneath TB-DAQ, namely the Spy-DAQ, was confirmed as our preferred solution for future use and development.

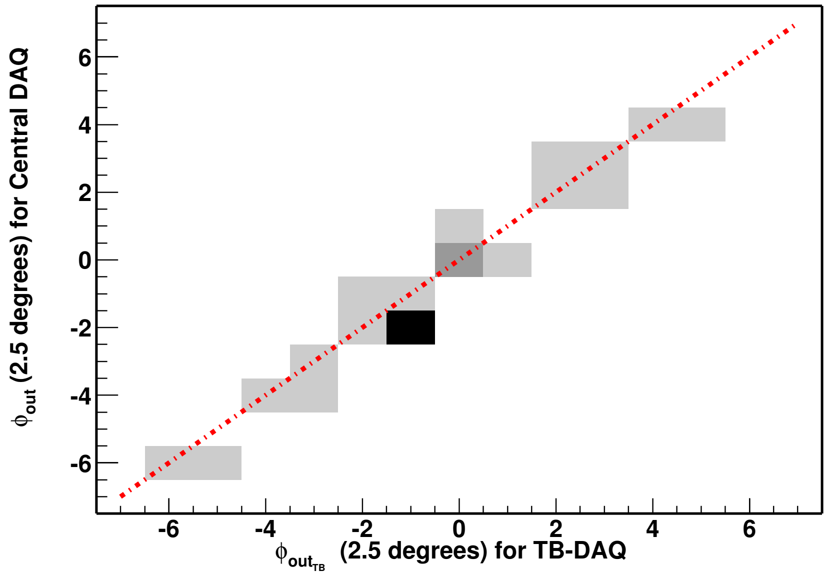

Figure 5.13: *Comparison of the readout of ϕ_{out} for the two DAQ systems.*

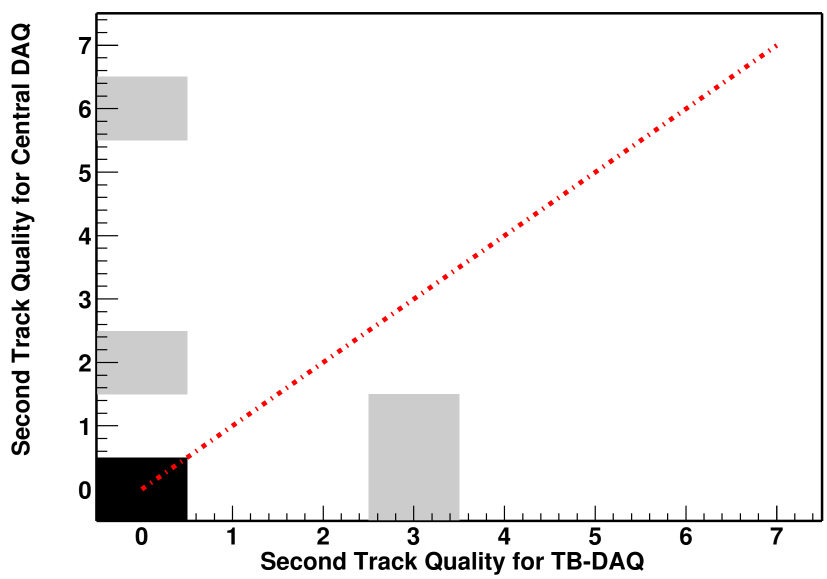

Figure 5.14: *Comparison of the readout of the quality word assigned to the second muon track reconstructed by the PHTF. The values shown by the Central DAQ do not have sense in the Beam Test context.*

Chapter 6

The DTTF Trigger performance at 2004 Beam Test

The work developed before and during the Beam Test has been described in the previous chapter. In this chapter we discuss in detail the DTTF Trigger performance. Results on the data analysis are presented.

The data analysis is structured as follows. First, an introduction to the PHTF Trigger performance at the Beam Test is presented. The performance of the main steps of the track finding algorithm is described. Second, we present the comparison between the hardware response and the emulator response. Then, the PHTF performance on single muons is discussed in terms of occupancy and efficiency. A study of the PHTF performance on ghost (fake) Local Trigger reconstructions and on 'out-of-time' muons follows. Next, the transverse momentum assignment performance, including the PHTF turn-on curves, is covered. The last section summarizes the most important results.

6.1 Introduction

The PHTF algorithm was described in detail in Chapter 4. In this section, we use the data collected for a $4 \cdot 10^4$ triggers run to overview the behavior of the system at the Beam Test. The discussion is structured according to the PHTF algorithm steps that were not trivial at the Beam Test: extrapolation and physical parameters assignment.

At every bunch crossing (25 ns) the PHTF receives up to two track segments from each of the MB chambers' Local Trigger devices. At the Beam Test, only track segments from MB1 and MB2 were received. In such conditions, the PHTF is able to reconstruct a muon track when, at the same bunch crossing, it receives a non null track segment from each DT Local Trigger. We denote this kind of event as a 'coincidence'. Ideally, when a coincidence occurs the PHTF sorts the information delivered by the Local Triggers by matching to a full track only those track segments that actually correspond to a muon. We will denote a successful match as a 'PHTF extrapolation'.

The PHTF occupancy for the different subsamples described above is discussed in the following. The motivation is to provide a qualitative understanding both of the PHTF

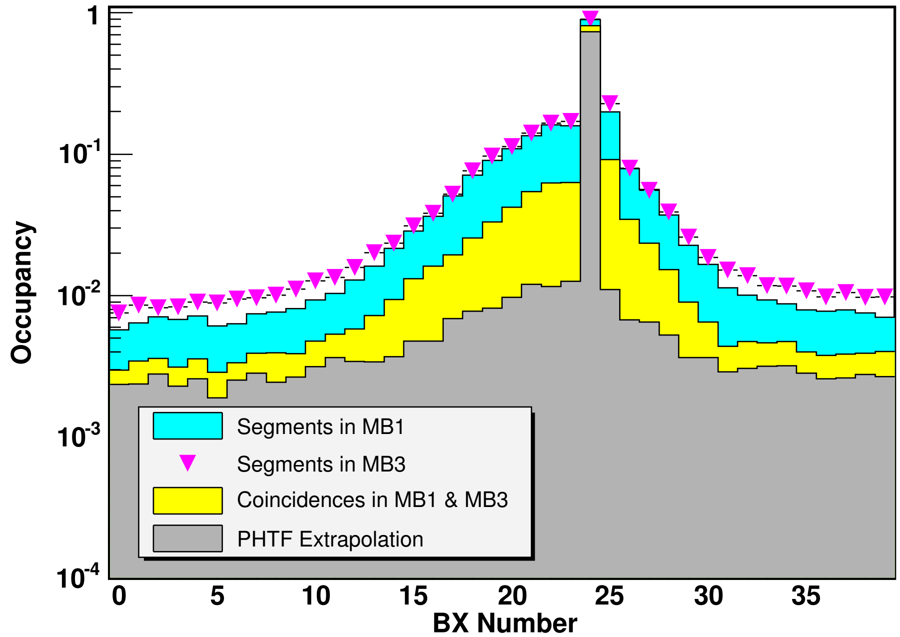

Figure 6.1: *Occupancy plot for run 2598. The trigger signal coming from the plastic scintillators came at bunch crossing (BX) number 24.*

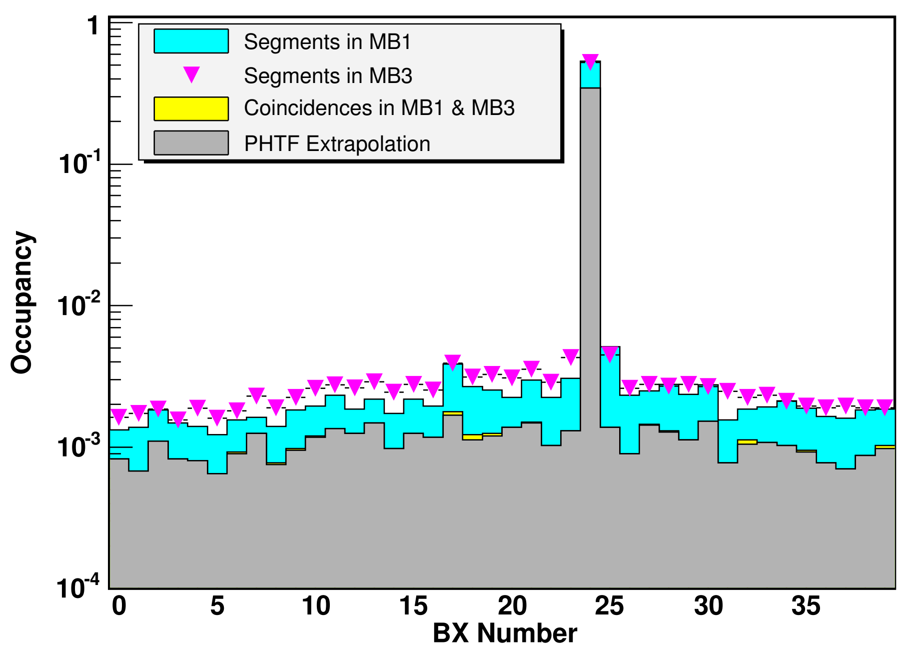

Figure 6.2: *Occupancy plot for high quality coincidences at run 2598. The noise and ghost occupancy is drastically reduced.*

input data and of the PHTF working principle. Data from a $4 \cdot 10^4$ triggers run, taken when the beam energy was 150 GeV, are used. Fig. 6.1 plots the occupancy as a function of the bunch crossing (BX) number for different selection cuts: events with a non null MB1 track segment, events with a non null MB2 track segment, events with non null track segments in both MB chambers (coincidences) and events on which the PHTF successfully extrapolated a muon track from MB1 and MB2 segments (PHTF extrapolation).

The bunch crossing number corresponding to the scintillator trigger was 24. Therefore, at BX=24 the track segments reconstructed by the Local Trigger are expected to be caused by real muons. Occupancy values shown in Fig. 6.1 illustrate this statement. The occupancy of all the subsamples notably increases when BX=24. In addition, it must be noted that for BX=24 the occupancy values for the different subsamples are very similar (above a 60%). First, the occupancy of track segments at each MB chamber (blue histogram and pink triangles) is very similar to the coincidences' occupancy (yellow histogram). If a segment was reconstructed at MB1 it is very likely that the MB2 Local Trigger also reconstructed a segment as signals at the MB chambers were caused by a muon. Furthermore, the occupancy of coincidences and of PHTF extrapolations (gray histogram) is very similar. The PHTF reconstructed a full muon track from most of the track segments it received, thus achieving a high efficiency. This description is consistent with the expected behavior of the DT trigger system when a real muon [1] crosses the MB chambers.

At the bunch crossings before the scintillator trigger signal (BX<24), signals at the MB chambers are not related to a muon. Therefore , the description of the occupancy values is different from the one given for BX=24. At BX<24, track segments delivered to the DTTF are mainly caused by noise or ghost Local Trigger reconstructions of muons crossing the MB chambers at BX=24. Ghosts are generated in the immediately previous bunch crossings, thus all the subsamples occupancy increase from BX=0 to BX=23. It must be noted that the occupancy of ghosts already decrease when segment coincidences are considered. The probability of reconstructing ghost segments at both chambers is lower than the probability of reconstructing a ghost segment at a single chamber. The PHTF performs the simplest regional trigger task already at the inputs. It requires time coincidence to the track segments reconstructed by the Local Trigger. However, the PHTF job shows up when comparing the coincidences occupancy with the extrapolations occupancy. The PHTF rejects most of the ghost track segments coincidences. As a consequence, at BX<24 the muon track occupancy is kept under a 1%.

This analysis is better understood when high quality track segments (q=6 at Table 3.1) at both MB chambers are considered. The occupancy values are shown in Fig. 6.2. The same subsamples are considered. At BX=24, the coincidences occupancy is clearly lower than the track segment occupancy at a single MB chamber. Most important is that the noise and ghost background is suppressed by demanding high quality to the track segments. By definition, it is very unlikely to achieve a ghost reconstruction of track segment with a high quality value. Finally, it must be noted that the occupancy of the coincidences and of the extrapolations is almost the same at every bunch crossing. Namely,

[1] We denote 'real muons' to those causing a 'scintillator trigger'.

the PHTF achieves a very high efficiency when considering high quality coincidences.

6.1.1 PHTF Extrapolation Performance

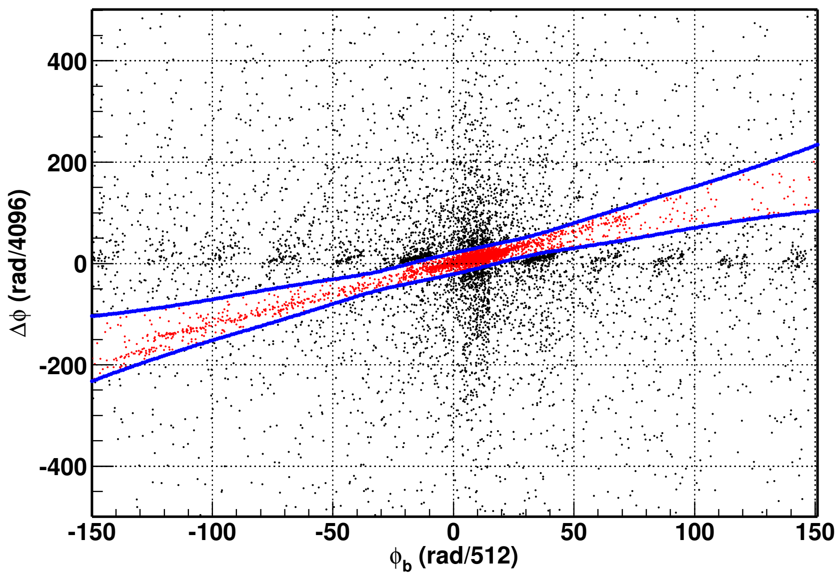

Figure 6.3: *Extrapolation principle illustration. The $\Delta\phi - \phi_B$ relationship is used to validate a coincidence. Red points represent coincidences used by the PHTF to reconstruct a muon track while black points represent rejected coincidences*

The extrapolation principle used by the PHTF to reconstruct a muon track from the segments delivered by the DT Local Triggers located at each MB chamber has been described in Section 4.2. At the Beam Test, only track segments from MB1 and MB2 were received. Therefore, the reconstruction of a muon track relies only in the success of the extrapolation from MB1 to MB2. Fig. 6.3 illustrates the extrapolation working principle for a $4 \cdot 10^4$ triggers run, taken when the beam energy was 150 GeV. All bunch crossings were considered. Coincidences which $(\Delta\phi, \phi_b)$ relationship are between the thresholds defined by the 99%-efficiency Look-Up-Tables (blue lines in the figure) must be used to reconstruct a muon track and the corresponding track segments' information forwarded to the next logical steps of the PHTF algorithm. Coincidences which $(\Delta\phi, \phi_b)$ relationship are outside the LUT's thresholds must be rejected as muon track candidates and not considered any more. In Fig. 6.3 red points represent pairs of track segments that were used for a muon track reconstruction while black points represent rejected pairs of track segments. The extrapolation principle performance worked as expected for 100% of the events. Namely, all red points fell inside the 99% efficiency windows while all black points fell outside them.

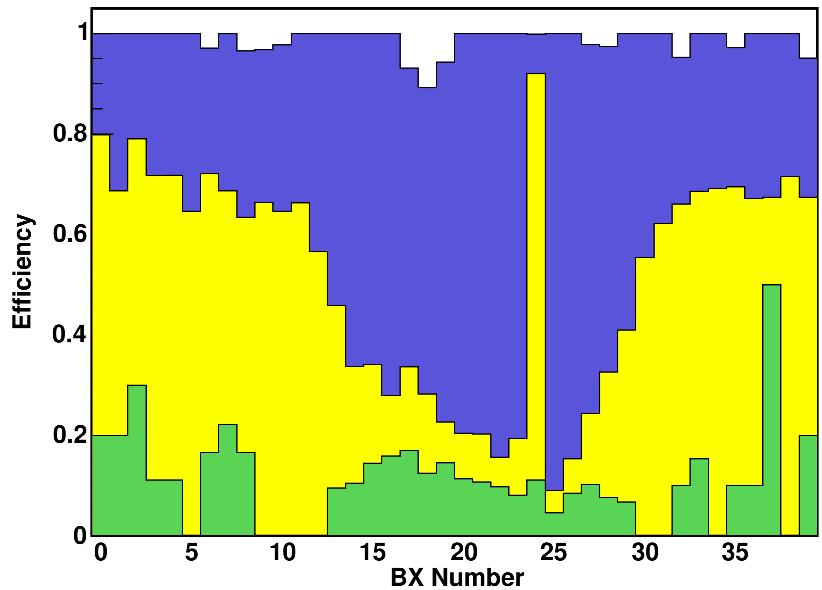

Figure 6.4: *Efficiency values for different quality samples as a function of the bunch crossing number. Blue, green and yellow histograms plot the efficiency for high, low and all quality samples respectively.*

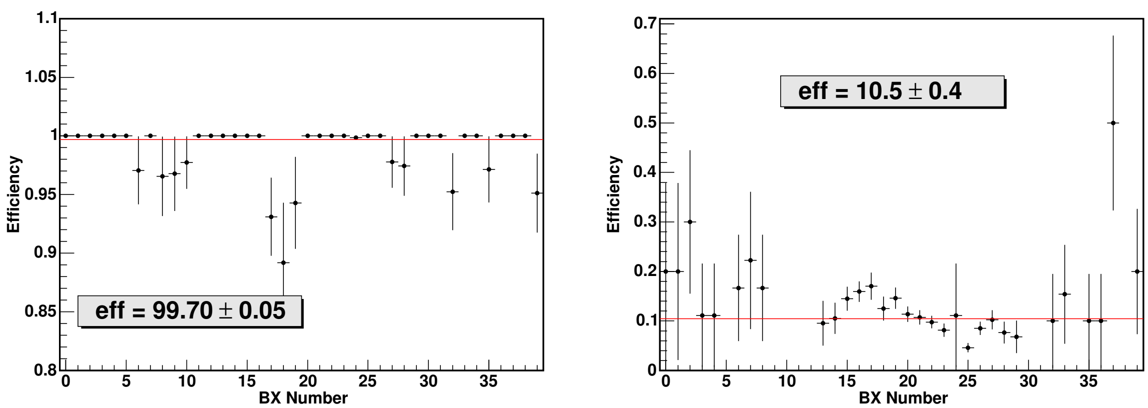

Figure 6.5: *Linear fits to the distribution of efficiency against the bunch crossing number for high (left) and low (right) quality coincidences.*

It is also interesting to study the efficiency achieved by the system. The efficiency of the PHTF can be defined as the ratio of muons found by the PHTF with respect to the total number of events with a coincidence. Fig. 6.4 shows the efficiency of the PHTF as a function of the bunch crossing number for different samples defined according to the quality of the segments: all qualities (yellow histogram), high quality ($q_{MB} = 6$) (blue histogram) and low quality ($q_{MB} = 0$) (green histogram) segments. The high quality sample achieves high efficiency values at all bunch crossings while the low quality sample achieves low efficiency values, i.e. high rejection power. The overall efficiency shows an irregular distribution due to the high ghosts' occupancy at the bunch crossings around the trigger. Muons coming at the BX=24 are efficiently reconstructed by the PHTF and the efficiency is above a 90%. Around BX=24 the ghost occupancy is high and the PHTF achieves a high rejection power by lowering the efficiency to a ∼20%. Track segments at bunch crossings far away from BX=24 are expected to be caused mainly by muons coming out of time, thus the efficiency increases. A linear fit is performed for the high quality and the low quality samples in Fig. 6.5. A 99.7±0.5 % efficiency is reached when high quality coincidences are considered. Low quality coincidences are used to reconstruct a muon with a 10.5±0.4 % efficiency, i.e the PHTF achieves a rejection power of 9.5±0.4. This values confirm the expected behavior of the PHTF. High quality track segments, which are caused by muons, are efficiently joint to form a muon track. On the other hand, low quality track segments, mainly caused by ghost reconstructions, are efficiently rejected, i.e. a low efficiency value is achieved.

The detailed analysis of the efficiency and rejection power of the system is carried out in dedicated sections of this chapter.

6.1.2 Parameter Assignment

Following the PHTF algorithm scheme shown in Fig. 4.6, after the extrapolation step has been performed and a track successfully assembled, the PHTF assigns physical parameters to the muon candidate: transverse momentum, position in the '$r-\phi$' projection, charge and a quality word. At the Beam Tests only one extrapolation (1-2) was possible, thus the Track Assembling step of the algorithm was trivial. In this section we analyze the Parameter Assignment step of the algorithm by comparing the actual results with the expected response of the PHTF.

Transverse Momentum Assignment

The two inner muon stations with a valid extrapolation are used as a magnetic spectrometer for transverse momentum assignment: the value of p_T is estimated from the measured value of $\Delta\phi$ using a relation stored in hardware LUTs. At the Beam Test the $\Delta\phi = \phi_{MB2} - \phi_{MB1}$ was used to assign transverse momentum to reconstructed muons. Though the muon beam had a fixed energy, its spread simulated different transverse momentum values, as it was already explained in Section 5.3.

Look-Up-Tables loaded in the hardware are used to assign the p_T. As it has been already explained in Chapter 4, two sets of LUTs , one for high-p_T muons and other for low-p_T, are used depending on the bending angle (ϕ_b) measured at the inner station.

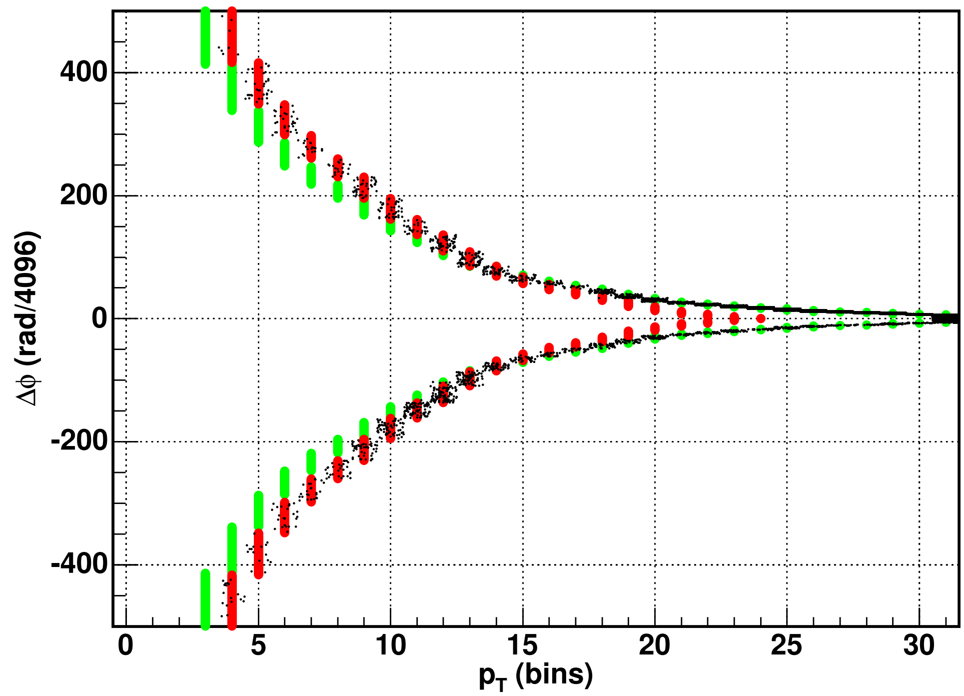

Figure 6.6: *$\Delta\phi - p_T$ distribution on top of the p_T-assignment Look-Up-Tables.*

In Fig. 6.6 the $\Delta\phi - p_T$ distribution (black points) is shown on top of the p_T-assignment LUTs. Red points correspond to the low-p_T LUT, while green points represent the high-p_T LUT. As expected, the transverse momentum assigned to a muon track is calculated from the corresponding LUT. Namely, black points perfectly follow the p_T-assignment LUTs' points. Furthermore, the change from the low-p_T to the high-p_T LUT is achieved at the given ϕ_b threshold.

Azimuthal Position Assignment

The azimuthal coordinate position (ϕ) is assigned attending to the ϕ value measured at MB2. If no actual track segment was found at MB2, an extrapolation from MB1 or MB4 is performed to predict the ϕ position of the muon track at MB2. This extrapolation procedure is implemented using LUTs downloaded in the hardware.

In the Beam Test only a MB1 and a MB2 delivered data to the DTTF. Therefore, if a muon track is found, the PHTF will assign its azimuthal coordinate position applying a coordinate conversion to the ϕ value measured at MB2. There is no need to use the extrapolation procedure. Figure 6.7 illustrates the ϕ assignment algorithm. The ϕ value measured at MB2 is plotted as a function of the ϕ value assigned to the track. The big

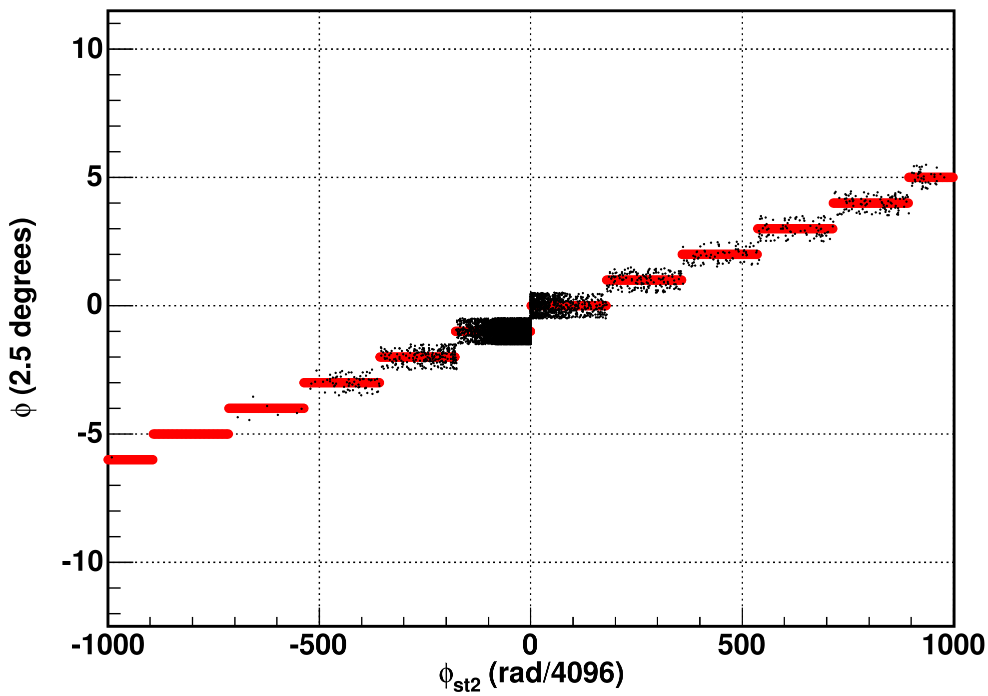

Figure 6.7: *Azimuthal position (ϕ) assigned to the track as a function of the position measured at MB2.*

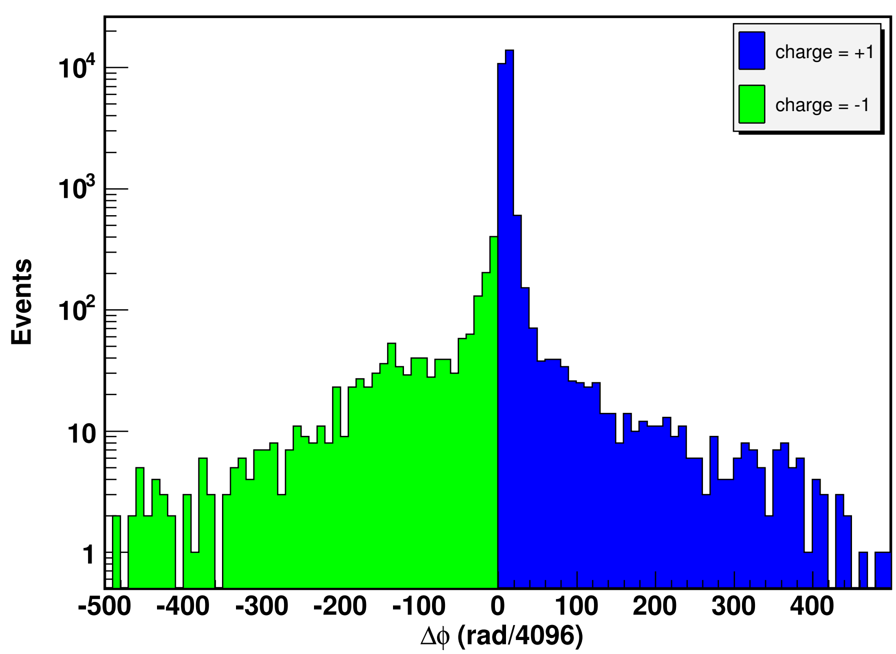

Figure 6.8: *Distribution of $\Delta\phi$. Charge values assigned to the muon track are represented with different colors.*

red points of the figure correspond to the ϕ conversion expected values. The azimuthal position assignment is performed as expected in 100% of the events.

Charge Assignment

The assignment of the charge to the muon track is performed considering the bending of the muon track in the iron yoke due to the magnetic field. The $\Delta\phi$ value is used to determine this bending. Positive $\Delta\phi$ values correspond to $q = +1$ while negative values to $q = -1$. Fig. 6.8 plots the $\Delta\phi$ measurement as a function of the charge assigned to the track. The charge assignment is performed as expected in 100% of the events

6.2 Comparison to the C++ Emulator

To validate the electronics implementation of the PHTF algorithm, a comparison between the response of the hardware and the response from a simulation of the system must be done. As described in Section 5.4, a tool to emulate the PHTF response from the DT Local Trigger inputs was developed in the ORCA framework. The DTTF module of the ORCA simulation was modified to cope with the Beam Test conditions. The emulator is used to validate the DTTF Trigger response. The PHTF hardware output data is compared event-by-event with the emulator output values.

The first variable that must be compared is the muon track quality. The quality word codifies how the PHTF reconstructed the muon track, i.e. from which MB stations came the track segments involved in the reconstruction. Table 4.2 summarized the meaning of the possible quality codes. At the Beam Test only two possible track qualities were expected. When no muon track could be reconstructed, the PHTF output to the Wedge Sorter a quality value of 0. If the reconstruction was successful, a quality value of 3 had to be assigned to the track as only track segments from MB1 and MB2 could be involved in the reconstruction.

The comparison of the track quality allows to understand the PHTF hardware trigger response, i.e. if a muon is found or not. Fig. 6.9 illustrates this comparison. The left figure shows the comparison for the first track while the figure on the right shows the comparison for the second track. As it is shown, a 100% agreement is found between the hardware and the simulation response.

It is also interesting to evaluate the transverse momentum assignment. The comparison between the the p_T assigned by the emulator and the value assigned by the hardware (as readout from the Local DAQ system) is shown in Fig. 6.10. The comparison was performed for the two tracks output by the DTTF. The left figure shows the result for the first track while the right figure shows the result for the second track. In both cases the p_T bin (from 0 to 31) assigned to the track is used as unit, instead of GeV/c.

Both for the track quality and the transverse momentum assigned to the muon candidates, the agreement between the hardware and the emulated response is perfect. The emulator reproduces the PHTF hardware trigger decision for 100% of the events. Therefore, the PHTF algorithm hardware implementation is completely understood and its

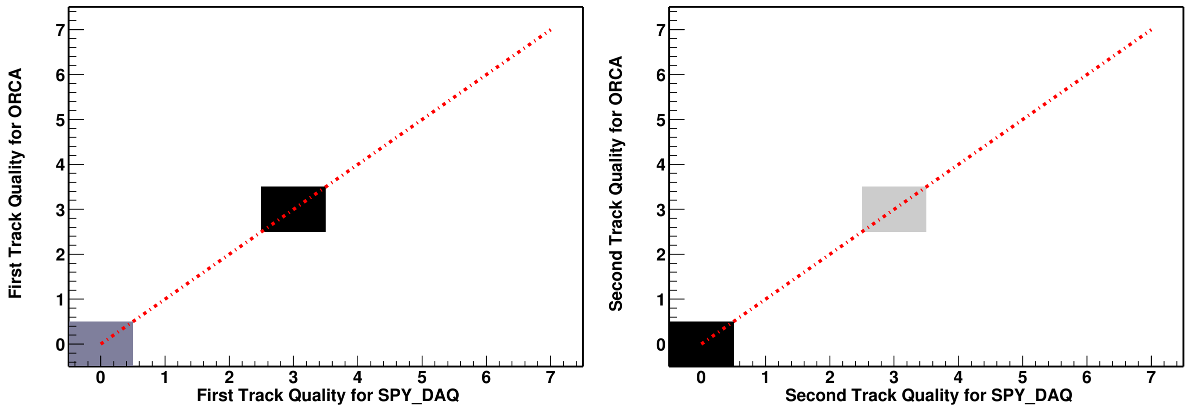

Figure 6.9: *Comparison of the DTTF extrapolation results for the first (left) and the second (right) track output by the system. The simulation result is plotted on the vertical axis while the PHTF result is plotted on the horizontal axis.*

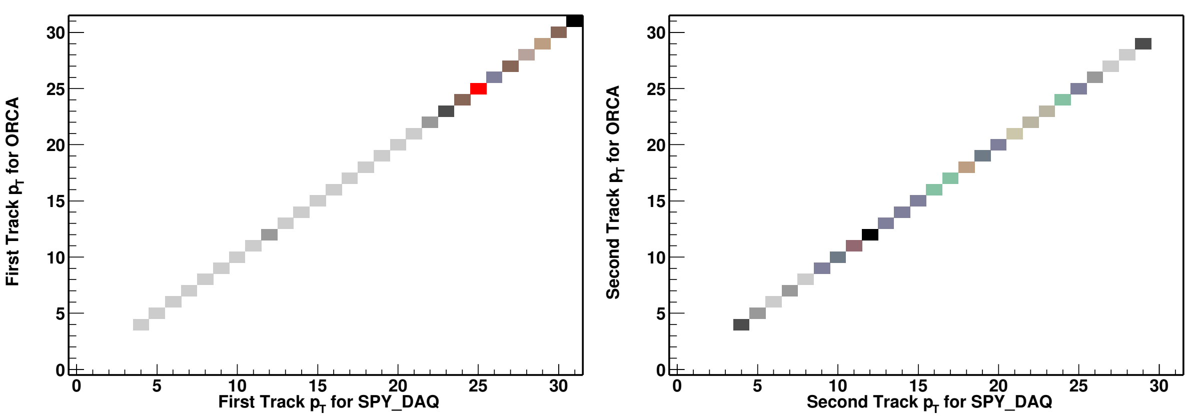

Figure 6.10: *Comparison of the DTTF p_T assignment results for the first (left) and the second (right) track output by the system. The simulation result is plotted on the vertical axis while the PHTF result is plotted on the horizontal axis.*

electronics implementation is validated. Next sections will be devoted to the detailed analysis of the DTTF Trigger performance.

6.3 Analysis of the PHTF Input data

The DTTF Trigger system receives its input data (track segments) from each of the DT Local Trigger devices located at every MB chamber. Track segments are reconstructed from hits recorded in the MB chambers' DT cells. The goal of this sections is to overview the performance of the track segments' reconstruction, from the muons' hits recorded in the DT cells to the DTTF input data. First, the structure of the muon beam as reconstructed by the MB chambers is analyzed. Then, we will study the performance of the DT Local Trigger, for both MB stations.

6.3.1 DT Chambers Performance

The most precise measurement of the passage of muons through a MB chamber are the hits recorded in the DT cells. They are used in the track segment reconstruction performed by the DT Local Trigger but they are also recorded for offline muon track reconstruction. The passage of a muon through a MB chamber is characterized by two variables: the position (mm) and the angle (mrad).

To study the muon beam structure we use muons efficiently reconstructed by the MB chambers. When a muon is reconstructed from a fit to a straight segment of four hits in both ϕ superlayers (4+4) it is considered a efficiently reconstructed muon. Therefore, the position (Fig.6.11) and the angle (Fig. 6.12) calculated from the offline reconstruction of '4+4' muons are used as the most precise measurement to study the muon beam structure.

The sharp limits of the position distribution (Fig. 6.11) are explained attending to the plastic scintillators geometrical coverage. The muon beam width is $\sim$ 100 mm. Regularly spaced gaps in the distribution are understood attending to the I-beam effect. Drift tubes within a layer are separated by a beam of non-negligible width. Layers within a superlayer are organized with a half DT cell offset. If the muon trajectory is perpendicular to a MB chamber and it crosses a layer through a I-beam, it will leave, at most, two hits in each superlayer. Therefore, such muons are not efficiently reconstructed and the I-beams positions at the ϕ layers are observed as gaps in the muon position distribution. However, the MB chambers were aligned in such a way that a muon suffering the I-beam effect in one of them did not suffer it in the other (gaps at MB1 are not aligned with gaps at MB2).

The bending angle (ϕ_b) distribution (Fig. 6.12) is centered in 0, as expected for a perpendicular incident muon beam. An angular size of 2 mrad is achieved by both MB chambers.

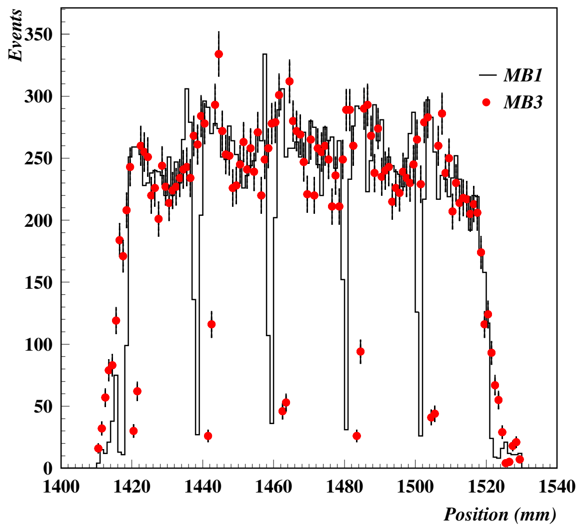

Figure 6.11: *Beam Profile as seen by the MB chambers. Points corresponds to MB3 (pseudo-MB2) and histogram to MB1.*

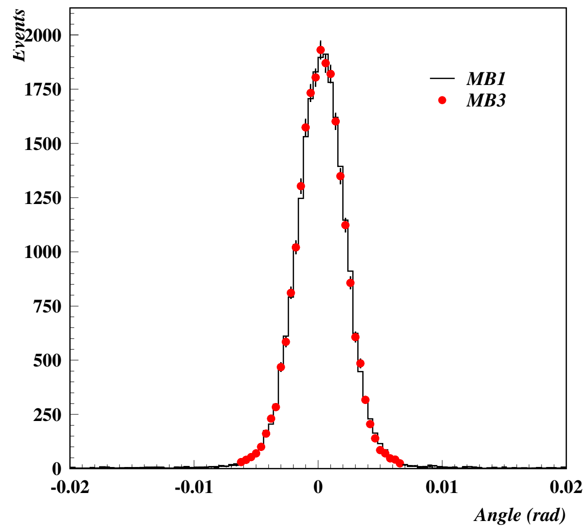

Figure 6.12: *Incident angle as seen by MB chambers. An angular size of 2 mrad is observed.*

6.3.2 DT Local Trigger Performance

In Section 3.4.4 a detailed description of the DT Local Trigger was presented. Each DT Local Trigger forwards to the DTTF system up to two track segments. Segments are characterized by their position along the chamber (ϕ), the bending angle of the muon within the chamber (ϕ_b) and a quality word that codifies how the track segment was reconstructed.

The DT Local Trigger performance can be studied following the approach taken in [32] for the analysis of 2003 Beam Test. Information from the DT cells is used for the offline reconstruction of muons. Segments reconstructed from 4 hits in both ϕ superlayers of a MB chamber (4+4-hit) are considered 'good muons' and used to study the local trigger performance.

The position resolution of the DT Local Trigger is defined as the difference between the position calculated from the offline reconstruction of the segment and the position value assigned to it by the Local Trigger. Fig. 6.13 shows the Local Trigger resolution for MB1 and MB2. In both cases, 'good muons' (4+4 hits) are used in the calculation. The σ of the Gaussian fit to the position resolution distribution is 0.54 mm.

Two components contribute to the position resolution. The first component is related to the intrinsic resolution of the Local Trigger algorithm. The Local Trigger calculates the muon position with a finite precision due to the finite TRACO Look-Up-Tables granularity. Thus, it achieves a lower resolution than the offline reconstruction. The second

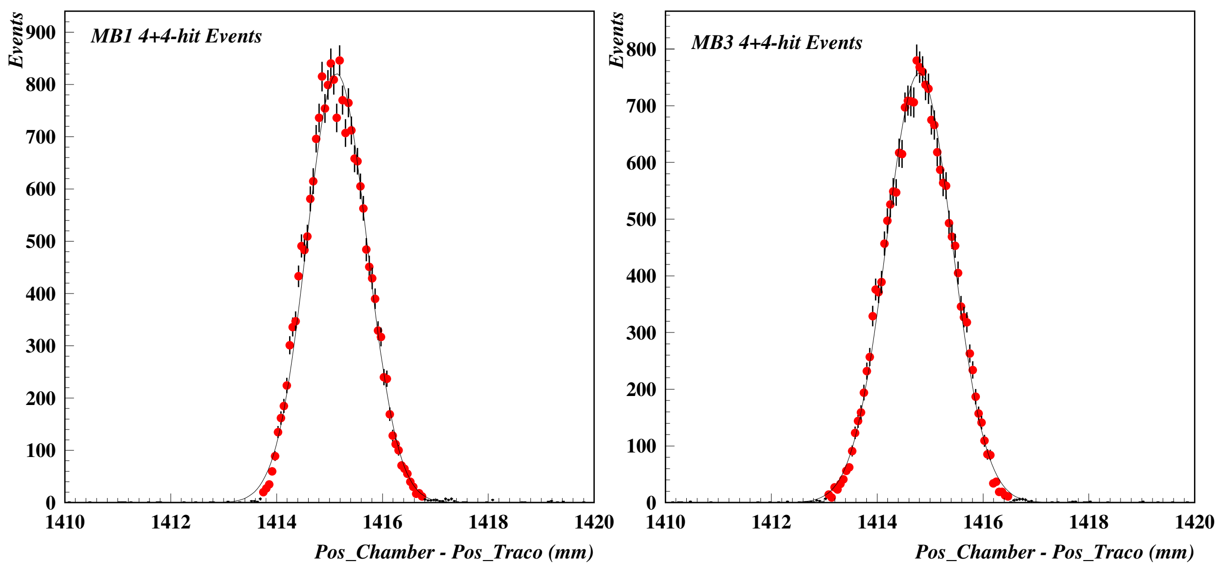

Figure 6.13: *Local Trigger position resolution for MB1 (left) and MB3 (pseudo-MB2) (right). The width of the Gaussian fit is 0.54 mm.*

component is related to the dependence of the resolution on the position where the muon hit the chamber. Both components can be distinguished by plotting the Local Trigger position resolution as a function of the position where the muon crossed the chamber (Fig. 6.14). The solid black line on the figures corresponds to the total position resolution as shown in Fig. 6.13. The 'intrinsic' component is observed as the resolution at a fixed position of the chamber. The total position resolution is dominated by this component.

Finally, the DT Local Trigger performance can be also studied attending to the quality (Table 3.1) assigned to the track segment. Ideally, 'good muons' (4+4) should be tagged as HH ($quality = 6$) track segments. Deviations from this principle are caused by Local Trigger inefficiencies.

Fig. 6.15 shows the quality assigned to 4+4-hit muons for both MB chambers. Muons are reconstructed with the maximum quality with a 90% efficiency for both MB chambers. Only 1% of the 4+4 muons are not triggered at all, i.e. the DT Local Trigger is completely inefficient for these events. For the remaining muons (always below 10%), segments are reconstructed with a lower quality than the expected from the offline reconstruction.

6.3.3 Conclusions

The performance of the MB chambers and of the DT Local Trigger has been studied in this section. Precise measurements of the muon beam have been performed from the MB chambers data. The beam was characterized by a spread of 100 mm and an angular size of 2 mrad.

The DT Local Trigger performance has been studied by comparing its data with the

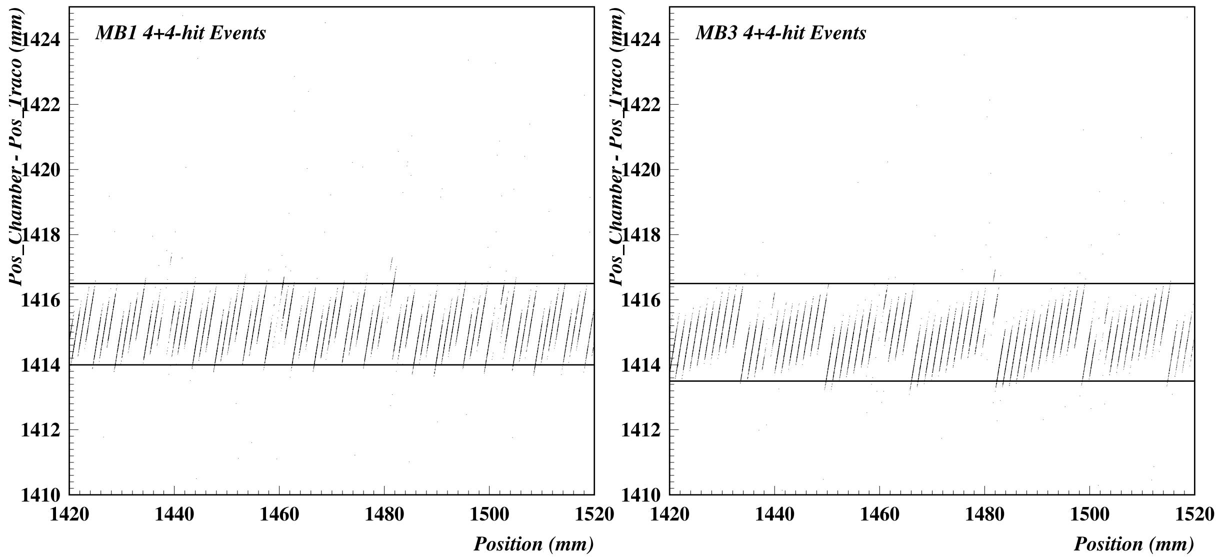

Figure 6.14: *Position resolution as a function of the position as reconstructed from the DT cells hits for MB1 (left) and MB3 (pseudo-MB2) (right).*

offline reconstruction of the DT cells data. A 90% efficiency and a position resolution of 0.54 mm summarize the DT Local Trigger performance.

6.4 Single Muon Trigger Performance

The PHTF input can be classified attending to the physical origin of the Local Trigger segment reconstruction. Ideally, only segments caused by muons are delivered by the DT Local Trigger to the DTTF system. However, noise coming from the drift tubes or ghost generation mechanisms (described in Section 3.4.4) can lead to fake segment reconstructions. The probability of reconstructing a fake segment at both Local Triggers within the same bunch crossing is not negligible.

In this section we analyze the PHTF Trigger performance on muons that caused a scintillator trigger. They are delivered to the PHTF at the bunch crossing were the plastic scintillators gave the trigger signal to the system, i.e. BX=24. Next section is dedicated to the study of signals coming when BX<24.

The input to the PHTF can also be classified attending to the quality of the track segments delivered by the DT Local Trigger of each MB chamber. The quality word associated to a track segment codifies how the Local Trigger reconstructed it, i.e. how many ϕ superlayers and how many Drift Tube layers within each of them were used. The segment quality codes were already summarized in Table 3.1. For the analysis of the PHTF data, we can simplify the description. From now on, segments reconstructed by correlating hits in the two ϕ superlayers of a MB chamber will be denoted as 'High quality' ($q_{MB} \geq 4$). Segments reconstructed from hits of a single ϕ superlayers will be

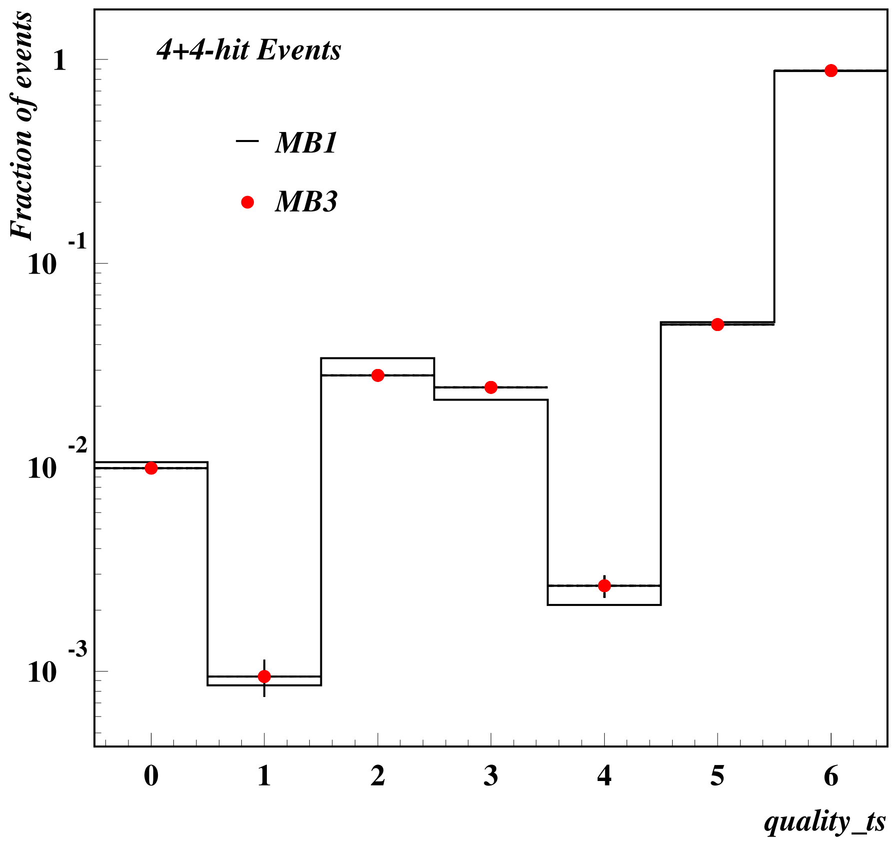

Figure 6.15: *Quality assignment of the DT Local Trigger. Only 1% of good muons (4+4 hits) are not triggered (quality=0) at all.*

referred as 'Low quality' ($q_{MB} < 4$).

Attending to this agreement, we can classify the PHTF input data at the Beam Test in three different quality samples:

'H+H' Sample: Both MB chambers deliver High quality track segments.

'H+L-L+H' Sample: The track segment from one of the MB chambers has High quality while the track segment of the other has Low quality.

'L+L' Sample: Track segments from both chambers have Low quality.

To analyze the single muon Trigger performance, first we will study the PHTF occupancy at BX=24. After we will study the Trigger performance in terms of efficiency. Different run conditions, namely beam energy and the presence/absence of iron absorbers in the muon beam trajectory, are considered. The following selection cuts are applied for the analysis :

- Segments delivered at the scintillator trigger, BX=24.
- Single muon events. Only one track segment is delivered by each DT Local Trigger.
- -50 mm $< \phi_{MB1} <$ 50 mm and -50 mm $< \phi_{MB2} <$ 50 mm. The muon occupancy at BX=24 is determined by the geometrical acceptance of the plastic scintillators (Fig. 6.16). Therefore, we will only consider segments within the position range covered by them.

Two different sets of runs are considered: those where the iron slabs were located in front and between the MB chambers, and those without iron slabs.

6.4.1 Occupancy

The overall occupancy is defined as the ratio between the events where a coincidence occurred and the total number of events. In order to understand the occupancy nature, we will study the contribution to the overall occupancy of the different quality samples.

Tables 6.1 and 6.2 show the overall occupancy and the contribution (in %) to it of different quality samples. Table 6.1 show the results for runs without iron slabs while in Table 6.2 runs with iron slabs are considered. These numbers are plotted as a function of the beam energy in Figures 6.17 and 6.18.

The overall occupancy at BX=24 ranges from 59% to 63%. The contribution of each quality sample to this number is slightly dependent on the run conditions. Nevertheless, the occupancy distribution among the quality samples leads to a general conclusion. The high quality sample (HH) represents a ~75% of the overall occupancy. On the other hand, the low quality sample (LL) does not contribute significantly to it (~2%). Therefore, track segments reconstructed from signals left by real muons are characterized by high quality values. It is unlikely that a muon which caused a scintillator trigger was reconstructed with low quality values at the DT Local Trigger level.

Runs without iron slabs

RUN ID	ENERGY (GeV)	OVERALL OCCUPANCY (%)	QUALITY CONTRIBUTIONS		
			HH	HL-LH	LL
2600	50	61.3 ± 0.4	76.0 ± 0.2	21.9 ± 0.2	2.06 ± 0.1
2555	100	62.5 ± 0.4	76.7 ± 0.2	21.7 ± 0.2	1.66 ± 0.1
2597	150	63.5 ± 0.4	78.9 ± 0.2	19.5 ± 0.2	1.60 ± 0.1
2729	250	62.4 ± 0.4	79.0 ± 0.2	19.4 ± 0.2	1.57 ± 0.1
2730	250	62.8 ± 0.6	78.9 ± 0.4	19.8 ± 0.4	1.3 ± 0.1
2734	250	62.8 ± 0.3	78.9 ± 0.2	19.7 ± 0.2	1.44 ± 0.1

Table 6.1: *Overall Occupancy and the contribution to it of the different quality samples for runs without iron slabs placed on the beam trajectory.*

Runs with iron slabs

RUN ID	ENERGY (GeV)	OVERALL OCCUPANCY (%)	QUALITY CONTRIBUTIONS		
			HH	HL-LH	LL
2601	50	60.2 ± 0.3	69.3 ± 0.3	27.9 ± 0.3	2.75 ± 0.1
2553	100	58.8 ± 0.4	70.9 ± 0.3	26.8 ± 0.3	2.3 ± 0.1
2554	100	58.9 ± 0.3	71.6 ± 0.3	25.8 ± 0.3	2.66 ± 0.1
2538	140	58.6 ± 0.3	71.1 ± 0.2	26.3 ± 0.2	2.57 ± 0.1
2598	150	59.5 ± 0.4	72.2 ± 0.3	25.5 ± 0.3	2.3 ± 0.1

Table 6.2: *Overall Occupancy and the contribution to it of the different quality samples for runs with iron slabs placed on the beam trajectory.*

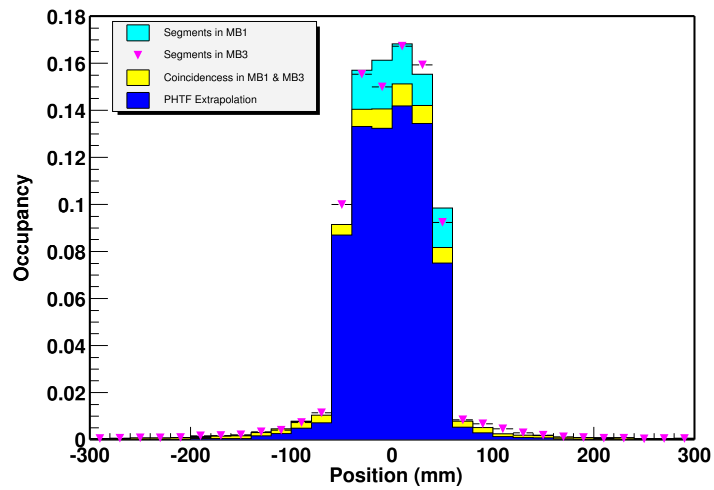

Figure 6.16: *Occupancy as a function of position for single muons at BX=24. The occupancy is determined by the plastic scintillators geometrical coverage.*

The PHTF occupancy dependency respect to the run conditions, namely the beam energy and the presence of the iron absorbers in the beam trajectory, is also understood. As expected, neither the overall occupancy nor the contribution to it of the different quality subsamples depend on the energy of the beam. A flat distribution is observed when plotting these variables (Figs. 6.17 ans 6.18). However, when the iron slabs were placed on the muon beam stream, a slight effect is observed, both on the overall occupancy and on the distribution of it among the different quality samples. In the figures, values calculated for runs taken with the iron absorbers are represented by red circles while blue squares represent the values for runs without the absorbers. The overall occupancy is ∼2% higher for runs with irons. The contribution to the overall occupancy of HH coincidences is a ∼6% higher for runs without the iron slabs that for runs with them. On the other hand, the contribution of HL-LH samples is a ∼6% lower for runs without iron slabs that for runs where the iron slabs were present. Finally, the contribution of the LL sample to the overall occupancy is a ∼0.8% higher for runs with iron slabs that for runs without them.

Results shown in [32] are useful to explain this behavior. Muons passing through a iron slab can suffer multiple scattering processes due to their interaction with the iron. Multiple scattering processes at the iron slabs can, with some probability, deflect the muon trajectory, which originally followed a straight direction. In such a case, the incidence of the muon into the MB chamber is not orthogonal any more, thus the bending angle (ϕ_B) differs from 0. As it was shown in [32], the quality of the track segment delivered to the DTTF by the DT Local Trigger of the chambers has a dependency on the ϕ_b angle. For high values of ϕ_b, the DT Local Trigger reconstructs track segments with lower quality values. Therefore, muons affected by multiple scattering processes could degrade their

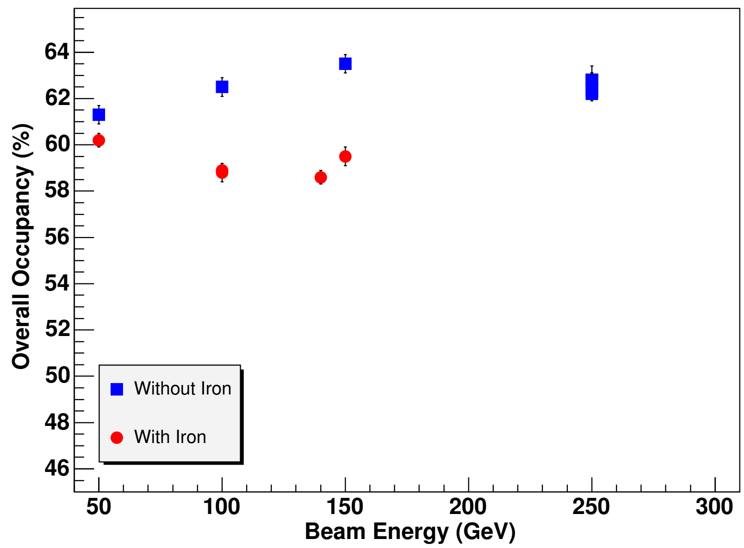

Figure 6.17: *Overall Occupancy for different beam energies. Blue points correspond to runs without iron slabs in the beam trajectory while red points are for runs with the iron slabs.*

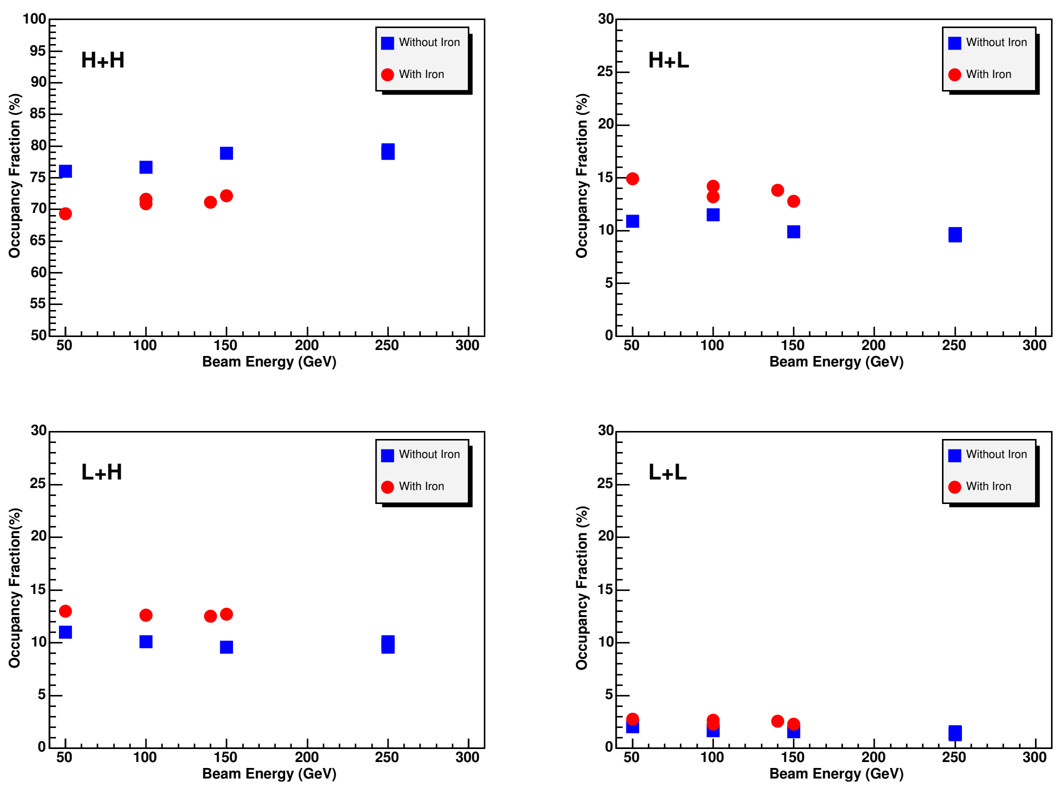

Figure 6.18: *Contribution to the Overall Occupancy of the different quality samples*

quality at the DT Local Trigger level.

Attending to these arguments, numbers given in Tables 6.1 and 6.2 and plots shown in Figures 6.17 and 6.18 are understood. When the iron slabs are interleaved in between the chambers a fraction of muons will suffer multiple scattering processes that deflect their path. From the DTTF point of view, this effect is observed as a transference of track segment coincidences from a given quality sample to a lower one. When the iron slabs are placed on the muon beam stream, a fraction of coincidences that would have belong to the HH quality sample are transferred to the HL-LH sample. Furthermore, coincidences in the latter are transferred to the LL sample. Eventually, a small fraction of what would have been LL muons could cross the MB chambers without originating a segment reconstruction. The latter effect explains the slight lower overall occupancy of the runs with iron slabs with respect to the runs without them.

However, the iron absorbers are not an outstanding issue for the DTTF Trigger performance. The low slab thickness (5 cm) at the Beam Test does not allow to simulate the effects of the CMS iron yoke, which is much more thick (~50 cm).

6.4.2 Efficiency

In this section we will analyze in detail the muon track reconstruction performance of the PHTF during the Beam Test. In previous sections (6.1.1) we validated the behavior of the extrapolation principle during the Beam Test. The response of the PHTF was confirmed to be as expected. However, to analyze the DTTF Trigger performance, a detailed analysis of the efficiency in reconstructing muon tracks must be carried out for different run conditions.

We define the efficiency as the ratio of muons found by the PHTF with respect to the total number of events with a coincidence. To study the efficiency of the PHTF we will analyze events at the bunch crossing when the scintillators gave a trigger (BX=24). Thus, the efficiency to reconstruct tracks from real muon signals will be studied. In next section the complementary study of the efficiency at BX<24 will be carried out.

The only dependency expected for the PHTF efficiency is on the quality of the track segments used to reconstruct the muon track. This dependency is well understood attending to the extrapolation principle used by the PHTF to match track segments. As it has been learned from previous Beam Tests, the resolution of the variables delivered by the DT Local Trigger (ϕ and ϕ_b) to the DTTF system depends on how the track segment was reconstructed, as coded in a quality word. Low quality reconstructions achieve lower ϕ and ϕ_B resolutions. The extrapolation principle used by the PHTF to reconstruct a muon track is based on the $(\Delta\phi, \phi_b)$ relationship, thus lower resolution in the Local Trigger variables is translated into lower PHTF efficiency values.

In Tables 6.3 and 6.4 the overall efficiency and the efficiency for the three different quality samples are shown. Figures 6.19 and 6.20 represent this numbers as a function of the energy of the muon beam.

The overall efficiency ranges from 96% to 98% depending on the presence of the iron slabs.

Runs without iron slabs

RUN ID	ENERGY (GeV)	EFFICIENCY (%)			
		OVERALL	HH	HL-LH	LL
2600	50	97.6 ± 0.1	99.89 ± 0.02	91.4 ± 0.3	79 ± 2
2555	100	97.9 ± 0.1	99.98 ± 0.01	91.8 ± 0.2	91 ± 1
2597	150	97.9 ± 0.1	99.95 ± 0.02	91.4 ± 0.4	79 ± 2
2729	250	98.0 ± 0.1	99.95 ± 0.01	91.7 ± 0.4	79 ± 2
2730	250	98.3 ± 0.1	99.95 ± 0.02	92.5 ± 0.5	83 ± 3
2734	250	98.2 ± 0.1	99.96 ± 0.01	92.5 ± 0.3	80 ± 2
2540	300	97.7 ± 0.3	99.99 ± 0.01	91.0 ± 1.0	85 ± 7
2550	300	97.6 ± 0.1	99.97 ± 0.02	90.1 ± 0.5	89 ± 2
2551	300	97.8 ± 0.1	99.99 ± 0.01	90.9 ± 0.4	92 ± 2

Table 6.3: *Overall Efficiency and efficiency of the different quality samples for runs without iron slabs.*

Runs with iron slabs

RUN ID	ENERGY (GeV)	EFFICIENCY (%)			
		OVERALL	HH	HL-LH	LL
2599	50	96.5 ± 0.1	99.93 ± 0.02	90.6 ± 0.3	78 ± 1
2553	100	96.3 ± 0.1	99.95 ± 0.02	90.3 ± 0.3	90 ± 2
2554	100	96.4 ± 0.1	99.99 ± 0.01	90.7 ± 0.2	88 ± 1
2538	140	96.2 ± 0.1	99.98 ± 0.01	89.9 ± 0.2	88 ± 1
2598	150	96.5 ± 0.1	99.95 ± 0.02	88.5 ± 0.4	78 ± 2
2539	300	96.3 ± 0.1	99.99 ± 0.01	90.3 ± 0.3	89 ± 1
2552	300	96.3 ± 0.1	99.96 ± 0.02	90.3 ± 0.3	90 ± 2

Table 6.4: *Overall Efficiency and efficiency of the different quality samples for runs with iron slabs.*

For the high quality (HH) subsample, a 99.9% efficiency is achieved. When the PHTF receives high quality track segments from the Local Trigger devices of both chambers, it reconstructs a muon track in practically all the events. Notice that there is no differences in the efficiency when considering runs with or without iron slabs.

The efficiency drops to 90%-92.5% when considering the 'HL-LH' quality subsample. An impact on the PHTF efficiency is observed when one of the track segments was reconstructed with a low quality value. The efficiency loss is more important (84%) when the low quality track segment is delivered by the MB1 local trigger, i.e. 'LH' subsample (plot on the bottom-left corner of Fig. 6.20). On the other hand, when the low quality track segment is delivered by the MB2 Local Trigger, i.e. 'HL' subsample (plot on the top-right corner of Fig. 6.20), the efficiency is kept on a 99%. The MB1 track segment variables play the most important role in the extrapolation performance, both the position and the bending angle are used. On the other hand, only the position of the MB2 track segment is used to join the track segments. As we have already mentioned, lower quality values mean lower resolutions. Therefore, the impact on the PHTF efficiency is higher when the low quality track segment is used as source of an extrapolation.

Finally, a ~80% efficiency is achieved for LL coincidences. However, attending to the occupancy values described in the previous section, the statistical significance of these subsample is negligible.

It must be noted that the overall efficiency for runs with iron slabs is a ~2% lower than for runs without them. The efficiency of the different quality samples remains the same with or without iron slabs in between the MB chambers. Therefore the difference on the overall efficiency between runs with iron slabs and runs without them must rely on the relative contributions to the overall efficiency of the different quality samples. As pointed out in the previous section, the contribution of the different quality samples to the overall occupancy depends on the presence/absence of the iron slabs. The dependency of the overall efficiency on the contribution to it of the different quality samples is described by expression 6.1. ϵ stands for the overall efficiency, ϵ_q for the efficiency achieved by each quality sample and O_q for the contribution to the occupancy of each quality sample.

$$\epsilon = \sum_q \epsilon_q O_q \tag{6.1}$$

Attending to the results described at Section 6.4.1, the contribution of the different quality samples differs when placing the iron slabs in the muon beam trajectory. Low quality samples (HL-LH and LL) contribute more when the iron slab is present. Thus, this runs will show lower overall efficiency values (Fig. 6.19). However, the use of the iron slabs was foreseen to simulate the CMS iron yoke. As it was already explained in Section 4.2.2, the effect of the CMS iron yoke on the muon trajectory is parametrized through the calculation of the extrapolation LUTs. Therefore, the iron absorbers are not an outstanding feature for the study of the PHTF trigger efficiency at the Beam Test.

Finally, it must be emphasized that the efficiency values achieved are completely satisfactory. Almost a 100% efficiency is achieved for high quality coincidences, while the overall efficiency does not drop below a 95%.

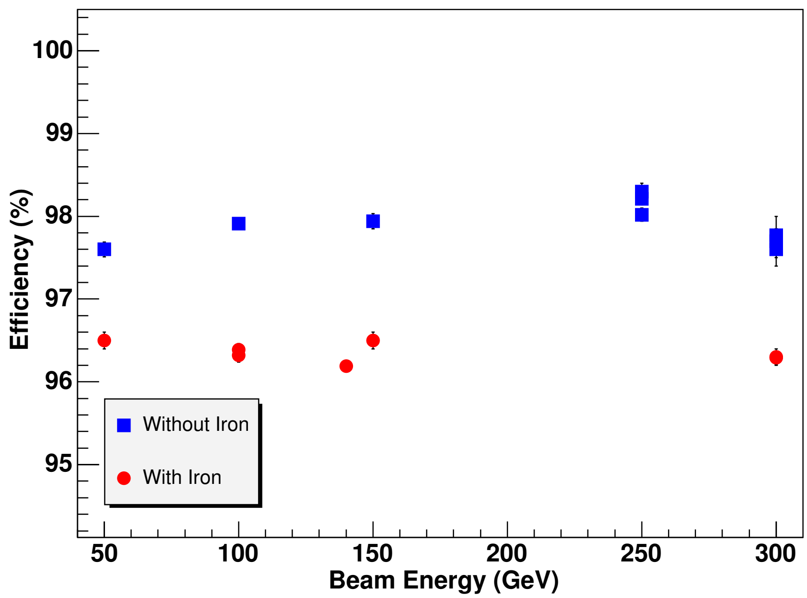

Figure 6.19: *Overall efficiency values as a function of the energy of the beam*

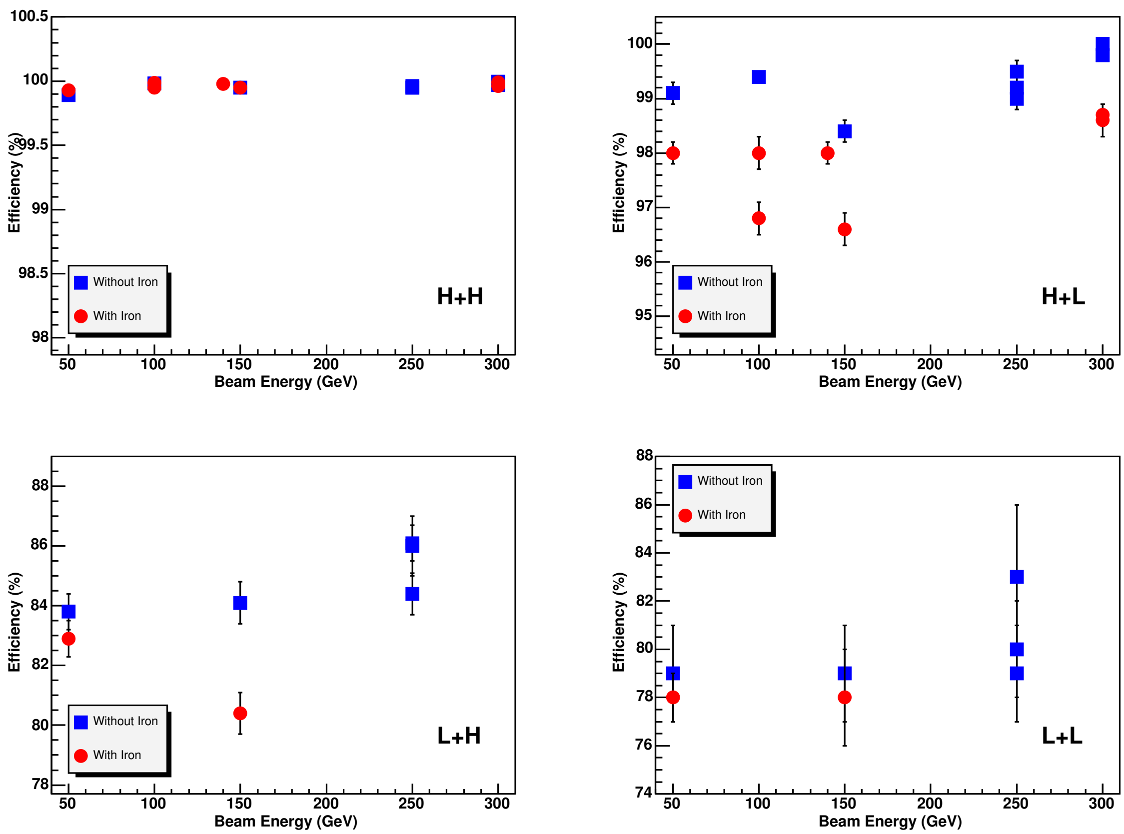

Figure 6.20: *Efficiency values for the different quality samples as a function of the energy of the beam*

6.5 Ghosts and Out-of-Time Muons Studies

The DTTF performance at bunch crossings preceding the scintillator trigger (BX<24) is studied in this section. At these bunch crossings the plastic scintillators did not give a L1 Accept signal. Local Trigger reconstructions are explained attending to two different kind of events:

Out-of-time Muons: They are muons hitting the chambers in a different bunch crossing from the scintillator trigger one. They hit the chambers in the region not covered by the plastic scintillators, thus they do not produce a trigger. Segment reconstructions from signals left by these muons achieve high quality values. They are expected to contribute more significantly to the occupancy at bunch crossings far away from BX=24. As they are real muons, the PHTF should find them efficiently.

Ghosts: They are fake reconstruction of real muons. They are delivered to the DTTF at the immediately previous bunch crossings to the scintillators trigger. The mechanism that produces this kind of Local Trigger reconstructions has already been explained in Section 3.4.4. Typically, they produce low quality signals and they are located around the beam spread. As they do not correspond to real muons but to ghost reconstructions of the DT Local Trigger, the PHTF should achieve a high rejection power for this kind of events.

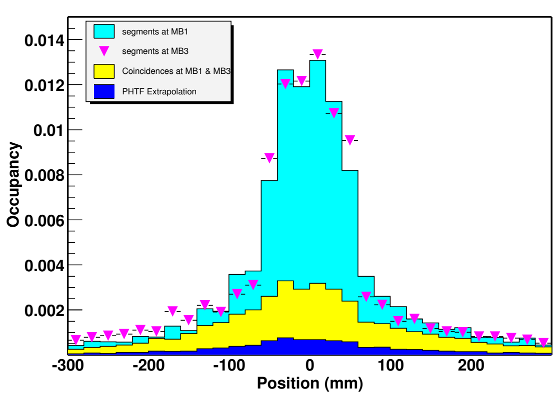

Figure 6.21: *Spatial distribution along the MB chambers of the occupancy for muons coming at 16<BX<24. Ghost track segments are reconstructed during these bunch crossings.*

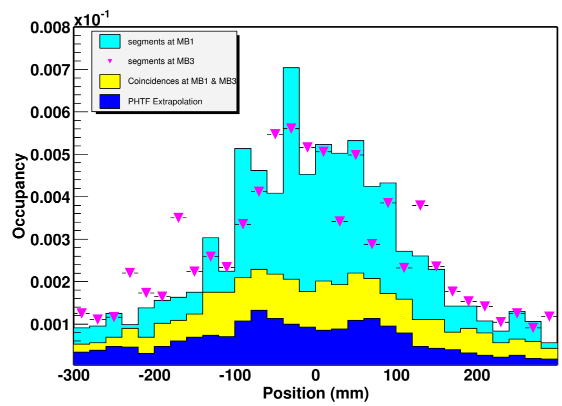

Figure 6.22: *Spatial distribution along the MB chambers of the occupancy for muons coming at BX<17. Muons coming out of time dominate the occupancy distribution at these bunch crossings.*

Figures 6.21 and 6.22 show the spatial distribution of two different bunch crossing samples. Ghosts (Fig. 6.21) are expected at bunch crossings immediately previous

(16<BX<24) to the scintillator trigger and are concentrated within the beam region, at the center of the chambers. Out-of-time muons (Fig. 6.22) are more significant, as the ghost background is lower, at bunch crossings much far away from the scintillator trigger. They are spread all along the chambers. In addition, the occupancy is much higher for ghosts than for out-of-time muons.

We will follow the same analysis strategy taken in Section 6.4. First, we analyze the occupancy for BX<24. After, the PHTF rejection power on the sample is studied. Finally, we discuss the performance of the noise and ghost suppression filters that can be applied at the DTTF level.

The sample will be split in the same quality subsamples already defined in Section 6.4. The following events are considered:

- Segments delivered before the scintillator trigger, BX<24.
- Single muon events. Only one track segment is delivered by each DT Local Trigger.

6.5.1 Ghosts and Noise Occupancy

In Table 6.5 and Table 6.6 we show the overall occupancy for runs without and with iron slabs respectively. In each table the overall occupancy and the contribution to it of the different quality samples are shown. Plots shown in Figs. 6.23 and 6.24 illustrate these results.

The overall occupancy is under a 1% for all runs. In addition, there are not significant differences between runs with and without iron. The high quality sample is expected to belong to out-of time muons. This muons arrived all along the chamber, thus the iron slabs, which were placed in the middle of the muon beam, does not affect them significantly. The occupancy of the low quality sample is not affected either, as it is due to ghost reconstructions of real muons arriving at the scintillator trigger bunch crossing. From the PHTF point of view, the presence of the iron slabs do not affect the noise and ghost occupancy, as data is already filtered by the DT Local Trigger.

Attending to the contribution of the different quality samples shown in Fig. 6.24, it has to be noted that the low quality sample dominates the whole sample. It contributes with a ∼75% to the overall occupancy. Therefore, in the bunch crossings where the scintillators did not give a trigger, the occupancy of the coincidences is dominated by ghost track segment reconstructions delivered in a wrong bunch crossing or noise in the chambers. The contribution to the overall occupancy of high quality coincidences, associated to muons coming out of time is rather low, i.e. ∼12%.

It is also interesting to confirm our statement that high quality signals correspond to real muons coming out of time. In general, if both MB chambers could correlate at least LTRG track segments of their two ϕ superlayers, it is very likely hat hits in the chamber were left by a real muon. However, it must be confirmed. A comparison of the High Quality sample (HH) structure at BX<24 with the same sample at BX=24 confirms our prediction. If both samples are formed by real muons, the nature of the 'HH' sample at BX<24 must be the same as the nature of the 'HH' sample at BX=24. The comparison of

Runs without iron slabs

RUN ID	ENERGY (GeV)	OVERALL OCCUPANCY (%)	QUALITY CONTRIBUTIONS		
			HH	HL-LH	LL
2600	50	0.75 ± 0.01	14.9 ± 0.3	14.0 ± 0.3	71.1 ± 0.4
2555	100	0.77 ± 0.01	10.7 ± 0.3	12.1 ± 0.3	77.3 ± 0.3
2597	150	0.98 ± 0.01	16.2 ± 0.3	16.0 ± 0.3	67.7 ± 0.4
2729	250	0.97 ± 0.01	18.1 ± 0.3	16.5 ± 0.3	65.4 ± 0.3
2730	250	0.97 ± 0.01	18.9 ± 0.5	16.2 ± 0.4	65.0 ± 0.5
2734	250	0.99 ± 0.01	18.8 ± 0.3	17.1 ± 0.3	64.1 ± 0.3
2540	300	0.84 ± 0.03	6.6 ± 0.8	12.0 ± 1.0	81.0 ± 1.0
2550	300	0.72 ± 0.01	5.1 ± 0.3	10.9 ± 0.4	84.0 ± 0.5
2551	300	0.69 ± 0.01	6.5 ± 0.3	11.3 ± 0.3	82.1 ± 0.4

Table 6.5: *Overall Occupancy and the contribution to it of the different quality samples for runs without iron slabs placed on the beam trajectory.*

Runs with iron slabs

RUN ID	ENERGY (GeV)	OVERALL OCCUPANCY (%)	QUALITY CONTRIBUTIONS		
			HH	HL-LH	LL
2601	50	0.70 ± 0.01	14.5 ± 0.3	13.9 ± 0.3	71.5 ± 0.4
2553	100	0.76 ± 0.01	9.4 ± 0.3	12.3 ± 0.3	78.3 ± 0.4
2554	100	0.78 ± 0.01	10.2 ± 0.2	12.2 ± 0.3	77.6 ± 0.3
2538	140	0.97 ± 0.01	12.1 ± 0.2	15.0 ± 0.2	72.9 ± 0.3
2598	150	0.97 ± 0.01	14.9 ± 0.3	15.6 ± 0.3	69.5 ± 0.4
2539	300	0.78 ± 0.01	6.5 ± 0.2	11.3 ± 0.3	82.2 ± 0.3
2552	300	0.70 ± 0.01	4.4 ± 0.2	9.8 ± 0.3	85.7 ± 0.4

Table 6.6: *Overall Occupancy and the contribution to it of the different quality samples for runs with iron slabs placed on the beam trajectory.*

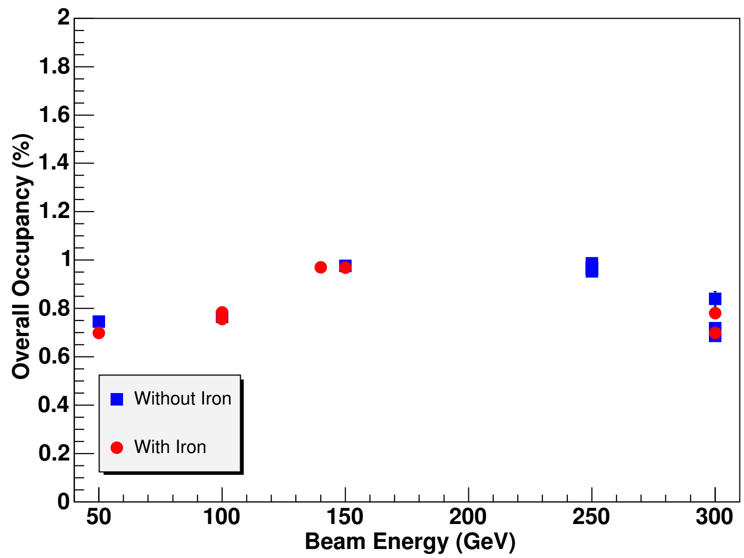

Figure 6.23: *Overall Occupancy for different beam energies at bunch crossings before the scintillators gave the trigger signal. Blue points correspond to runs without iron slabs in the beam trajectory while red points are for runs with the iron slabs.*

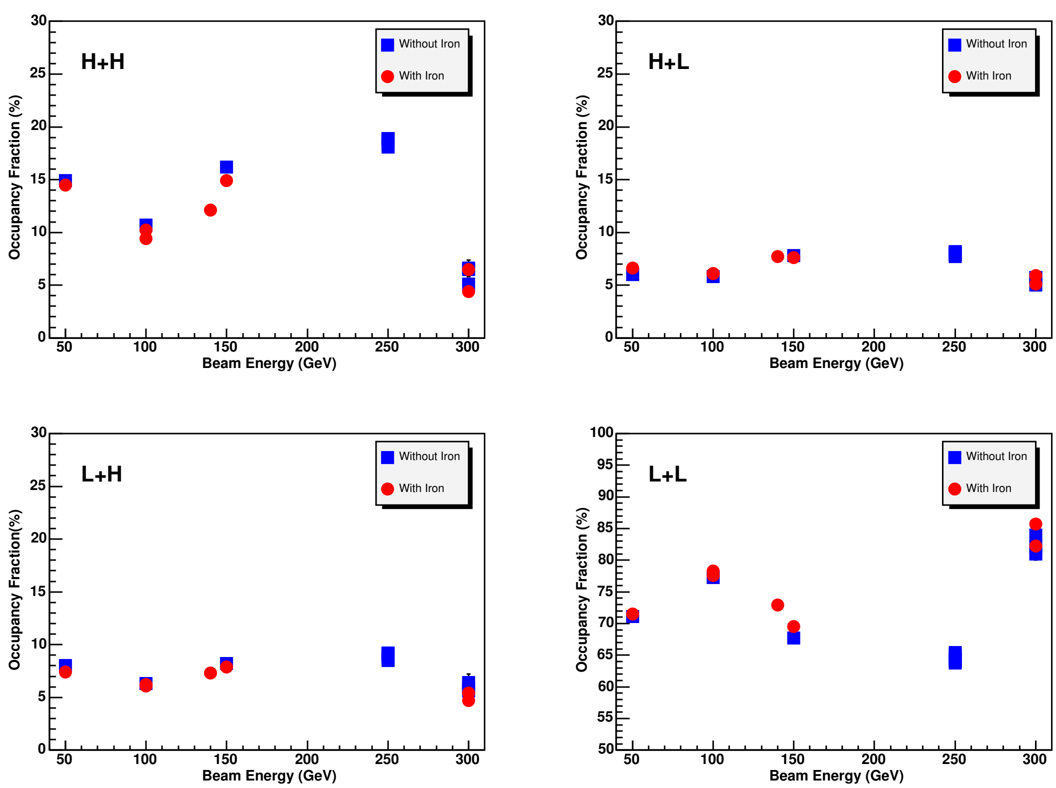

Figure 6.24: *Contribution to the Overall Occupancy of the different quality samples*

the ratio ‘66/HH’ can be used to evaluate this statement. The ‘66’ sample corresponds to muons that leaved a HTRG signal (the track segment was reconstructed from 4 hits of the corresponding ϕ-SL) in all the 4 (2+2) ϕ superlayers. For BX=24, ‘66/HH’=0.66±0.01, while for BX<24, ‘66/HH’=0.65±0.03. From these results one can conclude that real muons are in the physical origin of the HH signals at BX<24.

The same comparison can be carried out for the LL quality sample. The origin of the LL quality sample at BX=24 and BX<24 is expected to be very different. At BX=24 the sample is expected to be dominated by low quality reconstructions of real muons, while at BX<24 the noise and ghost reconstructions dominate the sample. The comparison of the ‘00/HH’ ratios confirms it. ‘00’ coincidences correspond to muons that only leaved a LTRG signal (the track segment was reconstructed from 3 hits in the ϕ-SL) in the inner superlayer of each MB chamber. At BX=24, ‘00/LL’=0.007±0.003, while at BX<24, ‘00/LL’=0.307±0.009. As expected, the structure of the low quality sample is different at BX<24. Ghost reconstructions of real muons dominate the latter.

6.5.2 Rejection Power

The task of the PHTF is to reconstruct real muon tracks and to reject noise and ghost signals generated by the Local Trigger devices of the MB chambers. The performance of the former task has been analyzed in Section 6.4. In this section we analyze the performance of the latter, which is measured through the rejection power of the system.

The rejection power is defined as the inverse variable of the efficiency, thus it is calculated as the ratio between the total number of events and the number of muon tracks reconstructed by the PHTF. A high rejection power is desirable for track segments coincidences that are not reconstructed from muon’s hits in the MB chambers but caused by ghost generation mechanism of the DT local trigger algorithm.

To study the rejection power performance at the Beam Test, a data sample statistically dominated by this kind of events is used. For that purpose, we analyze the PHTF response at the bunch crossings before the scintillator trigger (BX<24). Nevertheless, at these bunch crossings, track segments which correspond to real muons (out-of-time muons) are also reconstructed. Therefore, the response expected from the PHTF at BX<24 is as follows: high efficiency for high quality signals (caused by real muons), and low efficiency (high rejection power) for low quality signals, which correspond to fake track segment reconstructions.

This working principle can be qualitatively checked by comparing the quality distribution of the coincidences (Fig. 6.25) at BX<24 with the quality distribution of the track segments used by the PHTF to reconstruct a muon track (Fig. 6.26) at the same bunch crossings. In Fig. 6.25, the two kind of signals expected at BX<24, ghosts and out of time muons, are clearly identified in the low quality and high quality regions respectively. After the PHTF performs its extrapolating task (Fig. 6.26), the high quality region clearly dominates the distribution. The PHTF matches high quality track segments which correspond to real muons and discards low quality coincidences, more likely to be caused by noise at the MB chambers or ghost reconstructions of the Local Triggers.

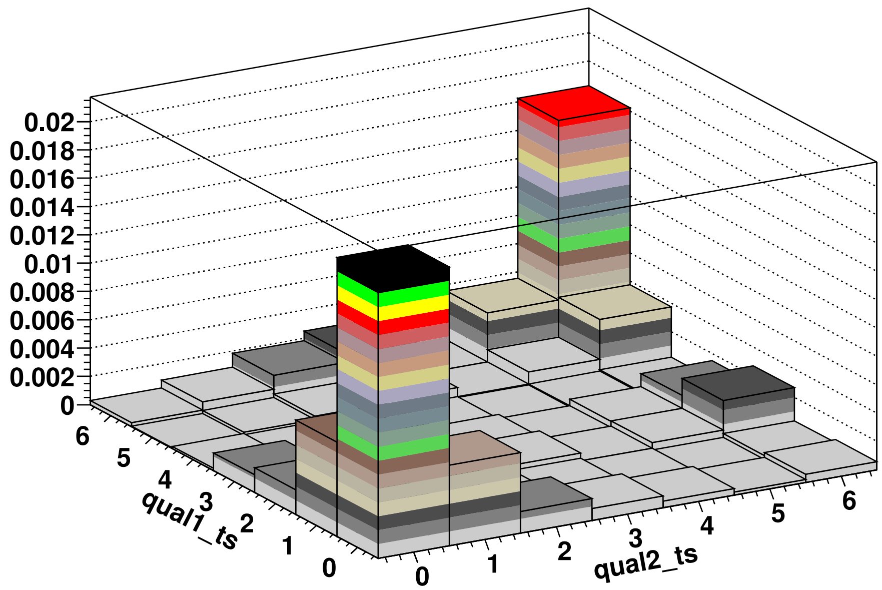

Figure 6.25: *Occupancy of track segment coincidences distributed attending at their quality for BX<17.*

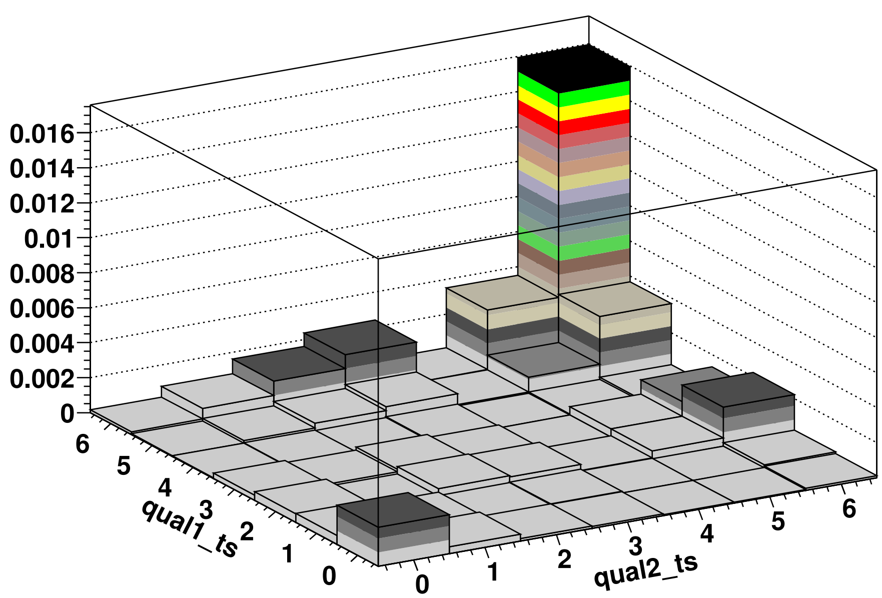

Figure 6.26: *Occupancy of track segment coincidences used by the PHTF to reconstruct a muon track, distributed attending at their quality for BX<17.*

A quantitative approach must also be followed. For that purpose, we analyze the rejection power of the PHTF at BX<24 for different run conditions. The trigger efficiency (inverse of the rejection power) results are shown in tables 6.7 and 6.8. Both he overall efficiency and the efficiency of the different quality samples are shown. Figs. 6.27 and 6.28 represent these numbers as a function of the energy of the muon beam.

Runs without iron slabs

RUN ID	ENERGY (GeV)	EFFICIENCY (%) OVERALL	HH	HL-LH	LL
2600	50	36.0 ± 0.4	98.8 ± 0.2	62 ± 1	17.6 ± 0.4
2555	100	48.1 ± 0.7	94.6 ± 0.7	59 ± 2	28.2 ± 0.8
2597	150	38.7 ± 0.4	97.9 ± 0.3	63.6 ± 0.9	18.5 ± 0.4
2729	250	38.6 ± 0.4	94.6 ± 0.4	58.5 ± 0.9	18.1 ± 0.3
2730	250	38.8 ± 0.6	93.9 ± 0.6	59 ± 1	17.9 ± 0.5
2734	250	39.0 ± 0.3	93.8 ± 0.4	59.1 ± 0.8	17.5 ± 0.3
2540	300	41 ± 3	97 ± 3	59 ± 6	24 ± 3
2550	300	38 ± 1	92 ± 2	53 ± 3	26 ± 1
2551	300	43 ± 1	94 ± 1	54 ± 2	29 ± 1

Table 6.7: *Overall Efficiency and efficiency of the different quality samples at BX<24 for runs without iron slabs*

Runs with iron slabs

RUN ID	ENERGY (GeV)	EFFICIENCY (%) OVERALL	HH	HL-LH	LL
2599	50	36.4 ± 0.4	98.8 ± 0.3	65 ± 1	18.3 ± 0.4
2553	100	46.7 ± 0.9	95.7 ± 0.8	56 ± 2	28 ± 1
2554	100	46.5 ± 0.7	94.1 ± 0.8	56 ± 2	26.4 ± 0.8
2538	140	47.3 ± 0.6	91.6 ± 0.8	56 ± 1	27.7 ± 0.8
2598	150	36.7 ± 0.4	97.4 ± 0.3	63 ± 1	17.9 ± 0.4
2539	300	39.5 ± 0.8	94 ± 1	49 ± 2	25.1 ± 0.8
2552	300	34.9 ± 0.9	92 ± 2	47 ± 2	24 ± 1

Table 6.8: *Overall Efficiency and efficiency of the different quality samples at BX<24 for runs with iron slabs*

The overall efficiency ranges between 35% an 45%, thus the rejection power is between 2.2 and 2.9. More interesting are the efficiency values achieved for the different quality samples. The efficiency for the high quality sample (HH) is around 95%. Although the efficiency is lower than for the same quality sample at BX=24, the PHTF still reconstructs efficiently muon tracks from high quality track segments. For the low quality sample (LL) a rejection power of ~5 is achieved. At BX=24, the rejection power of LL coincidences

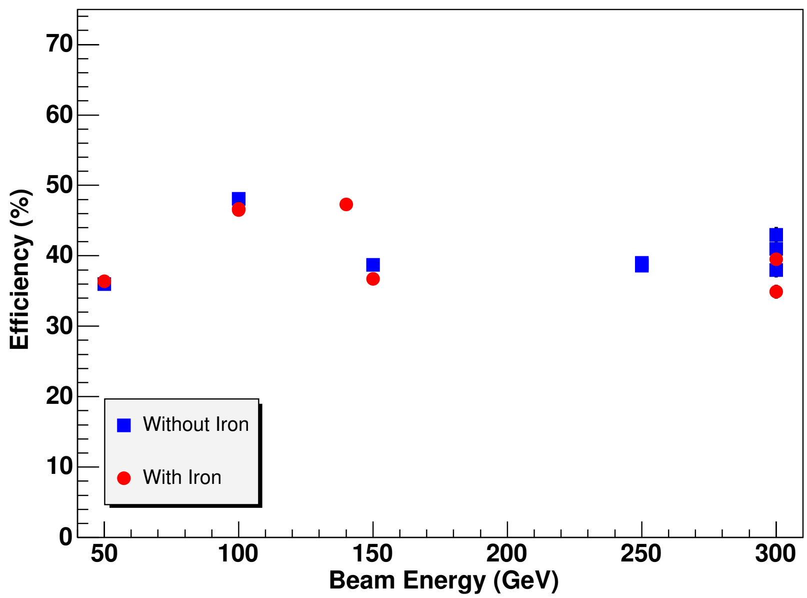

Figure 6.27: *Overall Efficiency for Iron and No Iron runs vs Beam Energy*

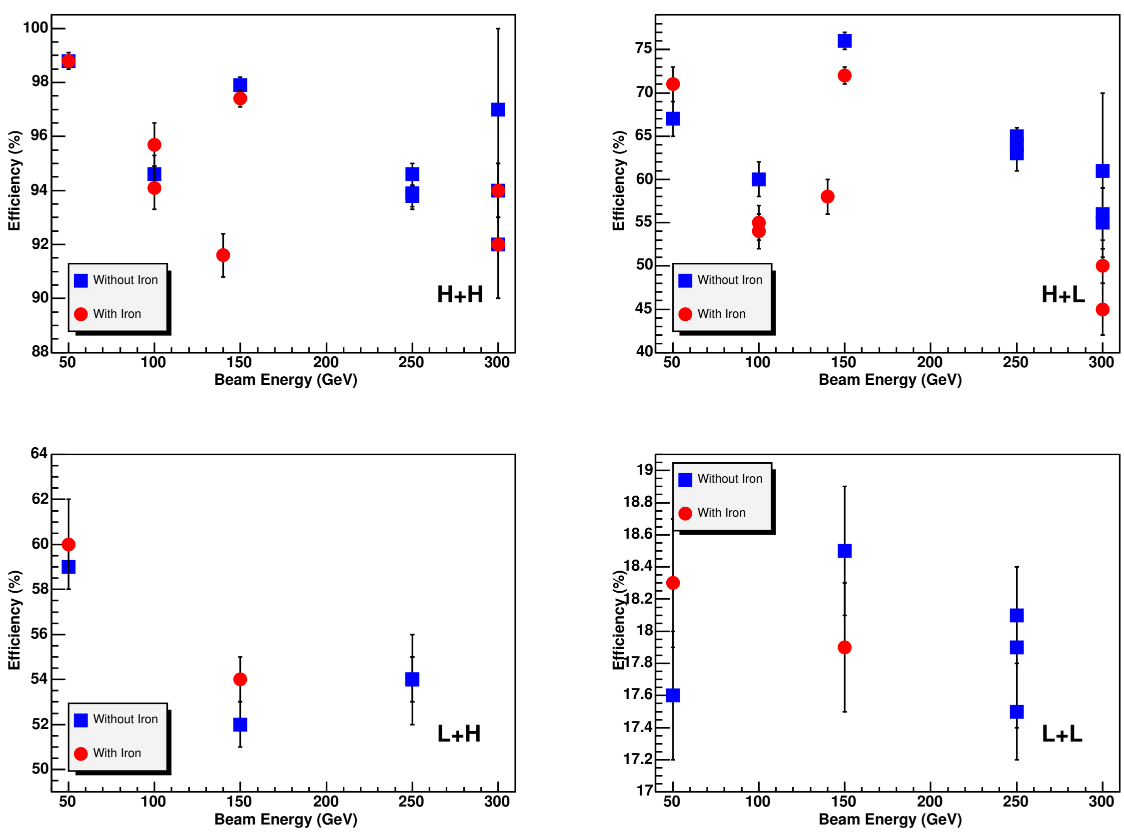

Figure 6.28: *Efficiency for the different quality samples*

was 1.25. Therefore, the PHTF is actually rejecting Local Trigger ghosts reconstructions four times more efficiently than low quality reconstructions of real muons. Furthermore, the rejection power increases to 8 when very low quality ($q_{MB1} = 0$ and $q_{MB2} = 0$) coincidences (00) are considered.

Due to the independence of the occupancy with the presence/absence of the iron slabs, the efficiency values of this two different sets of runs do not differ significantly.

In conclusion, the PHTF shows high efficiency (95%) when reconstructing what we have defined as out-of-time muons. The efficiency decreases by a factor 5 for ghosts, achieving a rejection power of ~5. Therefore, the PHTF is able to rule out fake-muon track segments from the Local Trigger while it reconstructs muon tracks from real-muon signals.

6.5.3 Ghost and Noise Suppression Filters

The DTTF system foresees the possibility of switching on two alternative filters for noise and ghost suppression. During the Beam Test, both filters were tested with dedicated runs of $4 \cdot 10^4$ triggers. The analysis approximation is to confirm the agreement between the scheme as implemented in the hardware and the corresponding off-line cut. Once the agreement is confirmed, it is possible to analyze the performance of the selected cut and compare it with a 'standard' run.

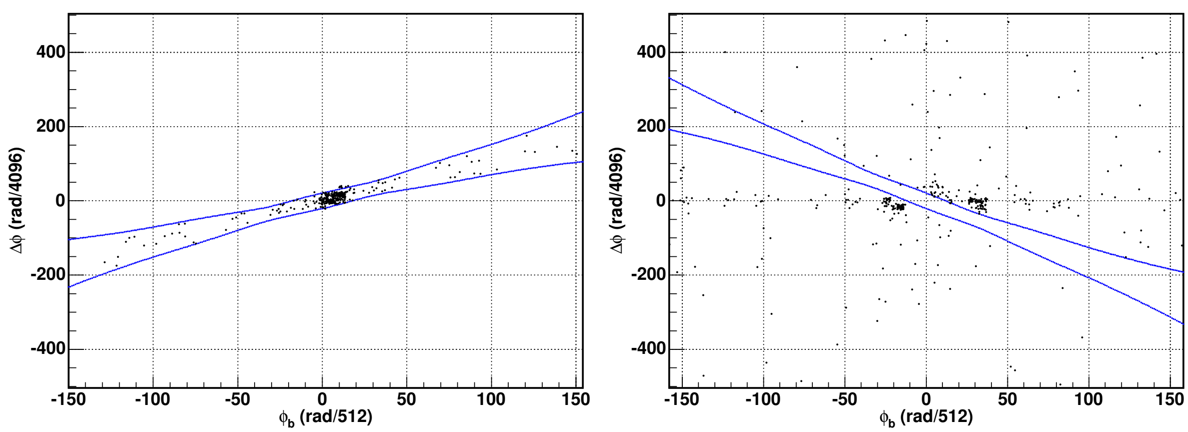

Figure 6.29: *Black points show the $(\Delta\phi, \phi_b)$ (left) and the $(-\Delta\phi, \phi_{bMB2})$ (right) distributions for the coincidences discarded by the PHTF to reconstruct a track, although they fall inside the 1-2 LUT. The left figure illustrates the cut principle.*

Extrapolation 2→1

The first of the runs was dedicated to the '2→1 scheme'. In the hardware, a extrapolation LUT with source segment at MB2 and target segment at MB1 (backward LUT) is loaded. For the Beam Test, a '2→1' LUT which took into account the experimental setup geometry was calculated. The details of the calculation were already given in Section 5.3.

When the '2→1 scheme' is switched on and a extrapolation from MB1 to MB2 is successful, the PHTF algorithm checks whether the extrapolation from MB2 to MB1 is also successful. If it is not the '1 → 2' extrapolation will be ruled out. In the Beam Test conditions, where a MB1 and a MB2 were available, the effect of this cut is easy to analyze. If it is not possible to perform a '2→1' extrapolation, even if the '1 → 2' was successful no muon track must be reconstructed.

Fig. 6.29 illustrates the cut working principle. In the figures, the black points represent track segments which $(\Delta\phi, \phi_b)$ relationship was between the 1 → 2 LUT thresholds but were not used to form a muon track. It is expected that the 2→1 cut made its work on those points. This statement is confirmed and illustrated in the right figure of Fig. 6.29 where the 2→1 $(\Delta\phi, \phi_b)$ relationship is shown for those points. As they all fell outside the 2→1 LUT thresholds, they were cut off and not used to reconstruct a muon track. Therefor, the filter hardware implementation is validated.

Quality cut

The other possible noise and ghost reduction scheme that can be switched on in the hardware will be referred as 'Quality cut'. If switched on, the PHTF will reject all track segments source of an extrapolation that do not pass a custom chosen quality level (track segment's quality codes are shown in Table 3.1). At the Beam Test only MB1 track segments could be source of an extrapolation (if the 2→1 feature is not switched on). Therefore, track segments delivered by the MB1 Local Trigger with a quality value under a certain threshold will be discard as possible source of an extrapolation and no muon track will be reconstructed from them.

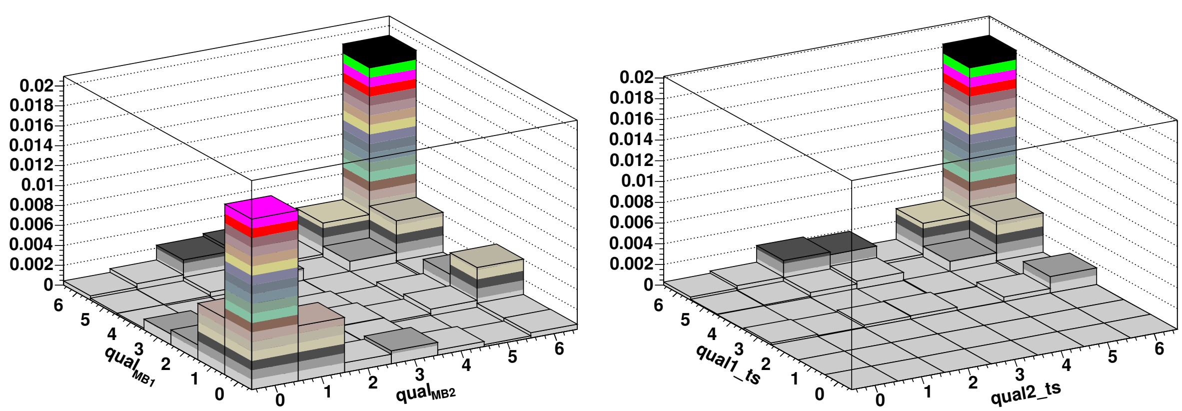

Figure 6.30: *Illustration of the 'Quality cut' working principle. The quality distributions for coincidences (left) and PHTF extrapolations (right) when BX<17 is shown. The 'Quality cut' works on the inputs by discarding all coincidences with* $q_{MB1} < 3$.

A dedicated run with the quality threshold for MB1 track segments set to 3 was taken. It was expected that only MB1 track segments with $q \geq 3$ segments were used to reconstruct muon tracks.

The 'Quality cut' working principle is illustrated in Fig. 6.30. The quality distribution when BX<17 for both coincidences and extrapolations is shown. The cut is not applied to the inputs, thus the left plot includes track segments with all possible quality values. Track segments at MB1 with a quality value below 3, are not used to reconstruct a muon track. Therefore, the PHTF extrapolations distribution (right plot) is completely empty at the region characterized by $q < 3$. In conclusion, the 'Quality cut' hardware implementation is validated.

Filters performance

Once the hardware implementation of the filters has been validated, the rejection power performance is analyzed. Their performance, both for single muons (BX=24) and ghosts (BX<24), is presented and compared with the performance of 'standard' runs, i.e. runs taken with the same experimental setup and the same muon beam conditions but without switching on any extrapolation filter.

RUN	DESC	ENERGY	OVERALL	HH	HL-LH	LL
2731	Q CUT	250	92.6 ± 0.1	99.94 ± 0.01	66.9 ± 0.6	33 ± 2
2732	2→1	250	96.2 ± 0.1	99.87 ± 0.02	83.6 ± 0.4	64 ± 2
2734	NO CUT	250	98.2 ± 0.1	99.96 ± 0.01	92.5 ± 0.3	80 ± 2
2729	NO CUT	250	98.0 ± 0.1	99.95 ± 0.01	91.7 ± 0.4	79 ± 2

Table 6.9: *Efficiency at BX=24 (real muons) for runs with noise and ghost suppression filters switched on.*

RUN	DESC	ENERGY	OVERALL	HH	HL-LH	LL
2731	Q CUT	250	27.4 ± 0.3	95.1 ± 0.3	41.9 ± 0.8	3.9 ± 0.2
2732	2→1	250	28.3 ± 0.3	93.7 ± 0.4	47.2 ± 0.8	3.8 ± 0.2
2734	NO CUT	250	39.0 ± 0.3	93.8 ± 0.4	59.1 ± 0.8	17.5 ± 0.3
2729	NO CUT	250	38.6 ± 0.4	94.6 ± 0.4	58.5 ± 0.9	18.1 ± 0.3

Table 6.10: *Efficiency at at BX<24, when noise and ghosts dominate the data sample, for runs with noise and ghost suppression filters switched on.*

Table 6.9, shows the efficiency values for a single muon sample at BX=24. Only the position range covered by the plastic scintillators is considered. The sample is expected to be formed by real muons' track segments. Therefore, the effect of the filters on the efficiency of real muons can be discussed. The overall efficiency of the 'Q cut' run is reduced a ∼6% respect to the standard runs. This efficiency is achieved by drastically cutting all events with low quality at MB1. For the '2→1' run the overall efficiency drops only a 2%. Most interesting is that, for the two runs considered, the high quality sample (HH) efficiency is not affected. All runs (standard and filtered) achieved a 99.9% efficiency. The impact on the LL sample is much higher for the 'Q cut' run (33% efficiency) than for the '2→1' run (64% efficiency). From these results it is concluded that switching on the filters does not have a significant impact on the PHTF task of reconstructing real muons.

However, the scenario where the performance of the extrapolation filters is to be tested should be characterized for a high occupancy of noise and ghost signals. Table 6.10 shows the efficiency values for these runs when BX<24 and single muons are considered. Fig. 6.31 illustrates these values.

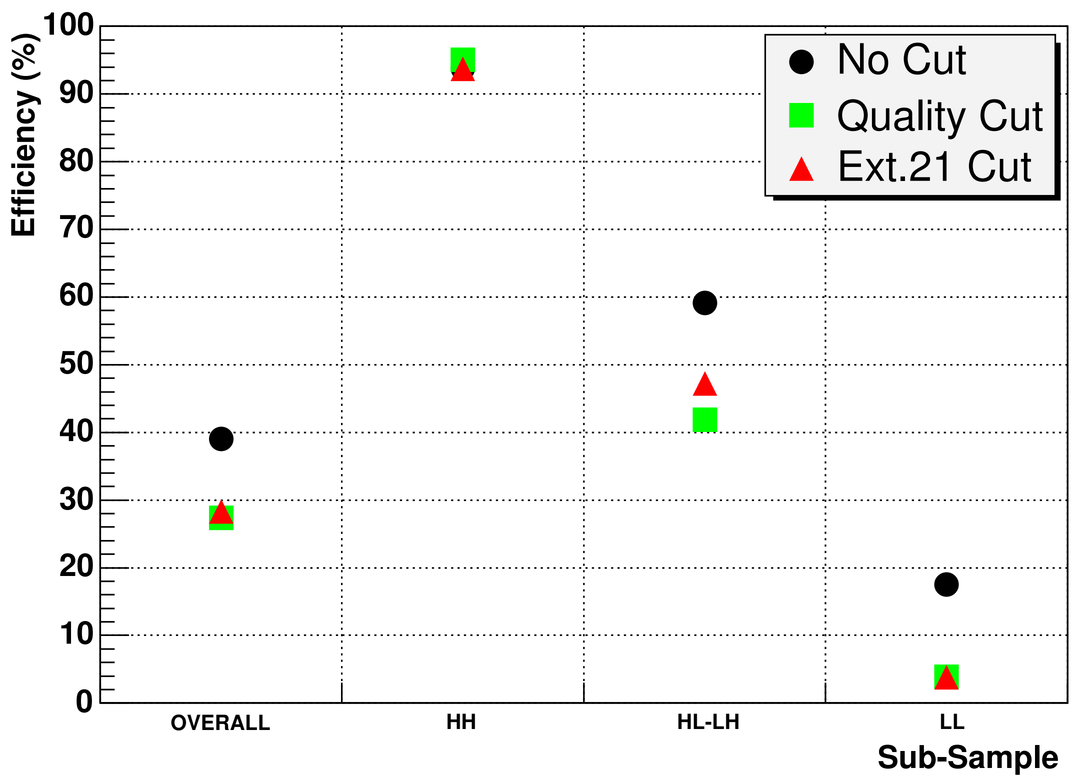

Figure 6.31: *Cuts comparison for BX<24.*

The overall efficiency drops a ∼10% for the 'Quality' and the '2→1' cuts. These losses are achieved by improving the rejection power for low quality coincidences in a factor 5. The efficiency for the LL quality sample drops from a 18% to a 4%, i. e. the rejection power increases from 5.5 to 26. Thus, track segments typically reconstructed from noise or ghosts generation mechanisms are rejected 5 times more 'efficiently' when the filters are switched on. Notice that the efficiency for high quality coincidences is maintained at a ∼94%, which is the same value achieved at the standard runs. Therefore, the PHTF still reconstructs efficiently real muons with the filters switched on.

It is also interesting to compare the performance of the different filters (Fig. 6.31). The effect of applying the 'Quality cut' and the '2→1 extrapolation cut' is very similar. The main difference is that the 'Quality cut' is filtering out all low quality muons for a given quality threshold. In particular, it 'drastically' achieves low efficiencies for the LH subsample. Thus, to its contribution to the overall efficiency. On the other hand the '2→1 extrapolation cut' achieves rather similar efficiency values for real muons (high quality track segment coincidences at BX<24 and all coincidences coming at BX=24) while it achieves the same rejection power value (∼25) for the LL quality sample. In conclusion, both cuts' work is rather similar. However, the '2→1 cut' is most interesting from the DTTF system point of view. The extrapolation principle is applied to reject ghost track segment signals, while the 'Q cut' performs its work based on the DT Local Trigger algorithm.

6.6 Transverse Momentum Assignment Performance

In this section we will analyze the DTTF Trigger performance in the assignment of transverse momentum to muon candidates. In previous sections we studied the performance of the system on reconstructing muon candidates from Local Trigger segments. However, the task of the DTTF is not only to find muon tracks but also to assign them physical parameters (p_T, position and charge). Those parameters are used in latter stages of the Trigger System to decide whether a muon track must be considered for further analysis.

When only MB1 and MB2 deliver data, the azimuth position assignment relies only in a conversion of the MB chambers coordinates into the whole detector coordinates. Therefore, the muon track position resolution is completely determined by the position resolution achieved by the MB2 Local Trigger (Fig. 6.13), i.e. 0.54 mm. The DTTF system delivers the ϕ position in 2.5^o units (0.04 rad).

The transverse momentum assignment is an outstanding feature for the CMS Trigger performance. Latter steps of the Level 1 Trigger algorithm rely in the p_T value assigned to the muon. In Section 6.1.2 we validated the PHTF p_T assignment algorithm by confirming that the Look-Up-Tables downloaded in the board were correctly used. However, the performance of the Look-Up-Tables was not discussed. In this section we will carry out this analysis by studying the resolution on the p_T assignment. First, we will analyze the p_T assignment in terms of the transverse momentum resolution distribution. After, the turn on curves will be discussed. The p_T turn-on curves plot the efficiency of the p_T assignment as a function of the muon p_T for different p_T thresholds applied.

6.6.1 Data Taking Strategy: $\Delta\phi$ Scan

At CMS, the transverse momentum measurement is performed by measuring the muon bending inside the high magnetic field. The bending of the muon is calculated from the change of the position from a MB chamber to another. However, at the Beam

Test no magnetic field was present. Therefore, to study the DTTF transverse momentum resolution, an analysis strategy had to be carried out.

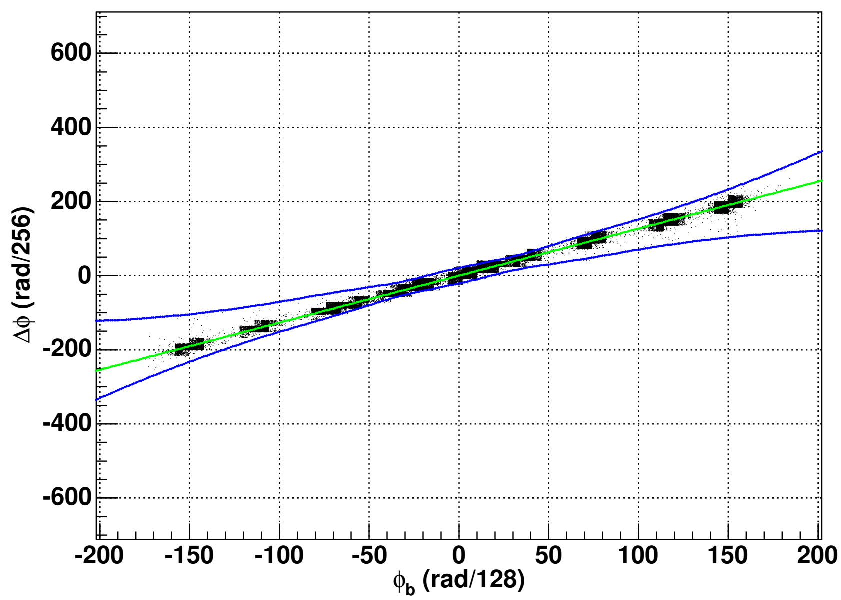

Figure 6.32: *$\Delta\phi$-ϕ_b distribution for the '$\Delta\phi$ Scan' runs. Different values of ϕ_b simulate different values of p_T.*

As we already described in Section 5.3, the perpendicular incidence of muons into the chambers ($\Psi \simeq 0$) is translated into an useful relation: $\phi \simeq -\phi_b$. The PHTF uses the $\Delta\phi$ value of the most inner stations from where the muon track was reconstructed to assign it a p_T value. Therefore, the beam spread (different values of ϕ_b at MB1), simulates different p_T values (Fig. 5.7).

For a detailed analysis of the p_T assignment performance, the $\Delta\phi$ range covered when MB chambers are at its nominal position, i.e. the $(\Delta\phi, \phi_b)$ distribution is placed in the center of the extrapolation Look-Up-Table, is not enough. The full range of $\Delta\phi$ has to be covered if all the p_T range is to be studied. For that purpose, a set of runs defined as '$\Delta\phi$ Scan' was taken. It was formed by 20 runs, of $5 \cdot 10^4$ triggers each, with different configurations of the MB chambers. The nominal beam energy was 100 GeV.

The $(\Delta\phi, \phi_b)$ distribution of the '$\Delta\phi$ Scan' runs is plotted in Fig. 6.32. Only tracks segments used to reconstruct a muon track (those that fall inside the Look-Up-Table) are shown. The distribution follows the mean $(\Delta\phi, \phi_b)$ relationship expected at the Beam Test (green line in the figure).

6.6.2 Transverse Momentum Resolution.

For the transverse momentum assignment, the PHTF relies on Look-Up-Tables. Such LUTs are calculated using data from simulations and are defined with a given efficiency, namely 50%, as was explained in Section 4.2.5. The performance of the transverse momentum assignment is evaluated considering the resolution achieved, which is given in terms of the $1/p_T$ residual distribution:

$$p_T \cdot \delta(\frac{1}{p_T}) = \frac{\Delta p_T}{p_T} \tag{6.2}$$

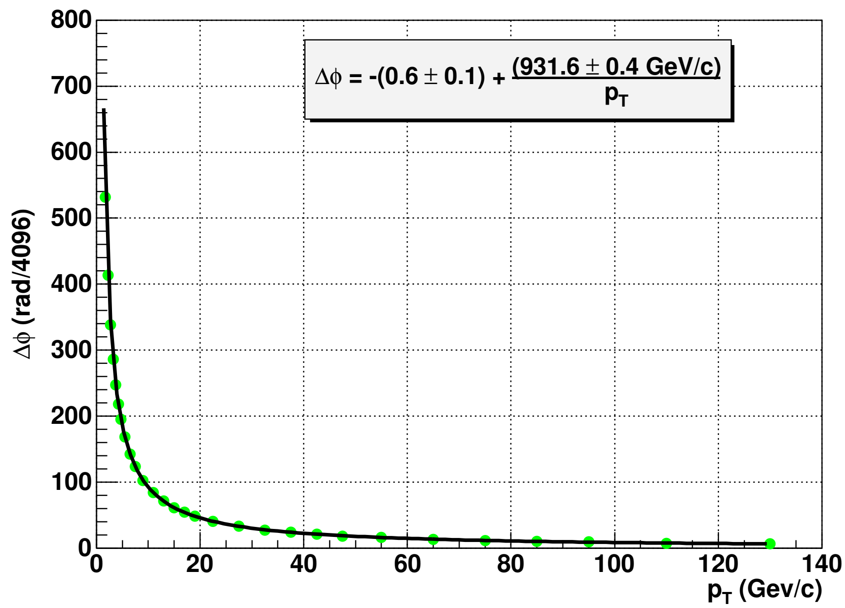

Figure 6.33: $\Delta\phi - p_T$ *correlation used to calculate* (p_{Tgen}) *for high-*p_T *muons.*

The error in the transverse momentum measure (Δp_T) is expressed as the difference between the actual value of the transverse momentum (p_{Tgen}) and the transverse momentum measured by the DTTF system (p_T). Then, the p_T resolution is given by the following expression:

$$\frac{\Delta p_T}{p_T} = \frac{p_{Tgen} - p_T}{p_T} \tag{6.3}$$

According to expression 6.3, to calculate the p_T resolution the p_{Tgen} value associated to the muon must be known. Therefore, we must be able to provide a method for its calculation. To determine which is the p_T of a muon, the difference on the spatial ϕ coordinate of the two innermost track segments, which in this case can only come from MB1 and MB2, is used. The bending angle (ϕ_b) at the innermost station (MB1 at the

Beam Test) is used to resolve the ambiguity in the $\Delta\phi$ -p_T relationship between low-p_T and high-p_T muons.

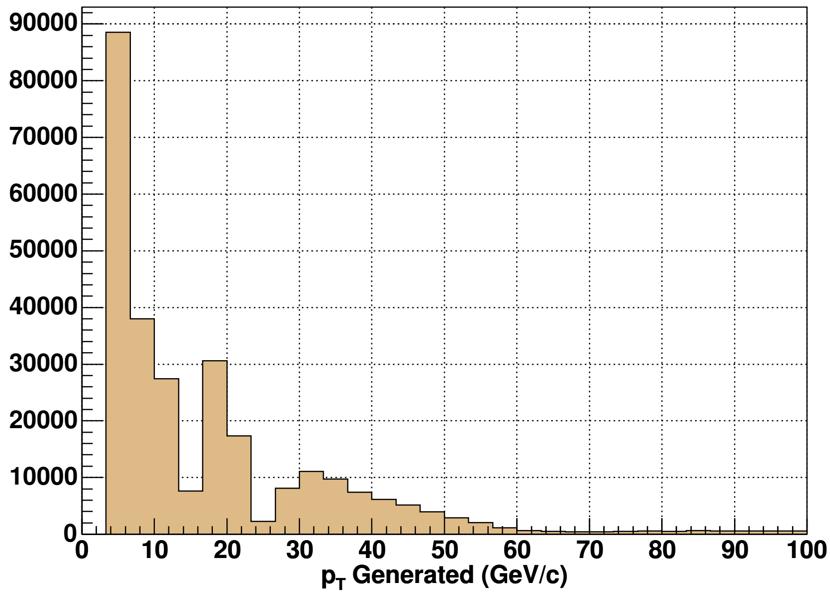

Figure 6.34: *Resulting p_T-generated spectrum calculated from the $\Delta\phi$ distribution measured by the MB chambers.*

Using data from the system simulations, the expected '$\Delta\phi - p_T$' and distribution is parametrized and converted into the LUTs format used by the hardware. The profile of each distribution is fitted with an appropriate function. Attending to the p_T-assignment algorithm, the '$\Delta\phi - p_T$' distribution should be fitted by two different functions: one for the low-p_T branch and another for the high-p_T branch. The fitting functions are converted into LUTs and loaded into the hardware. Fig. 6.33 shows the function that generated the high-p_T assignment LUT used at the Beam Test.

The fitting functions provide us a way to calculate the actual p_T of a muon as long as we can achieve an accurate measure of the $\Delta\phi$ value. The most precise measurement of the ϕ position that can be obtained by the DT system is given by the MB chambers hits themselves. Data recorded by the readout electronics provide us with the position where the muon hit the ϕ layers of the MB chamber. The offline reconstruction of these hits is the most accurate measurement of the position where the muon crossed the MB chamber. Therefore, we will use the $\Delta\phi$ values measured by the MB chambers and the inverted $\Delta\phi(p_T)$ relationship to estimate the p_T. This leads us to the p_{Tgen} value of the reconstructed muon, that will be used to calculate the p_T resolution.

The p_{Tgen} spectrum distribution (Fig. 6.34) is related to the $\Delta\phi$ distribution through the hyperbolic relation shown in Fig. 6.33. As the $\Delta\phi$ distribution of the Beam Test data is uniform, the p_{Tgen} spectrum is distributed as $1/p_T^2$. Gaps in the distribution correspond to gaps in the $\Delta\phi$ sample of the '$\Delta\phi$ Scan' set of runs (Fig. 6.32).

Once a method to calculate the p_{Tgen} has been presented, we can proceed to analyze the p_T-resolution achieved by the DTTF system. Expression 6.3 is used. The results are plotted in Fig. 6.35.

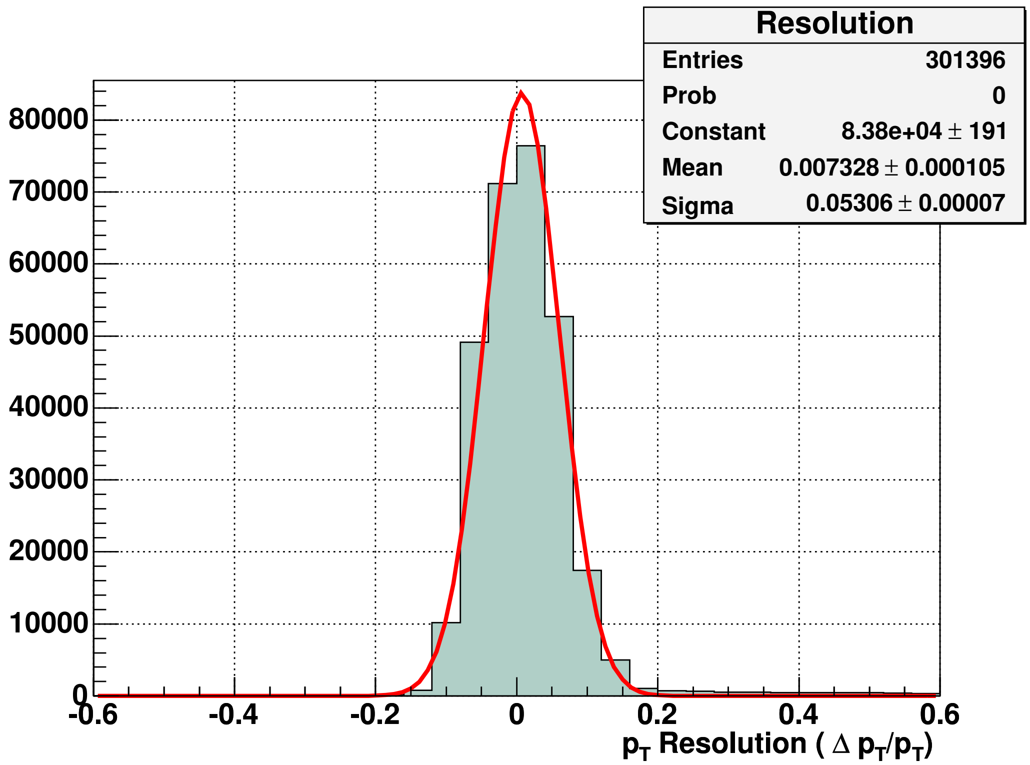

Figure 6.35: *p_T resolution distribution.*

It must be emphasized that it is the first time the DTTF p_T resolution has been measured from a real muon data sample. The resolution on the transverse momentum depends on the muon sample used through the dependence of $\Delta\phi$ with p_T. Simulated muon data samples, as those employed for the studies described in Section 4.7.2, are generated according to a chosen distribution in p_T. The results shown here do not depend on a particular choice of the simulated data. They are calculated from a real muon sample detected at the MB chambers.

The measured p_T-resolution is 5.3%. The p_T-resolution distribution is centered at $\frac{\Delta p_T}{p_T} = 0$. Despite the dependence of the resolution on the p_T spectrum of the data sample, a comparison to simulated results is possible. Simulated data samples employed for the study of the DTTF performance were typically generated with a similar p_T spectrum as the one under study here (Fig. 6.34). Resolution values obtained from simulated data when MB1 and MB2 track segments are used to reconstruct the muon track are 13.9% (Section 4.7.2).

Therefore, a difference in quadrature of an 12.8% on the p_T resolution is found between data taken at the Beam Test and simulated data. This difference must be explained in terms of the different conditions on where the Beam Test was developed respect to the conditions expected at CMS as coded in the simulation. Namely, the absence of dead material between the MB chambers. Considering the p_T-assignment algorithm, bad resolutions on p_T stem from bad resolutions and uncertainties in the $\Delta\phi$ measurement.

Uncertainties in the $\Delta\phi$ measurement at CMS were already discussed at Section 4.2.2, when the extrapolation LUTs principles were described. Two main effects were pointed as the main source of uncertainties. First, the finite resolution in the measurement of the ϕ position delivered by the DT Local Triggers to the DTTF. Second, the presence of dead material, i.e. iron yoke, between the MB chambers through multiple scattering and dE/dx processes.

At the Beam Test, no dead material was present between th MB chambers. Therefore, only the Local Trigger resolution of the ϕ position could affect the resolution of the p_T value. Comparing the results from simulations of the detector and the results of the Beam Test described here, it is possible to estimate the contribution of the dead material to the p_T resolution. The total resolution can be considered as the sum in quadrature

$$\sigma_{total} = \sigma_{Local\ Trigger} \oplus \sigma_{dead\ material} \tag{6.4}$$

of the two contributions defined above: the Local Trigger position resolution and the effect of the dead material on the muon path. Therefore, about a 12.8% resolution is due to the interaction of the muons with the dead material of the Muon System of CMS. Therefore, the unavoidable effect of the dead material completely dominates the expected p_T-resolution of the system.

Another difference is observed when comparing the Beam Test p_T resolution distribution with that obtained when using simulated data. Fig. 4.23, which plots the p_T resolution for simulated data, show a negative offset for the mean value of the p_T resolution distribution, namely -0.14. Our distribution is centered on 0, as we already said. At the simulations, 90% efficiency p_T-assignement LUTs were used while at the Beam Test 50% efficiency LUTs where loaded in the PHTF electronics. If the LUTs are calculated to achieve a 50% efficiency, attending to the p_T resolution expression (6.3), it is expected that half of the muon tracks are assigned a $p_T > p_{Tgen}$ and the other half a $p_T < p_{Tgen}$, thus the distribution is expected to be centered on 0. When the efficiency is set to the 90%, a negative offset is expected, as 90% of the tracks will be assigned with a $p_T > p_{Tgen}$.

6.6.3 Turn-on Curves

Once the p_T resolution distribution has been study, the p_T turn on curves must be discussed. The transverse momentum plays an outstanding role in the L1 trigger decision. The performance of the DTTF when applying cuts on certain p_T thresholds is a main issue in the analysis of the overall DTTF Trigger performance. This analysis can be performed by studying the p_T turn-on curves, where the p_T assignment trigger efficiency is plotted as a function of the generated muon $p_T(p_{Tgen})$, for different p_T thresholds applied.

Ideally the p_T turn-on curves should be a step function reaching the 100% efficiency plateau when $p_{Tgen} = p_T^{cut}$. If the resolution were perfect, the p_T value assigned to the muon track would perfectly agree with the actual muon p_T, as loaded in the LUTs. However, due to bad resolutions in measuring the muon $\Delta\phi$ value or the p_T-assignment LUTs unavoidable granularity, the turn-on curves differ from the ideal situation described above.

The p_T-assignment LUTs were calculated to achieve a 50% efficiency. Therefore, for a given p_T threshold (p_T^{cut}), a 50% of the reconstructed tracks with $p_{Tgen} \geq p_T^{cut}$ must be assigned with a p_T value greater than the threshold $p_T \geq p_T^{cut}$. Thus, the turn-on curves must reach a 50% efficiency at the given p_T threshold.

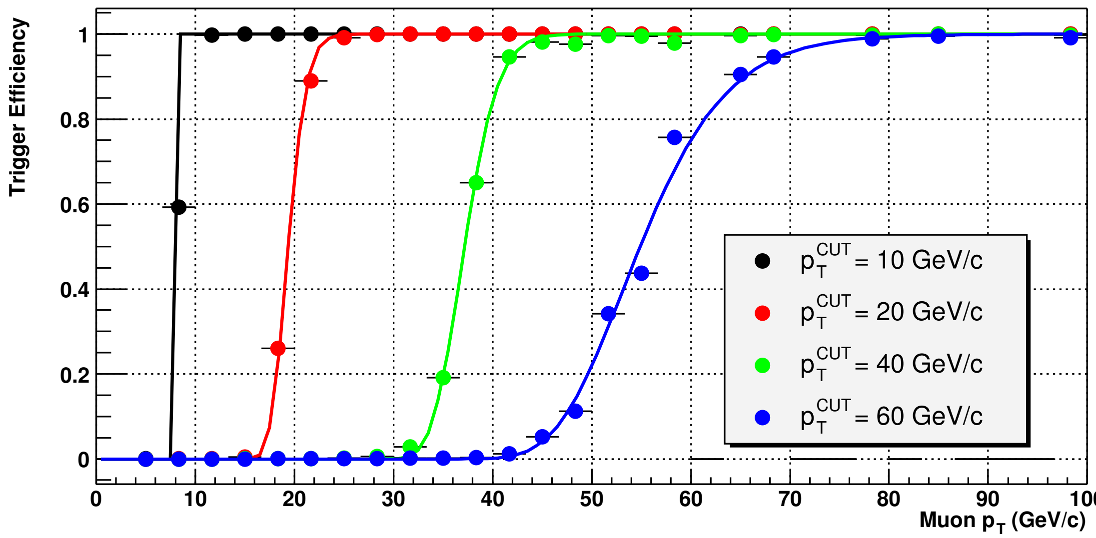

Figure 6.36: *Turn on Curves for different p_T thresholds.*

In Fig. 6.36 the p_T turn on curves are shown. As discussed in the previous section, the p_T resolution depends on p_T, through the dependence of p_T on $\Delta\phi$

$$\Delta\phi \sim \frac{1}{p_T} \tag{6.5}$$

As the resolution on $\Delta\phi$ is known to be a constant, and considering the dependence of p_T on $\Delta\phi$ (Expr. 6.5), the resolution on $1/p_T$ must also be a constant. We define this constant ('a') in Expr. 6.6:

$$a \equiv \sigma(\frac{1}{p_T}) \sim \text{constant} \tag{6.6}$$

Now, we can fit the turn-on curves with the error function expressed in 6.7:

$$Eff(p_T) = \frac{1}{2}\left[1 + Errf\left(\frac{1}{a}\left(\frac{1}{p_T} - \frac{1}{p_T^{50}}\right)\right)\right] \tag{6.7}$$

All the dependence on the p_T threshold applied is accomplished by the p_T^{50} term and 'a' is a parameter of the system (related to the resolution on $\Delta\phi$) which is given in units of $(\mathrm{GeV/c})^{-1}$. p_T^{50} determines the p_T value where the 50% efficiency is expected to be reached for the given p_T threshold. Ideally, p_T^{50} should be equal to the applied threshold. These statements have been confirmed with data. Table 6.11 shows the 'a' and p_T^{50} fitted values for the different p_T thresholds (turn-on curves).

p_T^{cut} (GeV/c)	p_T^{50} (GeV/c)	$a \cdot 10^{-3}$ $(\mathrm{GeV/c})^{-1}$
10	7.8 ± 0.1	1.0 ± 1.0
20	18.9 ± 0.1	0.7 ± 0.7
30	26.83 ± 0.02	1.04 ± 0.05
40	37.13 ± 0.02	1.07 ± 0.02
50	48.90 ± 0.03	1.03 ± 0.02
60	55.23 ± 0.05	1.12 ± 0.02

Table 6.11: *Fitting parameters of the Turn-on Curves.*

In general the curves reach the expected 50% efficiency at the given p_T threshold. However the definition of the bins in which the p_T value is assigned may cause that the 50% trigger efficiency is reached before the threshold, i.e at the beginning of the corresponding p_T bin. Fig. 6.37 plots the value where the 50% efficiency ir reached, p_T^{50}, as a function of the p_T threshold applied, p_T^{cut}, for the values shown in Table 6.11. The expected correlation is 1. The slight deviation from it is due to the p_T bins definition.

In Fig. 6.38, the fitted values of a shown in Table 6.11 are plotted as a function of the p_T threshold applied. The parameter a is independent of the p_T threshold applied, thus it can be considered as a parameter of the system p_T assignment efficiency.

Most interesting is the comparison to the turn-on curves obtained from simulated data (Fig. 4.27). Differences are clearly observed. In general, the same processes described in the previous section, i.e. position resolution of the Local Trigger and the interaction of the muon with the dead material of the detector, cooperate in separating the real situation from the ideal one, i.e. step functions for the turn on curves. These processes smooth the steps of the ideal turn-on curves degrading the resolution of the system. Nevertheless, as already discussed above, at the Beam Test there was no dead material between the chambers. Therefore, only the $\Delta\phi$ resolution has an effect in smoothing the turn-on curves.

This difference is clearly understood by comparing the results of the Beam Test shown at 6.36 with the turn-on curves calculated with simulated data (Fig. 4.27) discussed in Section 4.7.2. The only difference between these two plots is the absence of the iron yoke at the Beam Test. Again, the conclusion is that interaction of muons with the iron yoke dominates the DTTF p_T assignment resolution.

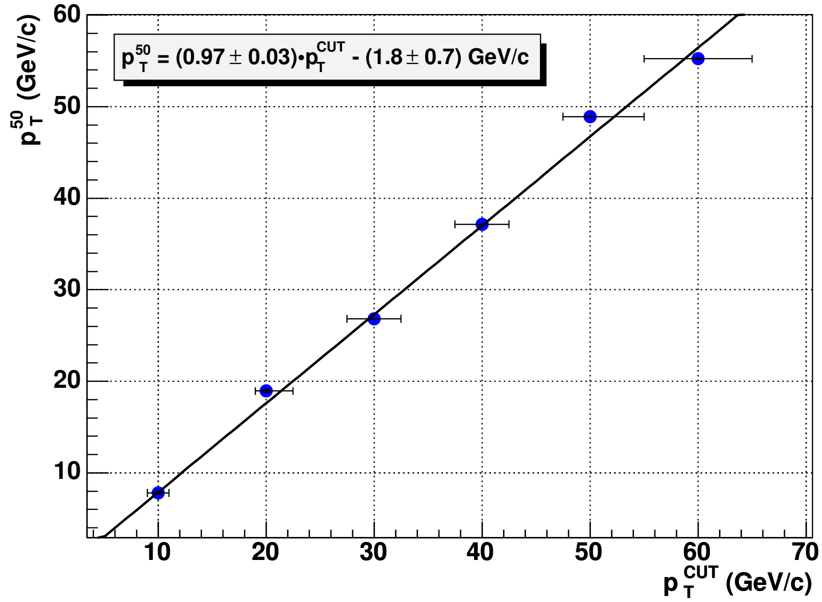

Figure 6.37: *Correlation between the 50% efficient p_T value and the p_T threshold applied.*

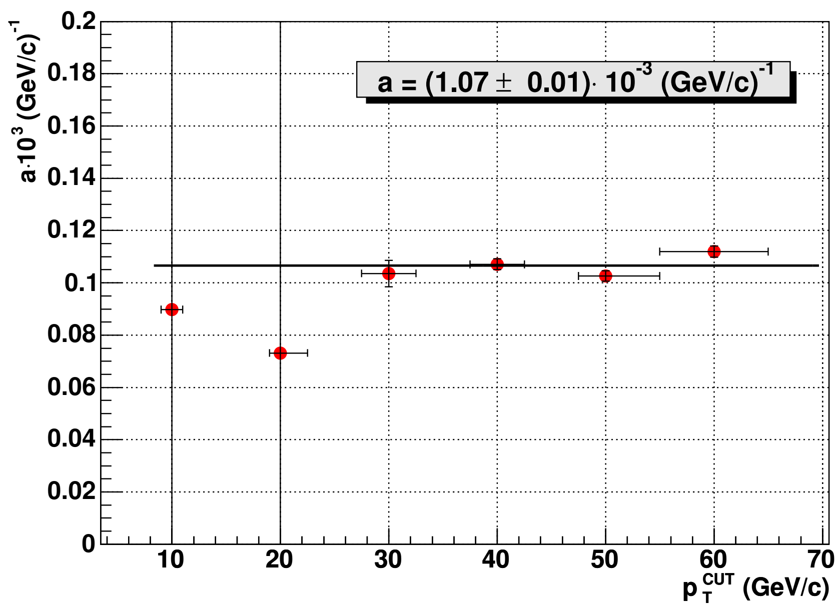

Figure 6.38: *Correlation between the σ value and the p_T threshold applied.*

6.7 Summary

The Bunched Beam Test carried out at CERN during the first weeks of October 2004 was the first time that the DTTF system operated integrated in the full Drift Tube Trigger chain. The DTTF reconstructed its first muon tracks from real muon data. Expectations for the system development and performance were achieved before, after and during the Beam Test.

First, the DT trigger chain got successfully through its first complete interconnection test. All parts of the system, from the DTBX to the Wedge Sorter, were synchronized and tested. They successfully performed their own task for triggering on muons every 25 ns. Besides, all hardware and software tools for configuration, synchronization and operation were tested and thoroughly used during the Beam Test.

From the DTTF point of view, several tools were tested under real data taking conditions. Large experience was accumulated during the system setup period. From the hardware point of view, all the system debugging steps were followed and provided good lessons for future development. The software solutions proved to be the appropriate tools on which the software programs that must be present at the CMS Control Room will be based. In particular, a Local DAQ system, TB-DAQ, was used. In addition to providing high quality data without causing any hang up or trouble, it was used to point out different errors on the Central DAQ system.

Regarding the data analysis, it has been the first time the DTTF system has performed its track finding tasks under real experimental conditions. All steps of the track finding algorithm were validated and understood. A comparison to C++ simulated output from DTBX inputs was carried out and agreement with the actual PHTF output was found in 100% of the events.

Finally, the DTTF Trigger performance was studied from a real muon data sample. The track finding task is performed with a 97% efficiency. This value increases to 99.9% when high quality segments are considered. The rejection power for ghost Local Trigger segment reconstructions is up to 5. The optional track finding ghost and noise filters performance was also analyzed: the rejection power increases a factor 5 (up to 25). Finally, the transverse momentum assignment performance was studied. The p_T assignment resolution at the Beam Test was 5.3%. The turn-on curves were from a real muon p_T distribution for the very first time. Comparison to the performance of the system from simulated data samples was performed as well.

In conclusion, results of the Beam Test can be considered completely satisfactory. Concerning the system setup, large experience has been gained and will be used in future tests of the system. All software and hardware tools employed at the Beam Test will serve as base versions for further development.

Chapter 7

Conclusions

This report contains the analysis of the performance of the CMS Drift Tube Track Finder (DTTF) system at CERN 2004 bunched Beam Test. The DTTF is the electronic system that implements the CMS Barrel Regional Muon Trigger. Historically, the DTTF has been the first L1 electronic trigger design using FPGAs.

The chapters first introduce the LHC collider and the CMS experiment in general, and the CMS trigger in particular. Then, the DTTF design, hardware implementation, online software and simulation tools, and connection to muon physics at CMS are discussed. Next, the description of the 2004 Beam Test setup and corresponding hardware and software tools is given. Finally, the physics data analysis is presented.

The 2004 Beam Test was the first opportunity to test the DTTF hardware and all the software tools for control, configuration, operation, and monitoring with real data. From a more general point of view, that was the first opportunity to test the full L1 DT Trigger chain with muons. The DTTF hardware included a PHTF PreProduction Prototype board, a TIM Prototype board, and a Wedge Sorter Prototype board. The DTTF software included first versions of all the programs expected to run at the CMS Control Room. In particular, a working version of a Local DAQ system, based on the original idea Spy DAQ, was developed and successfully operated.

The results of the data analysis were as expected. At the technical level, all functionalities were thoroughly tested, and the DTTF behavior was perfect in all cases (extrapolation, parameter assignment). At the physics level, the measured efficiencies were very close to 100% for high quality muons. The ghost suppression power was large enough, in particular when the alternative ghost suppression mechanisms were switched on (and without lose of efficiency). Inclusion of dead material between the chambers changed the quality of the DTTF inputs, but not the DTTF efficiency for a given quality. Finally, the p_T assignment resolution and corresponding turn-on curves were measured for the fist time. Comparing to the results of our C++ simulation we concluded that the system resolution is dominated by dead material effects (as it should be).

In conclusion, the electronic prototypes were successfully validated in a realistic physics environment. The performance of all the software tools was excellent, confirming our approach for online software solutions at CMS. A lot of valuable experience setting-up and operating the system was accumulated.

More complex tests of the DTTF system will take place before the LHC era. In 2006 the integrated CMS Trigger will be tested with cosmic muons at the Magnet Test/Cosmic Challenge. Production, installation, and commissioning of the DTTF trigger will happen in 2006 and beginning of 2007, to be ready for the first LHC collisions in April 2007.

Bibliography

[1] ALEPH, DELPHI, L3 and OPAL Collaborations, The LEP Working Group for Higgs Boson Searches, *Search for the Standard Model Higgs boson at LEP*, Phys. Lett. B 565 (2003), 61.

[2] F. Abe et al., CDF Collaboration, Phys. Rev. Lett. 81 (1998) 5748.

[3] D. Acosta et al., CDF Collaboration, Phys. Rev. Lett. 95 (2005) 051801.

[4] "The Large Hadron Collider. Conceptual Design", CERN/AC/95-05 (1995).

[5] CMS Collaboration, *The Compact Muon Solenoid. Technical Proposal*, CERN/LHCC/94-38 (1994).

[6] CMS Collaboration, *The Magnet project. Technical Design Report*, CERN/LHCC/97-10 (1997).

[7] CMS Collaboration, *The CMS Tracker System project. Technical Design Report*, CERN/LHCC/98-06 (1998).

[8] CMS Collaboration, *Addendum to the CMS Tracker Technical Design Report*, CERN/LHCC/00-16 (2000).

[9] CMS Collaboration, *The CMS Electromagnetic Calorimeter. Technical Design Report*, CERN/LHCC/97-33 (1997).

[10] CMS Collaboration, *The CMS Hadron Calorimeter project. Technical Design Report*, CERN/LHCC/97-31 (1997).

[11] CMS Collaboration, *The Muon Project. Technical Design Report*, CERN/LHCC/97-32 (1997).

[12] CMS Collaboration, *The Trigger and Data Acquisition Project, Volume I. The Level-1 Trigger. Technical Design Report*, CERN/LHCC/00-38 (2000).

[13] CMS Collaboration, *The Trigger and Data Acquisition Project, Volume II. Data Acquisition and High Level Trigger. Technical Design Report*, CERN/LHCC/02-26 (2002).

[14] M. Campbell et al., *The CDF Trigger*, NIM A265 (1988) 326.

[15] M. Abolins et al., *The Fast Trigger for the D0 Experiment*, NIM A289 (1990) 543.

[16] M. Arignon et al., *The Trigger System of the OPAL Experiment at LEP*, NIM A313 (1992) 103.

[17] R. Carlin et al., *The Trigger of ZEUS, a Flexible System for a High Bunch Crossing Rate Collider*, NIM A379 (1996) 542.

[18] ATLAS Collaboration, *The Level 1 Trigger. Technical Design Report*, CERN/LHCC/98-14 (1998).

[19] C. Albajar, G. Wrochna, *Isolated Muon Trigger*, CMS Note 2000/067 (2001).

[20] C. Albajar, J.F. de Trocóniz, J. Rohlf, G. Wrochna, *Conceptual design of an improved CMS RPC Muon Trigger using the Hadron Outer scintillators*, NIM A 545 (2005) 97.

[21] F. Gasparini et al., *Bunch crossing identification at LHC using a mean-timer technique*, NIM A 336 (1993) 91.

[22] J.F. de Trocóniz, I. Mikulec, CMS Note in preparation.

[23] C. E. Wulz, *Concept of the First Level Global Trigger for the CMS Experiment at LHC*, CMS Note 2000/052 (2000).

[24] M. Brugger, M. Fierro, C. E. Wulz, *Drift Tube Based Pseudorapidity Assignment of the Level-1 Muon Trigger for the CMS Experiment.*, CMS Note 2001/027 (2001).

[25] J. Ero, *The Data Spy Feature in the Drift Tube Track Finder.*, CMS Internal Note 2004/054 (2004).

[26] CMS Software and Computing Group, *Object Oriented Reconstruction for CMS Analysis.*, CMS Internal Note 1999/001 (1999).

[27] J. Ero, *Control of the Functionality Evaluation Prototype Board for the Drift Tube Track Finder.*, CMS Internal Note 2002/072 (2002).

[28] The XDAQ Home page, http://xdaq.web.cern.ch/xdaq/

[29] C. Albajar et al., *Test Beam analysis of the first CMS Drift Tube Muon Chamber.*, NIM A 525 (2004) 464.

[30] P. Arce et al., *Bunched Deam Test of the CMS Drift Tubes Local Muon Trigger.*, NIM A 534 (2004) 441.

[31] J.F. de Trocóniz, *Calibration and Alignement Procedures at the 2001 Testbeam Analysis.*, CMS Internal Note 2003/020 (2003).

[32] J. Caballero et al., *Some Results on the DT Local Muon Trigger performance from the 2003 Testbeam.*, CMS Internal Note 2004/035 (2004).